INAUGURAL-DISSERTATION

zur Erlangung der Doktorwürde der

NATURWISSENSCHAFTLICH - MATHEMATISCHEN
GESAMTFAKULTÄT

der

RUPRECHT-KARLS-UNIVERSITÄT
HEIDELBERG

vorgelegt von
Diplom-Mathematiker

Stefan Frei

aus Freudenstadt

Tag der mündlichen Prüfung: __________

Eulerian finite element methods
for interface problems
and fluid-structure interactions

Gutachter: **Prof. Dr. Thomas Richter**

Abstract

In this thesis, we develop an accurate and robust numerical framework for interface problems involving moving interfaces. In particular, we are interested in the simulation of fluid-structure interaction problems in Eulerian coordinates.

Our numerical model for fluid-structure interactions (FSI) is based on the monolithic “Fully Eulerian” approach. With this approach we can handle both strongly-coupled problems and large structural displacements up to contact.

We introduce modified discretisation schemes of second order for both space and time discretisation. The basic concept of both schemes is to resolve the interface locally within the discretisation. For spatial discretisation, we present a locally modified finite element scheme that is based on a fixed patch mesh and a local resolution of the interface within each patch. It does neither require any remeshing nor the introduction of additional degrees of freedom. For discretisation in time, we use a modified continuous Galerkin scheme. Instead of polynomials in direction of time, we define polynomial functions on space-time trajectories that do not cross the interface.

Furthermore, we introduce a pressure stabilisation technique based on “Continuous Interior Penalty” method and a simple stabilisation technique for the structural equation that increases the robustness of the Fully Eulerian approach considerably. We give a detailed convergence analysis for all proposed discretisation and stabilisation schemes and test the methods with numerical examples.

In the final part of the thesis, we apply the numerical framework to different FSI applications. First, we validate the approach with the help of established numerical benchmarks. Second, we investigate its capabilities in the context of contact problems and large deformations. We study contact problems of a falling elastic ball with the ground, an inclined plane and some stairs including the subsequent bouncing. For the case that no fluid layer remains between ball and ground, we use a simple contact algorithm.

Furthermore, we study plaque growth in blood vessels up to a complete clogging of the vessel. Therefore, we use a monolithic mechano-chemical fluid-structure-interaction model and include the fast pulsating flow dynamics by means of a temporal two-scale scheme. We present detailed numerical studies for all three applications including a numerical convergence analysis in space and time, as well as an investigation of the influence of different material parameters.

Zusammenfassung

In dieser Arbeit entwickeln wir akkurate und robuste numerische Methoden für Interface-Probleme mit beweglichen Interfaces. Der Fokus liegt hierbei auf der Simulation von Fluid-Struktur-Interaktionen in Eulerschen Koordinaten.

Unser numerisches Modell für Fluid-Struktur-Interaktionen (FSI) basiert auf einem monolithischen Ansatz in Eulerschen Koordinaten ("Fully Eulerian approach"). Mit diesem Ansatz sind wir in der Lage sowohl stark gekoppelte Probleme als auch Probleme mit großen Strukturdeformationen bis hin zu Kontakt zu simulieren.

Sowohl für die örtliche als auch für die zeitliche Diskretisierung entwickeln wir modifizierte Diskretisierungstechniken von zweiter Ordnung. Die grundlegende Idee beider Techniken besteht darin das Interface lokal in der Diskretisierung aufzulösen. Für die örtliche Diskretisierung stellen wir ein lokal modifiziertes Finite-Elemente-Schema auf Basis eines festen Patchgitters vor. Das Verfahren kommt ohne Remeshing und ohne die Einführung von zusätzlichen Freiheitsgraden aus. Für die Zeitdiskretisierung entwickeln wir ein Zeitschrittschema auf Basis eines modifizierten stetigen Galerkinansatzes. Anstatt Polynome in der Zeit zu verwenden, definieren wir polynomiale Funktionen auf Raum-Zeit-Trajektorien, die nur innerhalb eines Teilgebietes verlaufen.

Desweiteren stellen wir eine Druckstabilisierungstechnik basierend auf der "Continuous Interior Penalty"-Methode und eine einfache Stabilisierungstechnik für die Strukturgleichungen vor, welche die Robustheit des Eulerschen Ansatzes für FSI wesentlich erhöht. Wir geben eine detaillierte Konvergenzanalyse für alle genannten Diskretisierungs- und Stabilisierungstechniken und testen die Methoden anhand von numerischen Beispielen.

Im letzen Teil dieser Arbeit wenden wir den entwickelten Eulerschen Ansatz auf verschiedene FSI-Anwendungen an. Zunächst beschäftigen wir uns mit etablierten numerischen Benchmarks, um den Ansatz numerisch zu validieren. Anschließend behandeln wir zwei Anwendungen mit großen Strukturdeformationen und Kontakt.

Als erstes untersuchen wir Kontaktprobleme eines frei fallenden elastischen Balles mit dem Boden, einer schiefen Ebene und mit Treppenstufen und dessen anschließendes Auf- und Abspringen. Für den Fall, dass zwischen Ball und Boden keine Fluidschicht bleibt, wenden wir einen einfachen Kontaktalgorithmus an. Desweiteren simulieren wir das Wachstum von Plaque in Blutgefäßen bis hin zur kompletten Verstopfung mithilfe eines mechano-chemischen FSI-Modells. Die schnell pulsierende Strömungsdynamik geht hierbei mithilfe eines zeitlichen Zweiskalenalgorithmus ein.

Für alle drei Anwendungen präsentieren wir detaillierte numerische Studien, zeigen numerische Konvergenz in Raum und Zeit und analysieren den Einfluss von verschiedenen Materialparametern.

Contents

1 Introduction

The interaction of a fluid flow with a moving or deformable structure plays an important role in many physical processes in medicine, biology and engineering applications. Prominent examples include the interaction of planes, vehicles or wind turbines with the surrounding air in aerodynamics, as well as the interaction of blood flow with the surrounding vessels or the mitral valves in hemodynamics.

These problems have in common that a fluid force causes a deformation or movement of the structure. This, on the other hand, might have a considerable influence on the surrounding fluid flow. In this thesis, we are particularly interested in two-way-coupled problems, meaning that both subproblems have a strong influence onto each other.

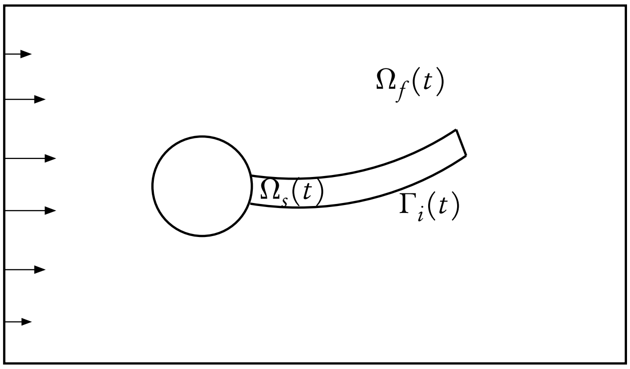

Figure 1.1. Prototypical fluid-structure interaction configuration (Hron & Turek[88]). Fluid forces in the domain $\Omega_f(t)$ cause a displacement and elastic deformations of a beam $\Omega_s(t)$ which is attached to a fixed and rigid cylinder. The coupling takes place at the fluid-structure interface $\Gamma_i(t)$.

In Figure 1.1, we illustrate a prototypical fluid-structure interaction problem. This example is a well-studied numerical benchmark introduced by Hron & Turek[88]. The complete domain Ω is divided into a fluid subdomain $\Omega_f(t)$ and a solid subdomain $\Omega_s(t)$ with a lower-dimensional fluid-structure interface $\Gamma_i(t)$ between them. The governing equations are the incompressible Navier-Stokes equations in the fluid domain, and a hyperelastic material law in the solid domain. The subproblems are coupled by the continuity of velocities and the continuity of normal forces across the fluid-structure interface.

In Eulerian coordinates the complete system is given by

$$\left.\begin{aligned} \rho_f \partial_t v_f + \rho_f (v_f \cdot \nabla) v_f - \operatorname{div} \sigma_f &= \rho_f f_f \\ \operatorname{div} v_f &= 0 \end{aligned}\right\} \quad \text{in } \Omega_f(t),$$
$$\left.\begin{aligned} J \rho_s^0 (\partial_t v_s + v_s \cdot \nabla v_s) - \operatorname{div} \sigma_s &= J \rho_s^0 f_s \\ \partial_t u_s + v_s \cdot \nabla u_s - v_s &= 0 \end{aligned}\right\} \quad \text{in } \Omega_s(t),$$
$$\left.\begin{aligned} v_f &= v_s \\ \sigma_f n &= \sigma_s n \end{aligned}\right\} \quad \text{on } \Gamma_i(t).$$

Here, v_f and v_s are the fluid and solid velocity, u_s the solid deformation, σ_f and σ_s are the Cauchy stress tensors, ρ_f and ρ_s^0 denote the fluid and solid density and f_f and f_s are volume forces.

In the benchmark configuration, an inflow at the left boundary of the fluid domain $\Omega_f(t)$ causes elastic deformations and displacements of a solid beam $\Omega_s(t)$ that is attached to a fixed, rigid cylinder. If this movement is large enough, we observe a strong feedback to the flow where vortices develop. This again has an effect on the solid deformation, etc. Depending on the material parameters of fluid and solid, the beam will either move towards a stationary configuration or describe an oscillatory movement.

Fluid-structure interaction problems pose a number of numerical challenges:

- While the solid equations are traditionally formulated in the *particle-centred* Lagrangian coordinate framework, *spatial-centred* Eulerian coordinates are commonly used for the fluid equations. Consequently, the numerical methods that have been developed for the subproblems in the past decades are based on different coordinate frameworks. Thus, it is not simply a matter of combining them into one method to tackle the whole problem.

- The type of the equations changes from the solid to the fluid domain. While the fluid equations have a parabolic-like character, the solid equations behave similarly to hyperbolic equations. Among other difficulties, e.g. regarding the choice of time discretisation schemes, this leads to a regularity gap between fluid and solid velocity at the interface.

- The fluid-structure interface moves with time, and hence the subdomains $\Omega_f(t)$ and $\Omega_s(t)$ are variable. A point $x \in \Omega_f(t_1)$ at time t_1 might belong to $\Omega_s(t_2)$ at another time t_2 and vice-versa. This has to be carefully taken into account in the design of a numerical algorithm, especially regarding time discretisation.

- If solid and fluid density are of the same magnitude, the coupling between the subproblems is typically so strong that *partitioned* algorithms that iterate between solvers for the subproblems converge very slowly or show no convergence at all. In this case *monolithic* algorithms that tackle the whole problem in an implicit way as one are preferable.

- In many applications, the structure undergoes large displacements or deformations. In some situations, even contact of different structures or a structure with a wall have to be considered. This leads to topology changes in the fluid domain, which is a problem for many numerical approaches that are typically used to simulate fluid-structure interaction problems.

Fluid-structure interactions have been studied numerically at least since the early 1970s (see e.g. Peskin[117]). Significant progress has been made since then, and a multitude of different approaches have been proposed to tackle these problems numerically. For weakly-coupled problems, meaning that one of the subsystems has a much greater influence on the other (which is typical in aerodynamics), *partitioned* approaches are typically used (see e.g. Nobile & Vergara[114], Deparis et al.[49], Piperno et al.[118]). On the other hand, for strongly-coupled problems, where both subsystems influence each other considerably, *monolithic* approaches are usually needed (Gee et al.[73], Dunne et al.[57], Crosetto et al.[47]).

The most common way to deal with the mismatch of coordinate frameworks is to transform the fluid equations into an artificial coordinate framework on a reference domain $\hat{\Omega}_f$, called *Arbitrary Lagrangian Eulerian* (ALE) coordinates (Donea et al.[50], Belytschko et al.[19], Hughes et al.[91]). However, the ALE approach has one severe drawback. The transformation of the equations into ALE coordinates requires a map $T : \hat{\Omega}_f \to \Omega_f(t)$ of sufficient regularity. The construction of such a map is challenging in the case of large deformations or movements of the structure. Furthermore, topology changes (e.g. contact between two structures or one structure with a wall) cannot be modelled within this approach.

Large structural deformations and contact problems arise in many relevant applications. One of the most-studied fluid-structure interaction problems is the interaction of the pulsating blood flow with the mitral valves that open and close due to the fluid forces. In the absence of a strong fluid flow, these valves are almost in contact. A similar example in an engineering application are valves that control the flow of water in a channel. The channel is closed when they are in contact with the outer channel wall. In this thesis, we will study the plaque growth in arteries. Here, growth of the vessel walls might lead to clogging of the vessel, meaning that upper and lower vessel walls are almost in contact with each other.

An alternative approach that is able to handle both strongly-coupled problems and large deformations and contact is the *Fully Eulerian* approach introduced by Dunne & Rannacher[56]. Instead of transforming the fluid equations, the solid equations are formulated in Eulerian coordinates as well. The whole system of equations can then be solved in a *monolithic* way all at once. As there is no artificial map included that requires regularity, this approach can handle very large deformations and even topology changes arising in contact problems.

In its original version, the *Fully Eulerian* method suffered from bad approximations in the interface region. In this thesis, we study these problems in detail and propose accurate discretisation schemes in space and time to improve the accuracy as well as the robustness of the approach. The proposed discretisation schemes are not restricted to fluid-structure interaction problems, but might be used for a much larger class of interface problems in Eulerian coordinates, e.g. multiphase flows or multicomponent structures.

In particular, the following novel discretisation schemes and results are derived in this thesis:

- We develop a novel space discretisation for interface problems in Eulerian coordinates that is based on a fixed, coarse background mesh consisting of quadrilateral patches.

Within each patch, we resolve the interface locally by splitting it into eight triangles in the interface region and into four quadrilaterals elsewhere. This approach belongs to the class of *fitted finite element methods*, but can be interpreted as an *enriched finite element method* as well. Compared to other popular enrichment methods (e.g. Extended finite elements - XFEM, Moes et al.[111]), the number of unknowns and the structure and connectivity of the system matrix remains unchanged independent of the interface location. We show optimal-order a priori estimates and by using a hierarchical basis of the finite element space, we can furthermore guarantee that the condition number of the system matrix remains bounded by $\mathcal{O}(h^{-2})$ independent of the interface location.

- We use the aforementioned discretisation scheme to solve the Stokes equations on moving domains with *equal-order finite elements* for velocity and pressure. To ensure the well-posedness of the discrete system, we use a pressure stabilisation technique based on penalising jumps of pressure gradients over edges (*Continuous Interior Penalty* stabilisation, Burman & Hansbo[36]). For this approach, we show optimal-order error estimates. To the best of the author's knowledge, this is the first time that optimal error estimates are shown for this stabilisation technique on anisotropic grids.

- We introduce a second-order time discretisation scheme that is based on a space-time continuous Galerkin (cG(1)) approach. Instead of defining the trial and test functions to be polynomial on trajectories in direction of time that might cross the interface, we define piecewise polynomial functions on space-time trajectories that stay within a subdomain and do not cross the interface. We provide a complete a priori error analysis for the resulting time-stepping scheme. The scheme shares some similarities with schemes that have been used in the *Fixed mesh ALE method* (Codina et al.[42]) or the *Universal mesh method* (Gawlik & Lew[72]). To the best of the author's knowledge, however, this is the first time-stepping scheme of Crank-Nicolson/$cG(1)$ type for which second-order estimates are proven.

- We propose a stabilisation term for the structure equation that is added to the velocity-displacement relation, in strong formulation

  $$\partial_t u_s - v_s \cdot \nabla u_s - v_s + \alpha h^s \Delta v_s = 0 \quad \text{in } \Omega_s(t).$$

  We show that this stabilisation does not affect the accuracy of the finite element method in the L^2-norm for $s \geq 5/2$ and in the energy norm for $s \geq 3/2$, but it increases the robustness of the approach significantly.

- In the last part, we use the aforementioned discretisation and stabilisation techniques for full fluid-structure interaction problems. In order to validate the approach, we study a set of benchmark problems of Hron & Turek[88]. For the first time within a *Fully Eulerian approach*, we observe very good convergence behaviour in space and time.

- Furthermore, we show the capability of handling large deformations and contact by simulating a free falling elastic ball, its contact with the ground and the subsequent rebound. Depending on the fluid and solid parameters, it comes either to "real" contact with the ground or a small layer of fluid remains between them. In the first case, we apply a simple contact algorithm that prevents the ball from fully touching the ground. With this algorithm, we are able to simulate a ball bouncing down some stairs.

- Finally, we use the *Fully Eulerian* approach to simulate a mechano-chemical fluid-structure interaction problem, namely plaque growth in blood vessels. This application contains all the challenges of fluid-structure interaction mentioned above. First of all, solid and fluid density are very similar such that a monolithic approach is preferable. Secondly, in the extreme case, plaque growth might lead to a clogging of the vessel and thus to contact of the upper and lower vessel wall. Additionally, the fluid flow and plaque growth have very different time-scales (milliseconds to seconds for the pulsating flow and days to months for the plaque growth). Here, we use a temporal two-scale approach to be able to resolve the flow dynamics. To model plaque growth, we include a simple ordinary differential equation for the foam cell concentration, as well as a multiplicative splitting of the deformation gradient into an elastic and a growing part (Rodriguez et al. [126]).

Structure of the thesis

The thesis is divided into three main chapters:

I Modelling

II Discretisation

III Applications

In **Chapter I** on **Modelling**, we introduce the relevant coordinate systems and review the derivation of the underlying equations in **Section 2**. All the equations are derived from the balances of mass and momentum in Eulerian coordinates.

In **Section 3**, we show different approaches to couple the fluid and solid equations. We begin with the aforementioned *Fully Eulerian* approach that will be the starting point for the developments in this thesis. Furthermore, we give an overview of other related or important classes of approaches, namely the *Arbitrary Lagrangian Eulerian method* [19,50,91], *Lagrange multiplier/Fictitious domain methods* [5,77,102], *Nitsche-based finite element methods* [34,80,107] and *Immersed boundary methods* [21,117].

Finally, in **Section 4** we give an overview over known theoretical results for fluid-structure interaction problems. We comment on the regularity gap for the velocities on the fluid-structure interface and review known existence and uniqueness results of solutions of the coupled problem as well as convergence of discrete solutions.

In **Chapter II** on **Discretisation**, we propose and analyse different discretisation and stabilisation schemes. First, we describe accuracy and stability issues that might arise when using standard discretisation schemes within an Eulerian approach in Section 5.

In **Section 6**, we introduce a novel *locally modified finite element scheme* for spatial discretisation of interface problems. We analyse this scheme in detail for elliptic interface problems and show convergence results of optimal order as well as an optimal bound for the condition number of the system matrix. Finally, the findings are substantiated by means of numerical results.

Next, we use the same spatial discretisation for solving the Stokes equations with an *equal-order* finite element approach in **Section 7**. We show error estimates of optimal order using a *Continuous Interior Penalty* stabilisation technique.

In **Section 8**, we introduce a modified time discretisation scheme of second order based on a cG(1) Galerkin discretisation. The underlying idea is to use trial and test spaces of polynomial functions on space-time trajectories that do not cross the (moving) interface. We give a complete error analysis for parabolic interface problems involving moving interfaces and present numerical examples that confirm the theoretical analysis.

Next, in **Section 9**, we analyse the wave equation as a prototypical solid equation on a moving domain by using the aforementioned discretisation techniques in space and time. We show that with the help of an additional stabilisation term, we increase the stability and robustness of the approach significantly. We compare this stabilisation technique with pure *Streamline-Upwind Petrov-Galerkin* (SUPG) stabilisation and certain damping techniques for the structure equation that have been used by Larsson et al.[100] and Wick[143].

We combine the discretisation and stabilisation techniques in the context of fluid-structure interaction problems in **Section 10**. We use Rothe's method and formulate the monolithic discrete system. Furthermore, we give some additional practical implementation details.

In **Chapter III**, we present different **Applications** to validate this Eulerian approach and to show its ability to handle both strongly-coupled systems and large deformations up to contact.

First, in **Section 11**, we study well-known FSI benchmark problems (Hron & Turek[88]). We show numerical convergence in space and time towards given reference values in different functionals.

Next, in **Section 12**, we consider the contact problem of an elastic ball free-falling towards the ground and its rebound due to elastic compression. We address the question of whether the ball is in contact with the ground or a small layer of fluid remains between. In the case of "real contact", we apply a simple contact algorithm to simulate the rebound. We investigate the influence of the contact algorithm and illustrate the capabilities of the Eulerian approach by simulating a ball bouncing down some stairs.

Finally, in **Section 13**, we simulate the formation of plaque in a vessel wall that might lead to clogging of the vessel. Therefore, we introduce a mechano-chemical fluid-structure interaction system including an ordinary differential equation for the chemistry. To resolve the highly different scale of the pulsating fluid flow and the plaque growth, we introduce a simple two-scale approach in time. Again, we show the ability of the Eulerian approach to incorporate contact as well as to handle a strongly-coupled system.

Notation

We use the usual Lebesgue spaces $L^p(\Omega)$ and Sobolev spaces $H^k(\Omega)$ and their corresponding norms. For the $L^2(\Omega)$-norm, we will use the notation $||\cdot||_\Omega$ and sometimes skip the domain index if it is clear from the context.

Part I

Modelling

2 Continuum mechanics

In this section, we will briefly review the continuum mechanical principles we use to model fluid-structure interaction problems. Due to the importance of different coordinate systems, we start by introducing Eulerian and Lagrangian coordinates. Then, we derive conservation principles for the fluid and the solid part and introduce the material laws we will use. Note that the whole derivation is done in Eulerian coordinates.

2.1 Coordinate systems

Traditionally there are two coordinate systems of interest in fluid and solid mechanics: spatial-centered Eulerian coordinates and particle-centered Lagrangian coordinates. In Figure 2.1, we sketch a moving volume $V(t)$ and its stress-free initial configuration $\hat{V}$. While a function $f(x,t)$ in Eulerian coordinates describes the value of f at the spatial point x at time t (right), a function $\hat{f}(\hat{x},t)$ in Lagrangian coordinates gives the value of $\hat{f}$ in the particle that has been at position $\hat{x}$ in the initial state (left). Throughout this thesis we will use the "hat" notation for Lagrangian quantities. If the movement $\hat{T}: \hat{V} \times I \to V(t)$ is known, we can relate Eulerian quantities f to their Lagrangian counterpart $\hat{f}$ by the relation

$$f(x,t) = f(\hat{T}(\hat{x},t),t) = \hat{f}(\hat{x},t). \tag{2.1}$$

The difference between Lagrangian and Eulerian coordinates is called displacement denoted by $\hat{u}$

$$x = \hat{T}(\hat{x},t) = \hat{x} + \hat{u}(\hat{x},t). \tag{2.2}$$

A prototypical fluid-structure interaction configuration has been shown in Figure 1.1. We will define and study this benchmark configuration in Section 11 in detail. As in this example, in fluid mechanics we are typically interested in flows within a certain spatial domain, e.g. the flow around an obstacle. The same holds true for typical fluid-structure interaction problems. In this case it is practically impossible to formulate the fluid dynamics in Lagrangian coordinates as the majority of the fluid particles that are within the frame of interest at time $t \gg 0$ were far away from it at time $t = 0$. On the other hand, solid equations can be formulated in both Lagrangian and Eulerian coordinates; the former one being the approach that is traditionally used in literature.

Finally, we introduce a third coordinate system without physical meaning that is often used to describe flows in moving domains. *Arbitrary Lagrangian Eulerian (ALE)* coordinates are based on an artificial map $\hat{T}_A : \hat{\Omega}_f \times I \to \Omega_f(t)$ from a reference domain $\hat{\Omega}_f$ to the Eulerian domain $\Omega_f(t)$. In Figure 2.2, we illustrate such a map for the described benchmark configuration. We

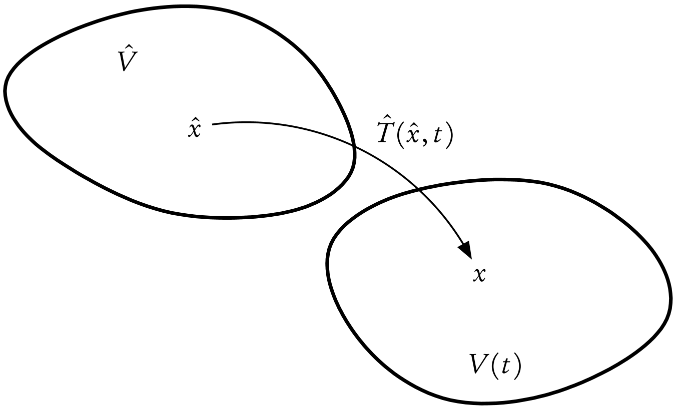

Figure 2.1. Moving volume $V(t)$ and stress-free reference state $\hat{V}$. Quantities in Lagrangian coordinates are given on the domain $\hat{V}$ (left), while Eulerian quantities are given in the moving volume $V(t)$ (right).

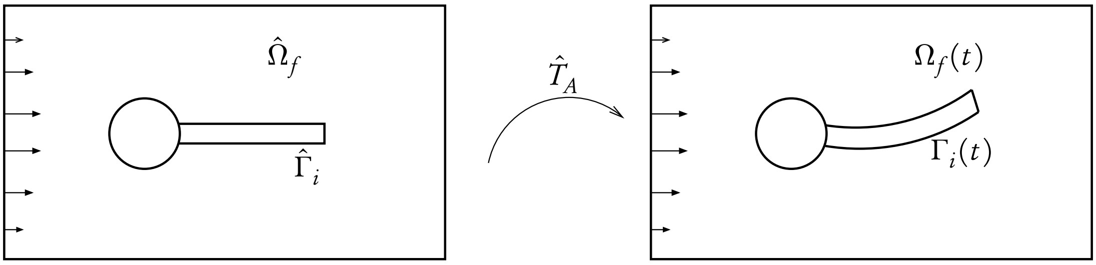

Figure 2.2. ALE map for the FSI benchmark configuration (Hron and Turek[88]).

relate quantities $\hat{f}_A$ in ALE coordinates to Eulerian quantities f by the relation

$$\hat{f}_A(\hat{x}_A,t)=f(\hat{T}_A(\hat{x}_A,t),t). \tag{2.3}$$

Here we do not follow particles but define arbitrary trajectories staying within the frame of interest. In the benchmark configuration all the trajectories stay within the outer bounding box.

By $T:\bigcup_{t\in I}(t,V(t))\to\hat{V}$ we denote the inverse mapping to $\hat{T}$ defined by

$$T(\hat{T}(\hat{x},t),t)=\hat{x}. \tag{2.4}$$

Due to (2.2), this mapping is related to the Eulerian displacement u (defined by $u(x,t)=\hat{u}(\hat{x},t)$) by

$$T(x,t)=x-u(x,t). \tag{2.5}$$

Furthermore, we define the Lagrangian and the Eulerian deformation gradient by

$$\hat{F}=\hat{\nabla}\hat{T}=I+\hat{\nabla}\hat{u}, \qquad F=\nabla T=I-\nabla u$$

where I stands for the identity matrix. Their respective determinants are denoted by

$$\hat{J}=\det\hat{F}, \quad J=\det F.$$

Differentiating (2.4) by $\hat{x}$ yields with the help of the chain rule

$$F(x)\hat{F}(\hat{x}) = I \quad \Rightarrow \quad F(x) = \hat{F}^{-1}(\hat{x}). \tag{2.6}$$

2.2 Equations

The derivation of fluid and solid equations can be found in various textbooks (e.g. Truesdell[138], Holzapfel[87], Richter[122]). Nevertheless, we will briefly review this derivation in order to show that both solid and fluid equations rely on the same conservation principles that are both derived in an Eulerian coordinate framework. We start with a brief derivation of the physical conservation laws in Section 2.2.1. Next, we will introduce the material laws that will be used in this thesis in Section 2.2.2 and specify the coupling conditions between fluid and structure in Section 2.2.3. We close this section by stating the complete set of equations in Section 2.2.4.

2.2.1 Conservation principles

Let $V(t) \subset \Omega(t) \subset \mathbb{R}^d$ be a *continuum*, i.e. a connected volume that is moving with time. An important tool for the derivation of constitutive equations is Reynold's transport theorem.

Lemma 2.1 (Reynold's transport theorem). *Let $V(t) \subset \mathbb{R}^d$ be a continuum whose movement is described by a map $\hat{T} : \hat{V} \times I \to V(t)$. We define the domain velocity by the total derivative $v = d_t \hat{T}$. For a sufficiently smooth function Ψ on $V(t)$, it holds that*

$$\frac{d}{dt} \int_{V(t)} \Psi \, dx = \int_{V(t)} \partial_t \Psi + \operatorname{div}(\Psi v) \, dx.$$

Proof. See e.g. Holzapfel[87]. □

The first conservation principle we will exploit is conservation of mass, i.e.

$$\frac{d}{dt} m(t) = \frac{d}{dt} \int_{V(t)} \rho \, dx = 0.$$

where ρ denotes the density of the fluid or material. With the help of Reynold's transport theorem and assuming continuity of ρ, we derive

$$\partial_t \rho + \operatorname{div}(\rho v) = 0 \quad \text{in } \Omega. \tag{2.7}$$

Second, conservation of momentum or Newton's second law states that the change in momentum equals the external forces, i.e. surface and volume forces. Due to Cauchy's stress theorem a surface force t can be expressed by the Cauchy stress tensor $\sigma \in \mathbb{R}^d \times \mathbb{R}^d$ as (see e.g. Holzapfel[87])

$$\sigma n = t.$$

The Cauchy stress tensor σ relates directions (in this case the normal vector n) in the Eulerian framework to forces (in here t) in the Eulerian framework. Conservation of momentum reads

$$\frac{d}{dt} \int_{V(t)} \rho v \, dx = \int_{\partial V(t)} \sigma n \, do + \int_{V(t)} \rho f \, dx.$$

We apply again Reynold's transport theorem for the left-hand side and transform the surface integral to a volume integral by means of the divergence theorem. Assuming again continuity of all of the integrands, we have the pointwise relation

$$\partial_t(\rho v) + \operatorname{div}(\rho v \times v) - \operatorname{div}\sigma = \rho f \quad \text{in } \Omega(t)$$

where × denotes the external product of two vectors. By using conservation of mass (2.7), this simplifies further to

$$\rho\partial_t v + \rho(v\cdot\nabla)v - \operatorname{div}\sigma = f \quad \text{in}\,\Omega(t). \tag{2.8}$$

2.2.2 Material laws

Equation (2.8) will be the constitutive equation for both fluid and structure mechanics. To close the system of equations, it remains to specify the dependency of the stress tensor σ on the primal variables velocity v, pressure p and displacement u. This will be done by so called material laws. While the derivation of (2.8) was based on physical laws, material laws vary strongly for different materials and can only be considered as approximation of the reality.

In this thesis, we will consider incompressible fluids. Here we have the additional constraint

$$\frac{d}{dt}|V(t)| = \frac{d}{dt}\int_{V(t)} 1\,dx = 0$$

in the fluid domain Ω_f. By means of Reynold's transport theorem this is equivalent to

$$\operatorname{div} v = 0 \quad \text{in } \Omega_f(t),$$

assuming again the continuity of the integrand. A large class of fluids can be modelled as Newtonian fluids, i.e. the stress depends linearly on the strain rate tensor $\dot{\epsilon} = \nabla v + \nabla v^T$

$$\sigma_f = \rho_f \nu_f \dot{\epsilon} - p_f I$$

where $\nu_f > 0$ is the kinematic viscosity of the fluid, ρ_f its density and p_f stands for pressure. In this thesis, we will only consider incompressible Newtonian fluids. Most of the methodology presented in this thesis, however, is also applicable for generalised- or non-Newtonian fluids.

In solid mechanics, we will consider compressible materials. Here we will use a different formulation for the conservation of mass. Let $\rho^0 = \rho(0)$ be the density at initial time $t = 0$. Conservation of mass means that for all times t, it holds that

$$\int_{V(0)} \rho^0\,dx = \int_{V(t)} \rho(x,t)\,dx. \tag{2.9}$$

We transform the integral on the left-hand side to the corresponding current volume element $V(t)$ by following the trajectory $x(t) = \hat{T}(\hat{x}, t)$

$$\int_{V(0)} \rho^0\,dx = \int_{V(t)} J\rho^0(x,t)dx = \int_{V(t)} \rho(x,t)\,dx. \tag{2.10}$$

By assuming continuity of the integrands on $\Omega(t)$, (2.9) and (2.10) yield the pointwise relation

$$\rho(x,t) = J\rho^0(T(x,t),t).$$

In contrast to fluid mechanics, the solid material law is typically formulated in terms of deformations of the solid body rather than on velocity

$$\sigma_s = \sigma_s(u_s).$$

Furthermore, there is a whole bunch of different material models available, describing the properties of specific materials either more or less accurately. These material laws are mostly formulated in a Lagrangian description. A relatively simple material law that will be used exemplary in thesis is the St. Venant Kirchhoff law

$$\hat{\Sigma}_s = 2\mu_s \hat{E}_s + \lambda_s \mathrm{tr}(\hat{E}_s) \tag{2.11}$$

with the second Piola-Kirchhoff stress tensor $\hat{\Sigma}_s$, the Lamé constants $\mu_s, \lambda_s > 0$ and the Green-Lagrange strain tensor

$$\hat{E}_s = \frac{1}{2}\left(\hat{F}^T\hat{F} - I\right). \tag{2.12}$$

In contrast to the Cauchy stress tensor σ_s, Σ_s relates directions in the Lagrangian framework to forces in Lagrangian coordinates. In Eulerian coordinates, relation (2.11) reads

$$\Sigma_s = 2\mu_s E_s + \lambda_s \mathrm{tr}(E_s) \tag{2.13}$$

where the Eulerian version of the second Piola-Kirchhoff stress tensor Σ_s and the Green-Lagrange strain tensor E_s are related to their Lagrangian counterparts by relation (2.1). We remark that from a physical point of view it might be unusual to use the second Piola-Kirchhoff tensor in Eulerian coordinates, but here this will only be an artificial quantity on the way to derive the material law in Eulerian coordinates. By relation (2.6) for the deformation gradients, the Eulerian Green-Lagrange strain tensor is given by

$$E_s = \frac{1}{2}\left(F^{-T}F^{-1} - I\right).$$

The relation between Cauchy stress tensor and Piola-Kirchhoff stress tensor is given by

$$\sigma_s = JF^{-1}\Sigma_s F^{-T} = JF^{-1}\left(2\mu_s E_s + \lambda_s \mathrm{tr}(E_s)\right)F^{-T}$$

(see e.g. Holzapfel[87], Richter[122]). We remark that the choice of the material law is exemplarily and that again the presented methodology can be applied directly to further material laws, e.g. the (incompressible) Neo-Hookean law (see e.g. Holzapfel[87], Dunne[55]).

2.2.3 Coupling conditions for fluid-structure interactions

We assume that an overall domain $\Omega(t)$ is split into subdomains $\Omega_f(t)$ and $\Omega_s(t)$ with a lower-dimensional interface $\Gamma_i(t)$ such that

$$\Omega(t) = \Omega_f(t) \cup \Gamma_i(t) \cup \Omega_s(t)$$

(see Figure 1.1). Solid and fluid equations are coupled by means of physical principles. The first principle we exploit is called the *kinematic* condition and stems from the observation that a viscid fluid follows the motion of the neighbouring solid at the fluid-structure interface. This implies the continuity of fluid and solid velocity at the interface Γ_i

$$v_s = v_f \quad \text{on}\, \Gamma_i. \tag{2.14}$$

This assumption relates to the *no-slip* condition often used in fluid mechanics and is justified for viscid fluids. In the case of a small viscosity we can only assume the continuity of the normal velocity

$$n \cdot v_s = n \cdot v_f \quad \text{on } \Gamma_i.$$

In this thesis, however, we will restrict ourselves to the case of viscid fluids. The second physical principle we will exploit is the third Newton law *"actio = reactio"*. We will refer to this as *dynamic condition*. It says that fluid forces and solid forces in normal direction are equal at the interface, i.e.

$$\sigma_f n = \sigma_s n \quad \text{on } \Gamma_i. \tag{2.15}$$

Here, n might denote either the outer normal n_f of the fluid domain or the outer normal $n_s = -n_f$ of the solid domain.

2.2.4 Complete system of equations

In addition to the equations derived in the previous sections, we make use of the physical coupling between solid velocity and solid displacement

$$v_s = d_t T(x(t), t) = d_t u_s(x(t), t) = \partial_t u_s + v_s \cdot \nabla u_s,$$

where d_t denotes the total (Lagrangian) time derivative. In the last relation we have used the chain rule. The complete set of equations is given by

$$\begin{aligned} \left.\begin{aligned} \rho_f \partial_t v_f + \rho_f (v_f \cdot \nabla) v_f - \operatorname{div} \sigma_f &= \rho_f f \\ \operatorname{div} v_f &= 0 \end{aligned}\right\} &\quad \text{in } \Omega_f(t), \\ \left.\begin{aligned} J \rho_s^0 (\partial_t v_s + v_s \cdot \nabla v_s) - \operatorname{div} \sigma_s &= J \rho_s^0 f \\ \partial_t u_s + v_s \cdot \nabla u_s - v_s &= 0 \end{aligned}\right\} &\quad \text{in } \Omega_s(t), \\ \left.\begin{aligned} v_f &= v_s \\ \sigma_f n &= \sigma_s n \end{aligned}\right\} &\quad \text{on}\, \Gamma_i(t). \end{aligned} \tag{2.16}$$

The solid Cauchy stress tensor is given by

$$\sigma_s = J F^{-1} \left(2\mu_s E_s + \lambda_s \operatorname{tr}(E_s) \right) F^{-T} \tag{2.17}$$

with the Green-Lagrange stress tensor E_s defined in (2.12). The fluid Cauchy stress reads

$$\sigma_f = \frac{\rho_f \nu_f}{2} \left(\nabla v_f + \nabla v_f^T \right) - p_f I. \tag{2.18}$$

For the sake of completeness, we define further boundary conditions on the outer solid boundary Γ_s and the outer fluid boundary Γ_f that will be used in the following

$$\begin{aligned} v_f &= v_f^d \quad \text{on } \Gamma_f^d, \quad & \rho_f \nu_f \partial_n v_f - p_f n &= 0 \quad \text{on } \Gamma_f \setminus \Gamma_f^d, \\ u_s &= u_s^d \quad \text{on } \Gamma_s^d, & \sigma_s n &= 0 \quad \text{on } \Gamma_s \setminus \Gamma_s^d. \end{aligned} \tag{2.19}$$

While for the solid part Γ_s, Γ_s^d or $\Gamma_s \setminus \Gamma_s^d$ might be empty, we assume that Γ_f^d and $\Gamma_f \setminus \Gamma_f^d$ are non-empty. Finally, the system of equations is supplemented with suitable initial values

$$\begin{aligned} v(x,0) &= v^0(x) \quad \text{in } \Omega(t) \\ u(x,0) &= u^0(x) \quad \text{in } \Omega_s(t). \end{aligned}$$

We conclude this section by mentioning that in some situations the system might reach a stationary state. In this case, the time derivative of the solid displacement u_s and hence, the solid velocity v_s vanish in the limit. Thus, the latter one can be eliminated from the overall system and one can solve for the stationary state directly by considering the following system of equations:

$$\begin{aligned} \left.\begin{aligned} \rho_f (v_f \cdot \nabla) v_f - \operatorname{div} \sigma_f &= \rho_f f \\ \operatorname{div} v_f &= 0 \end{aligned}\right\} &\quad \text{in } \Omega_f(t), \\ -\operatorname{div} \sigma_s = J \rho_s^0 f \qquad &\quad \text{in } \Omega_s(t), \\ \left.\begin{aligned} v_f &= 0 \\ \sigma_f n &= \sigma_s n \end{aligned}\right\} &\quad \text{on } \Gamma_i(t). \end{aligned} \tag{2.20}$$

3 Coupling techniques for fluid-structure interactions

In this section, we will combine the derived models into one monolithic variational formulation including the coupling conditions.

3.1 Fully Eulerian approach

The approach used in this thesis is based on the *Fully Eulerian* approach introduced by Dunne [54] and Dunne & Rannacher [56]. The *Fully Eulerian* approach belongs to the class of monolithic variational coupling approaches. The idea is to formulate both the solid as well as the fluid equations in Eulerian coordinates as in the derivation of the constitutive equations in the previous sections. The complete system of equations is formulated in one monolithic variational formulation. Coupling conditions are included by means of variational principles in the following way: The *kinematic condition* is included by the definition of a global ansatz space for solid and fluid velocity

$$v \in v^d + \mathcal{V}, \quad \mathcal{V} = [H_0^1(\Omega(t);\Gamma_f^d)]^2,$$

where $v|_{\Omega_f} = v_f$ and $v|_{\Omega_s} = v_s$. By means of the trace theorem a function $v \in \mathcal{V}$ fulfils

$$v_f = v_s \text{ a.e. in } \Gamma_i(t).$$

The *dynamic condition* is included by adding the fluid and solid momentum equations and choosing the global space $\mathcal{V}$ also for the test functions ϕ. This can be seen as follows: By adding the equations in their weak form, we obtain

$$\begin{aligned}(\rho_f(\partial_t v_f + v_f \cdot \nabla v_f), \phi)_{\Omega_f(t)} + (\rho_s(\partial_t v_s + v_s \cdot \nabla v_s), \phi)_{\Omega_s(t)} + (\sigma_f, \nabla\phi)_{\Omega_f(t)} + (\sigma_s, \nabla\phi)_{\Omega_s(t)} \\ - (\rho_f \nu_f \nabla v_f^T n_f, \phi)_{\Gamma_f \setminus \Gamma_f^d} = (\rho_f f, \phi)_{\Omega_s(t)} + (J\rho_s^0 f, \phi)_{\Omega_s(t)} \quad \forall \phi \in \mathcal{V}.\end{aligned}$$

The fluid boundary term on the left-hand side stems from the fact that the full symmetric stress tensor σ_f enters the fluid equations while the *do-nothing* condition on $\Gamma_f \setminus \Gamma_f^d$ includes the reduced stress tensor $\sigma_f^{\text{red}} = \rho_f \nu_f \nabla v_f - p_f I$.

Assuming sufficient regularity for the primal variables u_s, v_s, v_f and p_f, we recover the strong formulation of fluid and solid equations (see (2.16)). Therefore, we use integration by parts for the fluid and solid stress terms and choose a test function $\phi \in H_0^1(\Omega(t))$. This yields

$$\begin{aligned}(\sigma_f, \nabla\phi)_{\Omega_f(t)} + (\sigma_s, \nabla\phi)_{\Omega_s(t)} = -(\operatorname{div} \sigma_f, \phi)_{\Omega_f(t)} - (\operatorname{div} \sigma_s, \phi)_{\Omega_s(t)} \\ + (\sigma_f n_f, \phi)_{\Gamma_i(t)} + (\sigma_s n_s, \phi)_{\Gamma_i(t)}.\end{aligned}$$

By the fundamental theorem of variational calculus, we obtain the *dynamic condition*

$$\sigma_f n = \sigma_s n \quad \text{a.e. in } \Gamma_i(t),$$

where again n might denote either the outer normal of the solid or fluid domain. Altogether the monolithic variational formulation in fully Eulerian coordinates reads:

Find the global velocity $v \in v^d + \mathcal{V}$, the solid displacement $u_s \in u_s^d + \mathcal{W}_s$, and the fluid pressure $p_f \in \mathcal{L}_f$ such that

$$\begin{aligned}
(\rho(\partial_t v + v \cdot \nabla v), \phi)_\Omega + (\sigma, \nabla\phi)_\Omega - (\rho_f \nu_f \nabla v^T n_f, \phi)_{\Gamma_f \setminus \Gamma_f^d} &= (\rho f, \phi)_\Omega \qquad && \forall \phi \in \mathcal{V},\\
(\partial_t u_s + v \cdot \nabla u_s - v, \psi_s)_{\Omega_s(t)} &= 0 && \forall \psi_s \in \mathcal{W}_s,\\
(\operatorname{div} v, \xi_f)_{\Omega_f(t)} &= 0 && \forall \xi_f \in \mathcal{L}_f.
\end{aligned}$$

Here we have used the abbreviations $\rho|_{\Omega_s} = \rho_s = J\rho_s^0$ and $\rho|_{\Omega_f} = \rho_f$. Furthermore, we have defined $\sigma|_{\Omega_f} = \sigma_f$ and $\sigma|_{\Omega_s} = \sigma_s$ and analogously for the right-hand side f. The function spaces are given by

$$\mathcal{V} = [H_0^1(\Omega(t); \Gamma_f^d \cup \Gamma_s^d)]^2, \quad \mathcal{W}_s := H_0^1(\Omega_s(t); \Gamma_s^d), \quad \mathcal{L}_f := L^2(\Omega_f(t)).$$

The *Fully Eulerian* approach is a relatively young approach that has first been introduced by Dunne[54] and Dunne & Rannacher[56] in 2006 (see also the PhD thesis of Dunne[55]). Independently, Cottet and co-workers[43,44] derived a very similar formulation in the context of finite difference discretisations. Further contributions have been made by Rannacher & Richter[119], Richter & Wick[124], Richter[121] and Wick[145]. A survey of the fundamentals as well as recent developments can be found in[67], an overview about several applications in[68].

Recently, the *Fully Eulerian* method has been applied to study solid growth and clogging in a vessel up to contact of the outer vessel walls[69], see also Section 13. Furthermore, it has been used to study a coupled chemical fluid-structure interaction problem arising in cardiac cells by Ladhaari et al.[99]. Sugiyama et al. applied a *Fully Eulerian* method with a finite difference discretisation to different fluid-structure interaction problems using a St.Venant-Kirchhoff, a Neo-Hookean and a Mooney-Rivlin material law for the structure[96],[134]. Later on, Ii et al. used the method for simulating deformable blood cells and platelets in capillary vessels[94]. Wick combined the *Fully Eulerian* approach with an ALE approach to simulate the flapping of the heart valves[146].

For discretisation, we divide the whole domain Ω into cells by a triangulation Ω_h and use a monolithic finite element approach. If the outer domain $\Omega = \Omega_f(t) \cup \Gamma_i(t) \cup \Omega_s(t)$ stays fixed, the same triangulation can be used for all times $t \in I$. Therefore, the *Fully Eulerian* method belongs to the class of *Fixed-grid methods*.

The coupling conditions carry over directly to the discrete formulation. While the kinematic condition is evident in the case of a conforming ansatz space $\mathcal{V}_h \subset \mathcal{V}$, the dynamic condition holds in the discrete case only within a reasonable accuracy if the interface is resolved by mesh lines (see Chapter 5). However, in the case of a moving interface, resolving the interface in each time step might be challenging and expensive in terms of computational costs. Alternatively,

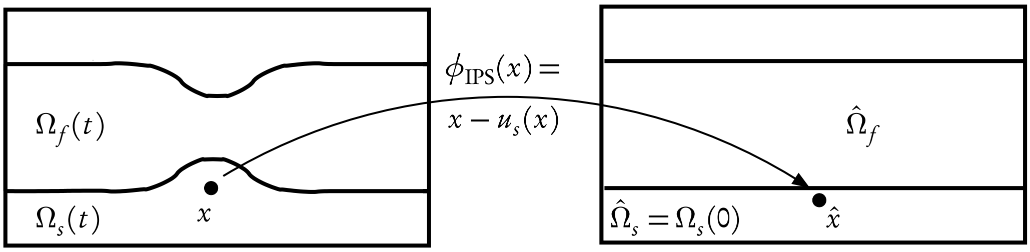

Figure 3.1. The Initial point set function Φ_{IPS} traces back points x to the initial position in order to determine their domain affiliation. Example: Flow through a growing elastic channel.)

the finite element space might be suitably enriched by e.g. *Extended finite elements* (XFEM)[111]. In Section 6, we will present a novel *fitted finite element* scheme that ensures that the interface is accurately resolved while using the same fixed background mesh for all times.

To summarise, the *Fully Eulerian method* is capable of handling both strongly-coupled systems (as a monolithic approach) as well as large deformations and topology changes in the fluid domain. On the other hand, there are a number of challenges for discretisation that we will address in Chapter II in detail.

3.1.1 Initial point set method

To close the system of equations, we need to be able to determine the domain affiliation in a specific point $x \in \Omega$, i.e. we need to be able to find out whether it lies in the fluid or solid domain. Therefore, Dunne & Rannacher[56] introduced the *Initial point set function*. Independently, Cottet and co-workers [43] proposed a very similar way to capture the interface. The idea is to trace back x to its initial position in $\Omega(0)$. This is straight-forward within the solid domain $\Omega_s(t)$ as the solid displacement u_s as a primal variable is known in each time step. In the fluid domain, an extension of u_s is used with the only restriction that points in the fluid domain do not cross the interface. The *Initial point set function* reads

$$\Phi_{\mathrm{IPS}}(x,t) := \begin{cases} x - u_s(x,t) & x \in \Omega_s(t), \\ x - \mathrm{ext}(u_s)(x,t) & x \in \Omega_f(t). \end{cases} \tag{3.1}$$

The domain affiliation is then given by

$$\begin{aligned} \Phi_{\mathrm{IPS}}(x,t) \in \Omega_s(0) \quad &\Leftrightarrow \quad x \in \Omega_s(t), \\ \Phi_{\mathrm{IPS}}(x,t) \in \Omega_f(0) \quad &\Leftrightarrow \quad x \in \Omega_f(t). \end{aligned}$$

An illustration is given in Figure 3.1. It has been noted by Richter[121] that an extension by one layer of mesh cells into the fluid domain is already sufficient if the time step size is sufficiently small (such that the interface does not move over more than one mesh cell within one time step). As we do not require any regularity of the domain map, the *Fully Eulerian* method is able to handle arbitrary displacements up to contact of different structures.

Alternatively, the domain affiliation can be determined by *Level-set functions*, as in Ladhaari & al.[99] and Sugiyama & al.[96]. This, however, requires to solve at least one additional equation per time step. In both approaches, the interface is captured at each time step of the calculation, and mesh cells may change their domain affiliation from one time step to another. Thus, the *Fully Eulerian* approach belongs to the class of *Interface-capturing* approaches.

3.2 Related approaches

There is a large number of approaches that have been proposed and used for fluid-structure interaction simulations in the past decades. In this section, we try to give a brief overview of the most important classes of methods, especially those who are in some sense related to the *Fully Eulerian* approach used in this thesis.

Due to the multitude of approaches in literature a categorisation is not easy. There are at least two (obvious) criteria that could be used. The first one is based on the coordinate systems that are used to formulate the subproblems. As motivated in Section 2.1 the fluid problem might be formulated in Eulerian or in ALE coordinates, while for the solid problem the Eulerian or Lagrangian coordinate framework is possible. Secondly, we could classify approaches into partitioned and monolithic approaches.

3.2.1 Partitioned and monolithic approaches

Monolithic approaches formulate and solve the complete system of equations including fluid and solid equations as well as coupling conditions all at once in one system of equations. Most of them are *variational coupling* approaches, where the coupling conditions are included in a variational, i.e. in a weak sense, see e.g. Section 3.1. These approaches typically use the finite element method for discretisation as for a Galerkin method the coupling conditions carry over directly to the discrete formulation.

On the other hand, in *partitioned* approaches, fluid and solid equations are solved separately. Typically, one of the boundary conditions (2.14) or (2.15) is assigned to each of the subproblems. Therefore, these algorithms are often classified as *Dirichlet-Neumann* (DN) or *Neumann-Dirichlet* (ND) iterations (see e.g. Nobile & Vergara[114], Deparis et al.[49]). In most cases, an iteration between both subproblems is necessary (but not always sufficient) in order to ensure that both interface conditions are fulfilled within a certain accuracy.

Partitioned approaches have the advantage that existing fluid and solid solvers can be used for the subproblems which might reduce both the computational cost as well as the cost for development and implementation considerably. On the other hand, it is *a priori* not guaranteed that the iteration converges. If one of the interface conditions is assigned to each of the subproblems, the one assigned to the first subproblem is typically not valid anymore after the second subproblem has been solved and vice-versa. Hence, such an approach can be used especially in cases where -roughly speaking- one of the two subproblems has a much stronger influence on the other.

Typical examples can be found e.g. in aerodynamics where the solid has typically a much stronger influence on the surrounding fluid. In general, however, it is not straight-forward to design an iteration procedure that ensures convergence to a solution of the complete system of equations including both interface conditions. The usage of relaxation techniques (e.g. Aitken relaxation[98]) is often necessary to improve the convergence behaviour.

A measure for the decision if a partitioned approach can be used or not is the ratio of densities ρ_s/ρ_f. For $\rho_s \approx \rho_f$ the complete system of equations is strongly coupled and convergence might be very slow or cannot be ensured at all for partitioned approaches. A typical example is the interaction between blood flow and the surrounding vessel walls as well as the embedded mitral valves in hemodynamics. On the other hand, for $\rho_s \gg \rho_f$ the iteration might converge after one or only a few iterations. This is typically the case in aerodynamics.

These observations can be substantiated by the so called *added-mass effect*. Roughly speaking, one might view the fluid problem as an *added mass* acting on the solid problem. Causin et al.[38] showed (in a very simplified setting of the subproblems including a thin-wall structure) that the solid problem can be rewritten as

$$(\rho_s I + \rho_f \mathcal{M}_A)\partial_t v_s + \operatorname{div} \sigma_s = p_{\text{ext}}$$

where $\mathcal{M}_A$ is the so-called *added-mass* operator and p_{ext} denotes an external fluid pressure. A similar analysis for more general structures has been carried out by Richter[122]. A stability analysis reveals that convergence of iterative schemes depends essentially on the ratio of densities ρ_s/ρ_f, see[38,122].

Recently some authors succeeded in using the advantages of partitioned solvers within monolithic approaches (see e.g. Brummelen et al.[32], Heil et al.[83], Gee et al.[73], Richter[123]). Here, a partitioned solver is used as a preconditioner within a monolithic Krylov space solver or as smoother within a monolithic multigrid iteration. This combines the advantages of partitioned and monolithic schemes.

A further advantage of variationally coupled monolithic schemes is that they allow in a straight-forward way for goal-oriented error estimation (Dunne[54], Richter[120], Fick et al.[64], Zee et al.[154]) and gradient-based optimisation (see e.g. Wick[143], Richter & Wick[125]). We believe that both of them will be of increasing interest in the future. That is why we will be especially interested in such coupling approaches in the following. Nevertheless, we will also present important classes of partitioned schemes.

Overview

As most of the monolithic approaches can be used as partitioned methods in a straight-forward way, we will categorise the coupling techniques by means of the coordinate systems that are used for fluid and solid subproblems. As mentioned previously, the solid equations might be formulated both in Eulerian and Lagrangian coordinates, while for the fluid equations Eulerian or Arbitrary Lagrangian Eulerian (ALE) coordinates might be used.

We begin in Section 3.2.2 with the popular *Arbitrary Lagrangian Eulerian* (ALE) method that uses ALE coordinates for the fluid and Lagrangian coordinates for the solid equations. As the *Fully Eulerian* approach, the ALE method can be used as a *variationally coupled monolithic* approach, but it is often used as a partitioned method as well.

Next, in Section 3.2.3, we describe two important classes of methods that use Eulerian coordinates for the fluid and Lagrangian coordinates for the solid equations. Here, the challenge lies in the incorporation of interface conditions. We present approaches that are based on the *Fictitious domain method* using Lagrange multipliers for the coupling and on relatively new methods using Nitsche's method for the weak incorporation of interface conditions.

Finally, in Section 3.2.4, we describe *Immersed boundary methods*. In these partitioned approaches, Eulerian coordinates are used for the fluid equations as well as for an artificial extension of the fluid equations to the solid domain. Then, solid forces are evaluated in a Lagrangian framework and enter the right-hand side of the fluid equations. The structure is thus included by a combination of Eulerian and Lagrangian coordinates. These methods are typically used for rigid body motions, low-dimensional structures or structures occupying no volume.

3.2.2 Arbitrary Lagrangian Eulerian method

The most popular monolithic coupling method is the *Arbitrary Lagrangian Eulerian method* (ALE). Its first ideas within a Finite Volume or Finite Difference discretisation date back to the 1960s in the work of Noh[115] (1964) and Franck & Lazarus[65] (1964). In the finite element context, the ALE method has first been applied by Donea et al.[50] (1977), Belytschko et al.[19] (1980) and Hughes et al.[91] (1981). A detailed survey can be found in Donea et al.[51]. A very similar approach in a space-time Galerkin framework called *deforming spatial domain/space time (DSD/ST)* has been proposed by Tezduyar and co-workers[15,136].

Here, the solid equations are solved in the Lagrangian coordinate framework. For the fluid part, we define a domain $\hat{\Omega}_f$ whose boundary matches the boundary $\hat{\Omega}_s$ at the interface and a map $\hat{T}_f : \hat{\Omega}_f \times I \to \Omega_f(t)$. A suitable choice for $\hat{\Omega}_f$ is e.g. the initial fluid domain $\Omega_f(0)$. The map $\hat{T}_f$ is *arbitrary* inside $\hat{\Omega}_f$ with the condition to match the solid boundary at the interface (see Figure 2.2).

As in Section 2.1, we relate Eulerian quantities f to ALE quantities $\hat{f}$ by the relation

$$\hat{f}(\hat{x},t) = f(\hat{T}_f(x,t),t).$$

If the map $\hat{T}_f$ is a $C^{1,1}$-diffeomorphism, an equivalent variational formulation of the Navier-Stokes equations on the fixed domain $\hat{\Omega}_f$ is given by

$$\left.\begin{aligned} \hat{J}_f \rho_f \partial_t \hat{v}_f + \hat{J}_f \rho_f \hat{F}_f^{-1}(\hat{v}_f - \partial_t \hat{T}_f) \cdot \hat{\nabla} \hat{v}_f - \widehat{\operatorname{div}}(\hat{J}_f \hat{\sigma}_f \hat{F}_f^T) &= \hat{J}_f \rho_f \hat{f} \\ \widehat{\operatorname{div}}(\hat{J}_f \hat{F}_f^{-1} \hat{v}_f) &= 0 \end{aligned}\right. \quad \text{in } \hat{\Omega}_f,$$

where $\hat{F}_f = \hat{\nabla} \hat{T}_f$ and $\hat{J}_f = \det \hat{F}_f$ (see e.g. Dunne et al.[57], Richter[122]). As in the *Fully Eulerian* approach the coupling conditions can be included by choosing a global ansatz and test space $\mathscr{V}$. Altogether the complete system of equations reads:
Find $\hat{v} \in v^d + \mathscr{V}, \mathscr{V} := H_0^1(\hat{\Omega}_f; \hat{\Gamma}_f^d)$, *displacement* $\hat{u} \in u^d + \mathscr{W}$, $\mathscr{W} := H_0^1(\hat{\Omega}; \hat{\Gamma}_s^d)$ *and fluid pressure* $\hat{p}_f \in \mathscr{L}_f := L^2(\hat{\Omega}_f)$ *such that*

$$\begin{aligned} (\hat{J} \rho \partial_t \hat{v}, \hat{\phi})_{\hat{\Omega}} + (\hat{J} \rho_f \hat{\nabla} \hat{v}_f \hat{F}^{-1}(\hat{v}_f - \partial_t \hat{T})), \hat{\phi})_{\hat{\Omega}_f} &+ (\hat{J} \hat{\sigma} \hat{F}^{-T}, \hat{\nabla} \hat{\phi})_{\hat{\Omega}} \\ -(\rho_f \nu_f \hat{J} \hat{F}^{-1} \hat{\nabla} \hat{v}_f^T \hat{F}^{-T} \hat{n}, \hat{\phi})_{\hat{\Gamma}_f \setminus \hat{\Gamma}_f^d} &= (\hat{J} \hat{\rho} \hat{f}, \hat{\phi})_{\hat{\Omega}} && \forall\, \hat{\phi} \in \mathscr{V} \\ (\operatorname{div}(\hat{J} \hat{F}^{-1} \hat{v}_f), \hat{\xi}_f)_{\hat{\Omega}_f} &= 0 && \forall\, \hat{\xi}_f \in \mathscr{L}_f. \\ (d_t \hat{u} - \hat{v}_s, \hat{\psi}_s)_{\hat{\Omega}_s} &= 0 && \forall\, \hat{\psi}_s \in \mathscr{L}_s := L^2(\hat{\Omega}_s), \\ (\hat{\nabla} \hat{u}, \hat{\nabla} \hat{\psi}_f)_{\hat{\Omega}_f} &= 0 && \forall\, \hat{\psi}_f \in \mathscr{W}_f := H^1(\hat{\Omega}_f). \end{aligned} \tag{3.2}$$

Here we have used a harmonic extension $\hat{u}_f$ of $\hat{u}_s$ to the fluid domain in order to define the ALE mapping

$$\hat{T}_f = \mathrm{id} + \hat{u}_f.$$

The continuity between the solid deformation $\hat{u}_s$ and its extension $\hat{u}_f$ is ensured by choosing the global ansatz space $\mathcal{W}$ for $\hat{u}$. The coupling conditions

$$\hat{v}_f = \hat{v}_s \quad \text{and} \quad \hat{J}_f \hat{\sigma}_f \hat{F}_f^T = \hat{J}_f \hat{\sigma}_f \hat{F}_f^T \quad \text{on } \hat{\Gamma}_i$$

follow as for the *Fully Eulerian* approach by means of variational principles.

The key advantage of the ALE method is that for all times t the system of equations is defined on fixed domains $\hat{\Omega}$, $\hat{\Omega}_f$ and $\hat{\Omega}_s$ that are independent of the movement of the physical domains. In a discrete context, this is especially advantageous for the dynamics in the interface region; if the interface is resolved accurately by mesh lines at time $t = 0$, it will be resolved accurately for all times (up to discretisation errors). Thus, both interface conditions are fulfilled accurately on the interface $\hat{\Gamma}_i$. Furthermore, in contrast to *fixed-grid* methods no interface-capturing has to be applied, but the interface is tracked naturally by evolving mesh lines. Therefore, the ALE method belongs to the class of *interface-tracking methods*.

In fact, there are two different ways of implementing the ALE method. The first one is to solve the whole system (3.2) in a monolithic way on the fixed domains $\hat{\Omega}$, $\hat{\Omega}_f$ and $\hat{\Omega}_s$ (see e.g. Hron & Turek[89], Dunne & Rannacher[56], Wick[143]). Here, the domain movement is included in the variables $\hat{u}_s, \hat{u}_f$ which enter the system of equations either implicitly or explicitly. Explicitly means that $\hat{F}$ and $\hat{J}$ are evaluated at the previous time step as $\hat{F}^{n-1}$,$\hat{J}^{n-1}$. The current physical domains are then given by

$$\Omega(t) = \hat{T}(\hat{\Omega}, t), \quad \Omega_s(t) = \hat{T}(\hat{\Omega}_s, t), \quad \Omega_f(t) = \hat{T}(\hat{\Omega}_f, t).$$

On the other hand, the system of equations might also be solved decoupled using a partitioned algorithm. Here, it is not required that fluid and solid domains match at the interface. Thus, the ALE method might also be applied in a different way: After each step all the mesh lines of the fluid mesh are moved by the artificial deformation $\hat{u}_f$ and the next step is solved on the moved domain

$$\Omega_f^{n+1} = T(\Omega_f^n, t_{n+1})$$

(Deparis et al.[49]). Up to numerical errors this fluid problem is equivalent to the ALE formulation on a fixed domain $\hat{\Omega}_f$. Therefore, the ALE method belongs to the class of *moving-mesh* methods. In fact, one can even use this technique within a monolithic approach (see e.g. Crosetto et al.[47]). If the mesh resolution of the interface does not change over time, a map between interface grid points of the two meshes is naturally given by the solid displacement u_s. This can be used to include the interface conditions in a monolithic formulation.

The disadvantage of the ALE approach lies in the regularity requirement for the ALE map $\hat{T}_f$. This requirement rules out changes of topology, e.g. contact of the solid body with a wall. Furthermore, the ALE map might lose its regularity in the case of large solid displacements. Here, it may help to use a linear elastic or biharmonic extension (Stein et al.[132], Wick[142])

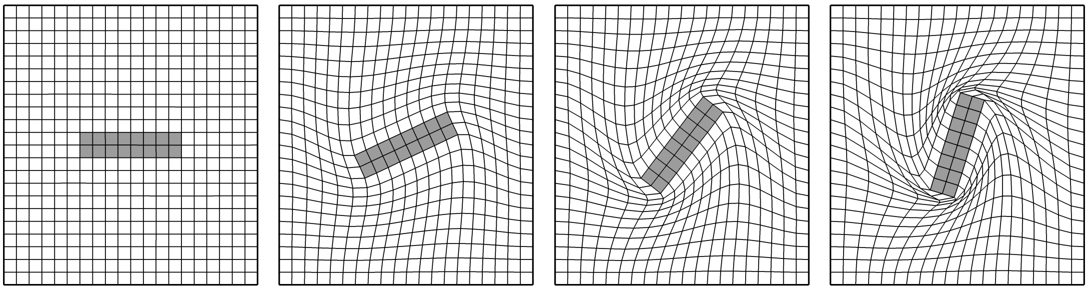

Figure 3.2. Rotating beam with the ALE method using a biharmonic extension in the fluid domain. Due to degeneration of mesh cells near the beam, the simulation breaks down before the beam completed a quarter of a full rotation.

instead of the harmonic extension used in (3.2). Especially the latter one might allow for considerably larger solid displacements as the solution to the biharmonic extension has typically more regularity than the harmonic one, even in the case of reentrant corners.

However, in the case of large structural displacements, all of these techniques might fail. As an example consider the rotation of a beam, see Figure 3.2, where all of the mentioned extensions lead to degenerate mesh cells at some time t before the beam completes a quarter of a full rotation. In Section 8.6.2, we will study a very similar configuration within an Eulerian framework.

In this example, the limitations of the ALE method might be overcome by remeshing techniques. This means that at a certain time t_m, before the mesh cells degenerate, the solution is projected to a new regular mesh Ω_h^m which will be used as reference domain from then. The difficulty, especially in a three-dimensional setting, lies in the construction of such a mesh that resolves the interface. Furthermore, the projection has to be chosen carefully, as hereby a further error contribution might be introduced. A simple linear projection might decrease the accuracy considerably.

To overcome this difficulty Codina and co-workers[9,42] defined an interesting variant of the ALE method called *Fixed-mesh ALE* method. As in the ALE method they use a mesh-moving technique in each time step that follows the interface. Afterwards, however, they project the solution back to a fixed background mesh. In this way they are able to deal with large movements of the structure. We will come back to this method in Section 8 where we will derive a second-order accurate time-stepping scheme for an Eulerian approach and show its equivalence to a certain space-time variant of the *Fixed-mesh ALE* method.

3.2.3 Euler-Lagrangian methods

There is a big variety of different partitioned methods that solve the fluid equations in Eulerian coordinates and the solid equations in Lagrangian coordinates. It is out of the scope of this thesis to give a comprehensive overview over all of them. Instead, we want to concentrate on two particular classes of methods that allow for a monolithic formulation.

Coupling via Lagrange multipliers /Fictitious domain methods

The fundamental problem in Euler-Lagrangian methods is that the fluid domain $\Omega_f(t)$ and the solid domain $\hat{\Omega}_s$ do not match (see e.g. Figure 2.2) which makes the imposition of interface conditions rather challenging. A promising way to tackle this problem is to introduce Lagrange multipliers that are defined at the interfaces $\Gamma_i(t)$ and $\hat{\Gamma}_i$, respectively. This approach goes back to Glowinski et al.[77].

Here, we follow the works of Baaijens[5] and Legay, Chessa and Belytschko[102] who applied *Fictitious domain methods* to fluid-structure interaction problems. The idea is to formulate the kinematic interface condition (2.14) weakly in an integral sense but with separate test functions defined only on the interface $\Gamma_i(t)$. To obtain a well-posed system of equations that fulfils the dynamic condition (2.15), we introduce a further variable λ at the interface that has the function of a Lagrange multiplier. This approach was inspired by domain-decomposition methods[20] where such variable are often called *mortars*.

The variational formulation reads as follows:
Find fluid velocity $v_f \in v_f^d + \mathcal{V}_f$, fluid pressure $p_f \in \mathcal{L}_f$, solid velocity $\hat{v}_s \in \mathcal{V}_s$, solid displacement $\hat{u}_s \in u_s^d + \mathcal{W}_s$ and a Lagrange multiplier $\lambda \in \mathcal{Z}_i$ such that

$$
\begin{aligned}
(\rho_f(\partial_t v_f + v_f \cdot \nabla v_f), \phi)_{\Omega_f(t)} + (\sigma_f, \nabla\phi)_{\Omega_f(t)} & \\
-(\rho_f \nu_f \nabla v^T n_f, \phi)_{\Gamma_f \backslash \Gamma_f^d} - (\lambda, \phi)_{\Gamma_i(t)} = (\rho_f f, \phi)_{\Omega_f(t)} & \qquad \forall \phi \in \mathcal{V}_f, \\
(\operatorname{div} v, \xi_f)_{\Omega_f(t)} = 0 & \qquad \forall \xi_f \in \mathcal{L}_f, \\
(v_f - v_s, \eta_i)_{\Gamma_i(t)} = 0 & \qquad \forall \eta_i \in \mathcal{Z}_i. \\
(\rho \partial_t \hat{v}_s, \hat{\phi})_{\hat{\Omega}_s} + (\hat{J}\hat{\sigma}\hat{F}^T, \hat{\nabla}\hat{\phi})_{\hat{\Omega}_s} + (\hat{\lambda}, \hat{\phi})_{\hat{\Gamma}_i} = (\hat{\rho}_s^0 \hat{f}, \hat{\phi})_{\hat{\Omega}_s} & \qquad \forall\, \hat{\phi} \in \mathcal{V}_s, \\
(d_t \hat{u}_s - \hat{v}_s, \hat{\psi})_{\hat{\Omega}_s} = 0 & \qquad \forall\, \hat{\psi} \in \mathcal{W}_s.
\end{aligned}
\tag{3.3}
$$

Note that the Lagrange multiplier appears in the solid equation $\hat{\lambda}$ and in the fluid equation as λ. $\hat{\lambda}$, however, is no additional variable but the Lagrangian counterpart of λ defined by

$$
\hat{\lambda}(\hat{x}, t) = \lambda(\hat{T}(\hat{x}, t), t)
$$

where $\hat{T}$ denotes the map from Lagrangian to Eulerian coordinates defined in Section 2.1. Hence, the dynamic condition (2.15) follows after integration by parts and a change of the coordinate system

$$
\sigma_f n_f = \lambda, \quad \hat{\lambda} = -\hat{J}\hat{\sigma}_s \hat{F}^T \hat{n}_s \qquad \Rightarrow \quad \sigma_f n = \sigma_s n.
$$

A similar approach has been proposed by Park et al.[116] and Gerstenberger & Wall[75]. The difference in their work is that a further additional variable v_i for the interface velocity (or alternatively the interface displacement) is introduced that is defined only on the interface. Then, the two interface conditions

$$
v_f = v_i \text{ on } \Gamma_i(t), \quad \hat{v}_i = \hat{v}_s \text{ on } \hat{\Gamma}_i
$$

are assigned to the respective fluid and solid subproblems. Again both conditions are implemented in a weak variational sense as constraints. To obtain a well-posed system of equations, two Lagrange multipliers λ_f and λ_s have to be introduced as additional variables and the additional equation

$$\lambda_f = \lambda_s \quad \text{on } \Gamma_i(t),$$

ensuring the dynamic condition (2.15), is added to the system of equations. In total, three interface variables λ_f, λ_s and v_i enter the system of equations in contrast to one in (3.3).

Moreover, a strategy to capture or track the interface has to be added to close the system of equations. While Legay et. al.[102] used a level-set method to capture the interface, Gerstenberger & Wall[75] proposed a Lagrangian tracking technique to evolve the interface from time step to time step.

In a finite element discretisation, an *inf-sup* condition has to be ensured for both fluid and solid subproblems. A popular choice for the Lagrange multipliers is to use polynomials of one degree lower than the velocity ansatz space. Gerstenberger & Wall[75] used e.g. equal-order biquadratic elements for velocities, pressure and solid displacements (including a pressure stabilisation term) and linear elements for the three additional variables on the interface.

A further difficulty is that, as in the *Fully Eulerian* method, the fluid domain $\Omega_f(t)$ changes with time. The idea of the *Fictitious domain* method is to use a fixed background mesh including the solid domain for all times. Here, however, the interface is not aligned with mesh cells. For an accurate representation of the interface forces, Gerstenberger & Wall used the *Extended Finite Element method* (XFEM[111]) for those elements that lie only partly in the fluid domain.

Finally, we want to remark that in the context of the Fictitious domain method, some authors use distributed Lagrange multipliers defined on the whole solid domain (see e.g. Yu[153]) and impose

$$v_f = v_s \quad \text{in } \Omega_s(t)$$

as weak constraint for a fluid velocity defined in the entire domain $\Omega(t)$. In this case the method shares certain similarities with the Immersed Boundary method (see Section 3.2.4).

Coupling via Nitsche's method

Nitsche' s method[113] was originally introduced to incorporate Dirichlet boundary conditions for elliptic problems weakly into the variational formulation. Hansbo & Hansbo extended this concept to interface conditions for elliptic problems with discontinuous coefficients[80]. Recently, this method has also been used for imposing interface conditions between non-matching grids for fluid-structure interaction problems (see e.g. Hansbo & Hermansson[82], Burman & Fernández[34], Massing et al.[107]).

As in the previous subsection, the idea is to use an Eulerian framework and a fixed grid for the fluid equations and a Lagrangian framework for the solid equations. Again, fluid domain $\Omega_f(t)$ and solid domain $\hat{\Omega}_s$ do not match at the interface. Nevertheless, the whole system of equations might be formulated into one common monolithic formulation by transforming the respective boundary conditions between the two coordinate systems. In contrast to the *Fully Eulerian* and the ALE method as formulated in Section 3.1 and Section 3.2.2, it is important that no global test or trial spaces are used for none of the variables and the spaces for fluid and solid variables remain separated.

Applying Nitsche's method to the kinematic interface condition, the system of equations reads: *Find fluid velocity* $v_f \in v_f^d + \mathcal{V}_f$*, fluid pressure* $p_f \in \mathcal{L}_f$*, solid velocity* $\hat{v}_s \in \mathcal{V}_s$ *and solid displacement* $\hat{u}_s \in u_s^d + \mathcal{W}_s$ *such that*

$$\begin{aligned}
&(\rho_f(\partial_t v_f + v_f \cdot \nabla v_f), \phi_f)_{\Omega_f(t)} + (\sigma_f, \nabla \phi_f)_{\Omega_f(t)} - (\rho_f \nu_f \nabla v^T n_f, \phi)_{\Gamma_f \setminus \Gamma_f^d} \\
&\qquad + (\rho_s \partial_t \hat{v}_s, \hat{\phi}_s)_{\hat{\Omega}_s} + (\hat{J} \hat{\sigma}_s \hat{F}^T, \hat{\nabla} \hat{\phi}_s)_{\hat{\Omega}_s} - (\sigma_f n_f, \phi_f - \phi_s)_{\Gamma_i(t)} \\
&\qquad - (v_f - v_s, S_f(\phi_f, \xi_f) n_f)_{\Gamma_i(t)} + \frac{\gamma \nu}{h}(v_f - v_s, \phi_f - \phi_s)_{\Gamma_i(t)} \\
&\qquad\qquad\qquad = (\rho_f f, \phi_f)_{\Omega_f(t)} + (\hat{\rho}_s^0 \hat{f}, \hat{\phi}_s)_{\hat{\Omega}_s} \quad \forall \phi_f \in \mathcal{V}_f, \hat{\phi}_s \in \mathcal{V}_s, \\
&\qquad (\operatorname{div} v, \xi_f)_{\Omega_f(t)} = 0 \quad \forall \xi_f \in \mathcal{L}_f, \\
&\qquad (d_t \hat{u}_s - \hat{v}_s, \hat{\psi})_{\hat{\Omega}_s} = 0 \quad \forall \hat{\psi} \in \mathcal{W}_s.
\end{aligned} \tag{3.4}$$

Here, the test function ϕ_s on $\Gamma_i(t)$ is defined by $\phi_s(x) = \hat{\phi}_s(T(x,t),t)$ and the operator

$$S_f(\phi_f, \xi_f) = \frac{1}{2}\rho_f \nu_f (\nabla \phi_f + \nabla \phi_f^T) - \xi_f I$$

is the Cauchy stress operator applied to the fluid test functions. Furthermore, $\gamma > 0$ denotes the Nitsche penalty parameter and the normal vector n_f is the outer normal of the fluid domain $\Omega_f(t)$. Due to the dynamic condition (2.15), σ_s and the solid stress operator $S_s(\phi_s)$ as well as a combination of fluid and solid stresses could be used instead of σ_f and $S_f(\phi_f, \xi_f)$ in the Nitsche interface terms.

To see that the interface conditions are included into the variational formulation, we apply integration by parts in (3.4). The resulting interface terms are

$$\begin{aligned}
&(\sigma_f n, \phi_f)_{\Gamma_i(t)} - (\sigma_s n, \phi_s)_{\Gamma_i(t)} - (\sigma_f n, \phi_f - \phi_s)_{\Gamma_i(t)} \\
&\quad - (v_f - v_s, S_f(\phi_f, 0) n)_{\Gamma_i(t)} + \frac{\gamma \nu}{h}(v_f - v_s, \phi_f - \phi_s)_{\Gamma_i(t)} = 0 \;\; \forall \phi_f \in \mathcal{V}_f, \hat{\phi}_s \in \mathcal{V}_s.
\end{aligned}$$

Here, we applied a transformation of solid stresses to the Eulerian interface $\Gamma_i(t)$. If we choose $\phi_s = 0$, we have

$$-(v_f - v_s, S_f(\phi_f, 0) n)_{\Gamma_i(t)} + \frac{\gamma \nu}{h}(v_f - v_s, \phi_f)_{\Gamma_i(t)} = 0 \quad \forall \phi_f \in \mathcal{V}_f$$

and hence $v_f = v_s$ almost everywhere. Thus, the kinematic conditions is assigned to the fluid problem in some sense. This is because we have chosen the fluid stresses in (3.4). Next, choosing $\phi_f = 0$ yields

$$-(\sigma_s n, \phi_s)_{\Gamma_i(t)} + (\sigma_f n, \phi_s)_{\Gamma_i(t)} - \frac{\gamma \nu}{h}(v_f - v_s, \phi_s)_{\Gamma_i(t)} = 0.$$

With the kinematic condition $v_f = v_s$, it follows that the dynamic condition (2.15) is also fulfilled.

Burman & Fernández showed in a theoretical analysis for a linear FSI problem both the well-posedness of the complete system of equations as well as convergence of discrete finite element solutions[34]. For discretisation, a Lagrangian (moving) mesh is used for the solid and an Eulerian (fixed) mesh for the fluid part. The fixed mesh covers either the complete domain $\Omega(t)$ or might be reduced in each time step by excluding those cells that lie completely within the solid domain. In any case, fluid and solid meshes overlap and fluid cells are cut by the interface in arbitrary portions. To ensure discrete coercivity, a stabilisation term $g_h(v_f, \phi_f)$ is added to the fluid part. The authors claim that the system matrix stays bounded independently of the position of the cut.

Hansbo & Hermansson[82] applied this method in a monolithic way to a simple stationary fluid-structure-vibration problem. On the other hand, Burman & Fernández[34] used the approach for a non-stationary Stokes problem coupled with a linear elastic structure both in a monolithic and in a partitioned way,

Again, as the fluid mesh does not resolve the interface, the interface stresses $\sigma_f n|_{\Gamma_i}$ might not be very accurate and thus the dynamic condition is fulfilled in a rough approximation only. To improve this, Massing et al.[107] proposed to split the fluid domain further in a fixed part and a moving part located around the structure whose mesh is aligned to the fluid-structure interface. The Nitsche coupling is then applied on an interior fluid-fluid interface between overlapping fluid meshes.

3.2.4 Immersed boundary methods

The *Immersed boundary method* introduced by Peskin[117] was originally designed for fibre-like or low-dimensional structures occupying no or only negligibly small volume. The idea is to formulate the whole system of equations as if it would be a flow problem and use the Navier-Stokes equations in the complete domain $\Omega(t)$. In order to simplify notation, let us for the moment assume that the source terms f on the right-hand side of fluid and solid equations are zero. The equations are then written in the following form

$$\begin{aligned} \rho_f \partial_t v + \rho_f (v \cdot \nabla) v - \operatorname{div} \sigma_f &= g_s \\ \operatorname{div} v &= 0 \end{aligned} \quad \text{in } \Omega(t). \tag{3.5}$$

The coupling is included by means of a force term g_s on the right-hand side that is zero in the fluid domain and that contains all the solid contributions subtracted by the fluid terms that appear on the left-hand side in the solid domain. To be precise g_s is defined by

$$g_s(x,t) = \begin{cases} (\rho_f - \rho_s)(\partial_t v + v \cdot \nabla v) + \operatorname{div}(\sigma_f - \sigma_s) & \text{in } \Omega_s(t) \\ 0 & \text{in } \Omega_f(t). \end{cases} \tag{3.6}$$

This force term can be equivalently represented with a Dirac distribution δ

$$g_s(x,t) = \int_{\Omega_s(t)} g_s(y,t) \delta(x-y) dy. \tag{3.7}$$

This representation will be used for discretisation. The *Immersed boundary method* has originally been used with finite difference discretisations on very simple, typically Cartesian fluid meshes.

The solid forces g_s are evaluated on a Lagrangian solid mesh that is typically much finer than the fluid mesh and that is moved with the fluid velocity. On this mesh, a discrete smooth Dirac delta function δ_h is used as approximation to δ. A lot of effort has been spent in literature (see e.g. Wang & Liu[141], Gil et al.[76]) on defining appropriate and accurate discrete approximations of the Dirac function. To the knowledge of the author, however, a theoretical analysis on how these approximations affect the convergence of discrete solutions is not yet available.

Later on, the method has been used as *Immersed finite element method* and with structures occupying a finite volume (Wang & Liu[141], Zhang et al.[155], Boffi et al.[22]). In this case it is possible to formulate the whole system of equations without the delta function by means of a variational formulation, see Boffi & Gastaldi[21]. However, the incompressible Navier-Stokes equations are used in the whole domain, which means in particular that the solid velocity is assumed to be divergence free.

While the continuous formulation might be formulated as a variational coupling approach[21], the *Immersed boundary method* is usually used as a partitioned approach, where the solid forces are evaluated before the solution of the fluid problem on a separate Lagrangian mesh. In fact, in most works, the method is applied for configurations where no extra solid equations have to be solved at all, but the solid forces under consideration can be directly calculated from interface quantities.

A typical partitioned algorithm looks as follows[22]:

```
For $m = 0, 1, \dots$
    1. Compute the source term $g_s$ by (3.7) on a Lagrangian (moving) mesh
    2. Solve equation (3.6) for the global velocity $v^m$ on a structured Eulerian mesh
    3. Move the vertices of the Lagrangian solid mesh by $x^{m+1} = x^m + k v^m(x^m)$ where
       $k$ denotes the time step size and go back to (1.)
```

Remark 3.1. *The dynamic coupling condition $\sigma_f n = \sigma_s n$ is hidden in (3.6). If one would apply the algorithm to the continuous formulation (hypothetically speaking), the dynamic coupling condition would be fulfilled almost everywhere on Γ_i after step 2. In the case of the Immersed finite element method this condition carries to the discrete formulation. As the interface is not resolved by the fluid mesh, however, the condition might only be fulfilled in a very rough approximation. The kinematic coupling condition, on the other hand, is valid after step 3, up to time discretisation errors.*

4 Theoretical results

The analysis of the well-posedness of the complete system of equations (2.16) is still an active field of research. One of the main difficulties is the incompatibility between the parabolic-like fluid equations and the hyperbolic-like solid equations. One important consequence of this is that the coupling via the kinematic condition (2.14) contains a regularity problem.

4.1 A regularity issue for non-stationary fluid-structure interactions

For ease of presentation we consider here a linear fluid-structure interaction problem, i.e. a non-stationary Stokes equation coupled to a non-stationary linear wave equation. We will consider the subproblems first. Therefore, we split the complete system of equations into fluid and solid problems and have a look at natural ansatz spaces and the regularity of their solutions.

The linearised fluid problem including the kinematic condition (2.14) reads

$$\begin{aligned} \rho_f \partial_t v_f - \rho_f \nu_f \Delta v_f - \nabla p_f = \rho_f f_f \text{ in } \Omega_f, \qquad \operatorname{div} v_f = 0 \text{ in } \Omega_f, \\ v_f = v_i \text{ on } \Gamma_i, \quad v_f = 0 \text{ on } \partial\Omega_f \setminus \Gamma_i, \qquad v(0) = v_f^0 \text{ in } \Omega_f(0). \end{aligned}$$

For the Stokes velocity, the natural trial space is given by

$$v_f \in \mathcal{V}_f := \{\phi \in L^2(I,V),\, \partial_t \phi \in L^2(I,V^*)\}, \qquad V := \{\phi \in v_{i,\text{ext}} + H_0^1(\Omega),\ \operatorname{div} \phi = 0\}.$$

Here, $v_{i,\text{ext}}$ denotes a suitable extension of the Dirichlet data v_i on Γ_i into the domain. Given a sufficiently smooth domain Ω_f, existence and uniqueness of a solution $v_f \in \mathcal{V}_f$ can be shown for data $f_f \in L^2(I,V^*)$ and compatible initial velocity $v_f^0 \in V$ and interface velocity $v_i \in L^2(I,H^{1/2}(\Gamma_i))$ (see e.g. Temam[135]).

Next, we consider the solid subproblem, i.e. a linear wave equation including the dynamic coupling condition (2.15), which reads in mixed formulation

$$\begin{aligned} d_t \hat{v}_s - \hat{\Delta} \hat{u}_s = \hat{f}_s \ \text{ in } \hat{\Omega}_s, \qquad d_t \hat{u}_s - \hat{v}_s = 0 \ \text{ in } \hat{\Omega}_s, \\ \hat{\partial}_{\hat{n}} \hat{u}_s = \hat{g}_f \text{ on } \hat{\Gamma}_i, \qquad \hat{u}_s = 0 \ \text{ on } \hat{\Gamma}_s := \partial\hat{\Omega}_s \setminus \hat{\Gamma}_i, \\ \hat{u}_s(\cdot,0) = \hat{u}^0 \text{ in } \hat{\Omega}_s, \qquad \hat{v}_s(\cdot,0) = \hat{v}^0 \text{ in } \hat{\Omega}_s. \end{aligned} \tag{4.1}$$

Here, the natural ansatz spaces for solid displacement and velocity are

$$\hat{u}_s \in L^2(I,H_0^1(\hat{\Omega}_s;\hat{\Gamma}_s)), \quad \hat{v}_s \in L^2(I,L^2(\hat{\Omega}_s)).$$

Existence and uniqueness of solutions within these spaces can be proven for right-hand side $\hat{f}_s \in L^2(I,L^2(\hat{\Omega}_s))$, Neumann data $\hat{g}_f \in L^2(I,H^{-1/2}(\hat{\Gamma}_i))$, initial data $\hat{u}^0 \in H_0^1(\hat{\Omega}_s;\hat{\Gamma}_s)$ and $\hat{v}^0 \in L^2(\hat{\Omega}_s)$ on a sufficiently smooth domain $\hat{\Omega}_s$ (see e.g. Wloka[147], Theorem 29.2).

However, the natural regularity $\hat{v}_s \in L^2(I, L^2(\hat{\Omega}_s))$ is not enough to allow for a well-defined trace v_i on Γ_i which could enter the fluid equations as a Dirichlet boundary condition. On the other hand the fluid velocity v_f lies naturally in $L^2(I, H^1(\Omega_f)) \subset \mathcal{V}_f$ such that the trace from the fluid side on Γ_i is well-defined. Thus, one could think of assigning the kinematic condition to the solid problem. This, however, does not solve the problem either as the variational formulation of the solid problem does not allow for a prescription of Dirichlet values for the solid velocity.

The problem persists if we view the system of equations from a monolithic point of view as the solid problem does not provide enough regularity to formulate the kinematic condition (2.14). To overcome this issue, most authors assume a priori that the data of the solid problem is regular enough to ensure the required regularity for the solution $\hat{v}_s$.

Remark 4.1. *We remark that this regularity issue is only present in the non-stationary fluid-structure interaction problem. In a stationary FSI problem, the equation*

$$d_t \hat{u}_s = \hat{v}_s \text{ in } \hat{\Omega}_s$$

reduces to $\hat{v}_s = 0$ *in* $\hat{\Omega}_s$. *Then, the solid velocity can be eliminated from the overall system and a homogeneous Dirichlet condition on* Γ_i *is added to the fluid system.*

Another way to overcome the regularity gap is to include damping terms in the solid equations

$$\left.\begin{aligned} d_t \hat{v}_s + \widehat{\operatorname{div}}\left(\hat{J}\hat{\sigma}_s \hat{F}^T\right) + \gamma_w \hat{v}_s - \gamma_s \hat{\Delta} \hat{v}_s &= \hat{f}_s \\ d_t \hat{u}_s - \hat{v}_s &= 0 \end{aligned}\right\} \quad \text{in } \hat{\Omega}_s. \tag{4.2}$$

The first damping term with $\gamma_w \geq 0$ is called *weak damping*, the second-order term including $\gamma_s > 0$ *strong damping*. Larsson & al.[100] showed that the solution $\hat{v}_s(t)$ of (4.2) has regularity $H^1(\hat{\Omega}_s)$ for all $t > 0$ for initial values $\hat{u}^0 \in H^1(\hat{\Omega}_s)$ and $\hat{v}^0 \in L^2(\hat{\Omega}_s)$. Furthermore, it belongs to $H^s(\hat{\Omega}_s)$ if $\hat{u}^0 \in H^s(\hat{\Omega}_s)$ and $\hat{v}^0 \in H^{s-2}(\hat{\Omega}_s)$ for $s \geq 2$ and sufficiently regular right-hand sides $\hat{f}_s$ and g_f, and domain $\hat{\Omega}_s$. Thus, $\hat{v}_s$ has a well-defined trace on $\hat{\Gamma}_i$.

The damping might even have physical relevance in some cases as many typical solid equations are idealised and do not include certain damping forces that prevent the solid from moving as *perpetuum mobile*. Strong and weak damping have been used by Wick[143] within an ALE approach to simulate cardiovascular dynamics. In this work, he found very good performance, e.g. regarding stability. We will study the effect of these damping terms within an Eulerian approach numerically in Section 11.

4.2 Existence and uniqueness results

In recent years, several advances have been made regarding the existence and uniqueness for stationary and non-stationary fluid-structure interaction problems. The following results have been shown for the case $\Gamma_f = \Gamma_f^d$. For a stationary fluid-structure interaction problem with the Navier-Stokes equations coupled to a St.Venant-Kirchhoff structure, existence and uniqueness have been proven by Grandmont[78].

Lemma 4.2 (Grandmont[78]). *Let the right-hand sides* $f_f \in L^p(\Omega_f(t)$ *and* $f_s \in L^p(\Omega_s(t))$ *sufficiently small and assume that there exists a sufficiently regular domain mapping* $T : \Omega_f(0) \to \Omega_f(t)$. *Then, the stationary system of equations (2.20) has a unique solution*

$$\begin{aligned} &v_f \in W^{2,p}(\Omega_f(t)) \cap W_0^{1,p}(\Omega_f(t)), \quad p_f \in W^{1,p}(\Omega_f(t)), \\ &u_s \in W^{2,p}(\Omega_s(t)) \cap W_0^{1,p}(\Omega_s(t); \Gamma_s). \end{aligned}$$

For the non-stationary case, Coutand & Shkoller showed local existence in time, first for a linearised structure equation[45] and in a second paper for the St.Venant-Kirchhoff model[46], both of them coupled to the incompressible Navier-Stokes equations and without any damping.

For the sake of clarity, we formulate an abbreviated statement of their main result. For the full set of compatibility condition, we refer to[46].

Lemma 4.3 (Coutand & Shkoller[46]). *Let* Ω, $\hat{\Omega}_s \subset \mathbb{R}^3$ *be bounded domains of class* H^4, $f \in H^k(I, H^{3-k}(\Omega))$ *for* $k = 0, \ldots, 3$ *and* $f(0), \partial_t f(0) \in H^4(\Omega)$. *Furthermore, let* $v_f^0 \in H^6(\Omega_f(t))$ *with* $\operatorname{div} v_f^0 = 0$, $\hat{v}_s^0 \in H^6(\hat{\Omega}_s)$ *and for the glued initial velocity assume* $v^0 \in H_0^1(\Omega)$. *Finally, we assume a set of compatibility conditions for the data corresponding to the interface conditions (for details see[46]). Then, there exists a positive time* $t^* \in I$ *and a unique solution to (2.16) in* $I^* = [0, t^*]$ *with regularity*

$$\begin{aligned} &v_f \in H^k(I^*, H^{4-k}(\Omega_f(t))), \quad k = 0, \ldots, 4, \\ &p_f \in H^k(I^*, H^{3-k}(\Omega_f(t)), \quad k = 0, \ldots, 2, \\ &\hat{u}_s \in C(I^*, H^4(\hat{\Omega}_s)). \end{aligned}$$

Global existence in time has been shown recently by Ignatova and co-workers[93]. In this article, they study the coupling between a fluid governed by the incompressible Navier-Stokes equations and a solid governed by a weakly damped wave equation

$$d_t^2 \hat{u}_s - \hat{\Delta} \hat{u}_s + \alpha d_t \hat{u}_s + \beta \hat{u}_s = 0 \quad \text{in } \hat{\Omega}_s$$

with constants $\alpha, \beta > 0$. Due to the incompatibility of fluid and solid equations, they relax the kinematic condition to

$$\hat{v}_f = \hat{v}_s + \gamma \hat{v}_s \hat{n}_s \quad \text{on } \hat{\Gamma}_i$$

for $\gamma > 0$. Using this type of damping and given sufficiently small data, they were able to prove a global in time existence result for the complete fluid-structure interaction system. For simplicity, the right-hand sides $f_f, \hat{f}_s$ are set zero. Again, we omit the compatibility conditions for better readability and refer to[93].

Lemma 4.4 (Ignatova et al.[93]). *Let* $\alpha, \beta, \gamma > 0$ *and* $\Omega_f, \hat{\Omega}_s \subset \mathbb{R}^3$ *be bounded and sufficiently smooth. Furthermore, let* $v_f^0 \in H^4(\Omega_f)$ *with* $\operatorname{div} v_f^0 = 0$, $\hat{u}^0 \in H^3(\hat{\Omega}_s)$ *and* $\hat{v}_s^0 \in H^2(\hat{\Omega}_s)$ *sufficiently small. Assuming compatibility conditions for the data on the interface[93], there exists a global in* *time solution to the fluid-structure interaction problem described above with regularity*

$$\begin{aligned}
&v_f \in W^{k,\infty}(I, H^{3-k}(\Omega_f(t))) \text{ for } k = 0, 1,\\
&v_f \in W^{2,\infty}(I, L^2(\Omega_f(t))) \cup H^2(I, H^1(\Omega_f(t))),\\
&p_f \in W^{k,\infty}(I, H^{2-k}(\Omega_f(t)) \text{ for } k = 0, 1,\\
&\hat{u}_s \in C(I, H^3(\hat{\Omega}_s)).
\end{aligned}$$

4.3 Convergence of finite element approximations

A priori error estimates for full fluid-structure interaction problems are still relatively rare. Tallec & Mani[101] showed in a pioneering work error estimates in both space and time for a linearised non-stationary fluid-structure interaction problem of a Stokes fluid coupled to a lower-dimensional shell structure. Later on, Du et al.[53] showed a priori estimates in space for a finite element discretisation of a stationary Stokes problem coupled to a stationary linear elastic structure. Furthermore, Astorino & Grandmont[3] analysed a non-stationary Stokes problem coupled to a linear elastodynamic structure and derived error estimates in both space and time.

Recently, rigorous error estimates have also been shown in the context of Euler-Lagrangian methods using Nitsche's method for coupling. In this context, Burman & Fernández[34] showed a first-order estimate for a space-discretisation with P_1 finite elements for the same problem.

We shall mention, however, that all of these estimates have been derived for the case of a **fixed** interface. To the best knowledge of the author, the case of a moving interface has not been tackled at all up to now concerning a priori error analysis.

Part II

Discretisation

5 Motivation

In this chapter, we will develop accurate discretisation techniques for interface problems in Eulerian coordinates. Examples are multiphase flows, multicomponent structures or fluid-structure interaction problems using an Eulerian approach.

In the case of non-stationary problems one main difficulty is that the interface moves with time. If the same finite element mesh Ω_h is used for all times, the interface moves over mesh cells. There will be certain interface cells that lie partially in two or more subdomains and the interface will not be resolved by the discretisation. For an illustration see Figure 5.1, where the grey and the white part represent two different subdomains of a fluid-structure interaction problem with a moving interface. This may give rise to accuracy and stability issues. The objective of the present section is to illustrate and discuss such problems.

5.1 Accuracy

In the case of FSI problems, the global velocity $v \in [H^1(\Omega(t))]^2$ is continuous (in the trace sense) across Γ_i due to the *kinematic* interface condition (2.14). Its derivative, however, is typically discontinuous which means that v has a kink across the interface. If the interface is not resolved by mesh lines, this kink cannot be represented accurately in the finite element space. This problem is already present in simple elliptic interface problems with a discontinuous coefficient κ across the interface, e.g.

$$-\operatorname{div}(\kappa \nabla u) = f \text{ in } \Omega, \quad [\kappa \partial_n u] = 0, \; [u] = 0 \text{ on } \Gamma_i.$$

We will study this model problem in detail in Section 6. It is well-known that discrete finite element solutions converge with order $\mathcal{O}(h^{1/2})$ in the energy norm independent of the polynomial degree of the finite element approach if the interface is not resolved with mesh lines (see e.g. Babuška[6]). For this simple problem, a large number of solutions is available in order to recover the optimal orders of convergence (see Section 6.2). One possibility is to use a harmonic averaging of the coefficient κ in the interface cells.

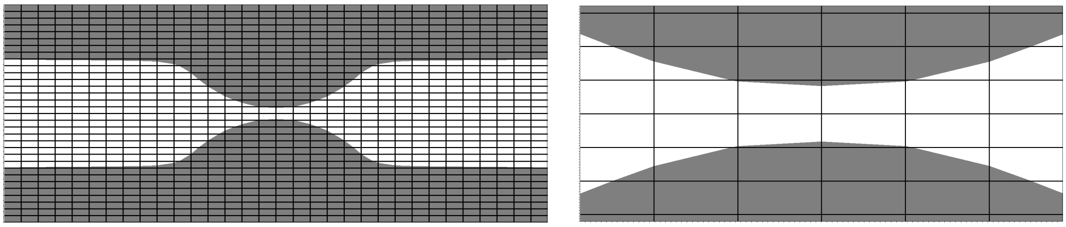

Figure 5.1. Example: Flow through a growing elastic channel in Eulerian coordinates on a fixed mesh. Interface and solid domain move over mesh cells and are thus not resolved by the interface. Right: Zoom-in of the central part.

To the best knowledge of the author a similar analysis for a full FSI problem is not yet available. Here, the additional difficulty is that the equations in fluid and solid domains are of different type. Furthermore, fluid and solid Cauchy stress tensor depend in very different ways on the primal variables. While the fluid tensor depends linearly on the velocity v_f and pressure p_f, the dependence of the solid tensor on the deformation u_s is typically highly non-linear. It is hence questionable if an averaging of stress tensors in interface elements might lead to a satisfactory approximation.

Such an approach has been used by Sugiyama et al.[96] in the context of the *volume-of-fluid* method[86]. For each mesh cell $T \in \Omega_h$, let $\omega_f(T)$ be the volume fraction of a cell that lies in the fluid domain. An averaged stress tensor in the interface cell T is then calculated by

$$\sigma = \omega_f \sigma_f + (1-\omega_f)\sigma_s.$$

This approach is often used for *multiphase flows* where the tensors have the same structure and differ only due to a discontinuous viscosity and density across the interface.

If the interface can be resolved, however, the optimal order of convergence can be recovered for the elliptic model problem. Furthermore, we can show that the interface condition $[\kappa \partial_n u_h] = 0$ is attained for $h \to 0$. For a finite element approach of order m, it holds that

$$\begin{aligned} ||[\kappa(\partial_n u_h)]||_{\Gamma_i} &= ||[\kappa \partial_n(u_h - u)]||_{\Gamma_i} \\ &\le C\left(h^{-1/2}||\nabla(u-u_h)||_{\Omega_1\cup\Omega_2} + h^{1/2}||\nabla^2(u-u_h)||_{\Omega_1\cup\Omega_2}\right) \\ &\le C h^{m-3/2}||\nabla^m u||_{\Omega_1\cup\Omega_2}. \end{aligned} \tag{5.1}$$

This is the same accuracy with which Neumann boundary values are attained in elliptic boundary value problems.

A similar estimate holds true for the *dynamic condition* in fluid-structure interactions

$$\begin{aligned} ||[\sigma_h n]||_{\Gamma_i} &= ||[(\sigma_h - \sigma)n]||_{\Gamma_i} \\ &\le C\Big(h^{-1/2}||\sigma_f(v,p) - \sigma_f(v_h,p_h)||_{\Omega_f} + h^{1/2}||\nabla(\sigma_f(v,p) - \sigma_f(v_h,p_h))||_{\Omega_f} \\ &\qquad + h^{-1/2}||\sigma_s(u) - \sigma_s(u_h)||_{\Omega_s} + h^{1/2}||\nabla(\sigma_s(u) - \sigma_s(u_h))||_{\Omega_s}\Big). \end{aligned}$$

Here, we have used the abbreviation σ_h for $\sigma(v_h, p_h, u_h)$. In the case of a linear structure equation, we obtain the same estimate as in (5.1). For non-linear material laws, some further assumptions on the tensor σ_s are necessary.

In the case of a moving interface, however, resolving the interface in each time step might be a challenging and expensive task in terms of computational cost. Alternatively, the finite element space might be suitably enriched by using e.g. *Extended finite elements* (XFEM)[111]. Here, additional degrees of freedom are added locally to the finite element space to include features of the solution such as kinks in the interior of cells. In Section 6, we will present a novel *fitted* finite element scheme that ensures that the interface is accurately resolved while using a fixed coarse mesh for all time steps and without altering the number of degrees of freedom.

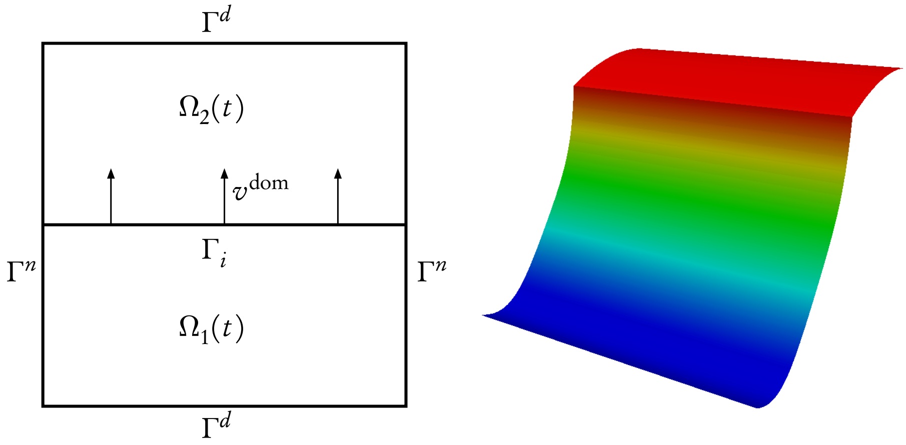

Figure 5.2. *Left:* Sketch of the domain and the interface movement. *Right:* Snapshot of the solution of the parabolic model problem at time $t = 0.2$.

5.2 Stability issues

Finally, the lack of accuracy in the interface region might lead to stability issues. To illustrate this, we consider a simple parabolic interface problem with a discontinuous diffusion coefficient

$$\partial_t u + v^{\text{dom}} \cdot \nabla u - \kappa \Delta u = f \text{ in } \Omega, \quad [\kappa \partial_n u] = [u] = 0 \text{ on } \Gamma_i,$$
$$\partial_n u = 0 \text{ on } \Gamma^n, \quad u = u^d \text{ on } \Gamma^d.$$

The diffusion coefficients are discontinuous across a moving interface that separates the subdomains $\Omega_1(t)$ and $\Omega_2(t)$:

$$\kappa = \begin{cases} 1 & \text{in } \Omega_1(t) = [-1,1] \times [-1,t] \\ 0.1 & \text{in } \Omega_2(t) = [-1,1] \times [t,1] \end{cases}$$

and the convection is given by the movement of the interface $v^{\text{dom}} = (0,1)$. A sketch of the domain as well as a snapshot of the solution is given in Figure 5.2.

In Figure 5.3, we compare the behaviour of the discrete solutions u_h obtained with a non-fitted standard discretisation with Q_1 finite elements on Cartesian meshes with 1024 cells and 4096 cells and the backward Euler time stepping scheme to discrete solutions obtained with the spatial and temporal discretisation techniques that we will introduce in the Sections 6 and 8. Therefore, we plot the L^2- and H^1- norm of discrete solutions over the whole domain Ω and on the interface Γ_i over time. The H^1-norm on the interface is the one as seen from Ω_2.

For the non-fitted standard approach, we observe oscillations in three of the functionals. Only the L^2-norm of the solution is represented accurately. The period of the oscillations is exactly the time that the interface needs to cross one mesh cell. The amplitude of the oscillations decreases in the $H^1(\Omega)$- and the $L^2(\Gamma_i)$-norm with mesh refinement, while on the other hand the frequency with which instabilities occur increases. In the $H^1(\Gamma_i)$-norm, the instabilities do not decrease at all.

In more complex problems, these oscillations might accumulate and give rise to severe stability issues. In the case that the interface location depends on one of the variables (e.g. the

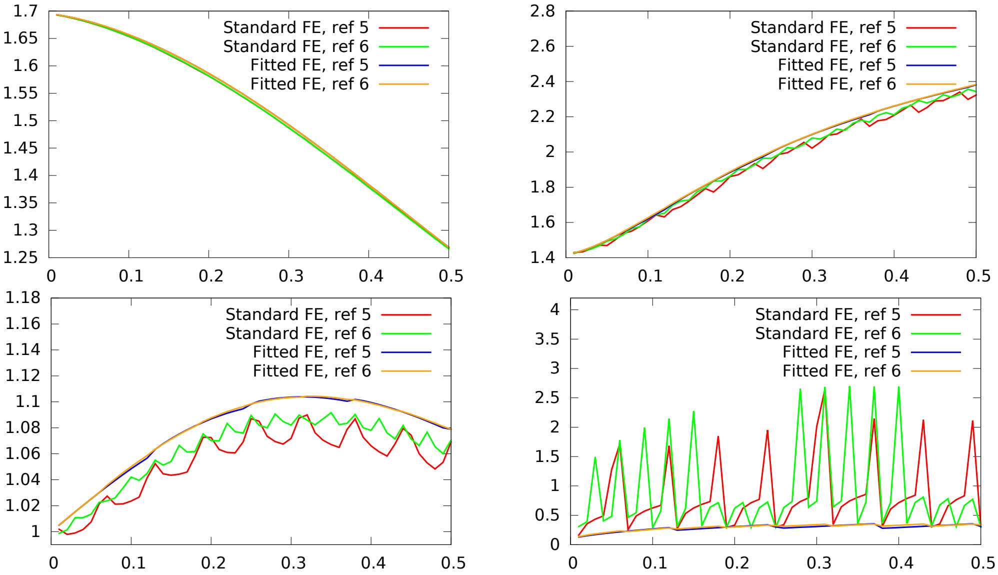

Figure 5.3. *Top:* $L^2(\Omega)$- and $H^1(\Omega)$-norm. *Bottom:* $L^2(\Gamma_i)$- and $H^1(\Gamma_i)$-norm (seen from Ω_2) for a parabolic interface problem with a discontinuous coefficient. A standard, non-fitted finite element approach leads to considerable oscillations in the latter three functionals when the interface jumps over mesh lines.

solid deformation in fluid-structure interactions), such instabilities may have the effect that the interface jumps back and forth over mesh lines in the worst case which intensifies the instabilities.

On the other hand, the fitted finite element approach in space and time shows no oscillations at all. The functional values on the coarser grid are very close to the ones obtained on the finer grid. For details on the construction of this approach, we refer to the Sections 6 and 8.

Structure of the discretisation chapter

The remainder of this chapter is organised as follows: In Section 6, we introduce a *locally modified finite element scheme* for the spatial discretisation and analyse it in detail for an elliptic interface problem. In Section 7, we apply this scheme to the Stokes equations in combination with a *Continuous Interior Penalty* approach for pressure stabilisation.

In Section 8, we introduce a second-order accurate time-stepping scheme for moving interface problems. Then, in Section 9, we study stabilisation techniques for the wave equation on a moving domain. Finally, in Section 10, we show how to combine the different discretisation and stabilisation techniques to tackle fluid-structure interaction problems in Eulerian coordinates.

6 Discretisation of elliptic interface problems

As mentioned earlier in Section 5, the accuracy of a finite element approach that does not resolve the interface might decrease severely. On the other hand, resolving the interface is a challenging task if the interface moves from time step to time step. Constructing a new *fitted mesh* in each time step and interpolating the old solution to the new domain may not not feasible for complex domains. As mentioned before, the problem already exists for simple elliptic interface problems which will be the subject of this section.

To be precise, we consider interface problems, where the solution is continuous on a domain $\Omega \subset \mathbb{R}^2$, but its derivative may have a jump in normal direction over an interior interface. Therefore, we propose an accurate, robust and easy-to-implement finite element method. Besides fluid-structure interaction, problems of this kind also arise in multiphase flows or multicomponent structures. All these examples have in common that the interface between the two phases is moving and may be difficult to capture due to small scale features. We will analyse the proposed method in detail for a simple model problem. The details have already been published in [66].

The organisation of this section is as follows: First, we introduce the simple model problem under consideration in Section 6.1, and give some insights in existing approaches in literature in Section 6.2. In Section 6.3 we describe the iso-parametric finite element approach we use to resolve the interfaces. We give an optimal order a priori error analysis for the modified finite element method in Section 6.4. In Section 6.5, we show, that using a hierarchical finite element basis the condition number of the system matrix is bounded by $\mathcal{O}(h^{-2})$ independent of the interface location. Section 6.6 gives some notes on an efficient implementation of the required modifications in finite element codes. Finally, in Section 6.7 we show numerical results that demonstrate the accuracy and robustness of our proposed method.

6.1 An elliptic model problem

We consider a simple Laplace equation with a discontinuous coefficient κ across an interface line

$$-\nabla\cdot(\kappa_i\nabla u)=f \text{ on } \Omega_i \ \ (i=1,2), \quad [u]=0, \quad [\kappa\partial_n u]=0 \text{ on } \Gamma, \tag{6.1}$$

with constants $\kappa_i > 0$. Here, we denote the subdomains by $\Omega_i, i=1,2$ and by $[u]$ the jump of u across the interface Γ. The variational formulation of this interface problem is given by

$$u\in H_0^1(\Omega): \quad a(u,\phi):=\sum_{i=1}^{2}(\kappa_i\nabla u,\nabla\phi)=(f,\phi) \quad \forall\phi\in H_0^1(\Omega), \tag{6.2}$$

and existence of solutions can be shown by standard arguments. We assume, that the partitioning of Ω into Ω_1 and Ω_2 is non-overlapping $\Omega_1\cap\Omega_2=\emptyset$ and that both subdomains Ω_i $(i=1,2)$ have

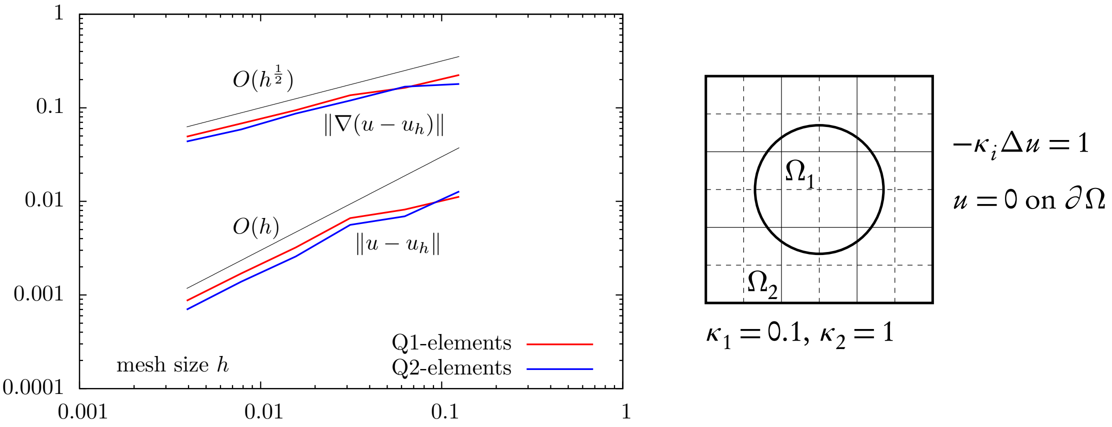

Figure 6.1. L^2- and H^1-error for a standard finite element method using Q_1 and Q_2 polynomials for an elliptic problem with a discontinuous diffusion coefficient. Configuration of the test problem in the right sketch. Details on this problem are given in Section 6.7.

a boundary with sufficient regularity such that for smooth right-hand sides

$$u \in H_0^1(\Omega) \cap H^{r+1}(\Omega_1 \cup \Omega_2),$$

for the solution of (6.1) for a given $r \in \mathbb{N}$, see Babuška[6].

Interface problems are elaborately discussed in literature. If the interface Γ cannot be resolved by the mesh, the overall error for a standard finite element ansatz will be bounded by

$$\|\nabla(u-u_h)\|_\Omega = \mathcal{O}(h^{1/2}),$$

independent of the polynomial degree r of the finite element space, see the early work of Babuška[6] or MacKinnon and Carey[106]. In Figure 6.1, we show the H^1- and L^2-norm errors for a simple interface problem with curved interface that is not resolved by the finite element mesh. Both linear and quadratic finite elements only give $\mathcal{O}(h^{1/2})$ accuracy in the H^1-seminorm and $\mathcal{O}(h)$ in the L^2-norm. This is due to the limited regularity of the solution across the interface.

6.2 Related approaches in literature

It has been shown, that for interface problems with jumping coefficients causing weak discontinuities, optimal convergence can be recovered by a harmonic averaging of the diffusion constants (Tikhonov & Samarskii[137], Shubin & Bell[130]). Such an averaging procedure has been applied to multiphase flows, it is however not suitable for problems, where two entirely different types of differential equations are coupled on the interface, as it is the case for fluid-structure interactions.

For fluid-structure interaction problems, the list of possible discretisation techniques that yield optimal order can be split roughly in two different groups.

Given a fitted finite element configuration, the optimal order of convergence is guaranteed[6,14,29,63,140]. If the interface is moving, curved or has small scale features, the repeated generation of fitted finite element meshes can exceed the feasible effort, however. Further

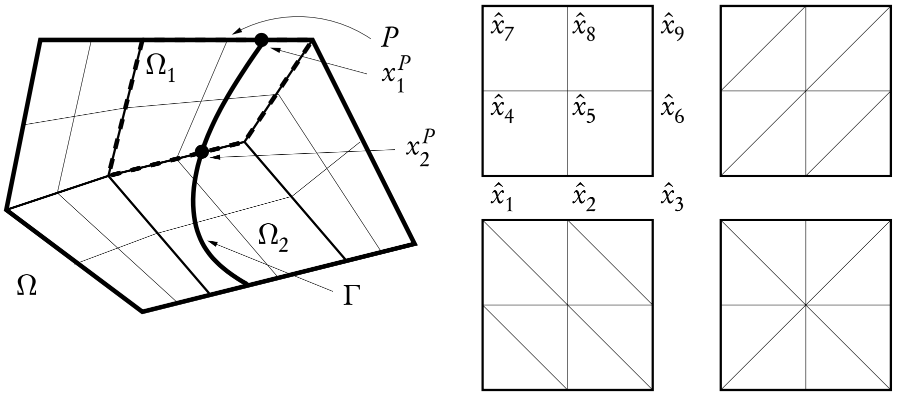

Figure 6.2. *Left:* triangulation Ω_h of a domain Ω that is split into Ω_1 and Ω_2 with interface Γ. The elements in Ω_h are arranged in a patched way. Patch P is cut by Γ at x_1^P and x_2^P. *Right:* subdivision of reference patches $\hat{P}_1, \hat{P}_2, \hat{P}_3, \hat{P}_4$ (top left to bottom right) into eight triangles each.

developments are based on local modifications of the finite element mesh, that only alter mesh elements close to the interface (Boergers[23], Xie et al.[148]). By combining local mesh modifications close to the interface with an isoparametric approximation of curved interfaces, higher order approximation could be shown (Fang[61]).

An alternative approach is based on unfitted finite elements, where the mesh is fixed and does not resolve the interface. Here, proper accuracy is gained by local modifications or enrichment of the finite element basis. Prominent examples for these methods are the the extended finite element method (XFEM, Moes et al.[111]), the generalised finite element method (Babuška et al.[8]) or the unfitted Nitsche method by Hansbo and Hansbo[80,81], that casts the XFEM method into a new light. These enrichment methods are well analysed and show the correct order of convergence. One drawback of these methods is a complicated structure that requires local modifications in the finite element spaces leading to a variation in the connectivity of the system matrix and number of unknowns.

Here, we propose a finite element technique for interface problems that fits both into the context of fitted methods and modified finite element schemes. We use a fixed patch mesh and resolve the interface locally within each patch. Instead of a motion of mesh nodes, we locally adapt the finite element in an implicit parametric way, such that the finite element basis can reflect weak discontinuities at the interface. This scheme requires neither an enrichment of the basis nor a modification of the mesh.

6.3 Interface finite elements

Let Ω_h be a form and shape-regular triangulation of the domain $\Omega \subset \mathbb{R}^2$ into open quadrilaterals. The mesh Ω_h does not necessarily resolve the partitioning $\Omega = \Omega_1 \cup \Gamma \cup \Omega_2$ and the interface Γ can cut the elements $K \in \Omega_h$. We further assume, that the mesh Ω_h has a patch-hierarchy in such a way, that each four adjacent quads arise from uniform refinement of one common father-element, see Figure 6.2. Such a mesh-hierarchy is naturally given for finite element methods based on adaptive mesh refinement and also commonly used for error estimation methods (Becker &

Rannacher[17]) or projection-based stabilisation schemes (Becker & Braack[16]). The interface Γ may cut the patches in the following way:

1. Each (open) patch $P \in \Omega_h$ is either not cut $P \cap \Gamma = \emptyset$ or cut in exactly two points on its boundary: $P \cap \Gamma \neq \emptyset$ and $\partial P \cap \Gamma = \{x_1^P, x_2^P\}$.
2. If a patch is cut, the two cut-points x_1^P and x_2^P may not be inner points of the same edge.

In principle, these assumptions only rule out two possibilities: a patch may not be cut multiple times and the interface may not enter and leave the patch at the same edge. Both situations can be avoided by refinement of the underlying mesh. If the interface is matched by an edge, the patch is not considered cut.

6.3.1 Modification of the finite element space

We define the finite element trial space $V_h \subset H_0^1(\Omega)$ as an iso-parametric space on the triangulation Ω_h:

$$V_h = \left\{ \phi \in C(\bar{\Omega}) \cap H_0^1(\Omega),\ \phi \circ T_P^{-1}\Big|_P \in \hat{Q}_P \text{ for all patches } P \in \Omega_h \right\},$$

where $T_P \in [\hat{Q}_P]^2$ is the mapping between the reference patch $\hat{P} = (0,1)^2$ and the patch $P \in \Omega_h$ such that

$$T_P(\hat{x}_i) = x_i^P, \quad i = 1, \dots, 9,$$

for the nine nodes $x_1^P, \dots, x_9^P$ of the patch, see Figure 6.2. The reference space $\hat{Q}_P$ is a piecewise polynomial space of degree 1, that will depend on whether a patch P is cut by the interface or not. For patches $P \in \Omega_h$ not cut by the interface, we choose the standard space of piecewise bilinear functions

$$\hat{Q}_P = \hat{Q} := \left\{ \phi \in C(\bar{P}),\ \phi\Big|_{K_i} \in \operatorname{span}\{1, x, y, xy\},\ K_1, \dots, K_4 \in P \right\}.$$

If a patch $P \in \Omega_h$ is cut by the interface, we divide the reference patch into eight triangles $T_1, \dots, T_8$ and define

$$\hat{Q}_P = \hat{Q}_{\text{mod}} := \left\{ \phi \in C(\bar{P}),\ \phi\Big|_{T_i} \in \operatorname{span}\{1, x, y\},\ T_1, \dots, T_8 \in P \right\}.$$

Depending on the position of the interface Γ in the patch P, three different reference configurations are considered, see the right sketch in Figure 6.2.

It is important to note, that the functions in $\hat{Q}$ and $\hat{Q}_{\text{mod}}$ are all piecewise linear on the edges ∂P, such that mixing different element types does not affect the continuity of the global finite element space. We denote by $\{\hat{\phi}^1, \dots, \hat{\phi}^9\}$ the standard Lagrange basis of $\hat{Q}$ or $\hat{Q}_{\text{mod}}$ with $\hat{\phi}^i(\hat{x}_j) = \delta_{ij}$. The transformation T_P is given by

$$T_P(\hat{x}) = \sum_{i=1}^{9} x_i^P \hat{\phi}_i(\hat{x}).$$

Next, we present the subdivision of interface patches P into eight triangles. We distinguish four different types of interface cuts, see Figure 6.3:

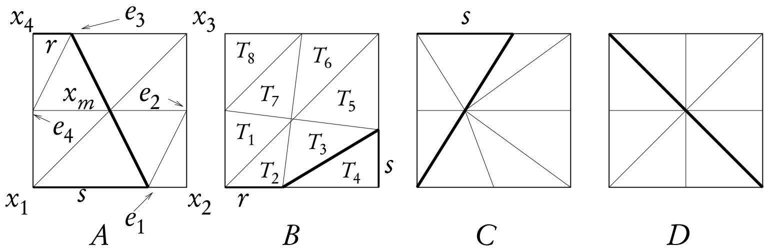

Figure 6.3. Different types of cut patches. The subdivision can be anisotropic with $r,s \in (0,1)$ arbitrary.

Configuration A The patch is cut at the interior of two opposite edges.

Configuration B The patch is cut at the interior of two adjacent edges.

Configuration C The patch is cut at the interior of one edge and in one node.

Configuration D The patch is cut in two opposite nodes.

Configurations A and B are based on the reference patches $\hat{P}_2$ and $\hat{P}_3$, configurations C and D use the reference patch $\hat{P}_4$, see Figure 6.2. By $e_i \in \mathbb{R}^2$, $i = 1,2,3,4$ we denote the vertices on the edges, by $x_m \in \mathbb{R}^2$ the grid point in the interior of the patch. The parameters $r,s \in (0,1)$ describe the relative position of the intersection points with the interface on the outer edges.

If an edge is intersected by the interface, we move the corresponding point e_i on this edge to the point of intersection. The position of x_m depends on the specific configuration. For configuration A, B and D, we choose x_m as the intersection of the line connecting e_2 and e_4 with the line connecting e_1 and e_3. In configuration C, we use the intersection of the line connecting e_2 and e_4 with the line connecting x_1 and e_3.

As the cut of the elements can be arbitrary with $r,s \to 0$ or $r,s \to 1$, the triangle's aspect ratio can be very large, considering $h \to 0$ it is not necessarily bounded. We can however guarantee, that the maximum angles in all triangles will be well bounded away from 180°:

Lemma 6.1 (Maximum angle condition). *All interior angles of the triangles shown in Figure 6.3 are bounded by* $144°$ *independent of* $r,s \in (0,1)$.

Proof. All interior angles can be estimated by basic geometric analysis depending on the parameters $r,s \in (0,1)$. We will show that in each triangle there is at least one angle larger than 36°. Hence, every angle will be bounded by 144°. Obviously, this is true for all triangles that are right-angled.

Configuration A and B: We number the eight triangles of a patch by $T_1, \dots, T_8$ (cf. Figure 6.3). The two outer triangles T_4 and T_8 are right-angled, such that $\alpha \le 90°$ for all interior angles in T_4 and T_8. Furthermore, in configuration A the angles of T_1 at point e_4 and T_5 at point e_2 are right-angled. For the angles in T_2 at e_1 and in T_6 at e_3 it holds that

$$\cos(\alpha_A) = \frac{(e_3 - e_1)\cdot(x_2 - x_1)}{|e_3 - e_1|\,|x_2 - x_1|} = \frac{r - s}{\sqrt{1 + (r-s)^2}} \in \left(-\frac{1}{\sqrt{2}}, \frac{1}{\sqrt{2}}\right),$$

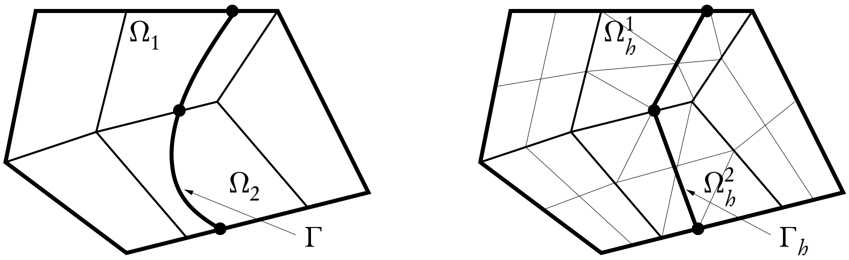

Figure 6.4. *Right:* Splitting of the mesh Ω into subdomains Ω_h^1 and Ω_h^2. The interface Γ_h is a linear approximation of the interface Γ shown on the left-hand side.

such that $\alpha_A \in (45°, 135°)$. In configuration B these four angles are given by

$$\cos(\alpha_B) = \frac{(e_3 - e_1)\cdot(x_2 - x_1)}{|e_3 - e_1||x_2 - x_1|} = \frac{1/2 - r}{\sqrt{1+(1/2-r)^2}} \in \left(-\frac{1}{\sqrt{5}}, \frac{1}{\sqrt{5}}\right),$$

which means $\alpha_B \in (70°, 110°)$. Finally, we have for the interior angles of T_3 and T_7 at x_m

$$\cos(\alpha) = \frac{(e_3 - e_1)\cdot(e_2 - e_4)}{|e_3 - e_1||e_2 - e_4|}.$$

Considering configuration A, it holds that

$$\cos(\alpha_A) = \frac{r - s}{\sqrt{1+(r-s)^2}} \in \left(-\frac{1}{\sqrt{2}}, \frac{1}{\sqrt{2}}\right) \quad \Rightarrow \quad \alpha_A \in (45°, 135°).$$

For configuration B, we get

$$\cos(\alpha_B) = \frac{s - r}{\sqrt{1+\left(s-\frac{1}{2}\right)^2}\sqrt{1+\left(r-\frac{1}{2}\right)^2}} \in \left(-\frac{4}{5}, \frac{4}{5}\right) \quad \Rightarrow \quad \alpha_B \in (36°, 144°).$$

Configuration C: Here, the four triangle touching nodes e_2 and e_4 all have one right angle. It remains to estimate the interior angles at nodes e_1 and e_3. For these angles, it holds that

$$\cos(\alpha_C) = \pm\frac{\begin{pmatrix}1\\0\end{pmatrix}\cdot\begin{pmatrix}s\\1\end{pmatrix}}{\left|\begin{pmatrix}s\\1\end{pmatrix}\right|} = \pm\frac{s}{\sqrt{1+s^2}} \in \left(-\frac{1}{\sqrt{2}}, \frac{1}{\sqrt{2}}\right) \quad \Rightarrow \quad \alpha_C \in (45°, 135°).$$

Configuration D: Obviously, all triangles are right-angled. □

6.3.2 Discrete variational formulation

In the case of a curved interface, the interface is resolved in a linear approximation by mesh lines. With the help of the discrete approximation of the interface, we introduce a second splitting of the domain Ω into the discrete subdomains

$$\Omega = \Omega_h^1 \cup \Omega_h^2,$$

such that all cells of the triangulation are either completely included in Ω_h^1 or in Ω_h^2, see Figure 6.4. Using this, we define a discrete bilinear form

$$a_h(u_h,\phi_h) := (\kappa_h \nabla u_h, \nabla \phi_h)_\Omega, \tag{6.3}$$

where

$$\kappa_h = \begin{cases} \kappa_1 & \text{in } \Omega_h^1, \\ \kappa_2 & \text{in } \Omega_h^2. \end{cases}$$

Note that κ_h differs from κ in a small layer between continuous interface Γ and discrete interface Γ_h. The discrete problem is to find $u_h \in V_h$ such that

$$a_h(u_h,\phi_h) = (f,\phi_h)_\Omega \quad \forall \phi_h \in V_h.$$

Together with (6.2), we have the Galerkin orthogonality

$$a(u,\phi_h) - a_h(u_h,\phi_h) = 0 \quad \forall \phi_h \in V_h. \tag{6.4}$$

6.4 A priori error analysis

The maximum angle conditions of Lemma 6.1 allows us to define robust Lagrangian interpolation operators $I_h : H^2(T) \cap C(\overline{T}) \to V_h$ for smooth functions $v \in H^2(T) \cap C(\overline{T})$ on an element T. For such a function, we have the standard error estimates

$$\|\nabla^k (v - I_h v)\|_T \le c h_{T,\max}^{2-k} \|\nabla^2 v\|_T, \quad k = 0,1, \tag{6.5}$$

with constants $c > 0$ and $h_{T,\max}$ is the maximum diameter of a triangle $T \in P$ (see e.g. Apel[2]). The interpolation error estimates are robust with respect to the maximum diameter $h_{T,\max} \approx h_P$ that is of the same order as the diameter of the patches P. We do not get (and will not depend on) an optimal interpolation result with respect to the anisotropic triangles in terms of short edges $h_{T,\min} \ll h_{T,\max}$.

The main difficulty for the a priori error analysis is that the continuous solution u is not smooth in some cells T that are affected by the interface such that (6.5) does not hold. We will denote the set of these cells by

$$S_h = \{ T \in \Omega_h \mid T \cap \Gamma \neq \emptyset \}. \tag{6.6}$$

Furthermore, let S be the part in between the discrete and the continuous interface and S_T the intersection with a cell T

$$S = \bigcup_{i=1,2} \left(\Omega_h^i \setminus \Omega_i \right), \qquad S_T = S \cap T. \tag{6.7}$$

Note that S is exactly the region where κ and κ_h and thus the bilinear forms $a(\cdot,\cdot)$ and $a_h(\cdot,\cdot)$ differ. Finally, for $T \in S_h$ let $\Gamma_{h,T}$ be the part of the discrete interface Γ_h that lies on the boundary of T and $\Gamma_T = \Gamma \cap T$ the part of the interface Γ lying in T.

We start the error analysis by providing an auxiliary lemma that estimates the smallness of the L^2-norm and the H^1-norm with respect to the interface region S.

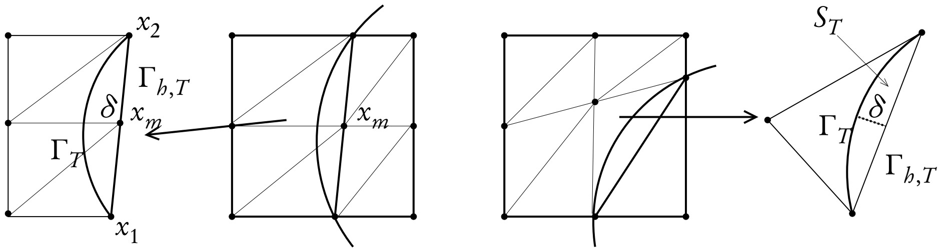

Figure 6.5. Two different patches and two triangles, that are affected by the interface intersection. The modified finite element mesh resolves the interface in a linear approximation.

Lemma 6.2. *Let Γ be a smooth interface with C^2-parametrisation and S the region, where the discrete and continuous bilinear form differ (defined in (6.7)). For a function $\phi \in H^1(\Omega_1 \cup \Omega_2)$, it holds that*

$$||\phi||_S \leq C h_P ||\phi||_{H^1(\Omega_1 \cup \Omega_2)}. \tag{6.8}$$

Furthermore, for a discrete function $\phi_h \in V_h$, we have

$$||\nabla \phi_h||_S \leq C h_P^{1/2} ||\nabla \phi_h||_{\Omega_1 \cup \Omega_2}. \tag{6.9}$$

Proof. In Figure 6.5 we see two possible configurations for patches, that are cut by the interface. In the patch on the right-hand side, one cell is affected by the interface, while on the left three cells are cut by the interface. For the sake of brevity, we will analyse the situation shown in the right sketch, the left one can be treated in a very similar way. As Γ_T has a C^2-parametrisation, it holds for the distance δ between $\Gamma_{h,T}$ and Γ_T that

$$\delta = \mathcal{O}(h_P^2), \quad |T| = \mathcal{O}(h_P^2), \quad |S_T| = \mathcal{O}(h_P^3).$$

In the case of a discrete function $\phi_h \in V_h$, $\nabla \phi_h$ is constant on an interface element T. Thus, it holds by a simple scaling argument that

$$||\nabla \phi_h||_{S_T}^2 \leq c h_P \, ||\nabla \phi_h||_T^2 .$$

(6.9) follows after summation over all cells $T \in S_h$. To show (6.8), we use the Poincaré-like estimate

$$||\phi||_{S_T}^2 \leq C \left(h_P^2 ||\phi||_{\Gamma_T}^2 + h_P^4 ||\nabla \phi||_{S_T}^2 \right), \tag{6.10}$$

(see e.g. Bramble & King[28], Ciarlet[40]). Here, the trace on Γ_T is the trace as seen from S_T. We sum over all elements $T \in S_h$

$$||\phi||_S^2 \leq C \left(h_P^2 ||\phi||_\Gamma^2 + h_P^4 ||\nabla \phi||_S^2 \right).$$

Finally, we apply the (global) trace inequality

$$||\phi||_\Gamma \leq C ||\phi||_{H^1(\Omega_1 \cup \Omega_2)}$$

to obtain (6.8). □

Lemma 6.2 can be used to estimate the difference between the continuous and discrete bilinear form. Therefore note that by definition of the bilinear forms, it holds that

$$\left|a(\phi,\psi)-a_h(\phi,\psi)\right| = \left|\,((\kappa-\kappa_h)\nabla\phi,\nabla\psi)_\Omega\,\right|.$$

As $\kappa-\kappa_h$ vanishes in $\Omega\setminus S$, it holds that

$$\left|a(\phi,\psi)-a_h(\phi,\psi)\right| \le C|\kappa_1-\kappa_2|\,\|\nabla\phi\|_S\,\|\nabla\psi\|_S.$$

Using Lemma 6.2, we have the following result:

Lemma 6.3. *Let Γ be a smooth interface with C^2-parametrisation. The difference between the continuous and discrete bilinear forms defined in (6.2) and (6.3) can be estimated by*

$$\left|a(\phi_h,\psi_h)-a_h(\phi_h,\psi_h)\right| \le C h_P \|\nabla\phi_h\|_\Omega \|\nabla\psi_h\|_\Omega, \tag{6.11}$$

in the case of discrete functions $\phi_h,\psi_h\in V_h$. For $\phi\in H^{k+1}(\Omega_1\cup\Omega_2),\psi\in H^{l+1}(\Omega_1\cup\Omega_2)$ ($k,l=0,1$) it holds that

$$\left|a(\phi,\psi)-a_h(\phi,\psi)\right| \le C h_P^{k+l} \|\nabla\phi\|_{H^k(\Omega_1\cup\Omega_2)} \|\nabla\psi\|_{H^l(\Omega_1\cup\Omega_2)}. \tag{6.12}$$

Next, we provide an interpolation estimate into the space V_h that takes into account that the discrete cells resolve the interface only in a linear approximation and thus the continuous solution is not smooth across the discrete interface. We define a slightly modified nodal interpolation I_h. A modification is necessary in interface patches that are cut in opposite edges (Case A) or where the interface goes through one or two corners (Case C and D), see Figure 6.3. Here, the midpoint x_m of the patch lies on the discrete interface Γ_h, but not on the continuous one Γ, see Figure 6.5. Setting the point value $u(x_m)$ for the interpolant $I_h u$ in x_m would not lead to estimates of optimal order. Instead, we use an interpolation of the outer points x_1,x_2 of the same patch that lie on both the discrete and the continuous interface.

To be precise, we define the interpolant $I_h u$ in a grid point $x_i\in\Omega_h$ as follows

$$I_h u(x_i) = \begin{cases} u(x_i) & \text{if } x_i\notin\Gamma_h \text{ or } x_i\in\Gamma_h\cap\Gamma \\ \frac{\|x_i-x_1\|}{\|x_2-x_1\|}u(x_2)+\frac{\|x_2-x_i\|}{\|x_2-x_1\|}u(x_1) & \text{else.} \end{cases} \tag{6.13}$$

Lemma 6.4. *Let $\Omega\subset\mathbb{R}^2$ be a domain with convex polygonal boundary and Γ a smooth interface with C^2-parametrisation. Let $u\in H^2(\Omega_1\cup\Omega_2)\cap H_0^1(\Omega)$ and $I_h u$ be the modified Lagrangian interpolation defined in (6.13). It holds that*

$$\|\nabla(u-I_h u)\|_\Omega \le C h_P \|u\|_{H^2(\Omega_1\cup\Omega_2)}. \tag{6.14}$$

Proof. If the interface Γ can be resolved exactly by the modified finite element scheme, the statement is standard, see (6.5). The argumentation we use here for a general C^2-parametrised interface not matched by the triangulation, is similar to the work of Basting & Prignitz[14].

We refer again to Figure 6.5 for two possible configurations of patches, that are cut by the interface. Let S_h be the set of elements T that are affected by the interface, see (6.6) and $S_h^i\subset S_h$

the subset belonging to Ω_h^i $(i = 1,2)$. For all other cells, we can use the standard interpolation estimate (6.5)

$$\begin{aligned} ||\nabla(u - I_h u)||_\Omega^2 &= ||\nabla(u - I_h u)||_{\Omega\setminus S_h}^2 + ||\nabla(u - I_h u)||_{S_h}^2 \\ &\le C h_P^2 ||\nabla^2 u||_{\Omega_1\cup\Omega_2}^2 + ||\nabla(u - I_h u)||_{S_h}^2. \end{aligned} \tag{6.15}$$

Here, we used (6.5) on $\Omega \setminus S_h$ and extended the domain to the complete domain Ω afterwards.

It remains to estimate the second term in (6.15). Therefore, let $\tilde{u}_i \in H^2(\Omega)$ (i=1,2) be a continuous extension of $u \in H^2(\Omega_i)$ to the complete domain Ω. Such an extension exists, as the boundary Γ is smooth, see e.g. the textbook of Wloka[147], and it holds that

$$||\tilde{u}_i - u||_{H^2(\Omega_i)} = 0, \quad ||\tilde{u}_i||_{H^2(\Omega)} \le C||u||_{H^2(\Omega_i)}, \quad i = 1,2. \tag{6.16}$$

We will derive an estimate for $||\nabla(u - I_h u)||_{S_h^1}^2$. The corresponding estimate on S_h^2 follows analogously. By the triangle inequality it holds that

$$\begin{aligned} ||\nabla(u - I_h u)||_{S_h^1} &\le ||\nabla(u - \tilde{u}_1)||_{S_h^1} + ||\nabla(\tilde{u}_1 - I_h \tilde{u}_1)||_{S_h^1} + ||\nabla(I_h \tilde{u}_1 - I_h u)||_{S_h^1} \\ &\le C||\nabla(u - \tilde{u}_1)||_{S_h^1} + ||\nabla(\tilde{u}_1 - I_h \tilde{u}_1)||_{S_h^1}. \end{aligned} \tag{6.17}$$

since $I_h u = I_h \tilde{u}_1$ on S_h^1 for the interpolant defined in (6.13). $u - \tilde{u}_1$ vanishes everywhere on S_h^1 besides on S. By using Lemma 6.2 and the continuity of the extension (6.16), we have that

$$||\nabla(u - \tilde{u}_1)||_{S_h^1} \le ||\nabla(u - \tilde{u}_1)||_S \le ||\nabla u||_S + ||\nabla \tilde{u}_1||_S \le Ch||u||_{H^2(\Omega_1\cup\Omega_2)}.$$

To estimate the interpolation error in (6.17), note that $\tilde{u}_1 \in H^2(\Omega)$. We will show a bound for the entire patch containing a cell $T \in S_h^1$. Therefore, we use the bilinear transformation (not the *piecewise* bilinear transformation $T_P \in \hat{Q}$) of the whole patch to the reference patch and apply the Bramble-Hilbert lemma there. This is possible as by the definition of the interpolation (6.13) the functional $||\nabla(\tilde{u}_1 - I_h \tilde{u}_1)||_P$ vanishes on $P_1(P)$

$$||\nabla(\tilde{u}_1 - I_h \tilde{u}_1)||_T \le ||\nabla(\tilde{u}_1 - I_h \tilde{u}_1)||_P \le C h_P ||\nabla^2 \tilde{u}_1||_P.$$

Summing over all cells $T \in S_h^1$ and using the continuity of the extension (6.16) yields

$$||\nabla(\tilde{u}_1 - I_h \tilde{u}_1)||_{S_h^1} \le C h_P ||\nabla^2 \tilde{u}_1||_\Omega \le C h_P ||\nabla^2 u||_{\Omega_1}. \tag{6.18}$$

The statement follows by combining (6.15), (6.17) and (6.18) and the analogous estimate on S_h^2. □

Now we are able to prove the main result of this section:

Theorem 6.5 (A priori estimate). *Let $\Omega \subset \mathbb{R}^2$ be a domain with convex polygonal boundary, split into $\Omega = \Omega_1 \cup \Gamma \cup \Omega_2$, where Γ is a smooth interface with C^2-parametrisation. We assume that Γ divides Ω in such a way that the solution $u \in H_0^1(\Omega)$ satisfies the stability estimate*

$$u \in H_0^1(\Omega) \cap H^2(\Omega_1 \cup \Omega_2), \quad ||u||_{H^2(\Omega_1\cup\Omega_2)} \le c_s ||f||.$$

For the corresponding modified finite element solution $u_h \in V_h$, it holds that

$$||\nabla(u - u_h)||_\Omega \le C h_P ||f||, \quad ||u - u_h||_\Omega \le C h_P^2 ||f||.$$

Proof. We start by estimating the H^1-seminorm error

$$\begin{aligned} c\|\nabla(u-u_h)\|_\Omega^2 &\le a_h(u-u_h,u-u_h)\\ &= a_h(u-u_h,u-I_hu)+a_h(u-u_h,I_hu-u_h). \end{aligned} \tag{6.19}$$

For the first part, we use the Cauchy-Schwarz inequality and the interpolation estimate (6.14) as usual. The second part can be estimated with the Galerkin orthogonality (6.4) and Lemma 6.3

$$\begin{aligned} a_h(u-u_h,I_hu-u_h) &= (a_h-a)(u,I_hu-u_h)\\ &\le Ch_P\|\nabla u\|_{H^1(\Omega_1\cup\Omega_2)}\|\nabla(I_hu-u_h)\|\\ &\le Ch_P\|f\|\left(\|\nabla(I_hu-u)\|+\|\nabla(u-u_h)\|\right). \end{aligned}$$

Here, we have used the notation $(a-a_h)(\cdot,\cdot)=a(\cdot,\cdot)-a_h(\cdot,\cdot)$ for better readability. By using Young's inequality and absorbing the last term into the left-hand side, we obtain

$$\|\nabla(u-u_h)\|^2 \le C\left(\|\nabla(u-I_hu)\|^2+h_P^2\|f\|^2\right). \tag{6.20}$$

The H^1-seminorm estimate follows with Lemma 6.4.

To estimate the L^2-norm error, we make use of a dual problem. Let $z\in H_0^1(\Omega)$ be the solution of

$$a(\phi,z)=\|u-u_h\|^{-1}(u-u_h,\phi)\quad \forall\phi\in H_0^1(\Omega). \tag{6.21}$$

The solution z lies in $H_0^1(\Omega)\cap H^2(\Omega_1\cup\Omega_2)$ and $\|z\|_{H^2(\Omega_1\cup\Omega_2)}\le c_s$. By testing (6.21) with $\phi=u-u_h$, we have

$$\|u-u_h\|=a(u-u_h,z)=a_h(u-u_h,z)+(a-a_h)(u-u_h,z). \tag{6.22}$$

For the second part, Lemma 6.3 gives

$$(a-a_h)(u-u_h,z)\le Ch_P\|\nabla(u-u_h)\|_\Omega\|z\|_{H^2(\Omega_1\cup\Omega_2)}.$$

Next, we insert the interpolant I_hz into the first part of (6.22) and use the Galerkin orthogonality (6.4)

$$\begin{aligned} a_h(u-u_h,z) &= a_h(u-u_h,z-I_hz)+a_h(u-u_h,I_hz)\\ &= a_h(u-u_h,z-I_hz)+(a_h-a)(u,I_hz)\\ &= a_h(u-u_h,z-I_hz)+(a_h-a)(u,I_hz-z)-(a_h-a)(u,z). \end{aligned}$$

For the first term, we use the Cauchy-Schwarz inequality, the remaining terms can be handled with Lemma 6.3

$$\begin{aligned} a_h(u-u_h,z-I_hz) &\le C\|\nabla(u-u_h)\|_\Omega\|\nabla(z-I_hz)\|_\Omega,\\ (a_h-a)(u,I_hz-z) &\le Ch_P\|u\|_{H^2(\Omega_1\cup\Omega_2)}\|\nabla(z-I_hz)\|_\Omega\\ -(a_h-a)(u,z) &\le Ch_P^2\|u\|_{H^2(\Omega_1\cup\Omega_2)}\|z\|_{H^2(\Omega_1\cup\Omega_2)}. \end{aligned}$$

Finally, we use Lemma 6.4, the H^1-seminorm estimate (6.20) and stability estimates for the primal and dual solutions to obtain

$$\|u-u_h\|_\Omega \le Ch_P^2\|u\|_{H^2(\Omega_1\cup\Omega_2)}\|z\|_{H^2(\Omega_1\cup\Omega_2)} \le Ch_P^2\|f\|_\Omega.$$

□

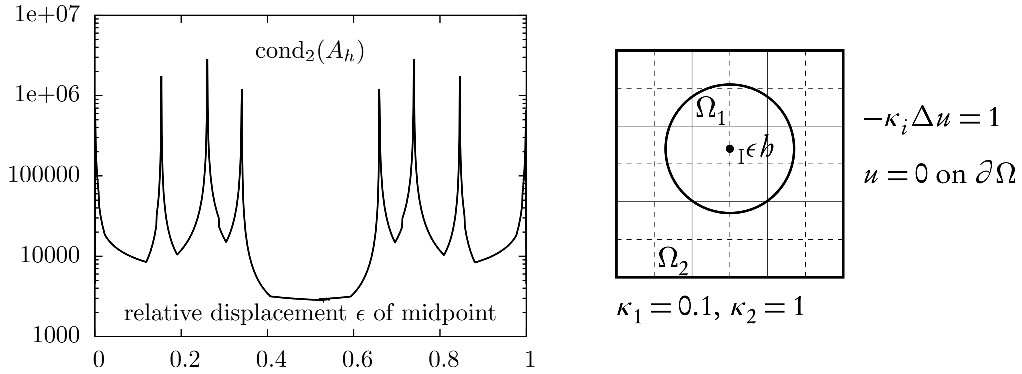

Figure 6.6. Condition number of the system matrix $\mathrm{cond}_2(A_h)$ depending on the displacement of the circle Ω_1.

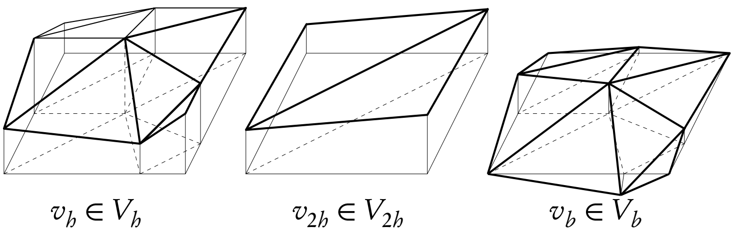

Figure 6.7. Example for a hierarchical splitting of a function $v_h \in V_h$ into coarse mesh part $v_{2h} \in V_{2h}$ and fine mesh fluctuation $v_b \in V_b$.

6.5 Condition number analysis

The modified finite element ansatz described above has one serious drawback. For certain anisotropies (e.g. $s, r \to 0$) the condition number of the stiffness matrix is not bounded. To illustrate this, we consider an interface problem where Ω_1 is a circle contained in the unit square Ω (see Figure 6.6, right sketch). To study the sensitivity with respect to anisotropies, we move the circle in vertical direction by ϵ. We will give further details on this example in Section 6.7. In Figure 6.6 left sketch, we show how the condition number changes for different ϵ. For $\epsilon \to 0$, the condition number increases with order $\mathcal{O}(1/\epsilon)$.

In this section, we will present a scaled hierarchical finite element basis for the space V_h, that will yield system matrices A_h that satisfy the usual bound $\mathrm{cond}_2(A_h) = \mathcal{O}(h_P^{-2})$ with a constant that does not depend on the position of the interface Γ relative to the mesh elements.

We split the finite element space V_h in a hierarchical manner

$$V_h = V_{2h} + V_b, \quad N := \dim(V_h) = \dim(V_{2h}) + \dim(V_b) =: N_{2h} + N_b.$$

The space V_{2h} is the standard space of piecewise bilinear or linear functions on the patches $P \in \Omega_h$ equipped with the usual nodal Lagrange basis $V_{2h} = \mathrm{span}\{\phi_{2h}^1, \dots, \phi_{2h}^{N_{2h}}\}$. Patches cut by the interface are split into two triangles.

The space $V_b = V_h \setminus V_{2h}$ collects all functions, that are needed to enrich V_{2h} to V_h. These functions are defined piecewise on $T_1, \dots, T_8$ in the remaining 5 degrees of freedom, see Figure 6.7

for an example. The basis of this patch is denoted by $V_b = \text{span}\{\phi_b^1, \dots, \phi_b^{N_b}\}$. The finite element space V_{2h} is fully isotropic and standard analysis holds. Functions in V_{2h} do not resolve the interface, while the basis functions $\phi_b^i \in V_b$ will depend on the interface location if $\Gamma \subset \text{supp}\ \phi_b^i$.

Remark 6.6. *By using the splitting $V_h = V_{2h} + V_b$, the proposed method can also be seen as an enrichment method (e.g. an extended finite element method, XFEM[111]). Therefore, we consider the space V_{2h} as the basic finite element space and the space V_b as the enrichment to capture the weak discontinuity at the interface.*

For a function $v_h \in V_h$ we use the (unique) splitting

$$v_h = \sum_i v_h^i \phi_h^i = \sum_{i=1}^{N_{2h}} v_{2h}^i \phi_{2h}^i + \sum_{i=1}^{N_b} v_b^i \phi_b^i = v_{2h} + v_b \in V_{2h} + V_b.$$

We use the notation $\boldsymbol{v}_h^i, \boldsymbol{v}_{2h}^i$ and $\boldsymbol{v}_b^i$ to indicate the degrees of freedom in the spaces V_h, V_{2h} and V_b and introduce the vectors $\boldsymbol{v}_h, \boldsymbol{v}_{2h}$ and $\boldsymbol{v}_b$ defined by these components.

Lemma 6.7 (Hierarchical finite element spaces)**.** *For every $v_h = v_{2h} + v_b \in V_h$, it holds that*

$$(i) \quad ||\nabla v_h||^2 \le 2||\nabla v_{2h}||^2 + 2||\nabla v_b||^2,$$

and further

$$(ii) \quad ||\nabla v_{2h}||^2 + ||\nabla v_b||^2 \le C||\nabla v_h||^2,$$

with a constant $C > 0$.

Proof. The first inequality follows from $v_h = v_{2h} + v_b$. To derive the second inequality, we need to exploit the hierarchical setup of the finite element spaces. First, by $i_{2h} : V_h \to V_{2h}$ we denote the nodal Lagrange interpolant into the coarse finite element space. Stability of this (discrete) interpolation gives the first half of the result

$$||\nabla v_{2h}|| = ||\nabla i_{2h} v_h|| \le C||\nabla v_h||.$$

By using the reverse triangle inequality, we get

$$||\nabla v_b|| \le ||\nabla(v_b + v_{2h})|| + ||\nabla v_{2h}|| \le (1 + C)||\nabla v_h||.$$

□

The following analysis will be based on two essential assumptions for the test functions of the spaces V_{2h} and V_b:

Assumption 6.8 (Finite element basis)**.** *There exists a constant $C > 0$ independent of h and the interface location, such that it holds for every basis function*

$$C^{-1} \le ||\nabla \phi_b^i|| \le C, \quad i = 1, \dots, N_b. \tag{6.23}$$

Further, there exists a constant $C > 0$ independent of h and the interface location, such that for all $v_b \in V_b$ it holds that

$$|\boldsymbol{v}_b^i| \le C||\nabla v_b||_{\mathcal{N}_i}, \quad i = 1, \dots, N_b, \tag{6.24}$$

where by $\mathcal{N}_i = \{K \in \Omega_h,\ x_i \in \bar{K}\}$ we denote the neighbourhood of all elements involving the Lagrange point x_i.

Both assumption hold true for standard finite element spaces on shape- and form-regular finite element meshes and can be shown by using inverse estimates. Assumption (6.23) is fulfilled after an appropriate scaling of the basis functions. Details for the modified hierarchical finite element spaces will be given below and in[66].

Next, we show two estimates for the largest and smallest eigenvalues. These two results will be combined in Theorem 6.11 to show a bound for the condition number of the system matrix. The proofs follow the ideas of Bank and Scott[11].

Lemma 6.9 (Large eigenvalues). *There exists a constant $C > 0$ independent of the interface location, such that it holds:*

$$\mathbf{v}_h^T \mathbf{A}_h \mathbf{v}_h = a(v_h, v_h) \le C \mathbf{v}_h^T \mathbf{v}_h \quad \forall v_h \in V_h.$$

Proof. It holds that

$$a(v_h, v_h) \le C\|\nabla v_h\|^2 = C \sum_{P\in\Omega_h} \|\nabla v_h\|_P^2 = C \sum_{P\in\Omega_h} \Big\| \sum_{x_i\in P} \mathbf{v}_h^i \nabla \phi_h^i \Big\|^2.$$

As only a finite number of basis functions have their support in P it holds that

$$a(v_h, v_h) \le C \sum_{P\in\Omega_h} \sum_{x_i\in P} |\mathbf{v}_h^i|^2 \|\nabla\phi_h^i\|_P^2$$

Using Assumption (6.23), it follows that

$$a(v_h, v_h) \le C \sum_{i=1}^{N} |\mathbf{v}_h^i|^2 = C \mathbf{v}_h^T \mathbf{v}_h.$$

where again we used, that every node x_i is part of only a limited number of patches. □

Next, we show an estimate for the small eigenvalues:

Lemma 6.10 (Small eigenvalues). *There exists a function $C > 0$ independent on the interface location, such that it holds that*

$$\mathbf{v}_h^T \mathbf{A}_h \mathbf{v}_h = a(v_h, v_h) \ge C h_P^2 \mathbf{v}_h^T \mathbf{v}_h \quad \forall v_h \in V_h.$$

Proof. Let $v_h = v_{2h} + v_b$. First, we will show the result for $v_{2h} \in V_{2h}$ and $v_b \in V_b$ separately.

(i) We start with functions $v_{2h} \in V_{2h}$. Let $v_{2h} = \sum_{i=1}^{N_{2h}} \mathbf{v}_{2h}^i \phi_{2h}^i$:

$$\mathbf{v}_{2h}^T \mathbf{v}_{2h} = \sum_{i=1}^{N_{2h}} (\mathbf{v}_{2h}^i)^2 \le \sum_{P\in\Omega_{2h}} \sum_{x_i\in P} (\mathbf{v}_{2h}^i)^2.$$

On a patch $P \in \Omega_{2h}$, it follows by using an inverse estimate for the standard nodal Lagrange basis that

$$\sum_{x_i\in P} (\mathbf{v}_{2h}^i)^2 \le C\|v_{2h}\|_{L^\infty(P)}^2 \le C h_P^{-2} \|v_{2h}\|_{L^2(P)}^2.$$

Then, by Poincaré's inequality on Ω, it finally holds that

$$v_{2h}^T v_{2h} \leq C h_P^{-2} \sum_{P \in \Omega_h} \|v_{2h}\|_{L^2(P)}^2 \leq C h_P^{-2} \|v_{2h}\|^2 \leq C h_P^{-2} \|\nabla v_{2h}\|^2. \tag{6.25}$$

(ii) Next, we treat the case $v_b \in V_b$. By using Assumption (6.24) we get immediately

$$v_b^T v_b = \sum_{i=1}^{N_b} (v_b^i)^2 \leq C \sum_{i=1}^{N_b} \|\nabla v_b\|_{\mathcal{N}_i}^2 \leq C \|\nabla v_b\|^2, \tag{6.26}$$

where the constant C depends on the overlap of elements in the neighbourhoods $\mathcal{N}_i$. The result follows as $h_P^{-2} \geq 1$ for $h < 1$.
(iii) We combine these two results. By Lemma 6.7 it holds that

$$\begin{aligned} v_h^T \mathbf{A}_h v_h = a(v_h, v_h) \geq C \|\nabla v_h\|^2 &\geq C \|\nabla v_{2h}\|^2 + C \|\nabla v_b\|^2 \\ &\geq C \left(a(v_{2h}, v_{2h}) + a(v_b, v_b) \right). \end{aligned}$$

Hence, using (6.25) and (6.26)

$$v_h^T \mathbf{A}_h v_h \geq C h_P^2 \left(v_{2h}^T v_{2h} + v_b^T v_b \right) = C h_P^2 v_h^T v_h.$$

□

Combining Lemma 6.9 and 6.10, we get an estimate for the condition number:

Theorem 6.11 (Condition number). *Under Assumption 6.8 it holds for the condition number that*

$$\mathrm{cond}_2(\mathbf{A}) \leq C h_P^{-2},$$

with a constant $C > 0$ not depending on the interface location.

6.5.1 Setup of the hierarchical finite element basis

In this section, we give some details on the hierarchical finite element basis and on Assumption 6.8.

To construct the basis functions of the space V_{2h} in an interface patch P, we split P into two large triangles by one of the two diagonal lines depending on the patch type. On these large triangles, we define the standard Lagrange basis function ϕ_i^{2h} ($i = 1...4$) with respect to the four outer mesh nodes.

Afterwards, the large triangles are both split into four subtriangles and the basis ϕ_i^b ($i = 1...5$) of the enrichment V_b is defined as in V_h as the Lagrangian basis on the remaining nodes. In Figure 6.8, we illustrate two hierarchical basis functions from V_{2h} and two basis functions from V_b for an isotropic element. If the splitting of patch elements in the non-hierarchical finite element method is chosen such that the diagonal line is resolved by mesh lines, the resulting finite element spaces are equal.

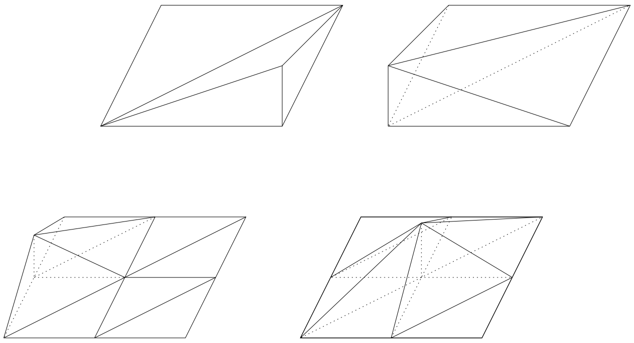

Figure 6.8. *Top:* Two basis functions $\phi_i^{2h} \in V_{2h}$. *Below:* Two basis functions $\phi_i^h \in V_h$.

It remains to give details on Assumption 6.8. The first assumption (6.23) can be fulfilled easily if we scale the hierarchical Lagrangian basis functions $\phi_i (i = 1 \ldots N)$ by appropriate scaling factors

$$\tilde{\phi}_i := \frac{\phi_i}{\|\nabla \phi_i\|}.$$

In a practical implementation, one can use the basis ϕ_i $(i = 1 \ldots N)$ to assemble the system matrix $\tilde{A}_h$ and apply a simple row- and column-wise scaling with the diagonal elements

$$\tilde{a}_{ij} = (\nabla \phi_j, \nabla \phi_i), \quad a_{ij} := \frac{\tilde{a}_{ij}}{\sqrt{\tilde{a}_{ii}\tilde{a}_{jj}}},$$

which yields directly

$$\|\nabla \tilde{\phi}_i\|^2 = a_{ii} = \frac{\tilde{a}_{ii}}{\tilde{a}_{ii}} = 1$$

(see also Section 6.6).
For the rather technical proof of the second assumption (6.24), we refer to [66]:

Lemma 6.12. *For the hierarchical splitting of the finite element space V_h defined above, there exists a constant $C > 0$, such that for all $i \in [0, N_h]$ it holds that*

$$(v_h^i)^2 \le C \|\nabla v_h\|^2_{\mathcal{N}_i} \quad \forall v_h \in V_h. \tag{6.27}$$

Proof. See Frei & Richter [66], Section A.2. □

6.6 Implementation

The modified finite element basis is implemented in a patchwise parametric approach. Instead of moving or changing the mesh, capturing the interface is realised by a special parametrisation of the finite element basis.

For this, the triangulation Ω_h consists of quadrilaterals, that we denote as patches $P \in \Omega_h$. Each patch P has nine degrees of freedom with coordinates x_i for $i = 1, \ldots, 9$. If the patch is not

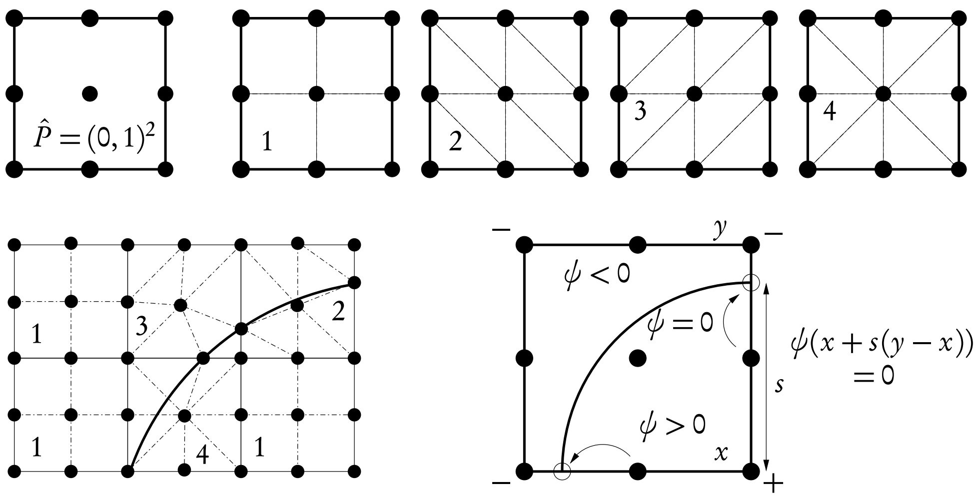

Figure 6.9. Implementation of the parametric patch-based approach. *Top row:* Four different patch types. *Lower left:* Sample mesh with all four variants. *Lower right:* Identification of the cut points.

cut by the interface, we imagine a partitioning into four quadrilaterals $K_1, \dots, K_4 \subset P$ and define the space of piecewise bilinear functions. However, if the patch is cut, we imagine a partitioning into eight triangles $T_1, \dots, T_8 \subset P$ instead and define the space of piecewise linear functions. Whatever splitting of the patch is applied, we still have nine degrees of freedom connected to the same coordinates. See Figure 6.9 for a small mesh, where three different patch types are present.

Next, let $\hat{P} = (0,1)^2$ be a reference domain and $\hat{Q}(P) = \operatorname{span}\{\hat{\phi}_1, \dots, \hat{\phi}_9\}$ the space of either piecewise bilinear functions or piecewise linear functions on the corresponding subdivision of the reference patch, see Figure 6.9. Then, the actual basis functions on $P \in \Omega_h$ are defined in a parametric sense

$$Q(P) := \operatorname{span}\{\phi_1, \dots, \phi_9\}, \quad \phi_i := \hat{\phi}_i \circ \hat{T}_P^{-1},$$

where the reference patch map $\hat{T}_P$ is defined in the usual iso-parametric way

$$\hat{T}_P(\hat{x}) := \sum_{j=1}^{9} x_j \hat{\phi}_j(\hat{x}). \tag{6.28}$$

In order to assign an element type to a patch, let us assume, that the interface is represented by an implicit function, e.g. as zero-contour of a Level-Set function $\psi(x)$.

We first notice that a patch is affected by the interface if ψ shows different signs in two of the outer mesh nodes. In the same way, we identify the edges cut by the interface. Let x and y be the two outer nodes of an edge with $\psi(x) > 0 > \psi(y)$, see Figure 6.9. In order to find the exact coordinate where the interface line crosses an edge, we use a simple Newton scheme to find the zero of

$$\psi\big(x + s(y-x)\big) = 0.$$

The new coordinate $x_m := x + s(y-x)$ replaces the coordinate of the edge midpoint in (6.28).

In order to incorporate the hierarchical basis of the finite element space defined in Section 6.5, we replace the basis functions corresponding to the outer mesh nodes by their hierarchical counterparts. The proper scaling of all test functions in order to fulfil (6.23) is simply achieved by a preconditioning of the linear system with the diagonal of the system matrix from left and right

$$\mathbf{A}\mathbf{x}=\mathbf{b} \quad \Leftrightarrow \quad \mathbf{D}^{-\frac{1}{2}}\mathbf{A}\mathbf{D}^{-\frac{1}{2}}\tilde{\mathbf{x}}=D^{-\frac{1}{2}}b, \quad \tilde{\mathbf{x}}=\mathbf{D}^{\frac{1}{2}}\mathbf{x},$$

where $\mathbf{D}=\operatorname{diag}(a_{ii})$.

One of the advantages of the presented scheme is that the number of unknowns within each patch is fixed independent of the location of the interface. Further, structure and connectivity of the system matrix stay identical and are known a priori even if the position of the interface varies. In contrast to e.g. the extended finite element method (XFEM), we do not need any blending elements as all basis functions are piecewise linear on edges.

6.7 Numerical examples

In this section, we present three different test cases to substantiate the theoretical findings. We will include all different types of interface cuts (configurations A to D) with arbitrary anisotropies including $r,s\to 0$ or $r,s\to 1$.

Example 1: Circular interface

This first example has already been considered to discuss the interface approximation in Section 6.3 and the dependence of the condition number on the interface in Section 6.5, see Figure 6.1 for a sketch of the configuration. The unit square $\Omega=(-1,1)^2$ is split into a ball $\Omega_1=B_R(x_m)$ with radius $R=0.5$ and midpoint $x_m=(0,\epsilon h_P)$ for an $\epsilon\in[0,1]$ and $\Omega_1=\Omega\setminus\bar{\Omega}_2$. As diffusion parameters we choose $\kappa_1=0.1$ and $\kappa_2=1$. We choose the analytical solution

$$u(x)=\begin{cases}-2\kappa_2\|x-x_m\|^4, & x\in\Omega_2,\\ -\kappa_1\|x-x_m\|^2+\frac{1}{4}\kappa_1-\frac{1}{8}\kappa_2 & x\in\Omega_1,\end{cases}$$

to define the right-hand side $f_i:=-\kappa_i\Delta u$ and the Dirichlet boundary data. After some steps of global refinement this simple example includes the configurations A to C. In Figure 6.10, we plot the H^1- and L^2-norm errors obtained on several levels of global mesh refinement. According to Theorem 6.5, we observe linear convergence in the H^1-norm and quadratic convergence in the L^2-norm. For comparison, Figure 6.1 shows the corresponding results using the standard non-fitting basis functions. A sketch of the solution is given on the right side of Figure 6.10.

Next, in Figure 6.11, we show a study of the condition number's dependency on the parameter $\epsilon\in[0,1]$ used to shift the midpoint of the circle $x_m=(0,\epsilon h_P)$. The scaled hierarchical ansatz space shows optimal behaviour $\mathcal{O}(h_P^{-2})$ with regard to mesh size h_P and no dependency on the shift ϵ, while the standard approach shows very large conditions numbers with $\operatorname{cond}_2(A_h)\to\infty$ for $\epsilon\to 0$ and $\epsilon\to 1$.

Example 2: Horizontal cuts

To study the different cuts of interface patches in more detail, let us next consider that $\Omega=(-1,1)^2$ is cut horizontally into

$$\Omega_1(\epsilon)=\{x\in\Omega\,|\,x_2<\epsilon h_P\},\quad \Omega_2(\epsilon)=\{x\in\Omega\,|\,x_2>\epsilon h_P\}.$$

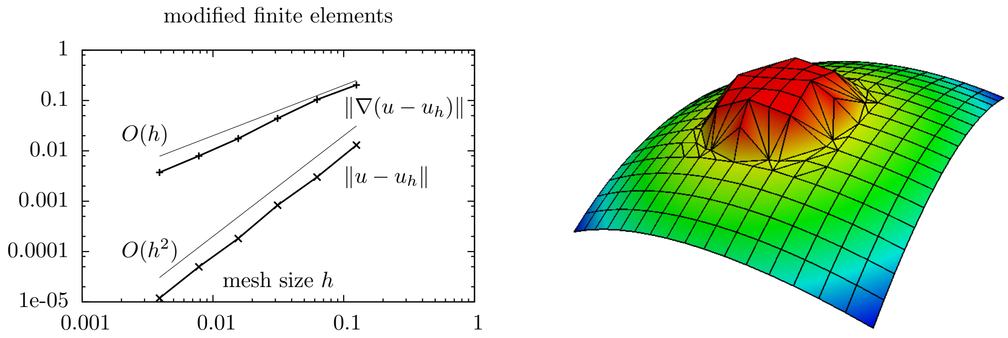

Figure 6.10. Example 1: H^1- and L^2-Error under mesh refinement. *Right:* Sketch of the solution.

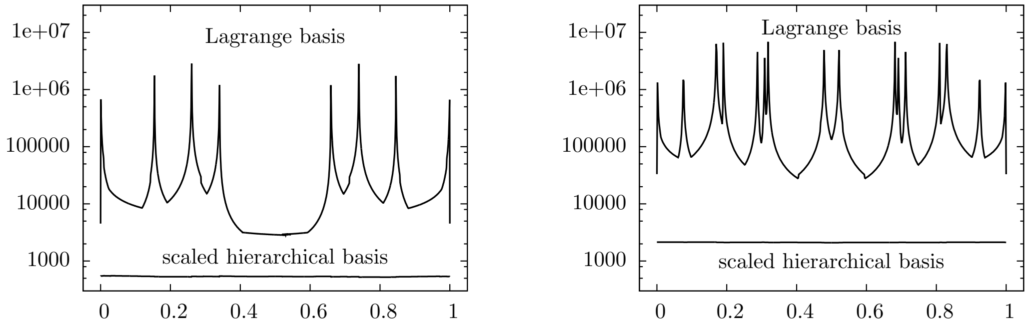

Figure 6.11. Example 1: condition number of the system matrix depending on the displacement of the circle Ω_1 by ϵh_P for $\epsilon \in [0,1]$. Standard Lagrange basis versus the scaled hierarchical basis introduced in Section 6.5. *Left:* $h_P = 1/16$, *right:* $h_P = 1/32$.

By varying $\epsilon \in [0,1]$, the interface patches of a Cartesian mesh will be split into rectangulars with vertical edge lengths ϵh_P and $(1-\epsilon)h_P$, $0 < \epsilon < 1$ that are divided into two triangles each. We choose the right-hand side $f = -\kappa_i \Delta u$ and the Dirichlet data according to the solution

$$u(x) = \begin{cases} \frac{\kappa_2}{\kappa_1}(x_2 - \epsilon h_P) - (x_2 - \epsilon h_P)^2 & x \in \Omega_1 \\ (x_2 - \epsilon h_P) + (x_2 - \epsilon h_P)^2 & x \in \Omega_2. \end{cases} \tag{6.29}$$

In Figure 6.12, we plot the L^2-norm and H^1-norm error for $0 \le \epsilon \le 1$ on meshes with patch size $h_P = 1/16$ and $h_P = 1/32$. Both errors clearly depend on the position ϵ of the cut. As one would expect, we get the smallest errors for $\epsilon = 0$, $\epsilon = \frac{1}{2}$ and $\epsilon = 1$, where the mesh is perfectly uniform and resolves the interface exactly. The largest error given for $\epsilon \to 0$ and $\epsilon \to 1$, where the anisotropy of the interface patches is maximal. Nevertheless, we see that the error remains bounded for all $\epsilon \in [0,1]$. The variations get smaller on the finer mesh.

To explain these error variations, we analyse the interpolation error briefly. The mesh consists of h_P^{-2} patches. Only h_P^{-1} patches are affected by the interface. These are cut into $2h_P^{-1}$ quads of size $h_P/2 \times \epsilon h_P$ and $2h_P^{-1}$ quads of size $h_P/2 \times (1-\epsilon)h_P$ (each of them divided into two triangles).

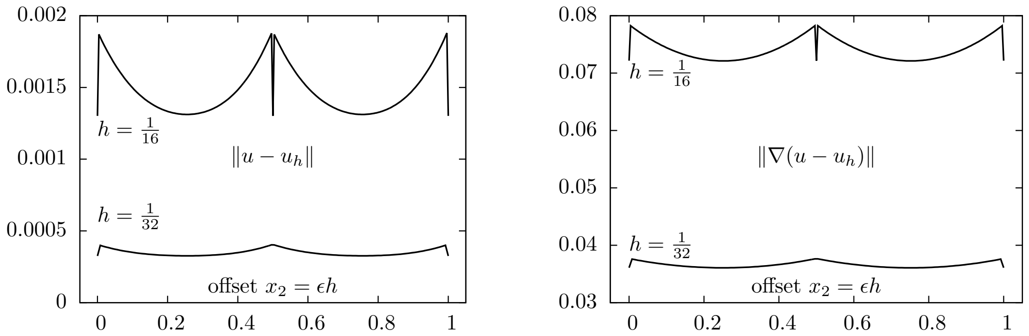

Figure 6.12. Example 2: L^2- and H^1-norm error depending on a vertical offset $x_2 = \epsilon h_P$ of the interface.

The remaining $4h_P^{-2} - 4h_P^{-1}$ quads have all the size $h_P/2 \times h_P/2$. As the interface is a horizontal line, the modified mesh is always Cartesian and due to superconvergence effects the errors we observe are essentially the interpolation errors $||u - I_h u||$. The solution u depends only on x_2, see (6.29). For the L^2-norm, it holds on a quad K of size $h_1 \times h_2$ that

$$||u - I_h u||_K^2 \le c h_2^4 ||\partial_{22} u||_K^2 \approx c h_1 h_2^5.$$

Summed over all elements $K \in \Omega_h$, we get the interpolation bound

$$||u - I_h u||_\Omega^2 \approx \left(4h_P^{-2} - 4h_P^{-1}\right)\frac{h_P^6}{64} + 2h_P^{-1}\epsilon^5\frac{h_P^6}{2} + 2h_P^{-1}(1-\epsilon)^5\frac{h_P^6}{2}.$$

In the best case, for $\epsilon = \frac{1}{2}$, it holds that

$$||u - I_h u||_\Omega^2 \approx \frac{h_P^4}{16},$$

while in the worst case for $\epsilon \to 0$ or $\epsilon \to 1$ we get

$$||u - I_h u||_\Omega^2 \approx \frac{h_P^4}{16}(1 + 15h_P).$$

Hence, the L^2-norm error varies by a factor of $\sqrt{1 + 15h_P}$ which relates to approximately $\sqrt{2} \approx 1.4$ for $h_P = 1/16$ and $\sqrt{3/2} \approx 1.2$ for $h_P = 1/32$. For the H^1-norm a similar analysis leads to a variation factor of $\sqrt{1 + 3h_P}$. In Table 6.1, we gather variation factors between maximum and minimum L^2- and H^1-norm on both meshes and find very good agreement with this prediction.

Example 3: Tilted interface line

Next, we consider two subdomains that are separated by a straight interface line through the origin, which might be horizontal ($\alpha = 0$), vertical ($\alpha = \pi/2$) or inclined ($0 < \alpha < \pi/2$

	H^1-error		L^2-error	
	$h_P = 1/16$	$h_P = 1/32$	$h_P = 1/16$	$h_P = 1/32$
Worst case ($\epsilon = 10^{-6}h$)	$7.864 \cdot 10^{-2}$	$3.774 \cdot 10^{-2}$	$1.904 \cdot 10^{-3}$	$4.077 \cdot 10^{-4}$
Best case ($\epsilon = h$)	$7.217 \cdot 10^{-2}$	$3.608 \cdot 10^{-2}$	$1.302 \cdot 10^{-3}$	$3.255 \cdot 10^{-4}$
Prediction	1.090	1.046	1.392	1.212
Variation	1.090	1.046	1.462	1.252

Table 6.1. Example 2: maximum and minimum error under vertical displacement ϵh_P of the interface line. Comparison of errors with the predicted error variation.

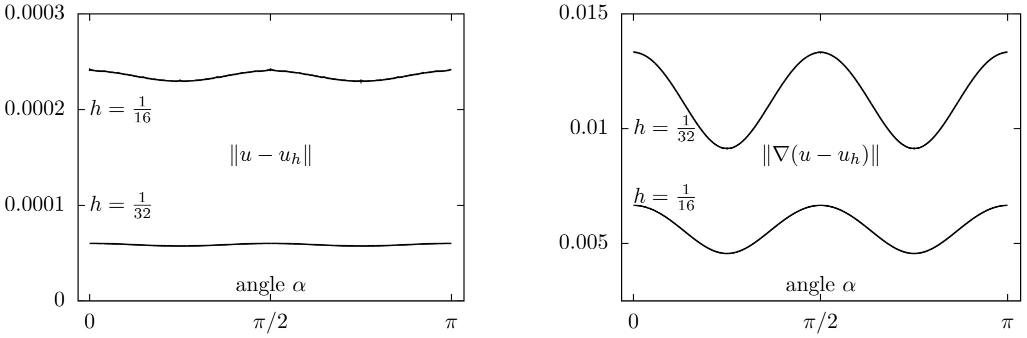

Figure 6.13. Example 3: L^2- and H^1-norm error for a line cutting at different angles $\alpha \in [0, \pi]$.

or $\pi/2 < \alpha < \pi$). The interface Γ_i is defined by the relation $\cos(\alpha)x_2 = \sin(\alpha)x_1$ and the subdomains are

$$\Omega_1^\alpha = \{x \in \Omega \,|\, \cos(\alpha)x_2 < \sin(\alpha)x_1\},$$
$$\Omega_2^\alpha = \{x \in \Omega \,|\, \cos(\alpha)x_2 > \sin(\alpha)x_1\}.$$

We choose the right-hand side $f = -\kappa_i \Delta u$ and the Dirichlet data according to the given exact solution:

$$u(x) = \begin{cases} \sin\left(\frac{\kappa_2}{\kappa_1}(\cos(\alpha)x_2 - \sin(\alpha)x_1)\right), & x \in \Omega_1 \\ \sin(\cos(\alpha)x_2 - \sin(\alpha)x_1) & x \in \Omega_2. \end{cases}$$

In Figure 6.13, we plot the L^2- and H^1-norm error for angles $\alpha \in [0, \pi]$ and two different refinement levels ($h_P = 1/16$ and $h_P = 1/32$). In the case $\alpha = \pi/2$ all the interface patches are of type D, while in the other cases types A to C appear with all kinds of anisotropies inside. Again, we observe linear convergence for the H^1-norm error and quadratic convergence in the L^2-norm. The error varies up to a factor of approximately $\sqrt{2}$ in the case of the H^1-norm and about 1.05 in the L^2-norm which can be explained similarly to the case of horizontal cuts. We emphasise that these variations are again bounded for all $\alpha \in [0, \pi]$.

7 Discretisation of the Stokes equations and pressure stabilisation

In this section, we study the discretisation of the linear Stokes equations on a curved domain using the *locally modified finite element method*. We consider the following problem

$$\begin{aligned} -\nu\Delta v - \nabla p &= f \\ \operatorname{div} v &= 0 \end{aligned} \quad \text{in } \Omega_f, \qquad \begin{aligned} v &= 0 \quad \text{on } \Gamma_f^d \subset \partial\Omega_f, \\ \nu\partial_n v - p &= 0 \quad \text{on } \Gamma_f^n := \partial\Omega_f \setminus \Gamma_f^d, \end{aligned} \tag{7.1}$$

with $\Gamma_f^d \neq \emptyset$. We assume that Ω_f is contained in a larger domain Ω that is discretised by a regular patch mesh (see Section 6). This discretisation is motivated by the fact that we want to consider moving domains in the following chapters and we do not want to construct a new mesh resolving Ω_f in each time step.

We split each of the patches into four quadrilaterals or eight triangles such that the interface is resolved in a linear approximation. This subdivision specifies a division of the domain Ω into cells $K \in \Omega_h^f$ and $K \in \Omega_h^s$, such that $\Omega = \Omega_h^s \cup \Omega_h^f$. Similar to Section 6, we define discrete spaces

$$\begin{aligned} V_h^0 &= \left\{ \phi \in C(\bar\Omega) \cap H_0^1(\Omega), \,\middle|\, \phi \circ T_P^{-1}|_P \in \hat Q_P \text{ for all patches } P \in \Omega_h, \phi = 0 \text{ in } \Gamma_{f,h}^d \cup \Omega_h^s \right\}, \\ V_h &= \Big\{ \phi \in C(\bar\Omega) \cap H_0^1(\Omega), \,\Big|\, \phi \circ T_P^{-1}|_P \in \hat Q_P \text{ for all patches } P \in \Omega_h, \\ &\qquad\qquad \phi(x_i) = 0 \text{ for grid points } x_i \in \Omega_h^s \Big\}. \end{aligned}$$

The mappings T_P as well as the local spaces $\hat Q_P$ are defined as in Section 6.

We will use V_h^0 for the velocities and V_h for the pressure ansatz space. To cope with the lack of *inf-sup stability* of this *equal-order elements*, we will add stabilisation terms to the variational formulation that are based on penalising pressure gradients or jumps of pressure gradients over element edges.

For this stabilisation technique, we will show optimal-order error estimates for velocity and pressure. For simplicity, we assume that the domain Ω_f is a polygonal domain that is exactly resolved within the space V_h. The more general case that $\partial\Omega_h^f$ is only a linear approximation of $\partial\Omega_f$ can be handled by the techniques used in the previous section. For the patch mesh Ω_{2h}, we assume again the regularity assumptions stated in Section 6.3.

7.1 H^1-stable interpolation and projection

Defining an H^1-stable interpolation operator that attains boundary values is not straight-forward. An H^1-stable operator could be obtained by defining a standard H^1-stable interpolation i_{2h} :

$H^1(\Omega) \to V_{2h}$ of Clément[41] or Scott-Zhang type[129] onto the patch grid and an interpolation to Ω_h. The H^1-stability follows from the regularity of the patch grid Ω_{2h}. This interpolant will not fulfil the boundary values, however, on boundary lines that lie in the interior of patches. A manipulation of this operator is not straight-forward, as simply setting the desired boundary values in interface nodes does not necessarily conserve the H^1-stability in anisotropic elements.

Ritz projection

For our purposes there is a simple solution, however. We can show that the Ritz projection operator $R_h : H^1(\Omega) \to V_h^0$ defined by

$$(\nabla R_h u, \nabla \phi_h)_{\Omega_f} = (\nabla u, \nabla \phi_h)_{\Omega_f} \quad \forall\, \phi_h \in V_h^0 \tag{7.2}$$

is H^1-stable. By definition, it also attains the boundary values. We summarise its approximation properties in the following lemma.

Lemma 7.1. *Let Ω_f be a convex polygonal domain that is exactly resolved within the finite element space V_h. It holds for $j = 0, 1$ that*

$$||\nabla^j (u - R_h u)||_{\Omega_f} \le C h_P^{2-j} ||\nabla^2 u||_{\Omega_f}. \tag{7.3}$$

Furthermore, the Ritz projection is H^1-stable and we have the estimate

$$||\nabla^j (u - R_h u)||_{\Omega_f} \le C h_P^{1-j} ||\nabla u||_{\Omega_f}. \tag{7.4}$$

Proof. The first estimate can be shown using the same techniques we used in Section 6 to show Theorem 6.5. Therefore, we extend the solution u by zero in the domain Ω_s. For details on the estimate, see also Richter[122]. The H^1-stability follows by definition of the Ritz-projection by testing 7.2 with $\phi_h = R_h u$. This directly implies (7.4) for $j = 1$. For the L^2-norm estimate, we define a dual problem: Let $z \in H_0^1(\Omega_f)$ be the solution of

$$(\nabla z, \nabla \phi)_{\Omega_f} = \left(\frac{u - R_h u}{||u - R_h u||}, \phi \right)_{\Omega_f} \qquad \forall \phi \in H_0^1(\Omega_f). \tag{7.5}$$

As Ω_f is a convex polygonal domain, z lies in $H^2(\Omega_f)$ and $||\nabla^2 z||_{\Omega_f} \le c$. Now, as usual, we test (7.5) with $\phi_h = u - R_h u$ and insert the nodal interpolation $I_h z$ by using Galerkin orthogonality

$$||u - R_h u||_{\Omega_f} = (\nabla(z - I_h z), \nabla(u - R_h u))_{\Omega_f} \le C h_P ||\nabla u||_{\Omega_f} ||\nabla^2 z||_{\Omega_f} \le C h_P ||\nabla u||_{\Omega_f}.$$

□

A projection operator for the discrete pressure gradient

Next, we introduce a projection that will be needed for the discontinuous gradient of p_h. We denote the space of discontinuous, piecewise linear functions by

$$V_h^{\mathrm{dc}} = \left\{ \phi : \Omega_f \to \mathbb{R}^2 \,\middle|\, (\phi \circ T_P^{-1})|_K \in P_1(K) \text{ for all cells } K \in \Omega_h^f,\ \phi = 0 \text{ in } \Omega_h^s \right\}.$$

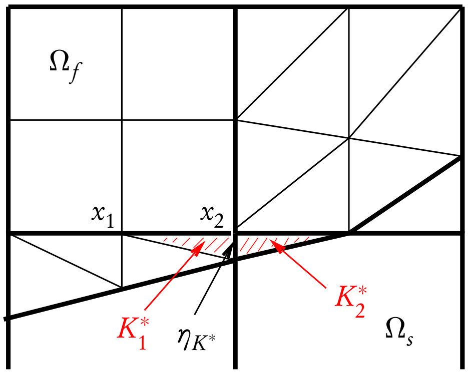

Figure 7.1. Cells K_1^*, K_2^* corresponding to grid points x_1, x_2 for the construction of the projection τ_h. In both x_1 and x_2 the shortest edge of the surrounding cells is the edge η_{K^*}. While in x_1 the choice of the cell K_1^* is uniquely determined, we can choose either K_1^* or K_2^* in x_2.

Note that the gradient of a function $p_h \in V_h$ lies in V_h^{dc}.

We define a projection $\tau_h : V_h^{\text{dc}} \to V_h^0 \cap H_0^1(\Omega_f)$. As V_h^0 is spanned by a Lagrangian basis, it is enough to specify the value of the projection $\tau_h v_h$ of a function $v_h \in V_h^{\text{dc}}$ in every grid point $x_i \in \Omega_f$. A function $v_h \in V_h^{\text{dc}}$ might be discontinuous in x_i, and thus a value $v_h(x_i)$ is not well-defined. Instead, we can specify values $v_h|_K(x_i)$ by extending the polynomial $v_h|_K$ to the boundary of K.

Let $\eta_{K,\min}$ be the shortest edge of a cell K. We denote its length by $h_{K,\min} = |\eta_{K,\min}|$. In x_i, we choose the value $v_h|_{K_i^*}(x_i)$ of a cell K_i^* that possesses the smallest edge of all surrounding cells (see Figure 7.1):

$$\tau_h v_h(x_i) = \begin{cases} v_{h|K_i^*}(x_i) & x_i \in \Omega_f, \\ 0 & x_i \in \partial\Omega_f \end{cases} \qquad \text{where } K_i^* = \operatorname*{argmin}_{K\in\Omega_h^f,\, x_i\in\overline{K}} h_{K,\min}. \tag{7.6}$$

In the case that this choice is not unique, we can pick any of the cells K for which $h_{K,\min}$ is minimal. We have the following stability result for the projection τ_h:

Lemma 7.2. *Let $p_h \in V_h^{dc}$ and τ_h the projection operator defined in (7.6). It holds that*

$$\left\|\nabla\tau_h\left(h_{\min}^2\nabla p_h\right)\right\|_{\Omega_f} \le C h_P \|\nabla p_h\|_{\Omega_f} \tag{7.7}$$

where $h_{\min}$ denotes the piecewise constant function defined by $h_{K,\min}$ in each cell K and C is a constant that is independent of the interface position.

Proof. Let $w_h := h_{\min}^2 \nabla p_h$. We start with an inverse inequality and use the definition of τ_h

$$\|\nabla\tau_h w_h\|_K^2 \le C h_{K,\min}^{-2}\|\tau_h w_h\|_K^2 \le \sum_{i=1}^{n} C h_{K,\min}^{-2}\|w_{h|K_i^*}(x_i)\|_K^2, \tag{7.8}$$

where n denotes the number of interior nodes of K. By transformation to the reference element, we estimate

$$\|w_{h|K_i^*}(x_i)\|_K^2 \le |K|\,\|w_h\|^2_{L^\infty(K_i^*)} \le C\frac{|K|}{|K_i^*|}\|w_h\|^2_{K_i^*} = C\frac{|K|}{|K_i^*|}h^4_{K_i^*,\min}\|\nabla p_h\|^2_{K_i^*}.$$

In combination with (7.8), this gives

$$\begin{aligned}\|\nabla\tau_h w_h\|_K^2 &\le C\sum_{i=1}^n \frac{|K|}{|K_i^*|}\frac{h^4_{K_i^*,\min}}{h^2_{K,\min}}\|\nabla p_h\|^2_{K_i^*} = C\sum_{i=1}^n \frac{h^3_{K_i^*,\min}h_{K_i^*,\max}}{h_{K,\min}h_{K,\max}}\|\nabla p_h\|^2_{K_i^*}\\ &\le C h_P \sum_{i=1}^n h_{K_i^*,\min}\|\nabla p_h\|^2_{K_i^*}.\end{aligned}$$

In the last step, we have used that by definition $h_{K_i^*,\min} \le h_{K,\min}, h_{K_i^*,\min} \le h_{K_i^*,\max}$ and $h_{K,\max} \le h_P$. □

7.2 Continuous Interior Penalty stabilisation

The challenge for pressure stabilisation lies in the anisotropies that are present in the boundary region including abrupt changes of anisotropy between neighbouring cells. As the discretisation is based on a background patch mesh one could think of a stabilisation based on *local projections* (LPS) onto the patch grid (Becker & Braack[16]). However, there are patches that lie only partly in the fluid domain Ω_f, such that $V^0_{2h} \not\subset V^0_h$ and it is not clear how to control the pressure in these interface cells by means of *local projections*.

Therefore, we will use a variant of the *Continuous Interior Penalty* (CIP) stabilisation technique introduced by Burman & Hansbo for convection-diffusion-reaction problems[35]. Later on, it has been used for pressure stabilisation within the Stokes[36] and the Navier-Stokes equations[37]. To the best knowledge of the author, an a priori error estimate for this technique on anisotropic grids is not available in literature yet. The original CIP technique is based on penalising jumps of the gradient over element edges weighted by a factor of $\mathcal{O}(h^s)$ for $s = 2$ or $s = 3$. This is not applicable for the case of abrupt changes of anisotropy, however, as the cell size of the two neighbouring cells can be very different. Hence, in the interface cells, we use the mean value of the pressure gradient instead of the jump terms.

To define the stabilisation term, we split the domain Ω_h^f into two parts. By $\Omega_h^{f,0}$, we denote the set of all rectangular cells and $\Omega_h^{f,i}$ denotes the set of all triangles. This means that $\Omega_h^{f,i}$ contains the fluid part of all patches that are cut by the interface and $\Omega_h^{f,0}$ all interior patches not cut by the interface. Furthermore, we also split the set of edges into two parts: By $\mathcal{E}_h^{f,0}$, we denote all edges that lie between two quadrilateral cells $K_1, K_2 \in \Omega_h^{f,0}$. By $\mathcal{E}_h^{f,i}$ we denote the edges that are edges of at least one triangular element $K \in \Omega_h^{f,i}$.

We define the stabilisation term by

$$S(p_h,\psi_h) := \gamma h_P^2\left(\sum_{e\in\mathcal{E}_h^{f,i}}\int_e \{h_n\nabla p_h\cdot\nabla\psi_h\}_e\,do + \sum_{e\in\mathcal{E}_h^{f,0}}\int_e h_n[\nabla p_h]_e\cdot[\nabla\psi_h]_e\,do\right), \tag{7.9}$$

where $\gamma > 0$ is a constant, h_n is the cell size in the direction normal to e, $[\cdot]_e$ denotes the jump term across the edge e and

$$\{v_h\}_e := \frac{1}{2}\left(v_{h|K_1} + v_{h|K_2}\right)$$

is the mean value from the two cells K_1, K_2 sharing the edge e. In the case that one of the cells K_1, K_2 does not lie in Ω_h^f, we set the respective contribution to zero. We will denote the cellwise contribution of an element $K \in \Omega_h^f$ by

$$S_K(p_h, \psi_h) := \frac{\gamma h_P^2}{2}\left(\sum_{e\in\mathcal{E}_h^{f,i}, e\subset\overline{K}} \int_e h_n \nabla p_{h|K} \cdot \nabla \psi_{h|K}\, do + \sum_{e\in\mathcal{E}_h^{f,0}, e\subset\overline{K}} \int_e h_n [\nabla p_h]_e \cdot [\nabla \psi_h]_e\, do\right).$$

The discrete formulation for the Stokes problem reads:
Find $v_h \in \mathcal{V}_h := (V_h^0)^2, p_h \in \mathcal{L}_h := V_h$ *such that*

$$A(v_h, p_h)(\phi_h, \psi_h) + S(p_h, \psi_h) = (f, \phi_h)_{\Omega_f} \quad \forall \phi_h \in \mathcal{V}_h, \psi_h \in \mathcal{L}_h, \tag{7.10}$$

where

$$A(v_h, p_h)(\phi_h, \psi_h) := \nu(\nabla v_h, \nabla \phi_h)_{\Omega_f} - (p_h, \operatorname{div} \phi_h)_{\Omega_f} + (\operatorname{div} v_h, \psi_h)_{\Omega_f}.$$

We summarise the properties of the stabilisation term that we will need in the following.

Lemma 7.3. *Let* $\psi_h \in V_h$. *There exists a constant* $C > 0$ *independent of the interface position such that for the set of boundary cells* $\Omega_h^{f,i}$, *it holds that*

$$h_P^2 \sum_{K\in\Omega_h^{f,i}} \|\nabla \psi_h\|_K^2 \le C S(\psi_h, \psi_h). \tag{7.11}$$

Furthermore, the stabilisation term is bounded above by

$$S(\psi_h, \psi_h) \le C h_P^2 \|\nabla \psi_h\|_{\Omega_f}^2. \tag{7.12}$$

For a function $p_h \in V_h$ *and the projection* τ_h *defined in (7.6), it holds for every cell* $K \in \Omega_h^f$ *that*

$$\left\| h_{K,\min}^2 \nabla p_h - \tau_h\left(h_{K,\min}^2 \nabla p_h\right)\right\|_K^2 \le C h_{K,\min}^2 \sum_{L\in\mathcal{N}(K)} S_L(p_h, p_h), \tag{7.13}$$

where $\mathcal{N}(K)$ *denotes the set of neighbouring cells that share at least one common grid point with* K.

Proof. Let $K \in \Omega_h^{f,i}$. As $\nabla \psi_h$ is constant in K, the first estimate follows by a simple scaling argument

$$S_K(\psi_h, \psi_h) = \gamma h_P^2 \sum_{e\in\overline{K}} h_n \|\nabla \psi_h\|_e^2 = C\gamma h_P^2 \|\nabla \psi_h\|_K^2.$$

This also proofs (7.12) in the interface part $\Omega_h^{f,i}$. For a quadrilateral $K \in \Omega_h^{f,0}$, we estimate the jump terms very roughly by

$$S_K(\psi_h, \psi_h) \le \gamma h_P^3 \sum_{e \in \overline{K}} \int_e (\nabla \psi_h)^2 \, do.$$

After transformation to the reference element, it suffices to show that the functionals

$$s_1(\hat{\psi}_h) = \left(\sum_{\hat{e} \in \overline{\hat{K}}} \|\hat{\nabla} \hat{\psi}_h\|_{\hat{e}}^2 \right)^{1/2} \quad \text{and} \quad s_2(\hat{\psi}_h) = \|\hat{\nabla} \hat{\psi}_h\|_{\hat{K}}$$

define both norms on the quotient space Q_1/P_0. The positivity follows from the fact that $s_i(\hat{\psi}_h) = 0$ implies $\hat{\psi}_h$=const in both cases ($i = 1, 2$). With this, the statement (7.12) follows by using the equivalence of norms on finite dimensional spaces.

To show (7.13), we set $w_h = h_{\min}^2 \nabla p_h$ and estimate cellwise for $K \in \Omega_h^f$

$$\|w_h - \tau_h w_h\|_K^2 \le |K| \sum_{i=1}^n \left(w_{h|K}(x_i) - \tau_h w_h(x_i) \right)^2,$$

where $n = 3$ for a triangle K and $n = 4$ for a quadrilateral. If $x_i \in \partial \Omega_f$, we have

$$|K| \left(w_{h|K}(x_i) - \tau_h w_h(x_i) \right)^2 = |K| \left(w_{h|K}(x_i) \right)^2.$$

For a piecewise linear function $w_{h|K}$ on an edge $e \subset \overline{K}$, a simple calculation for the two Lagrangian basis functions ϕ_1, ϕ_2 corresponding to the end points x_1^e, x_2^e yields

$$\int_e w_{h|K}^2 do = \int_e \left(w_{h|K}(x_1^e) \phi_1 + w_{h|K}(x_2^e) \phi_2 \right)^2 do \ge \frac{|e|}{6} \left(w_{h|K}(x_1^e)^2 + w_{h|K}(x_2^e)^2 \right). \tag{7.14}$$

Using this, we obtain for an edge $e_i \in K$ with $x_i \in \overline{e}_i$

$$|K| \left(w_{h|K}(x_i) \right)^2 \le C \frac{|K|}{|e_i|} \int_{e_i} w_{h|K}^2 \, do = C \int_{e_i} h_n h_{K,\min}^4 (\nabla p_h)^2 \, do \le C h_{K,\min}^2 S_K(p_h, p_h).$$

For $x_i \in \Omega_f \setminus \partial \Omega_f$, let us first assume that K and K_i^* share a common edge e_i. As $w_{h|K} - w_{h|K_i^*}$ is linear on e_i, it holds with the argumentation used in (7.14) that

$$|K| \left(w_{h|K}(x_i) - w_{h|K_i^*}(x_i) \right)^2 \le C \frac{|K|}{|e_i|} \int_{e_i} [w_h]_{e_i}^2 \, do.$$

If both K and K_i^* are quadrilaterals, we have $h_{K,\min} \sim h_P$ and thus

$$|K| \left(w_{h|K}(x_i) - w_{h|K_i^*}(x_i) \right)^2 \le C \int_{e_i} h_n h_P^4 [\nabla p_h]^2 \, do \le C h_P^2 S_K(p_h, p_h).$$

If at least one of the cells is a triangle, we estimate

$$\begin{aligned} |K|\left(w_{h|K}(x_i)-w_{h|K_i^*}(x_i)\right)^2 &\le C\int_{e_i}\{h_n h_{\min}^4(\nabla p_h)^2\}_{e_i}\,do \\ &\le C h_{K,\min}^2\left(S_K(p_h,p_h)+S_{K_i^*}(p_h,p_h)\right) \end{aligned} \tag{7.15}$$

as by definition $h_{K_i^*,\min}\le h_{K,\min}$. Finally, we have to consider the case that K and K_i^* do not share a common edge, but only the common point x_i. If K is a triangle, than also K_i^* is a triangle (remember that $h_{K_i^*,\min}\le h_{K,\min}$) and we can directly use the argumentation (7.15). If K is a quadrilateral, we have $h_{K,\min}=h_P$. We split in the following way

$$\begin{aligned} &|K|\left(w_{h|K}(x_i)-w_{h|K_i^*}(x_i)\right)^2 \\ &\qquad\le C|K|\left(\left(w_{h|K}(x_i)-w_{h|K_1}(x_i)\right)^2+\ldots+\left(w_{h|K_n}(x_i)-w_{h|K_i^*}(x_i)\right)^2\right), \end{aligned}$$

such that in each of the summands the cells share a common edge. Now, we apply the argumentation from above to each of the summands. □

Remark 7.4. *(Relation to LPS stabilisations). The three inequalities (7.11), (7.12) and (7.13) are the properties of the stabilisation that we will need in the following. In the case that the patch mesh already resolves the boundary ($V_{2h}^0\subset V_h^0$), it is usually sufficient to define the stabilisation terms over interior patch edges only. One can then show that this CIP stabilisation technique is equivalent to a local projection stabilisation (LPS) method. Here, however, using interior patch edges is not sufficient. In the argumentation used above, the estimate (7.13) requires stabilisation terms over outer patch edges. An argumentation based on a modified inf-sup condition as typically used to show stability for an LPS-type stabilisation*[16] *is not possible here due to the patches that are only partially contained in Ω_f.*

7.3 Stability and a priori error analysis

Now, we are ready to prove a stability result. We introduce the norm

$$|||(v_h,p_h)|||:=\left(\nu\|\nabla v_h\|^2+\|p_h\|^2+h_P^2\|\nabla p_h\|^2\right)^{1/2}.$$

The argumentation used in the following proofs is similar to the one used by Burman & Hansbo[36]. Here we have to modify their arguments in some parts, however, to account for the anisotropy of the mesh Ω_h. The main tool we use is the projection operator τ_h introduced in Section 7.1.

Theorem 7.5. *Let $(v_h,p_h)\in(\mathcal{V}_h\times\mathcal{L}_h)$ and let Ω_f be a convex polygonal domain. Furthermore, let the regularity assumptions on the patch mesh Ω_{2h} made in Section 6.3 be fulfilled. Then, it holds with a constant C that is independent of the boundary position*

$$|||(v_h,p_h)|||\le C\sup_{(\phi_h,\psi_h)\in\mathcal{V}_h\times\mathcal{L}_h}\frac{A(v_h,p_h)(\phi_h,\psi_h)+S(p_h,\psi_h)}{|||(\phi_h,\psi_h)|||}.$$

Proof. At first, we notice that

$$A(v_h,p_h)(v_h,p_h)+S(p_h,p_h)=\nu\|\nabla v_h\|^2_{\Omega_f}+S(p_h,p_h). \tag{7.16}$$

Next, we show a bound for the L^2-norm of the pressure p_h. Therefore, we use the surjectivity of the divergence operator (see e.g. Temam[135]) to define a function $\tilde{v}\in H^1_0(\Omega_f)$ by

$$(\operatorname{div}\tilde{v},\phi)_{\Omega_f}=-(p_h,\phi)_{\Omega_f}\quad\forall\phi\in L^2(\Omega_f).$$

It holds that

$$\|\nabla\tilde{v}\|_{\Omega_f}\le C\|p_h\|_{\Omega_f}. \tag{7.17}$$

Using the test function $(\phi_h,\psi_h)=(\varepsilon_1 R_h\tilde{v},0)$, where R_h is the Ritz projection operator introduced in Section 7.1 and $\varepsilon_1>0$, we obtain

$$A(v_h,p_h)(\varepsilon_1 R_h\tilde{v},0)=\varepsilon_1\nu(\nabla v_h,\nabla R_h\tilde{v})_{\Omega_f}-\varepsilon_1(p_h,\operatorname{div}(R_h\tilde{v}))_{\Omega_f}. \tag{7.18}$$

For the first term, we use the H^1-stability of the Ritz projection (Lemma 7.1) and (7.17) to get

$$\varepsilon_1\nu(\nabla v_h,\nabla R_h\tilde{v})_{\Omega_f}\ge -C\varepsilon_1\nu\|\nabla v_h\|_{\Omega_f}\|p_h\|_{\Omega_f}\ge -\frac{\nu}{4}\|\nabla v_h\|^2_{\Omega_f}-C\varepsilon_1^2\|p_h\|^2_{\Omega_f}.$$

In the second term in (7.18), we introduce $\pm\tilde{v}$ and use (7.17), integration by parts, the error estimate for the Ritz projection (Lemma 7.1) and Young's inequality

$$\begin{aligned}
-\varepsilon_1(p_h,\operatorname{div}R_h\tilde{v})_{\Omega_f}&=\varepsilon_1(p_h,\operatorname{div}(\tilde{v}-R_h\tilde{v}))_{\Omega_f}-\varepsilon_1(p_h,\operatorname{div}\tilde{v})_{\Omega_f}\\
&=\varepsilon_1(\nabla p_h,\tilde{v}-R_h\tilde{v})_{\Omega_f}+\varepsilon_1\|p_h\|^2_{\Omega_f}\\
&\ge -C\varepsilon_1 h_P\|\nabla p_h\|_{\Omega_f}\|p_h\|_{\Omega_f}+\varepsilon_1\|p_h\|^2_{\Omega_f}\\
&\ge -C\varepsilon_1 h_P^2\|\nabla p_h\|^2_{\Omega_f}+\frac{\varepsilon_1}{2}\|p_h\|^2_{\Omega_f}.
\end{aligned}$$

By combining the estimates, we have

$$A(v_h,p_h)(\varepsilon_1 R_h\tilde{v},0)\ge -\frac{\nu}{4}\|\nabla v_h\|^2_{\Omega_f}-C\varepsilon_1 h_P^2\|\nabla p_h\|^2_{\Omega_f}+\frac{\varepsilon_1}{4}\|p_h\|^2_{\Omega_f}. \tag{7.19}$$

Next, we will show a bound for the derivatives of p_h. Therefore, we test with the projection τ_h of the discontinuous function $h^2_{\min}\nabla p_h$

$$\begin{aligned}
&A(v_h,p_h)\left(\varepsilon_2\tau_h\left(h^2_{\min}\nabla p_h\right),0\right)\\
&\qquad=\varepsilon_2\nu\left(\nabla v_h,\nabla\tau_h\left(h^2_{\min}\nabla p_h\right)\right)-\varepsilon_2\left(p_h,\operatorname{div}\left(\tau_h\left(h^2_{\min}\nabla p_h\right)\right)\right).
\end{aligned} \tag{7.20}$$

We use the Cauchy-Schwarz inequality, the stability result (7.7) for the projection τ_h and Young's inequality for the first part

$$\begin{aligned}
\varepsilon_2\nu\left(\nabla v_h,\nabla\tau_h\left(h^2_{\min}\nabla p_h\right)\right)&\ge -C\varepsilon_2 h_P\nu\|\nabla v_h\|_{\Omega_f}\|\nabla p_h\|_{\Omega_f}\\
&\ge -C\varepsilon_2\nu\|\nabla v_h\|^2-\frac{\varepsilon_2 h_P^2}{32}\|\nabla p_h\|^2_{\Omega_f}.
\end{aligned}$$

For the second part in (7.20), we apply integration by parts and insert $\pm h_{\min}^2 \nabla p_h$

$$-\varepsilon_2\Big(p_h, \operatorname{div}\left(\tau_h\left(h_{\min}^2\nabla p_h\right)\right)\Big) = \varepsilon_2\left(\nabla p_h, \tau_h\left(h_{\min}^2\nabla p_h\right)\right)$$
$$= \varepsilon_2\left(\nabla p_h, \tau_h\left(h_{\min}^2\nabla p_h\right) - h_{\min}^2\nabla p_h\right) + \varepsilon_2\|h_{\min}\nabla p_h\|^2.$$

For the first term, Lemma 7.3 guarantees that

$$\varepsilon_2\left(\nabla p_h, \tau_h\left(h_{\min}^2\nabla p_h\right) - h_{\min}^2\nabla p_h\right) \geq -C\varepsilon_2\left(\sum_{K\in\Omega_h^f}\|\nabla p_h\|_K h_{K,\min}\left(\sum_{L\in\mathcal{N}(K)} S_L(p_h,p_h)\right)^{1/2}\right)$$
$$\geq -\frac{\varepsilon_2}{2}\|h_{\min}\nabla p_h\|_{\Omega_f}^2 - C\varepsilon_2 S(p_h,p_h).$$

We have thus shown that

$$\begin{aligned}&A(v_h,p_h)\left(\varepsilon_2\tau_h\left(h_{\min}^2\nabla p_h\right),0\right)\\ &\quad\geq -C\varepsilon_2\nu\|\nabla v_h\|^2 + \frac{\varepsilon_2}{2}\|h_{\min}\nabla p_h\|^2 - C\varepsilon_2 S(p_h,p_h) - \frac{\varepsilon_2 h_P^2}{32}\|\nabla p_h\|_{\Omega_f}^2.\end{aligned} \tag{7.21}$$

Finally, we combine (7.16), (7.19) and (7.21) and choose $\varepsilon_1 \ll \varepsilon_2 \ll 1$

$$\begin{aligned}&A(v_h,p_h)\left(v_h+\varepsilon_1 R_h\tilde{v}+\varepsilon_2\tau_h\left(h_{\min}^2\nabla p_h\right),p_h\right)+S(p_h,p_h)\\ &\quad\geq \frac{\nu}{2}\|\nabla v_h\|_{\Omega_f}^2 + \frac{1}{2}S(p_h,p_h) + \frac{\varepsilon_1}{4}\|p_h\|_{\Omega_f}^2 + \frac{\varepsilon_2}{2}\|h_{\min}\nabla p_h\|^2 - \frac{\varepsilon_2}{16}h_P^2\|\nabla p_h\|_{\Omega_f}^2.\end{aligned}$$

For the last term, we note that $h_{K,\min} \approx h_P/2$ in all cells $K \in \Omega_h^{f,0}$. The contributions in the interface elements can be estimated by the stability term (see Lemma 7.3). Thus, we have

$$h_P^2\|\nabla p_h\|_{\Omega_f}^2 \leq \|h_{\min}\nabla p_h\|^2 + CS(p_h,p_h).$$

Altogether we have shown that

$$|||(v_h,p_h)|||^2 \leq C\left(A(v_h,p_h)(\phi_h,p_h) + S(p_h,p_h)\right)$$

for

$$\phi_h = v_h + \varepsilon_1 R_h\tilde{v} + \varepsilon_2\tau_h\left(h_{\min}^2\nabla p_h\right).$$

Due to the stability results for the projection operators τ_h and R_h, we have $|||\phi_h,p_h)||| \leq C|||(v_h,p_h)|||$ and thus, the statement of the theorem is proven. □

Finally, we prove a priori error estimates for the discrete solutions of the stabilised Stokes problem.

Theorem 7.6. *Let (v,p) be the solution of (7.1) and (v_h,p_h) the solution of the stabilised discrete system (7.10). For $v \in H^2(\Omega_f) \cap H_0^1(\Omega_f)$ and $p \in H^1(\Omega) \cap L_0^2(\Omega_f)$, it holds under the conditions of Theorem 7.5 that*

$$|||(v - v_h, p - p_h)||| \leq C h_P \left(||\nabla^2 v||_{\Omega_f} + ||\nabla p||_{\Omega_f} \right). \tag{7.22}$$

Furthermore, for the L^2-norm error of the velocity, we have that

$$||v - v_h||_{\Omega_f} \leq C h_P^2 \left(||\nabla^2 v||_{\Omega_f} + ||\nabla p||_{\Omega_f} \right).$$

Proof. We first prove the energy norm estimate. Therefore, we split the error into an interpolation and a discrete part

$$|||(v - v_h),(p - p_h)||| \leq |||(v - R_h v),(p - R_h p)||| + |||(R_h v - v_h),(R_h p - p_h)|||.$$

By Lemma 7.1, we get the following bounds for the interpolation part

$$|||(v - R_h v),(p - R_h p)||| \leq C h_P \left(||\nabla p|| + ||\nabla^2 v|| \right).$$

For the discrete part, we apply Theorem 7.5 to get

$$\begin{aligned} &|||(R_h v - v_h, R_h p - p_h)||| \\ &\qquad \leq C \sup_{(\phi_h,\psi_h) \in \mathscr{V}_h \times \mathscr{L}_h} \frac{A(R_h v - v_h, R_h p - p_h)(\phi_h,\psi_h) + S(R_h p - p_h, \psi_h)}{|||(\phi_h,\psi_h)|||}. \end{aligned}$$

We use Galerkin orthogonality

$$\begin{aligned} A(R_h v - v_h,& R_h p - p_h)(\phi_h,\psi_h) + S(R_h p - p_h,\psi_h) \\ &= A(R_h v - v, R_h p - p)(\phi_h,\psi_h) + S(R_h p,\psi_h) \end{aligned}$$

and by means of the the Cauchy-Schwarz inequality, it follows that

$$\begin{aligned} A(R_h v - v,& R_h p - p)(\phi_h,\psi_h) + S(R_h p,\psi_h) \\ &\leq C \left(||\nabla(R_h v - v)||_{\Omega_f} + ||R_h p - p||_{\Omega_f} + S^{1/2}(R_h p, R_h p) \right) |||(\phi_h,\psi_h)|||. \end{aligned}$$

With the help of Lemma 7.3 and the stability of the interpolation operators, we obtain

$$|||(R_h v - v_h, R_h p - p_h)||| \leq C h_P \left(||\nabla p||_{\Omega_f} + ||\nabla^2 v||_{\Omega_f} \right).$$

To show the L^2-norm estimate, we make use of a dual problem. Let $(v^*,p^*) \in (H_0^1(\Omega_f;\Gamma_f^d) \times L^2(\Omega_f))$ the solution of

$$A(\phi,\psi)(v^*,p^*) = (v - v_h,\phi). \tag{7.23}$$

For a convex polygonal domain Ω_f, we have

$$||\nabla^2 v^*||_{\Omega_f} + ||\nabla p^*||_{\Omega_f} \leq C ||v - v_h||_{\Omega_f}.$$

Setting $\phi = v - v_h, \psi = p - p_h$ in (7.23) and making use of the Galerkin orthogonality gives

$$\begin{aligned}\|v - v_h\|_{\Omega_f}^2 &= \nu(\nabla(v - v_h), \nabla v^*) + (\operatorname{div}(v - v_h), p^*) + (p - p_h, \operatorname{div} v^*)\\ &= \nu(\nabla(v - v_h), \nabla(v^* - R_h v^*)) + (p - p_h, \operatorname{div}(v^* - R_h v^*))\\ &\quad + (\operatorname{div}(v - v_h), p^* - R_h p^*) + S(p_h, R_h p^*).\end{aligned}$$

For the last term, we have with Lemma 7.3

$$S(p_h, R_h p^*) \le S(p_h, p_h)^{1/2} S(R_h p^*, R_h p^*)^{1/2} \le C h_P^2 \|\nabla p_h\|_{\Omega_f} \|\nabla p^*\|_{\Omega_f}.$$

For the discrete pressure, we conclude from the energy norm estimate (7.22) that

$$\|\nabla p_h\|_{\Omega_f} \le \|\nabla p\|_{\Omega_f} + \|\nabla(p - p_h)\|_{\Omega_f} \le C\|\nabla p\|_{\Omega_f}.$$

Now the assertion follows by using the estimate for the Ritz projection (Lemma 7.1) and the energy norm estimate. □

Remark 7.7. *(Other possible choices for stabilisation) The proven convergence orders are optimal for the used combination of linear and bilinear finite elements. We note that the approximation orders could have been shown with the bigger stability term*

$$S(p_h, \psi_h) := \gamma h_P^2 \sum_{e \in \mathcal{E}_h} \int_e \{h_n \nabla p_h \cdot \nabla \psi_h\}_e \, do$$

as well. This stabilisation term has the advantage that in contrast to (7.9) no further couplings in the system matrix are introduced. We expect, however, that in the interior patches the stabilisation term (7.9) results in a better approximation, especially on coarser grids, by means of a much smaller constant.

Instead of the mean values over edges, we could also choose the simple stabilisation term

$$S_K(p_h, \psi_h) = \alpha h_P^2 (\nabla p_h, \nabla \psi_h)_K$$

in the triangular cells. It is well-known, however, that this artificial diffusion term may lead to bad approximations, especially when resolving boundary layers, as it tends to smoothen too much.

7.4 Numerical example

Finally, we present a numerical example with analytical solution to confirm the theoretical findings. We consider the Stokes equations given in (7.1) with viscosity $\nu = 1$. As geometry, we use the unit square and extract an inner circle of radius $r = 0.4$

$$\Omega = (-1,1)^2 \setminus B_{0.4}(x_0, y_0).$$

We discretise the unit square with a patch mesh and resolve the boundary of the circle with the *locally modified finite element* method. A sketch of a coarse mesh is given in Figure 7.2.

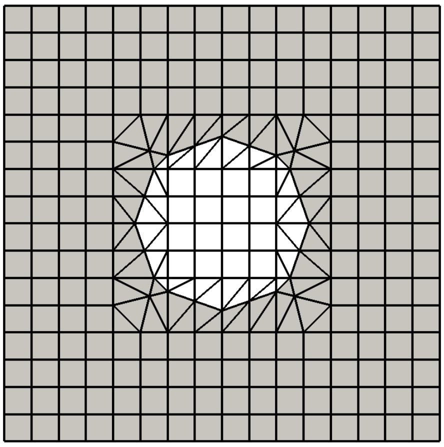

Figure 7.2. Illustration of the coarsest mesh used for the numerical example. The domain $\Omega_{h,f}$ is visualised in grey.

We impose a *do-nothing* boundary condition on the right boundary of the square

$$\partial_n v - pn = \begin{pmatrix} \partial_x v_1 \\ \partial_x v_2 \end{pmatrix} - \begin{pmatrix} p \\ 0 \end{pmatrix} = 0$$

and a homogeneous Dirichlet condition on the boundary of the circle. Furthermore, we use non-homogeneous Dirichlet data on the left, upper and lower boundaries as well as a volume force f that are calculated in such a way that a prescribed analytical solution solves the system.

To construct the analytical solution, we define the velocity field v as curl of a scalar function ψ (as $\operatorname{div}(\operatorname{curl}\psi) = 0$) and the pressure in such a way that the *do-nothing condition* holds:

$$\begin{aligned} v_1 &= \partial_y \psi = 4k(x,y)(x-1)^3(y-y_0) \\ v_2 &= -\partial_x \psi = -4k(x,y)(x-1)^3(x-x_0) - 3k(x,y)^2(x-1)^2 \\ p = \partial_x v_1 &= \partial_{xy}\psi = 8(x-x_0)(x-1)^3(y-y_0) + 12k(x,y)(x-1)^2(y-y_0). \end{aligned}$$

where $k(x,y) = (x-x_0)^2 + (y-y_0)^2 - r^2$. The corresponding function ψ is

$$\psi(x,y) = k(x,y)^2(x-1)^3.$$

First, we consider the case that the midpoint of the circle coincides with the origin $x_0 = y_0 = 0$. For ease of implementation, we extend v by zero in the inner circle and use a harmonic extension of the pressure there.

We use the following stabilisation terms that have been analysed in Theorem 7.5 and Theorem 7.6 and in Remark 7.7, respectively

$$\begin{aligned} S_1(p_h,\psi_h) &:= \gamma h_P^2 \left(\sum_{e\in\mathcal{E}_h^{f,i}} \int_e \{h_n \nabla p_h \cdot \nabla \psi_h\}_e \, do + \sum_{e\in\mathcal{E}_h^{f,0}} \int_e h_n [\nabla p_h]_e \cdot [\nabla \psi_h]_e \, do \right), \\ S_2(p_h,\psi_h) &:= \gamma h_P^2 \sum_{e\in\mathcal{E}_h} \int_e \{h_n \nabla p_h \cdot \nabla \psi_h\}_e \, do. \end{aligned}$$

h_P	$\|\|\nabla v - v_h\|\|_{L^2}$ S_1	S_2	S_3	S_4	$\|\|v - v_h\|\|_{L^2}$ S_1	S_2	S_3	S_4
0.25	18.05	18.03	18.04	18.13	$7.47 \cdot 10^{-1}$	$7.23 \cdot 10^{-1}$	$7.45 \cdot 10^{-1}$	$7.28 \cdot 10^{-1}$
0.125	9.06	9.05	9.06	9.09	$1.87 \cdot 10^{-1}$	$1.80 \cdot 10^{-1}$	$1.86 \cdot 10^{-1}$	$1.81 \cdot 10^{-1}$
0.0625	4.52	4.52	4.52	4.53	$4.67 \cdot 10^{-2}$	$4.48 \cdot 10^{-2}$	$4.67 \cdot 10^{-2}$	$4.51 \cdot 10^{-2}$
0.03125	2.26	2.26	2.26	2.26	$1.17 \cdot 10^{-2}$	$1.12 \cdot 10^{-2}$	$1.17 \cdot 10^{-2}$	$1.13 \cdot 10^{-2}$
Conv.	0.99	0.99	0.99	0.99	1.99	2.00	1.99	2.00
Expect.	1.00				2.00			

h_P	$\|\|p - p_h\|\|_{L^2}$ S_1	S_2	S_3	S_4
0.25	3.33	3.55	2.82	5.69
0.125	1.09	1.23	$9.09 \cdot 10^{-1}$	1.99
0.0625	$3.64 \cdot 10^{-1}$	$4.16 \cdot 10^{-1}$	$2.92 \cdot 10^{-1}$	$6.28 \cdot 10^{-1}$
0.03125	$1.23 \cdot 10^{-1}$	$1.43 \cdot 10^{-1}$	$9.72 \cdot 10^{-2}$	$1.98 \cdot 10^{-1}$
Conv.	1.60	1.53	1.63	1.54
Expect.	1.00			

Table 7.1. L^2- and H^1-norm of the velocity and L^2-norm error of the pressure for four different stabilisation variants. We estimated the convergence order by a least squares fit of the function $e(h) = ch^\alpha$ and show the expected convergence rates from Theorem 7.6.

Furthermore, we investigate modifications of the stabilisation terms for which we were not able to show stability estimates with the techniques used above. Here, we split the gradient in the stabilisation term into a normal part ∂_n and a tangential part ∂_τ. Instead of using the patch size h_P in the weight, we use the local element sizes h_τ and h_n. This is the usual weighting for stabilisation on anisotropic elements (see e.g. the anisotropic LPS method, Braack & Richter[24]).

$$
\begin{aligned}
S_3(p_h, \psi_h) &:= \gamma\Big(\sum_{e \in \mathcal{E}_h^{f,i}} \int_e \{h_n(h_n^2 \partial_n p_h \partial_n \psi_h + h_\tau^2 \partial_\tau p_h \cdot \partial_\tau \psi_h)\}_e \, do \\
&\qquad + \sum_{e \in \mathcal{E}_h^{f,0}} \int_e h_n^3 [\nabla p_h]_e \cdot [\nabla \psi_h]_e \, do \Big), \qquad (7.24) \\
S_4(p_h, \psi_h) &:= \gamma \sum_{e \in \mathcal{E}_h} \int_e \{h_n(h_n^2 \partial_n p_h \partial_n \psi_h + h_\tau^2 \partial_\tau p_h \cdot \partial_\tau \psi_h)\}_e \, do.
\end{aligned}
$$

Note that for the regular edges in $\mathcal{E}_h^{f,0}$ in S_3 the weight h_n equals h_P and furthermore, the jump of the tangential derivatives vanish.

In Table 7.1, we show the L^2- and the H^1-norm error of the velocity as well as the L^2-norm error of the pressure for the four stabilisations on four different meshes. Furthermore, we show an estimated convergence order based on the calculations. The stabilisation parameter is chosen $\gamma = 2.5 \cdot 10^{-3}$ for S_1 and S_2 and $\gamma = 10^{-2}$ for S_3 and S_4. We choose the latter by a factor of 4 larger, as on regular cells we have $h_n \approx h_\tau \approx h_P/2$.

The velocity errors are almost identical for all four stabilisation terms. The convergence

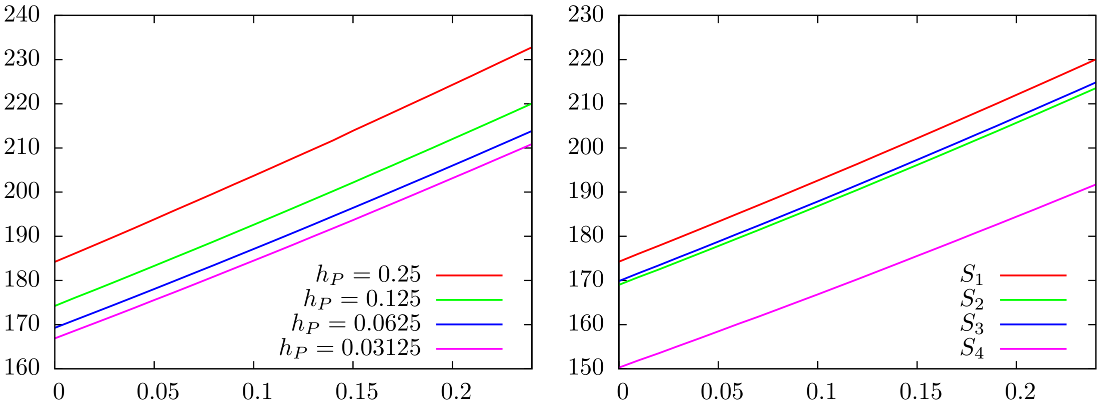

Figure 7.3. H^1-norm of the discrete pressure for different positions $(x_0,0)$ of the midpoint of the circle. *Left:* Stabilisation S_1 on different mesh levels, *right:* All four stabilisations for the mesh with patch size $h_P = 0.125$.

behaviour coincides almost perfectly with the theoretical analysis for S_1 and S_2 given above. The L^2-norm of the pressure converges with a higher order $\alpha \geq 1.5$ for all four stabilisations, while we had only shown first order convergence in Theorem 7.6.

This convergence order is expected for the stabilisation S_1. Due to the regularity of the solution, the jump of the pressure over edges vanishes and we can use

$$S_K(R_h p, R_h p) = S_K(R_h p - p, R_h p - p)$$

in cells K away from the interface region in the proof of Theorem 7.6. This can be used to get second order convergence in these parts of the domain. As the remaining cells span a domain of size $\mathcal{O}(h_P)$, we can show the convergence order $\mathcal{O}(h_P^{3/2})$.

Next, in order to study the effect of different anisotropies, we move the midpoint of the circle in intervals of 10^{-2} up to $x_0 = 0.24$ to the right. For $x = 0.25$ the midpoint would have moved by exactly one patch on the coarsest grid.

In Figure 7.3 (left sketch), we plot the H^1-norm of the pressure over the horizontal position of the midpoint for the stabilisation term S_1 and for the four different meshes. The norm increases uniformly when the circle moves to the right as the analytical solution p increases. We do not observe any instabilities on any of the four grids. Furthermore, we observe convergence for $h_P \to 0$ for every x_0 independent of the interface position.

In the right sketch, we compare the four different stabilisations on the second-coarsest mesh with $h_P = 0.125$. Again, we do not observe any oscillations but a uniform increase of the values for all stabilisations. The values for S_4 are smaller than for the other stabilisations. However, these deviations get smaller on finer grids and for all stabilisation techniques, the H^1-norm converges to approximately the same value.

We conclude that in this numerical example, the stabilisation terms S_3 and S_4 stabilise as well as S_1 and S_2. These results coincide with our findings in the context of fluid-structure interaction problems. In the applications in Chapter III, we will therefore use these stabilisation terms instead of S_1 and S_2. The theoretical analysis of their stability, however, remains open.

8 Discretisation of parabolic interface problems

In this section, we study parabolic interface problems and derive a second-order time-stepping scheme of Crank-Nicolson type. This time discretisation is not restricted to parabolic interface problems but can be applied to more complex interface problems as arising e.g. in fluid-structure interactions or multiphase flow problems. These problems have in common that an interface between two or more subdomains evolves in time. The solution is continuous across the interface, it is, however, not differentiable across it, neither in space nor in time. This is typically the case for the velocity in both fluid-structure interactions and multiphase problems.

8.1 A parabolic model problem

Here, we study the following parabolic interface problem. Let

$$Q := \{(t,\Omega(t)),\ t \in I := [0,T]\} \subset \mathbb{R}^{d+1}$$

be a space-time domain, that is split into two subdomains $Q = Q_1 \cup G \cup Q_2$ by an interface $G \subset \mathbb{R}^d$:

$$Q_i := \{(t,\Omega_i(t)),\ t \in I := [0,T]\} \subset \mathbb{R}^{d+1}, \quad G := \{(t,\Gamma(t)),\ t \in I := [0,T]\},$$

and, for every time t: $\Omega(t) = \Omega_1(t) \cup \Gamma(t) \cup \Omega_2(t)$ (see Figure 8.1). Given $u^0 \in L^2(\Omega(0))$, we define the model problem by

$$\begin{aligned} \partial_t u_i - \operatorname{div}\left(\kappa_i \nabla u_i\right) &= f_i && \text{in } Q_i,\ i = 1,2, \\ u_1 = u_2, \quad \boldsymbol{n}\cdot\kappa_1\nabla u_1 &= \boldsymbol{n}\cdot\kappa_2\nabla u_2 && \text{on } \Gamma(t), \\ u(\cdot,0) &= u^0 && \text{on } \Omega(0), \\ u(\cdot,t) &= 0 && \text{on } \partial\Omega(t), \end{aligned} \tag{8.1}$$

where the diffusion coefficient $\kappa : Q \to \mathbb{R}$ takes two values $\kappa_1,\kappa_2 \in \mathbb{R}$ in the sub-domains Q_1, Q_2.

We define the Bochner spaces

$$\begin{aligned} H^k(I,H^l(\Omega(t))) &:= \left\{ u : Q \to \mathbb{R} \,\middle|\, \|u\|_{H^k(I,H^l(\Omega(t)))} < \infty \right\}, \\ \|u\|_{H^k(I,H^l(\Omega(t)))} &:= \left(\int_I \|\partial_t^k u\|^2_{H^l(\Omega(t))}\,\mathrm{d}t \right)^{1/2}, \end{aligned}$$

and denote the space of functions that lie in these spaces on each of the subdomains by

$$\mathcal{H}^{k,l} := H^k\left(I,H^l(\Omega_1(t))\right) \cap H^k\left(I,H^l(\Omega_2(t))\right).$$

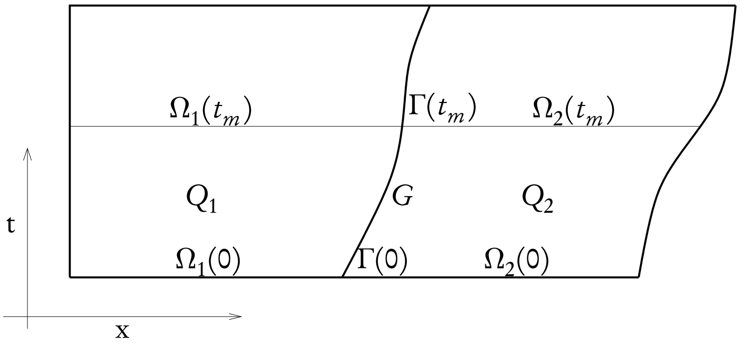

Figure 8.1. Space-time domain. Both the interface $\Gamma(t)$ and the outer boundary $\partial\Omega(t)$ might move in time.

By $H^0(\Omega)$ we denote the Lebesgue space $L^2(\Omega)$. On these spaces, we define the norms

$$||u||_{k,l} := \left(||u||^2_{H^k(I,H^l(\Omega_1(t)))} + ||u||^2_{H^k(I,H^l(\Omega_2(t)))}\right)^{1/2}.$$

With this notation, given smooth domains $Q = Q_1 \cup G \cup Q_2$, sufficient regularity of the right-hand side f, an regular initial u^0 that satisfies the compatibility conditions $-\kappa_i \Delta u^0 = f$ and $\kappa_1 \boldsymbol{n} \cdot \nabla u_1^0 = \kappa_2 \boldsymbol{n} \cdot \nabla u_2^0$ and positive diffusion coefficients $\kappa_1, \kappa_2 > 0$, Problem (8.1) has a solution $u = \{u_1, u_2\}$ that satisfies (Dziri & Zolésio[58])

$$||u||_{0,4} + ||u||_{1,2} + ||u||_{2,0} \leq c\left(||f||_{0,2} + ||f||_{1,0} + ||u^0||_{H^4(\Omega_1(0)\cup\Omega_2(0))}\right). \tag{8.2}$$

The solution u has no higher global spatial or temporal regularity across the interface $G := \{(t, \Gamma(t)),\ t \in I\}$, instead it carries a *weak discontinuity* in space and time.

8.2 Motivation

For spatial discretisation, we will use the *locally modified finite element method* introduced in Section 6. For time discretisation, we cannot use the method of lines, if the domain $\Omega(t) \subset \mathbb{R}^d$ is changing in time. Rothe's method relies on time-stepping $t_{m-1} \to t_m$. In the usual finite element setting, applying a simple one-step method like the backward Euler scheme, Rothe's method for the parabolic model problem reads

$$\frac{1}{t_m - t_{m-1}}(u^m - u^{m-1}, \phi) + (\kappa \nabla u^m, \nabla \phi) = (f(t_m), \phi) \quad \forall \phi \in V(t_m), \tag{8.3}$$

where $u^{m-1} \in V(t_{m-1})$ is the solution at time t_{m-1} and $u_m \in V(t_m)$ is the sought solution at time t_m. But again, in the case of moving domains, it holds $\Omega(t_{m-1}) \neq \Omega(t_m)$ and therefore $V(t_{m-1}) \neq V(t_m)$. The problem comes to the fore, if one considers the role of the scalar product $(u^m - u^{m-1}, \phi) = \int_\Omega (u^m - u^{m-1})\phi \,\mathrm{d}x$. Whether we choose $\Omega(t_{m-1})$ or $\Omega(t_m)$ as domain for integration, the integral is not defined for one of the solutions u^m or u^{m-1}.

Next, let us consider interface problems on a fixed domain $Q := I \times \Omega$ where only the interior interface moves, but where the outer boundary is fixed. Here, the problem looks less severe. Equation (8.3) is well defined. However, consider a point $x \in \Omega$ with $x \in \Omega_1(t_{m-1})$ and $x \in \Omega_2(t_m)$ close to the interface. Then, by $(u^m(x) - u^{m-1}(x))/(t_m - t_{m-1})$, no approximation to the time-derivative u' is given as u is not differentiable across the interface.

Related approaches

In the context of the *extended finite element method* (XFEM), recent advances have been made in literature for this problem. Fries and Zilian[70] presented a time-stepping scheme based on the backward Euler method and a number of numerical tests that indicate first-order convergence order. A complete error analysis for this problem has been presented by Zunino[156]. For a corresponding Crank-Nicolson-like approach, Fries and Zilian found a reduced convergence order of 1.5. To the best of our knowledge, there is, however, no rigorous convergence analysis available yet. A second-order scheme based on a space-time dG(1) approach has been presented by Lehrenfeld and Reusken[103] including error analysis in space and time. Their approach can not be generalised to a continuous Galerkin scheme, however, as the spatial number of unknowns varies from time step to time step in their scheme.

Another approach to construct accurate time-stepping schemes is to apply a transformation to a fixed reference domain $\hat{Q} := I \times \{\hat{\Omega}_1 \cup \hat{\Gamma} \cup \hat{\Omega}_2\}$. Let $\hat{T} : \hat{Q} \to Q$ be such a mapping. If $\hat{T}$ is a C^2-diffeomorphism, Problem (8.1) is equivalent to

$$\det(\hat{\nabla}\hat{T})\left(\partial_t \hat{u} - \partial_t \hat{T} \cdot \nabla \hat{u}\right) - \widehat{\operatorname{div}}\left(\det(\hat{\nabla}\hat{T})\hat{\kappa}\hat{\nabla}\hat{T}^{-1}\hat{\nabla}\hat{u}\hat{\nabla}\hat{T}^{-T}\right) = \det(\hat{\nabla}\hat{T})\hat{f} \text{ in } \hat{Q}. \tag{8.4}$$

This is the ALE-transform of the parabolic model problem (see e.g. Bänsch & Weller[12] or Section 3.2.2). Here, the domain $\hat{\Omega}$ allows a fixed partitioning $\hat{\Omega} = \hat{\Omega}_1 \cup \hat{\Gamma} \cup \hat{\Omega}_2$ that does not change in time. Standard spatial and temporal discretisation is possible. As discussed in Section 3.2.2, the ALE approach works only, if a mapping $\hat{T} : \hat{Q} \to Q$ with sufficient regularity can be constructed. For the case of large deformations Codina and co-workers proposed an alternative called *Fixed-mesh ALE method*[42]. In the Fixed-mesh ALE method, a moving mesh (ALE) technique is applied in each time interval, but the solution is projected back to an original fixed mesh afterwards. In this way, the requirement of global regularity of an ALE map is reduced to local regularity within each time interval. As the relative movement of boundaries and interfaces with respect to the previous time step is typically rather small, the method is able to deal with large movements.

Modified continuous Galerkin scheme

Here, we start from an Eulerian point of view and design a space-time Galerkin method on the space-time slots $Q^m = \{(t, \Omega(t)),\ t \in [t_{m-1}, t_m]\}$. In literature, this approach is known as the *continuous Galerkin (cG) method*, (see e.g. Aziz & Monk[4], Eriksson et al.[60]), and a Galerkin scheme of Crank-Nicolson type is found by using continuous and piecewise linear trial functions combined with discontinuous piecewise constant test functions. However, on space-time elements close to the (moving) interface or (moving) outer boundaries, we choose trial-functions, that are aligned to the element's faces: the solution is not linear in direction of time t, but linear in directions that stay within each subdomain or follow the interface line, see Figure 8.3 below.

It will turn out that the resulting time-stepping scheme can be seen as a variant of the Fixed-mesh ALE method in combination with a residual-based projection scheme. Similar schemes can be found as well within the frame of the *Universal Mesh method* by Gawlik & Lew[72].

The novelties of this section from an algorithmic point of view are the application of a Galerkin time discretisation within this framework and the usage of a particular projection. This enables us to derive a priori error estimates of optimal (second) order. To the knowledge of the authors no convergence results are available within the Fixed-mesh ALE framework yet in literature. Our proof of convergence follows the work of Meidner and Vexler[110]. There, duality-based techniques are applied to a Galerkin formulation of the Crank-Nicolson scheme on a fixed domain without interfaces.

The remainder of this section is as follows: Section 8.3 details the space-time Galerkin approach and derives a corresponding time-stepping method. In Section 8.4.1, we state the main result, an a priori estimate for the temporal discretisation error and give an outline of the proof which depends on several auxiliary results that will be proven in Section 8.4.2. In Section 8.5, we give some details on our practical implementation, with focus on numerical integration. Then, in Section 8.6, we will substantiate these results by numerical test cases.

8.3 Temporal discretisation

A variational formulation of (8.1) is given by: Find $u \in X$ such that

$$\begin{aligned} B(u,\phi) &= (f,\phi)_Q + (u^0,\phi(0))_{\Omega(0)} \quad \forall \phi \in X, \\ B(u,\phi) &:= (\partial_t u,\phi)_Q + (\kappa\nabla u,\nabla\phi)_Q + (u(0),\phi(0))_{\Omega(0)}, \end{aligned} \tag{8.5}$$

where $(f,g)_Q := \int_0^T (f(t),g(t))_{\Omega(t)}\,\mathrm{d}t$ and

$$X := W(0,T) = \left\{ v : Q \to \mathbb{R} \;\middle|\; v \in L^2(I,H_0^1(\Omega(t))),\ \partial_t v \in L^2(I,H^{-1}(\Omega(t))) \right\}.$$

Due to the continuous embedding $W(0,T) \subset C(I,L^2(\Omega(t)))$, point values $u(t_i)$ in time are well-defined and hence the initial condition can be included into the variational formulation as in (8.5). The well-posedness of this variational problem for moving outer boundaries has been studied by Dziri & Zolésio[58].

In order to derive a time-stepping scheme, we split the time interval into discrete subintervals

$$I = \{0\} \cup I_1 \cup I_2 \cup \ldots \cup I_M, \quad I_j = (t_{j-1},t_j].$$

For $j = 1,\ldots,M$, we denote the resulting space-time slabs by $Q^j := \{(x,t) \mid t \in I_j,\ x \in \Omega(t)\}$ and the space-time slabs corresponding to the subdomains by $Q_i^j := \{(x,t) \mid t \in I_j, x \in \Omega_i(t)\}$, $(i = 1,2)$. Let us first assume that the outer boundary $\partial\Omega(t)$ is fixed such that $\Omega(t) = \Omega$ for all times t. Then, similar to (8.3), we can write down a simple time-stepping scheme of Crank-Nicolson type

$$\begin{aligned} \frac{1}{k}(u^m - u^{m-1},\phi)_\Omega + \frac{1}{2}(\kappa(t_m)\nabla u^m,\nabla\phi)_\Omega + \frac{1}{2}(\kappa(t_{m-1})\nabla u^{m-1},\nabla\phi)_\Omega \\ = \frac{1}{2}(f(t_m),\phi)_\Omega + \frac{1}{2}(f(t_{m-1}),\phi)_\Omega \quad \forall \phi \in H_0^1(\Omega). \end{aligned} \tag{8.6}$$

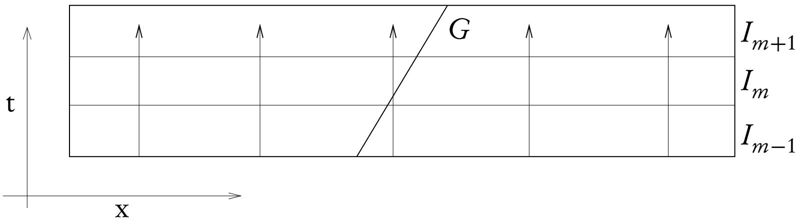

Figure 8.2. Space-time domain for a fixed outer domain $\Omega(t)=\Omega$. Functions $v_k\in\tilde{X}_k^0,\tilde{X}_k^1$ are polynomial on vertical lines (e.g. the indicated arrows).

Remember that in the case of a moving outer boundary, it is not straight-forward to write down a corresponding formulation, as u^m and u^{m-1} are defined on different domains $\Omega(t_m)$ and $\Omega(t_{m-1})$. It is well known that the Crank-Nicolson scheme (8.6) is equivalent to a space-time variational formulation with the following Galerkin ansatz and trial spaces

$$\begin{aligned} u_k\in\tilde{X}_k^1&=\left\{v\in C(\bar{I},H_0^1(\Omega))\,\middle|\, v_{|I_m}\in P_1(I_m,H_0^1(\Omega)), v(0)\in H_0^1(\Omega)\right\}\\ \phi_k\in\tilde{X}_k^0&=\left\{v\in L^2(I,H_0^1(\Omega))\,\middle|\, v_{|I_m}\in P_0(I_m,H_0^1(\Omega)), v(0)\in H_0^1(\Omega)\right\}. \end{aligned}\tag{8.7}$$

If the coefficient κ was continuous across the interface (in our case $\kappa_1=\kappa_2$), second-order convergence estimates for the discretisation error would be straight-forward. This is not the case for a discontinuous coefficient, however, as the scheme does not account for the (moving) discontinuity of κ, f and ∇u at the space-time interface G. Instead the functions $u_k\in\tilde{X}_k^1$ are polynomial on lines ζ that cross the interface (e.g. the arrow crossing the interface in Figure 8.2), which means $u_k\in C^\infty(\zeta)$. As for the spatial discretisation, it follows that, in general, there is no second-order in time interpolant within the space $\tilde{X}_k^1$ and we can only expect a reduced order of convergence.

To derive a second-order scheme (that will also be usable for moving outer boundaries), we introduce a modified continuous Galerkin ansatz in time. Therefore, we define a Galerkin space of functions that are polynomial on trajectories that stay within the subdomains and are aligned to the space-time boundary and the interface in their vicinity. The construction of a second-order interpolant in time will be straight-forward within this space. For deriving error estimates, it would be most convenient to introduce smooth global trajectories in the whole time-interval I. In practice, however, it might be a challenging task to define sufficiently smooth trajectories (consider for example large movements of the interface). Furthermore, the interface movement often depends on the solution itself and is therefore only known from time step to time step. Therefore, we define the trajectories piecewise in each time interval I_m (see Figure 8.2).

Specifically, we define the following (semi-discrete) test and trial spaces:

$$\begin{aligned} u_k\in X_k^1&=\left\{v\in C(\bar{I},H_0^1(\Omega))\,\middle|\,(v\circ T_m)|_{I_m}\in P_1(I_m,H_0^1(\Omega)),\ v(0)\in H_0^1(\Omega)\right\}\\ \phi_k\in X_k^0&=\left\{v\in L^2(I,H_0^1(\Omega))\,\middle|\,(v\circ T_m)|_{I_m}\in P_0(I_m,H_0^1(\Omega)),\ v(0)\in H_0^1(\Omega)\right\}. \end{aligned}\tag{8.8}$$

By T_m we denote an arbitrary transformation from a reference domain $\hat{\Omega}^m$ to the space-time domain Q^m that maps $\hat{\Gamma}^m$ to $\Gamma(t)$, $\hat{\Omega}_1^m$ onto $\Omega_1(t)$ and $\hat{\Omega}_2^m$ onto $\Omega_2(t)$. In this work, we

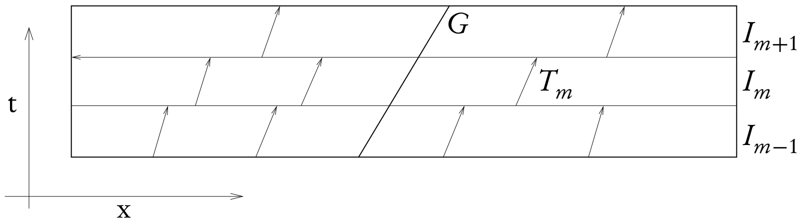

Figure 8.3. Illustration of the modified Galerkin ansatz spaces X_k^0, X_k^1. The functions $v_k \in X_k^0, X_k^1$ are polynomial on trajectories that stay within each subdomain Q_i, $i = 1,2$.

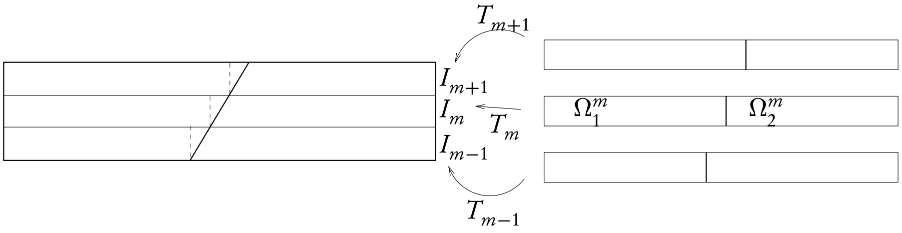

Figure 8.4. Piecewise definition of maps T_m. The reference domain (right sketch) corresponds to the *new* domain Ω^m and changes in each time step.

choose the domain at the new time step $\hat{\Omega}^m = \Omega(t_m)$ as reference domain. Other choices, e.g. $\hat{\Omega}^m = \Omega(t_{m-1})$ would be possible, as well. For $j = 1, ..., M$, we denote the space-time slabs in the reference system by $\hat{Q}^j := \hat{\Omega}^j \times I_j$, the space-time slabs of the subdomains ($i = 1,2$) by $\hat{Q}_i^j := \hat{\Omega}_i^j \times I_j$ and the interface slabs by $\hat{G}^j := \hat{\Gamma}^j \times I_j$. Functions $u \in X_1^k$ and $\phi \in X_0^k$ can be written as

$$\begin{aligned}(u \circ T_m)|_{I_m} &= \frac{t - t_{m-1}}{k}(u \circ T_m)(x, t_m) + \frac{t_m - t}{k}(u \circ T_m)(x, t_{m-1}) \\ &=: \frac{t - t_{m-1}}{k}\hat{u}^m(\hat{x}) + \frac{t_m - t}{k}\hat{u}^{m-1,+}(\hat{x}) \\ (\phi \circ T_m)|_{I_m} &= \hat{\phi}^m(\hat{x})\end{aligned}$$

with functions $\hat{u}^m, \hat{\phi}^m, \hat{u}^{m-1,+} \in H_0^1(\hat{\Omega}^m)$ and $\hat{x} = T_m^{-1}(x,t)$. We use the notation $\hat{u}^{m-1,+}$ to distinguish from $\hat{u}^{m-1}$ which is defined on another reference domain, namely $\hat{\Omega}^{m-1}$. Due to the continuity condition in X_k^1, it must hold that

$$\left(\hat{u}^{m-1,+} \circ T_m^{-1}\right)(t_{m-1}) = \hat{u}^{m-1}. \tag{8.9}$$

In order to simplify notation, we will often skip the second superscript and use the notation $\hat{u}^{m-1}$ instead of $\hat{u}^{m-1,+}$ in $\hat{Q}^m$.

Finally, we denote by $F_m = \nabla T_m$ the spatial derivative of the transformation and by $J_m = \det(F_m)$ its determinant. We define the following bilinear form in a time interval I_m, formulated both in Eulerian coordinates on Q^m and on the reference domain $\hat{Q}^m$ in ALE coordinates:

$$\begin{aligned}B^m(u,\phi) &:= (\partial_t u, \phi)_{Q^m} + (\kappa \nabla u, \nabla \phi)_{Q^m} \qquad (8.10) \\ &= \left(J_m \partial_t \hat{u} - \partial_t T_m (JF^{-T})_m \hat{\nabla}_m \hat{u}, \hat{\phi}\right)_{\hat{Q}^m} + \left(\hat{\kappa}(JF^{-T})_m \hat{\nabla}_m \hat{u}, F_m^{-T} \hat{\nabla}_m \hat{\phi}\right)_{\hat{Q}^m}.\end{aligned}$$

Here, the notation $\hat{\nabla}_m$ denotes the gradient with respect to the coordinates $\hat{x}_m$ on the reference domain $\hat{\Omega}^m$. For better readability, we will often skip the subscripts m if there is no risk for ambiguity. It holds that

$$B(u,\phi) = \sum_{m=1}^{M} B^m(u,\phi) + (u(0),\phi(0))_{\Omega(0)}.$$

The discrete formulation in the ansatz and trial space defined in (8.8) reads: Find $u_k \in X_k^1$ such that

$$B(u_k,\phi_k) = (f,\phi_k)_Q + (u^0,\phi(0))_{\Omega(0)} \quad \forall \phi_k \in X_k^0. \tag{8.11}$$

This formulation splits into the time-stepping scheme

$$B^m(u_k,\phi_k) = \left(J\hat{f},\hat{\phi}_k\right)_{\hat{Q}^m}, \tag{8.12}$$

where

$$\begin{aligned} B^m(u_k,\phi_k) :=& \frac{1}{k}\left(J(\hat{u}_k^m - \hat{u}_k^{m-1}),\hat{\phi}^m\right)_{\hat{Q}^m} \\ &- \left(\partial_t T J F^{-T}\left(\frac{t-t_{m-1}}{k}\hat{\nabla}\hat{u}_k^m + \frac{t_m - t}{k}\hat{\nabla}\hat{u}_k^{m-1}\right),\hat{\phi}^m\right)_{\hat{Q}^m} \\ &+ \left(\hat{\kappa} J F^{-T}\left(\frac{t-t_{m-1}}{k}\hat{\nabla}\hat{u}_k^m + \frac{t_m - t}{k}\hat{\nabla}\hat{u}_k^{m-1}\right),F^{-T}\hat{\nabla}\hat{\phi}^m\right)_{\hat{Q}^m}. \end{aligned} \tag{8.13}$$

In practice, the interface and boundary movement are often implicitly defined by the solution variables and might thus be available only at the time points t_{m-1} and t_m. Therefore, we will use a further simplification of (8.11). We use approximations of the form

$$a(t)b(t) \approx \frac{1}{4}(a(t_m) + a(t_{m-1}))(b(t_m) + b(t_{m-1})).$$

We use the notation $\overline{J}_m = \frac{1}{2}\left(J_m(t_m) + J_m(t_{m-1})\right)$ and analogously $\overline{JF}_m^{-T}$, $\overline{F}_m^{-T}$ and $\overline{\partial_t T}_m$. Again, we will skip the subscript m if there is no risk for ambiguity. We define the discrete bilinear forms

$$\begin{aligned} B_k^m(u,\phi) &= \left(\overline{J}\partial_t\hat{u},\hat{\phi}\right)_{\hat{Q}^m} - \left(\overline{\partial_t T}\,\overline{JF}^{-T}\hat{\nabla}\hat{u},\hat{\phi}\right)_{\hat{Q}^m} + \left(\hat{\kappa}\overline{JF}^{-T}\hat{\nabla}\hat{u},\overline{F}^{-T}\hat{\nabla}\hat{\phi}\right)_{\hat{Q}^m}, \\ B_k(u,\phi) &= \sum_{m=1}^{M} B_k^m(u,\phi) + (u(0),\phi(0))_{\Omega(0)}. \end{aligned}$$

For $u_k \in X_k^1$ and $\phi_k \in X_k^0$, it holds that

$$\begin{aligned} B_k^m(u_k,\phi_k) =& \frac{1}{k}\left(\overline{J}\left(\hat{u}_k^m - \hat{u}_k^{m-1}\right),\hat{\phi}_k^m\right)_{\hat{Q}^m} - \frac{1}{2}\left(\overline{\partial_t T}\,\overline{JF}^{-T}\hat{\nabla}\left(\hat{u}_k^m + \hat{u}_k^{m-1}\right),\hat{\phi}_k^m\right)_{\hat{Q}^m} \\ &+ \frac{1}{2}\left(\hat{\kappa}\overline{JF}^{-T}\hat{\nabla}\left(\hat{u}_k^m + \hat{u}_k^{m-1}\right),\overline{F}^{-T}\hat{\nabla}\hat{\phi}_k^m\right)_{\hat{Q}^m}. \end{aligned}$$

The corresponding discrete variational formulation reads: Find $u_k \in X_k^1$ such that

$$B_k(u_k, \phi_k) = (f, \phi_k)_Q + (u^0, \phi_k(0))_{\Omega(0)} \quad \forall \phi_k \in X_k^0. \tag{8.14}$$

As the continuous solution u fulfils

$$B(u, \phi_k) = (f, \phi_k)_Q + (u^0, \phi_k^0)_{\Omega(0)} \quad \forall \phi_k \in X_k^0,$$

we have the Galerkin orthogonality

$$B(u, \phi_k) - B_k(u_k, \phi_k) = 0 \quad \forall \phi_k \in X_k^0. \tag{8.15}$$

Remark 8.1 (Fixed-mesh ALE). *As already mentioned a similar time-stepping scheme results when applying the trapezoidal rule in time within the Fixed-mesh ALE method*[42]*. There are two main differences: The first one lies in the approximation of the quantities* J, F *and* $\partial_t T$ *related to the transformation. Secondly, to fit into their framework, we would have to define* $u_k^{m-1,+}$ *by the residual-based projection*

$$B_{old}^m(u_k^{m-1,+}, \phi) = B_{old}^{m-1}(u_k^{m-1,-}, \phi) \quad \forall \phi \in H_0^1(\Omega^m) \tag{8.16}$$

where

$$B_{old}^m(w, \phi) := \left(-\bar{J}\hat{w} + \frac{k}{2}\overline{\partial_t T}\,\overline{JF}^{-T}\hat{\nabla}\hat{w}, \hat{\phi} \right)_{\hat{\Omega}^m} + \frac{k}{2}\left(\hat{\kappa}\overline{JF}^{-T}\hat{\nabla}\hat{w}, \overline{F}^{-T}\hat{\nabla}\hat{\phi} \right)_{\hat{\Omega}^m}.$$

To the best of our knowledge such a projection has not been used before within the Fixed-mesh ALE framework. For our practical implementation that avoids the calculation of such a projection, see Section 8.5.

8.4 A priori error estimation

8.4.1 Main result

We begin this section by stating our main results. We give a proof that is split into several partial results that will be shown afterwards in a series of lemmata. We will make the following regularity assumptions for the domain movement T_m.

Assumption 8.2 (Regularity of the domain movement).
(i) For all intervals I_m*, there exists a map* $T_m : \hat{\Omega}^m \times I_m \to \Omega(t)$ *such that for* $t \in I_m$

$$T_m(\hat{\Omega}_i^m, t) = \Omega_i(t) \quad (i = 1, 2), \qquad T_m(\hat{\Gamma}^m, t) = \Gamma(t).$$

(ii) Furthermore, it holds for $i = 1, 2$ *that*

$$\sup_{t \in I_m} \left(\|T_m(t)\|_{W^{2,\infty}(\hat{\Omega}_i^m)} + \sum_{k=1}^{3} \|\partial_t^k T_m(t)\|_{W^{3-k,\infty}(\hat{\Omega}_i^m)} \right) \leq c$$

$$\sup_{t \in I_m} \left(\|T_m^{-1}(t)\|_{W^{2,\infty}(\hat{\Omega}_i^m)} + \sum_{k=1}^{2} \|\partial_t^k T_m^{-1}(t)\|_{W^{3-k,\infty}(\hat{\Omega}_i^m)} \right) \leq c.$$

(iii) Finally, we assume that T_m *and* $\partial_t T_m$ *are continuous across the interface* $\hat{\Gamma}^m$.

Remark 8.3 (Assumption 8.2)**.** *Assumption 8.2 implies that*

$$\sup_{t\in I_m} ||F_m(t)||_{W^{1,\infty}(\hat{\Omega}^m)} + \sup_{t\in I_m} ||F_m^{-1}(t)||_{W^{1,\infty}(\hat{\Omega}^m)} + \sup_{t\in I_m} ||J_m(t)||_{W^{1,\infty}(\hat{\Omega}^m)} \leq c.$$

The latter holds true as the determinant of F_m *can be written as a summed product of the entries of* F_m*.*

Remark 8.4 (Assumption 8.2)**.** *In many practical cases, the position of the interface and the outer boundaries depends on the solution itself and is only available at discrete points in time (e.g. by means of level set functions* ψ^m, ψ^{m-1}*). Let*

$$x^{m-1} := T_m(x^m, t_{m-1}) \in \Omega(t_{m-1}) \tag{8.17}$$

be the transformed coordinate corresponding to a point $x^m \in \Omega(t_m)$*. Then, a suitable transformation in the interval* I_m *is given by*

$$T_m(x^m, t) = \frac{t - t_{m-1}}{k} x^m + \frac{t_m - t}{k} x^{m-1}.$$

Here, the first time derivative is $\partial_t T_m = 1/k\,(x^m - x^{m-1})$*, while higher time derivatives vanish. Assumption 8.2 reduces to the boundedness of the velocity of the domain movement and its spatial derivatives.*

Remark 8.5 (Construction of a mapping T_m)**.** *Assume the interface movement is given by a vector-valued function*

$$\psi : \Gamma(t_m) \to \Gamma(t_{m-1}).$$

Such a function is available in the context of fluid-structure interactions by the Initial Point Set function (see e.g. Dunne & Rannacher[56] *or Section 8.6.2), sometimes also called the Backward Characteristics method (Cottet et al.*[43]*) that traces back points to their original position in* $\Omega(0)$*. An extension of* ψ *to the complete domain* $\Omega(t_m)$ *(again denoted by* ψ*) can be obtained by e.g. a harmonic extension. Then, a transformation* $T : \Omega(t_m) \to \Omega(t)$ *is given by*

$$T(x, t) = \frac{t - t_{m-1}}{k} x + \frac{t_m - t}{k} \psi(x).$$

The regularity of T *depends only on the regularity of the boundary movement* ψ *and its extension at time* t_m*.*

Remark 8.6 (Regularity)**.** *In contrast to the ALE approach (8.4), we need regularity of the transformations* T_m *only locally in each time interval* I_m*. No global regularity of a mapping* T *is required. This enables us to handle large movements of the interface.*

Let $e_k = u - u_k$ denote the difference between the continuous and the discrete solution. Our main results will be error estimates of second order in both the global space-time L^2-norm $||e_k||_Q$ as well as the spatial L^2-norm error at the end time T, $||e_k(T)||_{\Omega(T)}$. Both estimates will be based on dual problems. Therefore, we introduce the functionals

$$I_1(\phi) := (e_k, \phi)_Q, \quad I_2(\phi) := (e_k(T), \phi(T))_{\Omega(T)}.$$

We will use the notation $I(\phi)$ whenever we do not need the specific form of I_1, I_2 in the proof. It holds that

$$||e_k||_Q^2 = I_1(e_k), \quad ||e_k(T)||_{\Omega(T)}^2 = I_2(e_k).$$

We are now ready to state our main result:

Theorem 8.7. *Let $u \in X$ be the solution of (8.5) and $u_k \in X_k^1$ the time discrete solution of (8.14). For $f \in \mathcal{H}^{1,0} \cap \mathcal{H}^{0,2}$, $u^0 \in H^4(\Omega_1(0) \cup \Omega_2(0))$ and under Assumption 8.2, it holds that*

$$||u - u_k||_Q + ||u(T) - u_k(T)||_{\Omega(T)} \leq ck^2 \left(||f||_{1,0} + ||f||_{0,2} + ||u^0||_{H^4(\Omega_1(0) \cup \Omega_2(0))}\right).$$

Proof. We split the error $e_k = u - u_k$ into $\eta_k = u - i_k u$ and $\xi_k = i_k u - u_k$, where $i_k u$ denotes a time-nodal interpolant that will be defined in Section 8.4.2. We have

$$I(e_k) = I(\eta_k) + I(\xi_k). \tag{8.18}$$

The first part vanishes by definition for the case of the end time L^2-norm (I_1). For the global L^2-norm error, we will use the interpolation error estimate

$$||\eta_k||_Q \leq ck^2 ||u||_{H^2(Q_1 \cup Q_2)}. \tag{8.19}$$

which will be shown in Lemma 8.10. For the second part in (8.18), we make use of a dual problem. Let $z_k \in X_k^0$ be the solution of

$$B_k(\varphi_k, z_k) = I(\varphi_k) \quad \forall \varphi_k \in X_k^1.$$

By using the Galerkin orthogonality (8.15), we have

$$\begin{aligned}(e_k, \xi_k)_Q = B_k(\xi_k, z_k) &= B_k(i_k u, z_k) - B(u, z_k) \\ &= B_k(u, z_k) - B(u, z_k) - B_k(\eta_k, z_k).\end{aligned} \tag{8.20}$$

For the error between the continuous and the discrete bilinear form, we will show in Lemma 8.15

$$B(u, z_k) - B_k(u, z_k) \leq ck^2 ||u||_{H^2(Q_1 \cup Q_2)} ||\nabla z_k||_Q. \tag{8.21}$$

Furthermore, we will derive the dual stability estimate (Lemma 8.22)

$$||\nabla z_k||_Q \leq cI(e_k) \tag{8.22}$$

that will be based on primal stability estimates (Lemma 8.17 and Lemma 8.20). For the second part in (8.20), we will show in Lemma 8.25 that

$$B_k(\eta_k, z_k) \leq ck^2 \left(||f||_{1,0} + ||f||_{0,2} + ||u^0||_{H^4(\Omega_1(0) \cup \Omega_2(0))}\right)$$

which completes the proof. □

Remark 8.8. *If we assume the higher regularity* $f \in \mathcal{H}^{0,4} \cap \mathcal{H}^{1,2} \cap \mathcal{H}^{2,0}$ *and* $u^0 \in H^6(\Omega_1(0) \cup \Omega_2(0))$, *we can show second-order error estimates without using a dual problem. Therefore, we exploit Galerkin orthogonality for* $B_k(\xi_k, P_k^0 \xi_k)$, *where* P_k^0 *denotes a projection into the space of piecewise constant functions* X_k^0. *It follows that*

$$B_k(\xi_k, P_k^0 \xi_k) = B_k(u, P_k^0 \xi_k) - B(u, P_k^0 \xi_k) + B_k(\eta_k, P_k^0 \xi_k). \tag{8.23}$$

In combination with the estimate

$$\|e_k(t_m)\|_{\Omega(t_m)} = \|\xi_k(t_m)\|_{\Omega(t_m)} \leq C B_k(\xi_k, P_k^0 \xi_k)$$

(for its derivation see Lemma 8.17 and Remark 8.19 below) we can directly derive an error estimate for the L^2*-norm at the end time. A similar argumentation can be found e.g. in Luskin & Rannacher*[105]*. The problem, however, lies now in the estimation of the last term on the right-hand side of (8.23). An second-order error estimate is only possible if we have the regularity* $\partial_t^2 \nabla u \in L^2(Q)$ *which requires the aforementioned regularity assumptions on the data.*

8.4.2 Auxiliary estimates

In this section, we provide the auxiliary results needed to prove Theorem 8.7. We begin with the definition of interpolation and projections and the estimation of the corresponding interpolation and projection errors. Next, we estimate the difference between continuous and discrete bilinear form in Lemma 8.15 and derive stability estimates for the discrete solution u_k in Lemma 8.17 and Lemma 8.20. Then, we introduce a continuous and a discrete dual problem and show stability results as well as an a priori error estimate between the discrete and continuous dual solutions z_k and z in Lemma 8.22 and Lemma 8.24. Finally, these results will be needed in Lemma 8.25 to prove the smallness of the term $B_k(\eta_k, z_k)$.

Before we show these results, we state an auxiliary lemma that we will need frequently for transforming derivatives between a reference and the current system.

Lemma 8.9. *(Transformation of derivatives) Let Assumption 8.2 be valid and* $\hat{u}(\hat{x}) := (u \circ T_m^{-1})(x)$ *on* $\hat{Q}^m$. *For* $u \in H^1(Q)$, $\hat{u}$ *lies piecewise in* $H^1(\hat{Q}^m)$ *and it holds that*

$$\left\|\hat{\nabla} \hat{u}\right\|_{\hat{Q}^m} \leq c \|\nabla u\|_{Q^m} \quad \text{and} \quad \|\partial_t \hat{u}\|_{\hat{Q}^m} \leq c \left\{ \|\partial_t u\|_{Q^m} + \|\nabla u\|_{Q^m} \right\}. \tag{8.24}$$

For u *in* $\mathcal{H}^{2,0} \cap \mathcal{H}^{1,1}$ *it holds that*

$$\left\|\partial_t^2 \hat{u}\right\|_{\hat{Q}^m} \leq c \left\{ \left\|\partial_t^2 u\right\|_{Q^m} + \|\partial_t \nabla u\|_{Q^m} + \|\nabla u\|_{Q^m} \right\}. \tag{8.25}$$

Proof. The proof is standard, see e.g. Richter[122]. □

Interpolation and projection

We define the interpolation $i_k u$ as standard nodal interpolant in each reference space-time slab $\hat{Q}^m$. This is equivalent to setting

$$i_k u(t_m) = u(t_m) \quad \forall m = 1, \ldots, M$$

in each time-grid point t_m.

Lemma 8.10. *Assume Assumption 8.2. If $u \in H^1(Q_1 \cup Q_2)$, it holds for the interpolation error that*

$$\|u - i_k u\|_Q \leq ck \left\{ \|\partial_t u\|_Q + \|\nabla u\|_Q \right\}. \tag{8.26}$$

For $u \in H^2(Q_1 \cup Q_2)$, we have

$$\|u - i_k u\|_Q \leq ck^2 \left\{ \left\|\partial_t^2 u\right\|_{Q_1 \cup Q_2} + \|\partial_t \nabla u\|_{Q_1 \cup Q_2} + \|\nabla u\|_Q \right\}. \tag{8.27}$$

Proof. We transform to the reference domain and use a standard estimate there. The determinant J is bounded by Assumption 8.2

$$\|u - i_k u\|^2_{Q^m} = \left\| J^{1/2} \left(\hat{u} - \widehat{i_k u} \right) \right\|^2_{\hat{Q}^m} \leq \left(\sup_{t \in I_m} \|J\|_{\infty, \hat{\Omega}^m} \right) \|\hat{u} - i_k \hat{u}\|^2_{\hat{Q}^m} \leq ck^{2l} \|\partial_t^l \hat{u}\|^2_{\hat{Q}_1^m \cup \hat{Q}_2^m}$$

for $l = 1, 2$. Transformation of derivatives (Lemma 8.9), summation over $m = 1, \ldots, M$ and taking the square root complete the proof. □

Remark 8.11. *Even in the case of a fixed outer boundary $\partial\Omega(t)$, an analogous interpolation estimate is not possible for an interpolant in the space $\tilde{X}_k^1$ if the interface $\Gamma(t)$ is moving.*

Next, we define a projection into the space of piecewise constant functions by setting in each time interval I_m

$$P_k^0 : X \to X_k^0, \qquad \left(P_k^0 v \circ T_m \right)|_{I_m} = \frac{1}{2} \left(\hat{v}(t_m) + \hat{v}(t_{m-1}) \right). \tag{8.28}$$

Lemma 8.12. *Let $v \in \mathscr{H}^{1,0}$. For the projection $P_k^0 v$ defined by (8.28), it holds that*

$$\left\| v - P_k^0 v \right\|_Q^2 \leq ck^2 \sum_{m=1}^{M} \left\| J^{1/2} \partial_t \hat{v} \right\|^2_{\hat{Q}^m}.$$

Proof. The assertion follows similarly to Lemma 8.10 by transformation to the reference domains and applying standard estimates. □

Furthermore, we will need a modified L^2-projection into the space X_k^0. We define $L_k^0 : X \to X_k^0$ piecewise on each reference space-time slab $\hat{Q}^m$ by the relation

$$\left(\widehat{L_k^0 v} - \hat{v}, \hat{\phi}_k \right)_{\hat{Q}^m} = 0 \quad \forall \hat{\phi}_k \in L^2(\hat{\Omega}^m). \tag{8.29}$$

Lemma 8.13. *Let $v \in \mathscr{H}^{1,0}$. For the projection $L_k^0 v$ defined by (8.29), we have the stability and error estimates*

$$\left\| L_k^0 v \right\|_Q \leq c \|v\|_Q, \qquad \left\| v - L_k^0 v \right\|_Q^2 \leq ck^2 \sum_{m=1}^{M} \left\| J^{1/2} \partial_t \hat{v} \right\|^2_{\hat{Q}^m}.$$

Proof. Stability follows from the fact that on a reference domain $\hat{Q}^m$

$$\left(\widehat{L_k^0 v}, \widehat{L_k^0 v} \right)_{\hat{Q}^m} = \left(\widehat{L_k^0 v}, \hat{v} \right)_{\hat{Q}^m} \leq \left\| \widehat{L_k^0 v} \right\|_{\hat{Q}^m} \|\hat{v}\|_{\hat{Q}^m}.$$

The error estimate follows similarly to the statements of Lemmas 8.10 and 8.12. □

Error between the discrete and the continuous bilinear form

In this subsection, we provide an estimate of the difference between the bilinear forms $B(\cdot,\cdot)$ and $B_k(\cdot,\cdot)$. Before we show this, we provide an auxiliary result that will be frequently needed to deal with the domain movement.

Lemma 8.14. *Let* $a, b \in W^{1,\infty}(I, L^\infty(\Omega))$ *and define a function* $\overline{a}$ *by* $\overline{a} = 1/2(a(t_m) + a(t_{m-1}))$*. For arbitrary functions* $f, g \in L^2(\hat{\Omega}^m)$ *and a point* $t_i \in I_m$*, it holds that*

$$((a(t_i) - \overline{a})f, g)_{\hat{Q}^m} \le ck\big|(f, g)_{\hat{Q}^m}\big|, \tag{8.30}$$

$$((a - \overline{a})f, g)_{\hat{Q}^m} \le ck\big|(f, g)_{\hat{Q}^m}\big|, \tag{8.31}$$

$$\Big((a(t)b(t) - \overline{a}\overline{b})f, g\Big)_{\hat{Q}^m} \le ck\|f\|_{\hat{Q}^m}\|g\|_{\hat{Q}^m}. \tag{8.32}$$

For $g \in X_k^0$ *piecewise constant,* $f \in H^1(Q)$ *and* $a, b \in W^{2,\infty}(I, L^\infty(\Omega))$*, it holds that*

$$((a(t) - \overline{a})f, g)_{\hat{Q}^m} \le ck^2\|f\|_{H^1(I_m, L^2(\hat{\Omega}^m))}\|g\|_{\hat{Q}^m}, \tag{8.33}$$

$$\Big((a(t)b(t) - \overline{a}\overline{b})f, g\Big)_{\hat{Q}^m} \le ck^2\|f\|_{H^1(I_m, L^2(\hat{\Omega}^m))}\|g\|_{\hat{Q}^m}. \tag{8.34}$$

Similar results hold true for vector-valued functions.

Proof. (8.30) to (8.32) follow by simple interpolation arguments. To show (8.33), we add $\pm\overline{f}$

$$((a(t) - \overline{a})f, g))_{\hat{Q}^m} = \Big((a(t) - \overline{a})(f - \overline{f}), g)\Big)_{\hat{Q}^m} + \Big((a(t) - \overline{a})\overline{f}, g)\Big)_{\hat{Q}^m}. \tag{8.35}$$

We estimate the first term by using the Hölder inequality

$$\begin{aligned}\Big((a(t) - \overline{a})(f - \overline{f}), g)\Big)_{\hat{Q}^m} &\le \sup_{t \in I_m} \|a - \overline{a}\|_{\infty, \hat{\Omega}^m}\|f - \overline{f}\|_{\hat{Q}^m}\|g\|_{\hat{Q}^m} \\ &\le ck^2 \sup_{t \in I_m} \|\partial_t a\|_{\infty, \hat{\Omega}^m}\|\partial_t f\|_{\hat{Q}^m}\|g\|_{\hat{Q}^m}.\end{aligned} \tag{8.36}$$

For the second term, we notice that neither $\overline{f}$ nor g depend on time and thus, time integration reduces to an error estimate for the trapezoidal rule for a

$$\Big((a(t) - \overline{a})\overline{f}, g)\Big)_{\hat{Q}^m} = \int_{\hat{\Omega}^m} \overline{f} g \int_{I_m} (a(t) - \overline{a})\,\mathrm{d}t \le ck^2 \sup_{t \in I_m} \|\partial_t^2 a\|_{\infty, \hat{\Omega}^m}\|\overline{f}\|_{\hat{Q}^m}\|g\|_{\hat{Q}^m}. \tag{8.37}$$

The term including $\overline{f}$ can be estimated by

$$\|\overline{f}\|_{\hat{Q}^m} \le \|f - \overline{f}\|_{\hat{Q}^m} + \|f\|_{\hat{Q}^m} \le ck\|\partial_t f\|_{\hat{Q}^m} + \|f\|_{\hat{Q}^m}. \tag{8.38}$$

(8.35) to (8.38) imply (8.33). To show (8.34), we use a similar argumentation and split the corresponding first term into

$$\begin{aligned}\sup_{x \in \hat{\Omega}^m}\left(\int_{I_m} a(t)b(t) - \overline{a}\overline{b}\,\mathrm{d}t\right) = \sup_{x \in \hat{\Omega}^m}\Bigg(&\int_{I_m} (a(t) - \overline{a})\Big(b(t) - \overline{b}\Big)\,\mathrm{d}t \\ &+ \int_{I_m} (a(t) - \overline{a})\overline{b}\,\mathrm{d}t + \int_{I_m} \overline{a}\Big(b(t) - \overline{b}\Big)\,\mathrm{d}t\Bigg).\end{aligned}$$

□

Now we can show the following:

Lemma 8.15. *Let Assumption 8.2 be valid. For $u \in H^1(Q)$ and $z \in L^2(I, H^1(\Omega))$ it holds that*

$$\left|B(u,z) - B_k(u,z)\right| \leq ck\, \|u\|_{H^1(Q)} \|\nabla z\|_Q. \tag{8.39}$$

If $u \in H^2(Q_1 \cup Q_2)$ and $z_k \in X_k^0$ it holds that

$$\left|B(u,z_k) - B_k(u,z_k)\right| \leq ck^2\, \|u\|_{H^2(Q_1 \cup Q_2)} \|\nabla z_k\|_Q. \tag{8.40}$$

Proof. We show (8.40). (8.39) follows similarly. By definition, we have

$$\begin{aligned} B^m(u,z_k) - B_k^m(u,z_k) = &\left((J - \bar{J})\partial_t \hat{u} - \left(\partial_t T J F^{-T} - \overline{\partial_t T}\,\overline{JF}^{-T} \right) \hat{\nabla} \hat{u}, \hat{z}_k^m \right)_{\hat{Q}^m} \\ &+ \left(\hat{\kappa} \left(J F^{-1} F^{-T} - \overline{JF}^{-1} \overline{F}^{-T} \right) \hat{\nabla} \hat{u}, \hat{\nabla} \hat{z}_k^m \right)_{\hat{Q}^m}. \end{aligned} \tag{8.41}$$

We estimate the integrals on the domains $\hat{Q}_1^m$ and $\hat{Q}_2^m$ separately. Applying (8.33) for the determinant J, the first term in (8.41) is bounded by

$$\left((J - \bar{J})\partial_t \hat{u}, \hat{z}_k^m \right)_{\hat{Q}^m} \leq ck^2 \left(\|\partial_t^2 \hat{u}\|_{\hat{Q}_1^m} + \|\partial_t^2 \hat{u}\|_{\hat{Q}_2^m} \right) \|\hat{z}_k^m\|_{\hat{Q}^m}.$$

Similarly, we get for the remaining terms in (8.41) using the Poincaré inequality

$$\begin{aligned} &\left(\hat{\kappa} (J F^{-T} F^{-1} - \overline{JF}^{-T} \overline{F}^{-1}) \hat{\nabla} \hat{u}, \hat{\nabla} \hat{z}_k^m \right)_{\hat{Q}^m} - \left((\partial_t T J F^{-T} - \overline{\partial_t T}\,\overline{JF}^{-T}) \hat{\nabla} \hat{u}, \hat{z}_k^m \right)_{\hat{Q}^m} \\ &\leq ck^2 \left(\|\partial_t \hat{\nabla} \hat{u}\|_{\hat{Q}_1^m} + \|\partial_t \hat{\nabla} \hat{u}\|_{\hat{Q}_2^m} \right) \|\hat{\nabla} \hat{z}_k^m\|_{\hat{Q}^m}. \end{aligned}$$

Summation over $m = 1, \ldots, M$ and transformation of derivatives (Lemma 8.9) complete the proof. ☐

Primal stability estimates

In this section, we provide a set of stability estimates for the discrete solution u_k. Most of the stability results will be based on the following lemma.

Lemma 8.16 (Discrete Gronwall lemma). *Let $(w_n)_{n \geq 0}, (p_n)_{n \geq 0}, (a_n)_{n \geq 0}$ and $(b_n)_{n \geq 0}$ be sequences of non-negative numbers and $c_0 \geq 0$. Furthermore, let the inequality*

$$w_M + \sum_{n=1}^{M} p_n \leq \sum_{n=1}^{M} (a_n w_n + b_n) + c_0$$

be valid for all $n \geq 0$. For $\sigma_M = 1 - a_M > 0$, it holds that

$$w_M + \sum_{n=1}^{M} p_n \leq \exp\left(\sigma_M^{-1} \sum_{n=1}^{M} a_n \right) \left(c_0 + \sum_{n=1}^{M} b_n \right).$$

A proof for this result can be found e.g. in Heywood & Rannacher[84]. Using this, we can show stability estimates for the semi-discrete primal solution u_k.

Lemma 8.17. *Let $u_k \in X_k^1$ be the time discrete solution of (8.14) and assume Assumption 8.2. It holds that*

$$\|u_k(T)\|^2_{\Omega(T)} + \left\|\nabla P_k^0 u_k\right\|^2_Q \le \exp(cT)\left(\|f\|^2_{L^2(I,H^{-1}(\Omega))} + \left\|u^0\right\|^2_{\Omega(0)}\right). \tag{8.42}$$

Proof. We test (8.14) with $\phi = P_k^0 u_k$, which means $\hat{\phi}^m = \frac{1}{2}(\hat{u}_k^m + \hat{u}_k^{m-1})$. We get on every time interval I_m:

$$\begin{aligned}\frac{1}{2k}\left(\bar{J}(\hat{u}_k^m - \hat{u}_k^{m-1}), \hat{u}_k^m + \hat{u}_k^{m-1}\right)_{\hat{Q}^m} - \frac{1}{4}\left(\overline{\partial_t T}\,\overline{JF}^{-T}(\hat{\nabla}\hat{u}_k^m + \hat{\nabla}\hat{u}_k^{m-1}), \hat{u}_k^m + \hat{u}_k^{m-1}\right)_{\hat{Q}^m}&\\ + \frac{1}{4}\left(\hat{\kappa}\overline{JF}^{-T}\hat{\nabla}(\hat{u}_k^m + \hat{u}_k^{m-1}), \overline{F}^{-T}\hat{\nabla}(\hat{u}_k^m + \hat{u}_k^{m-1})\right)_{\hat{Q}^m} = \frac{1}{2}\left(J\hat{f}, \hat{u}_k^m + \hat{u}_k^{m-1}\right)_{\hat{Q}^m}.&\end{aligned} \tag{8.43}$$

Before we estimate (8.43) term by term, note that with the help of Lemma 8.14 and Assumption 8.2, we have for arbitrary functions $f, g \in L^2(\hat{\Omega}^m)$ and $i = m-1$ or $i = m$

$$\begin{aligned}\left(\bar{J}|f|, |g|\right)_{\hat{\Omega}^m} = (J(t_i)|f|, |g|)_{\hat{\Omega}^m} + \left(\left(\bar{J} - J(t_i)\right)|f|, |g|\right)_{\hat{\Omega}^m} &\ge (J(t_i)|f|, |g|)_{\hat{\Omega}^m} - ck(|f|, |g|)_{\hat{\Omega}^m}\\ &\ge (1-ck)\left(J(t_i)|f|, |g|\right)_{\hat{\Omega}^m}.\end{aligned}$$

The same argumentation can be used e.g. for F^{-T} instead of J. We get for the first term in (8.43)

$$\begin{aligned}\frac{1}{2k}(\bar{J}(\hat{u}_k^m - \hat{u}_k^{m-1}), \hat{u}_k^m + \hat{u}_k^{m-1})_{\hat{Q}^m} &= \frac{1}{2}\left\|\bar{J}^{1/2}\hat{u}_k^m\right\|^2_{\hat{\Omega}^m} - \frac{1}{2}\left\|\bar{J}^{1/2}\hat{u}_k^{m-1}\right\|^2_{\hat{\Omega}^m}\\ &\ge \left(\frac{1}{2} - ck\right)\left\|J(t_m)^{1/2}\hat{u}_k^m\right\|^2_{\hat{\Omega}^m} - \left(\frac{1}{2} + ck\right)\left\|J(t_{m-1})^{1/2}\hat{u}_k^{m-1}\right\|^2_{\hat{\Omega}^m}\\ &\ge \left(\frac{1}{2} - ck\right)\|u_k(t_m)\|^2_{\Omega(t_m)} - \left(\frac{1}{2} + ck\right)\|u_k(t_{m-1})\|^2_{\Omega(t_{m-1})}.\end{aligned}$$

For the second term we use Assumption 8.2, Lemma 8.14 and Young's inequality and obtain

$$\begin{aligned}&\frac{1}{4}(\overline{\partial_t T}\,\overline{JF}^{-T}\hat{\nabla}(\hat{u}_k^m + \hat{u}_k^{m-1}), \hat{u}_k^m + \hat{u}_k^{m-1})_{\hat{Q}^m}\\ &\qquad \ge -c\left\|\overline{JF}^{-T}\hat{\nabla}(\hat{u}_k^m + \hat{u}_k^{m-1})\right\|_{\hat{Q}^m}\left\|\hat{u}_k^m + \hat{u}_k^{m-1}\right\|_{\hat{Q}^m}\\ &\qquad \ge -c\|JF^{-T}\hat{\nabla}(\hat{u}_k^m + \hat{u}_k^{m-1})\|_{\hat{Q}^m} k^{1/2}\left(\|\hat{u}_k^m\|_{\hat{\Omega}^m} + \|\hat{u}_k^{m-1}\|_{\hat{\Omega}^m}\right)\\ &\qquad \ge -\frac{\kappa_{\min}}{8}\|\nabla P_k^0 u_k\|^2_{Q^m} - ck\left(\|u_k^m\|^2_{\Omega(t_m)} + \|u_k^{m-1}\|^2_{\Omega(t_{m-1})}\right).\end{aligned}$$

With similar arguments, we get for the third term

$$\frac{1}{4}\left(\hat{\kappa}\overline{JF}^{-T}\hat{\nabla}(\hat{u}_k^m + \hat{u}_k^{m-1}), \overline{F}^{-T}\hat{\nabla}(\hat{u}_k^m + \hat{u}_k^{m-1})\right)_{\hat{Q}^m} \ge (1-ck)\kappa_{\min}\|\nabla P_k^0 u_k\|^2_{Q^m}.$$

For the right-hand side, we use the Poincaré and Young's inequality

$$\begin{aligned}\frac{1}{2}\left(J\hat{f},\hat{u}_k^m+\hat{u}_k^{m-1}\right)_{\hat{Q}^m}=\left(f,P_k^0u_k\right)_{Q^m}&\le c\|f\|_{L^2(I_m,H^{-1}(\Omega))}\|\nabla P_k^0u_k\|_{Q^m}\\&\le\frac{c}{\kappa_{\min}}\|f\|^2_{L^2(I_m,H^{-1}(\Omega))}+\frac{\kappa_{\min}}{8}\|\nabla P_k^0u_k\|^2_{Q^m}.\end{aligned}$$

Altogether we have shown that

$$\begin{aligned}&\left\|u_k(t_m)\right\|^2_{\Omega(t_m)}-\left\|u_k(t_{m-1})\right\|^2_{\Omega(t_{m-1})}+\frac{\kappa_{\min}}{4}\left\|\nabla P_k^0u_k\right\|^2_{Q^m}\\&\qquad\le ck\left\{\|u_k(t_m)\|^2_{\Omega(t_m)}+\left\|u_k(t_{m-1})\right\|^2_{\Omega(t_{m-1})}\right\}+c\,\|f\|^2_{L^2(I_m,H^{-1}(\Omega))}.\end{aligned}$$

Finally, summation over m yields

$$\begin{aligned}&\|u_k(T)\|^2_{\Omega(T)}+\frac{\kappa_{\min}}{4}\|\nabla P_k^0u_k\|^2_Q\\&\qquad\le\|u^0\|^2_{\Omega(0)}+c\sum_{m=1}^{M}\left(k\|u_k(t_m)\|^2_{\Omega(t_m)}+\frac{1}{\kappa_{\min}}\|f\|^2_{L^2(I_m,H^{-1}(\Omega))}\right).\end{aligned}$$

Applying the discrete Gronwall lemma (Lemma 8.16) proves the assertion. □

Remark 8.18. *The exponential growth in time of the right-hand side of (8.42) is not optimal. It is well-known that for homogeneous right-hand side, the continuous solution u decays exponentially. In this case, we can use the inequality $\|u_k(T)\|\le\|u(T)\|+\|(u-u_k)(T)\|$ after showing the result of Theorem 8.7 to show that (8.42) even holds for a exponentially decaying constant for sufficiently small k.*

Remark 8.19. *By using the same techniques, we can show the estimate*

$$\|\xi_k(t_m)\|_{\Omega(t_m)}\le CB_k(\xi_k,P_k^0\xi_k)$$

by simply replacing u_k by ξ_k. As mentioned before in Remark 8.8, in combination with the Galerkin orthogonality (8.23) this can be used to show error estimates directly without the need for a dual problem. To show a second-order estimate, however, further assumptions on the regularity of the data and the domain would be necessary. Here, we will stick to the (optimal) regularity assumptions made in Section 8.1.

Next, we show a second stability estimate that gives a bound for the time derivative of u_k.

Lemma 8.20. *Let $u_k\in X_k^1$ be the time discrete solution of (8.14) and assume Assumption 8.2. It holds that*

$$\sum_{m=1}^{M}\|J^{1/2}\partial_t\hat{u}_k\|^2_{\hat{Q}^m}+\|\nabla u_k(T)\|^2_{\Omega(T)}\le\exp(cT)\left(\|f\|^2_Q+\left\|\nabla u^0\right\|^2_{\Omega(0)}\right).\tag{8.44}$$

Proof. We test (8.14) with the function $\phi_k \in X_k^0$ defined by $(\phi_k \circ T_m)|_{I_m} = \partial_t \hat{u}_k$:

$$\begin{aligned}(\bar{J}\partial_t \hat{u}_k, \partial_t \hat{u}_k)_{\hat{Q}^m} - \frac{1}{2k}\left(\overline{\partial_t T}\,\overline{JF}^{-T}(\hat{\nabla}\hat{u}_k^m + \hat{\nabla}\hat{u}_k^{m-1}), \hat{u}_k^m - \hat{u}_k^{m-1}\right)_{\hat{Q}^m} \\ + \frac{1}{2k}\left(\hat{\kappa}\overline{JF}^{-T}\hat{\nabla}(\hat{u}_k^m + \hat{u}_k^{m-1}), \overline{F}^{-T}\hat{\nabla}(\hat{u}_k^m - \hat{u}_k^{m-1})\right)_{\hat{Q}^m} = \left(J\hat{f}, \partial_t \hat{u}_k\right)_{\hat{Q}^m}.\end{aligned} \tag{8.45}$$

We proceed similarly to the proof of Lemma 8.17 and get on each space-time slab $\hat{Q}^m$

$$\begin{aligned}||J^{1/2}\partial_t \hat{u}_k||_{\hat{Q}^m}^2 + (1-ck)\left\|\kappa^{1/2}\nabla u_k(t_m)\right\|_{\Omega(t_m)}^2 \\ \leq (1+ck)\left\|\kappa^{1/2}\nabla u_k(t_{m-1})\right\|_{\Omega(t_{m-1})}^2 + c||f||_{Q^m}^2.\end{aligned} \tag{8.46}$$

Summation over $m = 1, ..., M$ and applying the discrete Gronwall Lemma yield the statement. ☐

Lemma 8.17 and 8.20 can be used to get stability bounds for the L^2-norm and the H^1 norm of the time-discrete solution u_k.

Corollary 8.21. *Let $u_k \in X_k^1$ be the time discrete solution of (8.14) and assume Assumption 8.2. It holds that*

$$||u_k||_Q^2 \leq \exp(cT)\left(||f||_{L^2(I,H^{-1}(\Omega))}^2 + \left\|u^0\right\|_{\Omega(0)}^2\right) \tag{8.47}$$

and

$$\left\|\kappa^{1/2}\nabla u_k\right\|_Q^2 \leq \exp(cT)\left(||f||_Q^2 + \left\|\nabla u^0\right\|_{\Omega(0)}^2\right). \tag{8.48}$$

Proof. We will show how to derive (8.48) from Lemma 8.20. (8.47) follows similarly from Lemma 8.17. We start by transformation to the reference domains. With Assumption 8.2, we get

$$\left\|\kappa^{1/2}\nabla u_k\right\|_Q^2 = \sum_{m=1}^M \left\|\hat{\kappa}^{1/2}J^{1/2}F^{-T}\hat{\nabla}\hat{u}_k\right\|_{\hat{Q}^m}^2 \leq (1+ck)\sum_{m=1}^M \left\|\hat{\kappa}^{1/2}\hat{\nabla}\hat{u}_k\right\|_{\hat{Q}^m}^2.$$

Using the triangle inequality and transformation of the second term from $\hat{Q}^m$ to $\hat{Q}^{m-1}$, we have

$$\begin{aligned}\sum_{m=1}^M \left\|\hat{\kappa}^{1/2}\hat{\nabla}\hat{u}_k\right\|_{\hat{Q}^m}^2 &\leq \sum_{m=1}^M \left(\frac{t-t_{m-1}}{k}\left\|\hat{\kappa}^{1/2}\hat{\nabla}\hat{u}_k^m\right\|_{\hat{Q}^m} + \frac{t_m - t}{k}\left\|\hat{\kappa}^{1/2}\hat{\nabla}\hat{u}_k^{m-1}\right\|_{\hat{Q}^m}\right)^2 \\ &\leq c\sum_{m=1}^M \left\|\hat{\kappa}^{1/2}\hat{\nabla}\hat{u}_k^m\right\|_{\hat{Q}^m}^2 \leq ck\sum_{m=1}^M \left\|\kappa^{1/2}\nabla u_k(t_m)\right\|_{\Omega(t_m)}^2.\end{aligned}$$

We use the statement (8.44) for the time grid point $T = t_m$ (cf. (8.46))

$$\left\|\kappa^{1/2}\nabla u_k(t_m)\right\|_{\Omega(t_m)}^2 \leq \exp(cT)\left\{||f||_Q^2 + \left\|\kappa^{1/2}\nabla u_k^0\right\|_{\Omega(0)}^2\right\}.$$

This yields

$$\sum_{m=1}^{M} \left\|\hat{\kappa}^{1/2}\hat{\nabla}\hat{u}_k^m\right\|_{\hat{Q}^m}^2 \le k\exp(cT)\sum_{m=1}^{M}\left\{||f||_Q^2 + \left\|\kappa^{1/2}\nabla u_k^0\right\|_{\Omega(0)}^2\right\}.$$

The sum on the right-hand side does not depend on m. Using $M = T/k$ completes the proof. □

Dual stability and a priori error estimates

In this section, we derive stability results for a continuous and discrete dual problem as well as a dual error estimate. The continuous dual problem is given by: *Find* $z \in X$ *such that*

$$B(\varphi, z) = I(\varphi) \quad \forall \varphi \in X \tag{8.49}$$

Standard regularity results (see e.g. Dziri & Zolésio[58]) yield

$$||\partial_t z||_{Q_1\cup Q_2} + ||\kappa\Delta z||_{Q_1\cup Q_2} \le cI(e_k). \tag{8.50}$$

The corresponding discrete dual problem is given by: Find $z_k \in X_k^0$ such that

$$B_k(\varphi_k, z_k) = I(\varphi_k) \quad \forall \varphi_k \in X_k^1. \tag{8.51}$$

We show a stability estimate:

Lemma 8.22. *Let* $e_k \in L^2(I, H^{-1}(\Omega))$ *for the case of the global* L^2*-norm error (*$I = I_1$*) and* $e_k \in L^2(\Omega(T))$ *for the case of the end time* L^2*-norm error (*$I = I_2$*). Under Assumption 8.2, it holds for the solution* $z_k \in X_k^0$ *of (8.51) that*

$$||\nabla z_k||_Q^2 \le cI(e_k).$$

Proof. We make use of an auxiliary problem. Let $v_k \in X_k^1$ be the solution of

$$B_k(v_k, \phi_k) = (\nabla z_k, \nabla\phi_k)_Q \quad \forall \phi_k \in X_k^0.$$

Then, by using (8.51), it follows that

$$||\nabla z_k||_Q^2 = B_k(v_k, z_k) = I(v_k). \tag{8.52}$$

For the case of the end time L^2-norm error, we have

$$I_2(v_k) = (e_k(T), v_k(T))_{\Omega(T)} \le ||e_k(T)||_{\Omega(T)}||v_k(T)||_{\Omega(T)}.$$

The stability estimate from Lemma 8.17 gives us

$$||v_k(T)||_{\Omega(T)} \le c\left(\int_I\Big(\sup_{\phi\in H_0^1(\Omega)}\frac{(\nabla z_k, \nabla\phi)_\Omega}{||\nabla\phi||_\Omega}\Big)^2 \mathrm{d}t\right)^{1/2} \le c||\nabla z_k||_Q.$$

For the case of the global L^2-norm error, we use the stability estimate (8.47)

$$I_1(v_k) = (e_k, v_k)_Q \le ||e_k||_Q||v_k||_Q \le c||e_k||_Q||\nabla z_k||_Q.$$

In both cases, the statement follows after dividing by $||\nabla z_k||_Q$. □

Next, we will need an error estimate between the continuous dual solution z and its discrete counterpart z_k. In order to prove this result, we provide a further auxiliary result based on the Piola transform of an interface integral on the reference domain. Here, $[\cdot]$ denotes the jump operator over the interface.

Lemma 8.23. *(Piola transform) Let* $f \in L^2(I_m, \hat{\Gamma}^m)$ *and* $\hat{n}$ *be the normal vector to the interface line* $\hat{\Gamma}^m$. *It holds that*

$$\int_{I_m} \int_{\hat{\Gamma}^m} [\overline{JF}^{-T}(t_m)\hat{n}] \cdot \hat{f} \, do \, dt = 0. \tag{8.53}$$

Proof. $JF^{-T}(t_k)\hat{n}$ is the Piola transform of the current normal n of the line $\Gamma(t_i)$ $(i = m-1, m)$. It holds that

$$\begin{aligned}
&\int_{I_m} \int_{\hat{\Gamma}^m} [\overline{JF}^{-T}(t_m)\hat{n}] \cdot \hat{f} \, \mathrm{do} \, \mathrm{d}t \\
&\qquad = \frac{1}{2} \int_{I_m} \int_{\hat{\Gamma}^m} \Big([JF^{-T}(t_m)\hat{n}] + [JF^{-T}(t_{m-1})\hat{n}] \Big) \cdot \hat{f} \, \mathrm{do} \, \mathrm{d}t \\
&\qquad = \frac{1}{2} \int_{I_m} \left(\int_{\Gamma(t_m)} [n] \cdot f \, \mathrm{do} + \int_{\Gamma(t_{m-1})} [n] \cdot (\hat{f} \circ T_m^{-1}(t_{m-1})) \, \mathrm{do} \right) \mathrm{d}t = 0.
\end{aligned}$$

□

Lemma 8.24. *Let* $z \in X$ *be the solution of (8.49) and* $z_k \in X_k^1$ *the time discrete dual solution of (8.51). It holds that*

$$\|z - z_k\|_Q \le ckI(e_k).$$

Proof. We split the error into two parts $z - z_k = (z - L_k^0 z) + (L_k^0 z - z_k)$ where $L_k^0 : X \to X_k^0$ denotes the modified L^2-projection introduced in (8.29). For the projection error, we have from Lemma 8.13

$$\left\| z - L_k^0 z \right\|_Q \le ck \, \|z\|_{H^1(Q)} \le ckI(e_k).$$

For the second part, we define an auxiliary problem: Let $v_k \in X_k^1$ be the solution of

$$B_k(v_k, \phi) = \left(L_k^0 z - z_k, \phi \right)_Q \quad \forall \phi \in X_k^0.$$

Using the Galerkin orthogonality $B_k(\phi_k, z_k) - B(\phi_k, z) = 0 \; \forall \phi_k \in X_k^1$, we have

$$\begin{aligned}
\left\| L_k^0 z - z_k \right\|^2 &= B_k(v_k, L_k^0 z - z_k) = B_k(v_k, L_k^0 z) - B(v_k, z) \\
&= B_k(v_k, L_k^0 z - z) - B(v_k, z) + B_k(v_k, z).
\end{aligned} \tag{8.54}$$

The second part is bounded by Lemma 8.15, the primal stability estimates (Lemma 8.20 and Corollary 8.21) and the regularity estimate (8.50) for the dual solution z

$$|B(v_k, z) - B_k(v_k, z)| \le ck \, \|v_k\|_{H^1(Q)} \, \|\nabla z\|_Q \le ck \left\| L_k^0 z - z_k \right\|_Q I(e_k).$$

The first term in (8.54) reads intervalwise

$$
\begin{aligned}
B_k^m(v_k, L_k^0 z - z) = \left(\bar{J}\partial_t \hat{v}_k, \widehat{L_k^0 z} - \hat{z}\right)_{\hat{Q}^m} + \left(\overline{\partial_t T}\,\overline{JF}^{-T}\hat{\nabla}\hat{v}_k, \widehat{L_k^0 z} - \hat{z}\right)_{\hat{Q}^m} \\
+ \left(\hat{\kappa}\overline{JF}^{-T}\hat{\nabla}\hat{v}_k, \overline{F}^{-T}\hat{\nabla}\left(\widehat{L_k^0 z} - \hat{z}\right)\right)_{\hat{Q}^m}.
\end{aligned}
$$

The first term vanishes by definition of the L^2-projection as $\bar{J}\partial_t \hat{v}_k$ is piecewise constant. By definition of the L^2-projection, we have for the convective term

$$
\begin{aligned}
\left(\overline{\partial_t T}\,\overline{JF}^{-T}\hat{\nabla}\hat{v}_k, \widehat{L_k^0 z} - \hat{z}\right)_{\hat{Q}^m} &= \left(\overline{\partial_t T}\,\overline{JF}^{-T}\hat{\nabla}\left(\hat{v}_k - \widehat{L_k^0 v_k}\right), \widehat{L_k^0 z} - \hat{z}\right)_{\hat{Q}^m} \\
&= -\left(\overline{\partial_t T}\,\overline{JF}^{-T}\hat{\nabla}\left(\hat{v}_k - \widehat{L_k^0 v_k}\right), \hat{z}\right)_{\hat{Q}^m}.
\end{aligned}
$$

We proceed with integration by parts

$$
\begin{aligned}
-\left(\overline{\partial_t T}\,\overline{JF}^{-T}\hat{\nabla}\left(\hat{v}_k - \widehat{L_k^0 v_k}\right), \hat{z}\right)_{\hat{Q}^m} &= \left(\hat{v}_k - \widehat{L_k^0 v_k}, \operatorname{div}\left(\overline{JF}^{-1}\overline{\partial_t T}\hat{z}\right)\right)_{\hat{Q}^m} \\
&\quad + \left(\hat{v}_k - \widehat{L_k^0 v_k}, [\hat{n}\cdot\overline{JF}^{-1}\overline{\partial_t T}\hat{z}]\right)_{\hat{G}^m}.
\end{aligned}
$$

The interface term vanishes due to Lemma 8.23. Using the estimate for the L^2-projection (Lemma 8.13) and Lemma 8.14, the remaining term is bounded by

$$
\left(\hat{v}_k - \widehat{L_k^0 v_k}, \operatorname{div}\left(\overline{JF}^{-1}\overline{\partial_t T}\hat{z}\right)\right)_{\hat{Q}^m} \le ck\,\|\partial_t \hat{v}_k\|_{\hat{Q}^m}\left\|\hat{\nabla}\hat{z}\right\|_{\hat{Q}^m} \le ck\left\|L_k^0 z - z_k\right\|_{Q^m}\left\|\hat{\nabla}\hat{z}\right\|_{\hat{Q}^m}.
$$

Finally, we use a similar argumentation for the diffusive term

$$
\begin{aligned}
&\left(\hat{\kappa}\overline{JF}^{-T}\hat{\nabla}\hat{v}_k, \overline{F}^{-T}\hat{\nabla}\left(\widehat{L_k^0 z} - \hat{z}\right)\right)_{\hat{Q}^m} = -\left(\hat{\kappa}\overline{JF}^{-T}\hat{\nabla}\left(\hat{v}_k - \widehat{L_k^0 v_k}\right), \overline{F}^{-T}\hat{\nabla}\hat{z}\right)_{\hat{Q}^m} \\
&\quad \le -\left(\hat{\kappa}JF^{-T}\hat{\nabla}\left(\hat{v}_k - \widehat{L_k^0 v_k}\right), F^{-T}\hat{\nabla}\hat{z}\right)_{\hat{Q}^m} + ck\left\|\hat{\nabla}\left(\hat{v}_k - \widehat{L_k^0 v_k}\right)\right\|_{\hat{Q}^m}\left\|\hat{\nabla}\hat{z}\right\|_{\hat{Q}^m}.
\end{aligned}
$$

We transform the first term to the current configuration and use integration by parts, the error estimate for the L^2-projection given in Lemma 8.13 and the primal stability estimates from Lemma 8.20 and Corollary 8.21. The second term is bounded by the stability of the L^2-projection and the same stability results. Altogether this yields

$$
\left(\hat{\kappa}\overline{JF}^{-T}\hat{\nabla}\hat{v}_k, \overline{F}^{-T}\hat{\nabla}\left(\widehat{L_k^0 z} - \hat{z}\right)\right)_{\hat{Q}^m} \le ck\left\|L_k^0 z - z_k\right\|_{Q^m}\left\|\hat{\nabla}\hat{z}\right\|_{\hat{Q}^m}
$$

After summation, the application of the dual regularity estimate (8.50) completes the proof. □

An interpolation estimate in the discrete bilinear form

In this section, we provide the last result that is required to prove Theorem 8.7.

Lemma 8.25. *Let $\eta_k = u - i_k u$ and $z_k \in X_k^0$ be the discrete dual solution of (8.51). For $f \in \mathscr{H}^{1,0} \cap \mathscr{H}^{0,2}$, $u^0 \in H^4(\Omega_1(0) \cup \Omega_2(0))$ and under Assumption 8.2, it holds that*

$$B_k(\eta_k, z_k) \leq ck^2 \left(\|f\|_{1,0} + \|f\|_{0,2} + \|u^0\|_{H^4(\Omega_1(0)\cup\Omega_2(0))} \right) I(e_k).$$

Proof. By definition, we have

$$B_k^m(\eta_k, z_k) = (\bar{J}\partial_t \hat{\eta}_k - \overline{\partial_t T}\,\overline{JF}^{-T}\hat{\nabla}\hat{\eta}_k, \hat{z}_k)_{\hat{Q}^m} + (\hat{\kappa}\overline{JF}^{-T}\hat{\nabla}\hat{\eta}_k, \overline{F}^{-T}\hat{\nabla}\hat{z}_k)_{\hat{Q}^m}. \tag{8.55}$$

The first term vanishes by the fundamental theorem of calculus

$$\left(\bar{J}\partial_t \hat{\eta}_k, \hat{z}_k\right)_{\hat{Q}^m} = \left(\bar{J}\hat{\eta}_k(t_m), \hat{z}_k\right)_{\hat{\Omega}^m} - \left(\bar{J}\hat{\eta}_k(t_{m-1}), \hat{z}_k\right)_{\hat{\Omega}^m} = 0.$$

For the convective term in (8.55), we use integration by parts. The interface term vanishes due the continuity of $\partial_t T$ (Assumption 8.2) and Lemma 8.23

$$\begin{aligned} -(\overline{\partial_t T}\,\overline{JF}^{-T}\hat{\nabla}\hat{\eta}_k, \hat{z}_k)_{\hat{Q}^m} &= \left(\hat{\eta}_k, \widehat{\operatorname{div}}\left(\overline{\partial_t T}\,\overline{JF}^{-1}\hat{z}_k\right)\right)_{\hat{Q}^m} + \left([\overline{JF}^{-T}\hat{n}], \hat{\eta}_k \overline{\partial_t T}\hat{z}_k\right)_{\hat{G}^m} \\ &\leq C\,\|\hat{\eta}_k\|_{\hat{Q}^m} \left\|\hat{\nabla}\hat{z}_k\right\|_{\hat{Q}^m}. \end{aligned}$$

After summation over $m = 1, \ldots, M$, the dual stability estimate (Lemma 8.22) and the interpolation estimate (Lemma 8.10) result in

$$-\sum_{m=1}^{M} (\overline{\partial_t T}\,\overline{JF}^{-T}\hat{\nabla}\hat{\eta}_k, \hat{z}_k)_{\hat{Q}^m} \leq Ck^2 \left(\|\partial_t^2 \hat{u}\|_{\hat{Q}_1 \cup \hat{Q}_2} \right) I(e_k).$$

It remains to estimate the diffusive term. We transform to the current configuration

$$\begin{aligned} (\hat{\kappa}\overline{JF}^{-T}\hat{\nabla}\hat{\eta}_k, \overline{F}^{-T}\hat{\nabla}\hat{z}_k)_{\hat{Q}^m} &\leq (\hat{\kappa}JF^{-T}\hat{\nabla}\hat{\eta}_k, F^{-T}\hat{\nabla}\hat{z}_k)_{\hat{Q}^m} + ck\left\|\hat{\nabla}\eta_k\right\|_{\hat{Q}^m}\left\|\hat{\nabla}\hat{z}_k\right\|_{\hat{Q}^m} \\ &\leq (\kappa\nabla\eta_k, \nabla z_k)_{Q^m} + ck^2\left\|\partial_t\hat{\nabla}\hat{u}\right\|_{\hat{Q}^m}\left\|\hat{\nabla}\hat{z}_k\right\|_{\hat{Q}^m}. \end{aligned}$$

For the first part, we add ±∇z

$$(\kappa\nabla\eta_k, \nabla z_k)_{Q^m} = (\kappa\nabla\eta_k, \nabla(z_k - z))_{Q^m} + (\kappa\nabla\eta_k, \nabla z)_{Q^m}. \tag{8.56}$$

Next, we will use integration by parts. As the jump $[n(\kappa\nabla z)]$ vanishes at the interface, we get for the second term

$$\begin{aligned} (\kappa\nabla\eta_k, \nabla z)_{Q^m} = -(\eta_k, \operatorname{div}(\kappa\nabla z))_{Q^m} &\leq \|\eta_k\|_{Q^m}\|\operatorname{div}(\kappa\nabla z)\|_{Q^m} \\ &\leq ck^2\|\partial_t^2 u\|_{Q^m}\|\operatorname{div}(\kappa\nabla z)\|_{Q^m}. \end{aligned}$$

The estimation of the first term in (8.56) is a bit more involved. After integration by parts, we get

$$(\kappa\nabla\eta_k, \nabla(z_k - z))_{Q^m} = -(\operatorname{div}(\kappa\nabla\eta_k), z_k - z))_{Q^m} + ([n(t)\cdot(\kappa\nabla i_k u)], z_k - z))_{G^m}. \tag{8.57}$$

For the divergence term in (8.57), we use the interpolation estimate (Lemma 8.10) for $v = \kappa\Delta u$ and the dual error estimate (Lemma 8.24)

$$\left(\operatorname{div}(\kappa\nabla\eta_k), z_k - z\right)_{Q^m} \leq \left\|\kappa\left(\Delta u - i_k\Delta u\right)\right\|_{Q^m} \|z_k - z\|_{Q^m} \leq ck^2 \|\partial_t(\kappa\Delta u)\|_{Q^m} I(e_k).$$

It remains to bound the interface term in (8.57). $[n(t)\cdot(\kappa\nabla i_k u)]$ does not vanish in general, as the interface moves and thus $n(t)$ changes with time. However, we can use $[n(t_i)\cdot(\kappa\nabla u(t_i))] = 0$ for $i = m-1, m$. We transform to the reference domain

$$\begin{aligned}
&\left([n(t)\cdot(\kappa\nabla i_k u)], z_k - z\right)_{G^m} \\
&\quad = \left(\left[\hat\kappa J F^{-T}(t)\hat n \cdot F^{-T}\hat\nabla \widehat{i_k u}\right], \hat z_k - \hat z\right)_{\hat G^m} \\
&\quad = \Big(\frac{t - t_{m-1}}{k}\left[(\hat\kappa\left(JF^{-T}(t) - JF^{-T}(t_m)\right)\hat n \cdot \left(F^{-T}\hat\nabla\hat u(t_m)\right)\right] \\
&\qquad + \frac{t_m - t}{k}\left[\hat\kappa\left(JF^{-T}(t) - JF^{-T}(t_{m-1})\right)\hat n \cdot \left(F^{-T}\hat\nabla\hat u(t_{m-1})\right)\right], \hat z_k - \hat z\Big)_{\hat G^m} \\
&\quad = \left(\left[\hat\kappa\left(JF^{-T}(t) - i_k(JF^{-T})\hat n\right)\cdot\left(F^{-T}\hat\nabla\hat u(t_m)\right)\right], \hat z_k - \hat z\right)_{\hat G^m} \\
&\qquad + \left((t_m - t)\left[\hat\kappa\left(JF^{-T}(t) - JF^{-T}(t_{m-1})\right)\hat n \cdot \left(F^{-T}\hat\nabla\partial_t\widehat{i_k u}\right)\right], \hat z_k - \hat z\right)_{\hat G^m} \\
&\quad =: \mathscr{I}_m^1 + \mathscr{I}_m^2.
\end{aligned} \tag{8.58}$$

Next, we apply the following trace inequality for a vector-valued function $f \in H^1(\Omega_1 \cup \Omega_2)^2$ and a scalar function $g \in H^1(\Omega_1 \cup \Omega_2)$

$$\begin{aligned}
(n\cdot f, g)_\Gamma &= (\operatorname{div} f, g)_{\Omega_1\cup\Omega_2} + (f, \nabla g)_{\Omega_1\cup\Omega_2} \\
&\leq \|\nabla f\|_{\Omega_1\cup\Omega_2}\|g\|_{\Omega_1\cup\Omega_2} + \|f\|_{\Omega_1\cup\Omega_2}\|\nabla g\|_{\Omega_1\cup\Omega_2}.
\end{aligned} \tag{8.59}$$

Applying (8.59) to the first part in (8.58) gives

$$\begin{aligned}
\mathscr{I}_m^1 \leq{}& \left\|\left(JF^{-1} - i_k(JF^{-1})\right)F^{-T}\hat\nabla\hat u(t_m)\right\|_{0,1} \|\hat z_k - \hat z\|_{\hat Q^m} \\
&+ \left\|\left(JF^{-1} - i_k(JF^{-1})\right)F^{-T}\hat\nabla\hat u(t_m)\right\|_{\hat Q^m} \left\|\hat\nabla(\hat z_k - \hat z)\right\|_{\hat Q^m}.
\end{aligned}$$

Making use of the interpolation estimates

$$\begin{aligned}
\left\|\hat\nabla\left(JF^{-1} - i_k(JF^{-1})\right)\right\|_{L^\infty(\hat\Omega^m)} &\leq ck\left\|\partial_t\hat\nabla(JF^{-1})\right\|_{L^\infty(\hat\Omega^m)} \\
\left\|\left(JF^{-1} - i_k(JF^{-1})\right)\right\|_{L^\infty(\hat\Omega^m)} &\leq ck^2\left\|\partial_t^2(JF^{-1})\right\|_{L^\infty(\hat\Omega^m)},
\end{aligned}$$

Lemma 8.14, the dual a priori estimate (Lemma 8.24), dual stability estimates and the Hölder inequality, we end up with

$$\sum_{m=1}^{m}\mathscr{I}_m^1 \leq ck^2\left(\sum_{m=1}^{M}\left\|\hat\kappa\hat\nabla^2\hat u(t_m)\right\|^2_{\hat Q_1^m\cup\hat Q_2^m}\right)^{1/2} I(e_k).$$

It remains to show the boundedness of the sum on the right-hand side. Therefore, we transform this term back to the current configuration Q_i^m ($i = 1,2$), use the fact that $\kappa\nabla^2 u(t_m)$ does not depend on time within one subdomain Q_i^m, $M = T/k$ and the continuous embedding $L^\infty(I) \subset H^1(I)$

$$\sum_{m=1}^{M} \left\| \hat\kappa \hat\nabla^2 \hat u(t_m) \right\|_{\hat Q_i^m}^2 \le cT \sup_{t\in I} \left(\left\| \kappa \nabla^2 u(t) \right\|_{\Omega_i(t)}^2 \right) \le cT \left\| \partial_t (\kappa \nabla^2 u) \right\|_{Q_i}^2 .$$

A similar argumentation gives for the second term in (8.58)

$$\begin{aligned} \mathscr{I}_m^2 \le{}& ck \sup_{t\in I_m} \left\| \left(JF^{-T} - (JF^{-T}(t_{m-1}) \right) \right\|_{L^\infty(\hat\Omega^m)} \left\| \partial_t \hat\nabla \widehat{i_k u} \right\|_{\hat Q^m} \left\| \hat\nabla (\hat z_k - \hat z) \right\|_{\hat Q^m} \\ &+ ck \sup_{t\in I_m} \left\| \hat\nabla \left(JF^{-T} - (JF^{-T}(t_{m-1}) \right) \right\|_{L^\infty(\hat\Omega^m)} \left\| \partial_t \hat\nabla^2 \widehat{i_k u} \right\|_{\hat Q^m} \| \hat z_k - \hat z \|_{\hat Q^m} \\ \le{}& ck^2 \left(\left\| \hat\nabla \left(\hat z_k - \hat z \right) \right\|_{\hat Q^m} \left\| \partial_t \hat\nabla \widehat{i_k u} \right\|_{\hat Q^m} + \| \hat z_k - \hat z \|_{\hat Q^m} \left\| \partial_t \hat\nabla^2 \widehat{i_k u} \right\|_{\hat Q^m} \right). \end{aligned}$$

Finally, we use the Hölder inequality, an inverse inequality in time, stability estimates for $i_k u$ and the primal stability estimate (8.2). Altogether, we have shown that

$$\sum_{m=1}^{M} \left([n(t) \cdot (\kappa \nabla i_k u)], z_k - z \right)_{G^m} \le ck^2 \left(\|f\|_{1,0} + \|f\|_{0,2} + \|u^0\|_{H^4(\Omega_1(0) \cup \Omega_2(0))} \right) I(e_k). \tag{8.60}$$

This completes the proof. □

8.5 Practical aspects

An important component of the numerical algorithm is the choice of a projection of the solution at the previous time step u_k^{m-1} from the old to the new reference domain. In this section, we will show that we do not need to calculate such a projection, as we can directly evaluate the integrals that include u_k^{m-1}. Therefore, we will derive a numerical integration scheme that integrates scalar products including functions from two different reference domains exactly. We will see in Section 8.6 that exact integration is crucial in order to obtain second-order accuracy.

For spatial discretisation, we will use the locally modified spatial discretisation scheme described in Section 6. In the context of time-stepping schemes, this spatial discretisation has the advantage that the underlying patch mesh is identical in each time step. The time discretisation scheme presented here is, however, not restricted to this spatial discretisation, other choices e.g. based on the extended finite element method (XFEM[111]), are possible.

In the time-stepping scheme (8.14), the old solution $\hat u_k^{m-1}$ appears as $\hat u_k^{m-1,+}$ on the new reference domain $\hat\Omega^m$. However, from the previous time step, $\hat u_k^{m-1}$ is given as a function on $\hat\Omega^{m-1}$. To evaluate the expressions in (8.14), we could apply a projection to the new reference domain. Using interpolation may lead to a reduced order of convergence (see Section 8.6). A residual-based projection that conserves the order of convergence is given in (8.16). Here, however, we will show that it is not necessary to calculate this projection explicitly. Instead, we can directly evaluate the integrals in (8.14).

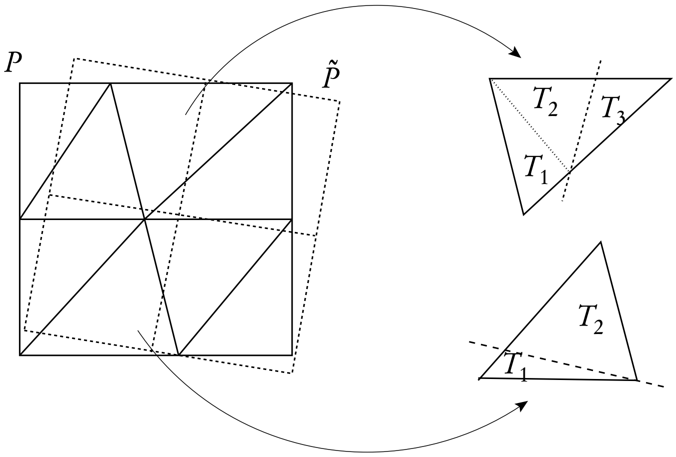

Figure 8.5. *Left*: Two overlapping elements $P \in \Omega_h^{m,c}$ and $\tilde{P} \in \tilde{\Omega}_h^{m-1,c}$. *Right*: A triangle can be cut by a line in two different ways: The cut goes through two edges or through an edge end a vertex. We add three or two triangles to the list $\mathscr{L}$, respectively.

By definition of the trial space X_k^1, we have the continuity relation (8.9)

$$\hat{u}_k^{m-1,+} = \hat{u}_k^{m-1} \circ T_m^{-1}(t_{m-1}),$$

i.e. continuity in the current configuration on $\Omega(t_{m-1})$. For the derivatives, we have

$$\hat{\nabla}_m \hat{u}_k^{m-1,+} = \left(F_{m-1}^{-T}(t_{m-1})\hat{\nabla}_{m-1}\hat{u}_k^{m-1}\right) \circ T_m^{-1}(t_{m-1}).$$

In our practical implementation we use these expressions to evaluate $\hat{u}^{m-1,+}$ on the old domain $\hat{\Omega}^{m-1}$. As an example, let us consider the evaluation of

$$\int_{\hat{\Omega}^m} \hat{u}_k^{m-1,+} \cdot \hat{\phi}_k^m \,\mathrm{d}\hat{x} = \int_{\hat{\Omega}^m} \left(\hat{u}_k^{m-1} \circ T_m^{-1}(t_{m-1})\right) \cdot \hat{\phi}_k^m \,\mathrm{d}\hat{x}. \tag{8.61}$$

While the first factor on the right-hand side is a smooth function on the cells of the moved grid $\tilde{\Omega}_h^{m-1} = T_m^{-1}(t_{m-1})(\Omega_h^{m-1})$, the second factor is smooth on Ω_h^m (see Figure 8.5 for an example of two overlapping patches $P \in \Omega_h^{m,c}$ and $\tilde{P} \in \tilde{\Omega}_h^{m-1,c}$). A high-order integration formula has to consider both the singularities of the integrands. For this purpose, we construct a cut grid consisting of triangles that contains the mesh lines of both grids. In two dimensions, this cut grid can be constructed by a rather simple algorithm.

Algorithm 8.1. *We initialise a list of triangles $\mathscr{L}$ that contains the elements of $\hat{\Omega}_h^m$ (quadrilaterals are split into two triangles). Then, we augment the list in the following way: For all mesh lines e_i in $\tilde{\Omega}_h^{m-1}$*

1. *Check which triangles in $\mathscr{L}$ are cut by e_i.*
2. *If a triangle is cut, eliminate the triangle from the list $\mathscr{L}$, split it into two or three subtriangles (see Figure 8.5) and add each of them to $\mathscr{L}$.*

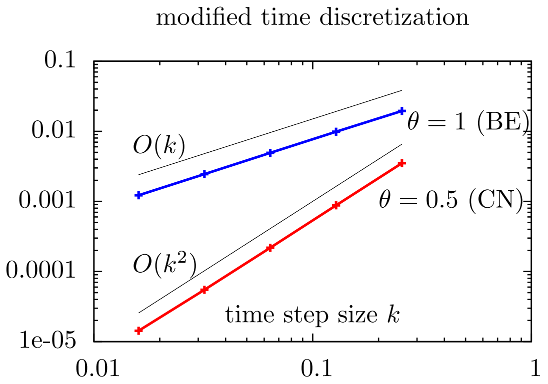

Figure 8.6. Errors of the modified dG(0) and cG(1) schemes for $k = h$ and a fixed outer boundary (interface movement prescribed by $y = T$).

Once the list $\mathscr{L}$ has been created, we use a standard Gauß quadrature rule on the triangles in $\mathscr{L}$.

Remark 8.26. *The movement $T_m^{-1}(t_{m-1})$ of grid cells is bounded by Assumption 8.2. In our practical implementation, we make the additional assumption that the interface does not jump over more than one patch within one time step. In the opposite case, we decrease the time step $k = t_m - t_{m-1}$. In this way, we only have to check if the triangles that are part of the same patch and the neighbouring patches are affected by e_i in 1.*

8.6 Numerical examples

8.6.1 Model example with analytical solution

We consider Problem (8.1) on a moving domain $\Omega(t) = \Omega_1(t) \cup \Omega_2(t) \cup \Gamma(t)$. The subdomains are defined by

$$\Omega_1(t) = [-1,1] \times [-1,t], \quad \Omega_2(t) = [-1,1] \times [t,1+t].$$

We use the diffusion coefficients $\kappa_1 = 1, \kappa_2 = 0.1$ and choose Dirichlet boundary data u^d and a right-hand side f such that the exact solution is given by

$$u(x,t) = \begin{cases} \sin(\frac{\kappa_2}{\kappa_1}(x_2 - t)), & x \in \Omega_1(t), \\ \sin(x_2 - t), & x \in \Omega_2(t). \end{cases}$$

In an interval $I_m = [t_{m-1}, t_m]$, we use the transformations

$$T_m(x,t) = \begin{cases} \left(x_1, x_2 - \frac{1+x_2}{1+t_m}(t_m - t)\right), & x \in \Omega_1(t), \\ \left(x_1, x_2 - t_m + t\right), & x \in \Omega_2(t) \end{cases}$$

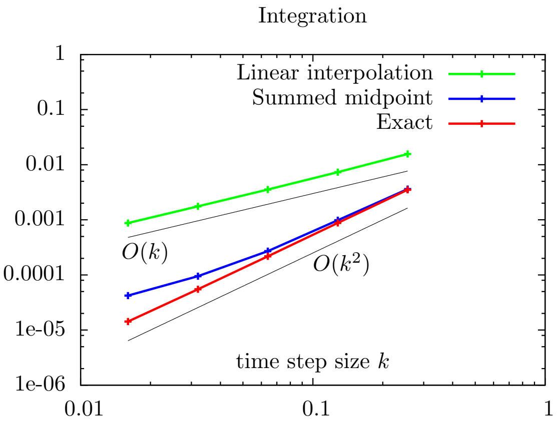

Figure 8.7. End time error for the modified cG(1) scheme applied to the model problem. We observe a reduced order of convergence when using non-exact integration formulas or projection schemes.

that fulfil the conditions of Assumption 8.2. In Figure 8.6, we plot the error at the end time $T = 0.512$ for the modified cG(1) scheme presented in this paper and a modified dG(0) scheme that is defined analogously using a dG(0) Galerkin ansatz in time. We decrease the spatial and temporal discretisation parameter simultaneously using $k = h$. As expected, we observe second-order convergence for the modified cG(1) scheme and first-order convergence for the modified dG(0) scheme.

Next, we study the effect of numerical integration and inexact projection schemes. First, we use a linear interpolation as projection from $\tilde{\Omega}_h^{m-1}$ to $\hat{\Omega}_h^m$ after every time step. The interpolation operator i_h^m is defined by the relation

$$i_h^m u_{kh}^{m-1,+}(\hat{x}_i) = \left(\hat{u}_{kh}^{m-1} \circ T_m^{-1}(t_{m-1})\right)(\hat{x}_i)$$

in each grid point $x_i \in \hat{\Omega}^m$. Secondly, we use a summed midpoint rule with 64 points per patch for the evaluation of integrals like (8.61) instead of the integration scheme presented in Section 8.5.

In Figure 8.7, we compare the errors for these two schemes to the exact integration rule described in Section 8.5. For the linear interpolation, we observe only linear convergence. As one would expect, the projection error dominates the total error. The midpoint rule behaves similarly to our quadrature formula for larger time steps k. For smaller time step size, however, we observe again a reduction in the order of convergence. For $k = h \approx 10^{-2}$ the convergence rate is close to linear convergence. Here, again, the quadrature error becomes the dominant part of the total error. Our integration scheme, on the other hand, does not affect the quadratic convergence behaviour of the time stepping method.

8.6.2 Rotating ellipsoid

As a second example, we consider a rotating ellipsoid $\Omega_{\text{ell}}(t)$ inside a fixed outer box $\Omega = [-1.2, 1.2]^2$. Initially, the ellipsoid has the Cartesian vectors as semi-principal axes with length

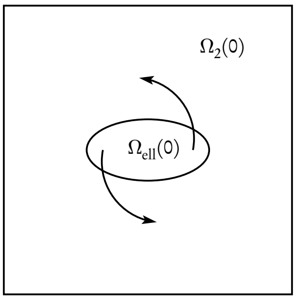

Figure 8.8. Subdomains of the second test configuration. The ellipsoid rotates counter-clockwise, while the outer domain Ω is fixed.

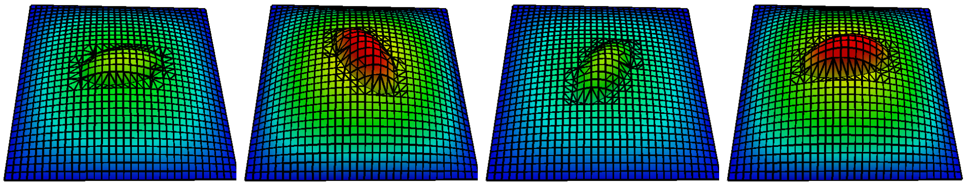

Figure 8.9. Snapshots at time $t \approx 0.5, t \approx 20, t \approx 40$ and $t = 63$. The ellipsoid rotates counter-clockwise.

0.25 in vertical and 0.5 in horizontal direction. We apply a counter-clockwise rotation of the ellipsoid driven by the prescribed velocity field $v^{\text{dom}} = 0.1(x_2, -x_1)^T$, see Figure 8.8. A standard approach to capture the interface would be to define a scalar level-set function Φ that moves with the interface

$$\partial_t \Phi + v^{\text{dom}} \cdot \nabla \Phi = 0 \quad \text{in } \Omega.$$

Here, however, we follow a slightly different approach to define suitable transformations T_m, inspired by fluid-structure interaction problems (Dunne & Rannacher[56]). We use the vector-valued Initial Point Set function $\Phi_{\text{IPS}}(t) : \Omega \to \mathbb{R}^2$ defined by the equation

$$\partial_t \Phi_{\text{IPS}} - v^{\text{dom}} \cdot \nabla \Phi_{\text{IPS}} = 0 \quad \text{in } \Omega$$

with initial value $\Phi_{\text{IPS}}(t = 0) = \text{id}$. This function traces back points $x \in \Omega_{\text{ell}}(t)$ to their original position in $\Omega_{\text{ell}}(0)$. Thus, we can define the inner subdomain $\Omega_{\text{ell}}(t)$ by the relation

$$x \in \Omega_{\text{ell}}(t) \quad :\Leftrightarrow \quad \Phi_{\text{IPS}}(x, t) \in \Omega_{\text{ell}}(0)$$

and the outer domain is given by $\Omega_2(t) = \Omega \setminus \Omega_{\text{ell}}(t)$. Note that we do not define any spatial boundary conditions for Φ_{IPS}, as this would lead to a degeneration of mesh cells before the ellipsoid completed a quarter of a full rotation. Using the Initial Point Set function Φ_{IPS}, a map that maps $\Omega_{\text{ell}}(t_m)$ to $\Omega_{\text{ell}}(t)$ and $\Gamma_i(t_m)$ to $\Gamma_i(t)$ for $t \in I_m$ is given by

$$\tilde{T}_m(t) = (\Phi_{\text{IPS}}(t))^{-1} \circ \Phi_{\text{IPS}}(t_m).$$

In our practical implementation, we determine the image $x^{m-1} = T_m(x^m) \in \Omega(t_{m-1})$ of a point $x^m \in \Omega(t_m)$ by solving

$$\Phi_{\text{IPS}}(t_{m-1})(x^{m-1}) = \Phi_{\text{IPS}}(t_m)(x^m)$$

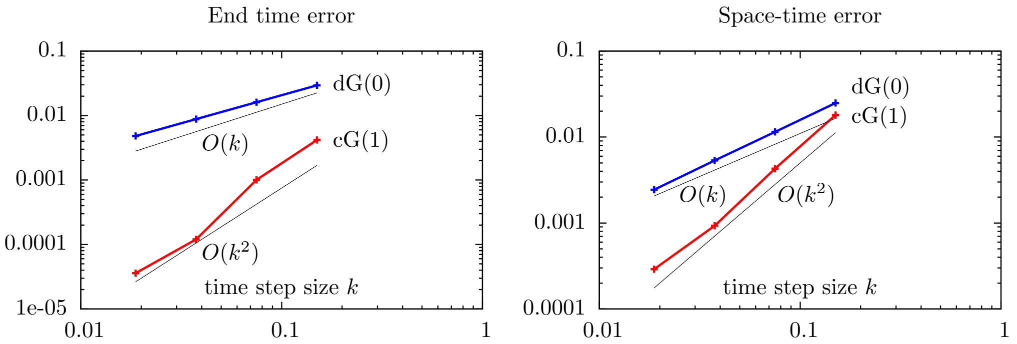

Figure 8.10. Functional errors for the ellipsoid problem in the end time L^2-norm and the L^2-norm over the space-time domain Q for $h = k \to 0$. As our theoretical results predict, we observe second-order convergence for the modified $cG(1)$ approach and first-order convergence for the modified $dG(0)$ approach.

	$\|\|u_k(T)\|\|_\Omega$		$\|\|u_k\|\|_Q$	
$k = h$	dG(0)	cG(1)	dG(0)	cG(1)
0.15	0.619	0.5858	2.121	2.1286
0.075	0.605	0.5890	2.134	2.1423
0.0375	0.598	0.5899	2.140	2.1456
0.01875	0.594	0.5900	2.143	2.1463
Extrap.	0.589	0.5901	2.146	2.1466
Conv.	0.87	2.01	1.11	2.08

Table 8.1. Functional values in the space-time L^2-norm and in the L^2-norm at time $T = 15$ for a modified $dG(0)$ and a modified $cG(1)$ time stepping scheme and $k = h$. Furthermore, we give an extrapolated functional value for $k = h \to 0$ and estimate the convergence orders. The convergence orders are in good agreement with the theoretical predictions.

with Newton's method and extend it linearly to the time interval I_m. To map the outer domain $\Omega_2(t_m)$ to $\Omega_2(t)$, we use an interpolation between the movement at the interface and the identity, id, at the outer boundary $\partial\Omega$

$$T_m(t) = g(x)\tilde{T}_m(t) + (1 - g(x))\,\mathrm{id},$$

where g denotes a smooth function with $g = 1$ in $\Omega_{\mathrm{ell}}(t_m) \cup \Gamma(t_m)$ and $g = 0$ on $\partial\Omega$.

As data, we choose $f = \sqrt{(1 + \cos(5t))}$ as well as homogeneous initial data $u^0 = 0$ and Dirichlet data $u^d = 0$. The diffusion coefficients are again given by $\kappa_1 = 1$ and $\kappa_2 = 0.1$. Some snapshots of the solution are given in Figure 8.9.

To study convergence, we compare the functional values for $||u_k(T)||_{\Omega(T)}$ and $||u_k||_Q$ for different time step sizes k, grid size $h = k$ and a modified cG(1) as well as a modified dG(0) scheme in Table 8.1. We calculate an extrapolated value e_0 as well as an estimated convergence order α by a least squares fit of the function $e(k) = e_0 + ck^\alpha$. For both functionals, we observe second-order convergence for the modified $cG(1)$ approach and first-order convergence for the $dG(0)$ variant. Finally, we plot the errors over the mesh and time step size $h = k$ in Figure 8.10 to illustrate the convergence behaviour.

9 Stabilisation of the wave equation on moving domains

We have discussed in Section 4.1 that the different character of fluid and solid equations give rise to a regularity problem for the velocities v. As the natural trial space for the solid velocity is $L^2(\Omega_s)$, a trace on the interface Γ_i needed for the *kinematic* interface condition (2.14) might not be well-defined. Furthermore, numerical tests show that the solid velocity is sensitive to stability problems caused by perturbations or discretisation errors, especially in the interface region (see also Section 9.1.3).

In this section, we will analyse the simplest form of a solid equation, a linear wave equation, and study different techniques to handle the aforementioned problems. In mixed variational formulation, the system of equations is given by: *Find* $u \in \mathcal{W}, v \in \mathcal{V}$ *such that*

$$\begin{aligned} (\partial_t v, \phi) + \lambda(\nabla u, \nabla \phi) &= 0 \quad \forall \phi \in \mathcal{W}, \\ (\partial_t u, \psi) - (v, \psi) &= 0 \quad \forall \psi \in \mathcal{V}, \end{aligned} \tag{9.1}$$

with a positive parameter $\lambda > 0$. It is well-known that the homogeneous wave equation is energy-conserving in the following sense (see e.g. Großmann & Roos[79])

$$\lambda \|\nabla u(t)\|_\Omega^2 + \|v(t)\|_\Omega^2 = \lambda \|\nabla u(0)\|_\Omega^2 + \|v(0)\|_\Omega^2. \tag{9.2}$$

Hence, any kind of perturbations will not be damped, but is in some sense "conserved" and may accumulate over time. Furthermore, (9.2) gives neither control over derivatives of v nor over the trace of v on the boundary of Ω. We will see that this may give rise to severe stability issues, already for this simple set of equations, when the domain Ω is moving.

We start by presenting a simple, but non-standard stabilisation technique in Section 9.1 for which we will show stability and error estimates, and provide numerical results. Next, in Section 9.2, we investigate if strong or weak damping of the solid equation as described in Section 4.1 is able to reduce the instabilities. Finally, in Section 9.3, we analyse the effect of *Streamline upwind Petrov Galerkin* (SUPG) stabilisation within this context.

9.1 A stabilised formulation for the solid equation

We define the discrete spaces

$$\mathcal{V}_h = \mathcal{Q}_1 \cap H^1(\Omega), \quad \mathcal{W}_h = \mathcal{Q}_1 \cap H_0^1(\Omega)$$

where $\mathcal{Q}_1$ denotes the space of piecewise bilinear finite element functions on a triangulation Ω_h. Furthermore, we define the discrete initial values by $u_h(0) = R_h u(0)$ and $v_h(0) = P_h v(0)$, where

$R_h : H_0^1(\Omega) \to \mathcal{W}_h$ denotes the Ritz projection operator and $P_h : L^2(\Omega) \to \mathcal{V}_h$ is the L^2-projection. For $k, l \geq 0$, we use again the Bochner spaces $H^k(I, H^l(\Omega))$ introduced in the previous section.

We consider the following stabilised formulation for the linear wave equation:
Find $u_h \in \mathcal{W}_h, v_h \in \mathcal{V}_h$ such that

$$\begin{aligned} (\partial_t v_h, \phi_h) + \lambda(\nabla u_h, \nabla \phi_h) &= 0 \quad \forall \phi_h \in \mathcal{W}_h, \\ (\partial_t u_h, \psi_h) - (v_h, \psi_h) - \alpha h^s (\nabla v_h, \nabla \psi_h) &= 0 \quad \forall \psi_h \in \mathcal{V}_h. \end{aligned} \tag{9.3}$$

As this stabilisation is non-standard, we will analyse it in this section in detail. Different choices for the exponent $s > 0$ will be discussed below. To motivate why this formulation might increase stability, we consider a standard time discretisation with the backward Euler method, multiply the second equation by -1 and write (9.3) in matrix form

$$\begin{pmatrix} \lambda A_h & \frac{1}{k} M_h \\ -\frac{1}{k} M_h & M_h + \alpha h^s A_h \end{pmatrix} \begin{pmatrix} u_h^{m+1} \\ v_h^{m+1} \end{pmatrix} = \begin{pmatrix} \frac{1}{k} v_h^m \\ -\frac{1}{k} u_h^m \end{pmatrix}.$$

Here, M_h is the discrete mass matrix and A_h the discrete Laplacian. We see that the stabilisation term increases the diagonal part of the matrix considerably, especially for $s \leq 2$.

9.1.1 Stability analysis

We have the following conservation property:

Lemma 9.1. *Let $(u_h, v_h) \in \mathcal{W}_h \times \mathcal{V}_h$ be the semi-discrete finite element solution of (9.3). For $t > 0$, energy is conserved in the following sense*

$$\begin{aligned} &\lambda \|\nabla u_h(t)\|_\Omega^2 + \|v_h(t)\|_\Omega^2 + \alpha h^s \|\nabla v_h(t)\|_\Omega^2 \\ &\qquad = \lambda \|\nabla u_h(0)\|_\Omega^2 + \|v_h(0)\|_\Omega^2 + \alpha h^s \|\nabla v_h(0)\|_\Omega^2. \end{aligned} \tag{9.4}$$

Proof. We test (9.3) with $\phi_h = \partial_t u_h$ and $\psi_h = -\partial_t v_h$. This yields

$$\lambda(\nabla u_h, \partial_t \nabla u_h) + (v_h, \partial_t v_h) + \alpha h^s (\nabla v_h, \partial_t \nabla v_h) = 0. \tag{9.5}$$

Next, we integrate in time over $I = [0, t]$ and use integration by parts. For the first term, we obtain

$$(\nabla u_h, \partial_t \nabla u_h)_{\Omega \times I} = -(\partial_t \nabla u_h, \nabla u_h)_{\Omega \times I} + \|\nabla u_h(t)\|_\Omega^2 - \|\nabla u_h(0)\|_\Omega^2$$

and thus

$$(\nabla u_h, \partial_t \nabla u_h)_{\Omega \times I} = \frac{1}{2} \left(\|\nabla u_h(t)\|_\Omega^2 - \|\nabla u_h(0)\|_\Omega^2 \right).$$

By applying the same argumentation to the remaining terms in (9.5), we obtain (9.4). □

Lemma 9.1 gives us control over the first derivative of the velocity and thus (by the trace lemma) for the trace of the velocity on $\partial\Omega$. The smaller the exponent s, the more control we get.

9.1.2 A priori error analysis

Next, we prove an error estimate for the solution of the stabilised formulation (9.3).

Lemma 9.2. *Let $(u,v)\in \mathcal{W}\times\mathcal{V}$ the solution of (9.1) and $(u_h,v_h)\in \mathcal{W}_h\times\mathcal{V}_h$ the semi-discrete finite element solution of the stabilised formulation (9.3). Furthermore, let $I=[0,T], Q=\Omega\times I$ and $u\in H^2(I,H^2(\Omega))$. For $s>0$ and $t\in I$, it holds that*

$$
\begin{aligned}
||u-u_h||_Q+||v-v_h||_Q+||(u-u_h)(t)||_\Omega+||(v-v_h)(t)||_\Omega& \\
\leq c(t)h^{min(2,s-1/2)}||u||_{H^2(I,H^2(\Omega))}& \\
||\nabla(u-u_h)||_Q+||\nabla(u-u_h)(t)||_\Omega \leq c(t)h^{min(1,s-1/2)}||u||_{H^2(I,H^2(\Omega))}&.
\end{aligned}
$$

Proof. We split the error into a projection error and a discrete part

$$
\begin{aligned}
u-u_h&=\eta_h^u+\xi_h^u=(u-R_hu)+(R_hu-u_h),\\
v-v_h&=\eta_h^v+\xi_h^v=(v-P_hv)+(P_hv-v_h).
\end{aligned}
$$

For the projection errors, we have the standard estimates ($l=0,1$)

$$
\begin{aligned}
||(u-R_hu)(t)||_{H^l(\Omega)}&\leq ch^{2-l}||u(t)||_{H^2(\Omega)}\leq ch^{2-l}||u||_{H^1(I,H^2(\Omega))},\\
||(v-P_hv)(t)||_{H^l(\Omega)}&\leq ch^{2-l}||v(t)||_{H^2(\Omega)}\leq ch^{2-l}||v||_{H^1(I,H^2(\Omega))}.
\end{aligned}
\tag{9.6}
$$

For the latter inequalities, we have used the one-dimensional Sobolev inequality in time. To estimate the discrete part, we set $I_t=[0,t], Q_t:=\Omega\times I_t$ and define the bilinear form

$$
A(w,\Phi)=(\partial_t v,\phi)_{Q_t}+\lambda(\nabla u,\nabla\phi)_{Q_t}+(\partial_t u,\psi)_{Q_t}-(v,\psi)_{Q_t},
$$

where $w=(u,v)$ and $\Phi=(\phi,\psi)$. We will use the Galerkin orthogonality

$$
A(w-w_h,\Phi_h)=-\alpha h^s(\nabla v_h,\nabla\psi_h)_{Q_t}\quad \forall\Phi_h=(\phi_h,\psi_h)\in(\mathcal{W}_h\times\mathcal{V}_h).
$$

This implies

$$
A(\xi_h^w,\Phi_h)=-A(\eta_h^w,\Phi_h)-\alpha h^s(\nabla v_h,\nabla\psi_h)_{Q_t}
\tag{9.7}
$$

where $\eta_h^w=(\eta_h^u,\eta_h^v)$ and $\xi_h^w=(\xi_h^u,\xi_h^v)$. Furthermore, for $\Phi_h=(\partial_t\xi_h^u,-\partial_t\xi_h^v)$, it holds that

$$
\begin{aligned}
-A(\xi_h^w,\Phi_h)&+\alpha h^s(\nabla\xi_h^v,\partial_t\nabla\xi_h^v)_{Q_t}\\
&=\lambda(\nabla\xi_h^u,\partial_t\nabla\xi_h^u)_{Q_t}+(\xi_h^v,\partial_t\xi_h^v)_{Q_t}+\alpha h^s(\nabla\xi_h^v,\partial_t\nabla\xi_h^v)_{Q_t}\\
&=\frac{1}{2}\left(\lambda||\nabla\xi_h^u(t)||_\Omega^2+||\xi_h^v(t)||_\Omega^2+\alpha h^s||\nabla\xi_h^v(t)||_\Omega^2\right).
\end{aligned}
$$

In the last step, we have used integration by parts and the fact that $\xi_h^u(0)=\xi_h^v(0)=0$ due to the definition of the initial values for u_h and v_h. Using the Galerkin orthogonality (9.7), it follows that

$$\begin{aligned}
\frac{1}{2}\Big(\lambda\|\nabla\xi_h^u(t)\|_\Omega^2 + \|\xi_h^v(t)\|_\Omega^2 + \alpha h^s\|\nabla\xi_h^v(t)\|_\Omega^2\Big)& \\
&= A(\eta_h^w,\Phi_h) + \alpha h^s(\nabla P_h v,\partial_t\nabla\xi_h^v)_{Q_t} \\
&= (\partial_t\eta_h^v,\partial_t\xi_h^u)_{Q_t} + \lambda(\nabla\eta_h^u,\partial_t\nabla\xi_h^u)_{Q_t} - (\partial_t\eta_h^u,\partial_t\xi_h^v)_{Q_t} \\
&\qquad + (\eta_h^v,\partial_t\xi_h^v)_{Q_t} + \alpha h^s(\nabla P_h v,\partial_t\nabla\xi_h^v)_{Q_t}.
\end{aligned} \tag{9.8}$$

The first, second and fourth term on the right-hand side vanish by definition of the L^2- and the Ritz projection, respectively. For the third term, we use integration by parts and the estimate (9.6)

$$\begin{aligned}
-(\partial_t\eta_h^u,\partial_t\xi_h^v)_{Q_t} &= (\partial_t^2\eta_h^u,\xi_h^v)_{Q_t} - (\partial_t\eta_h^u(t),\xi_h^v(t))_\Omega \\
&\le ch^2\left(\|\partial_t^2 u\|_{L^2(I_t,H^2(\Omega))}\|\xi_h^v\|_{Q_t} + \|\partial_t u(t)\|_{H^2(\Omega)}\|\xi_h^v(t)\|_\Omega\right).
\end{aligned}$$

To estimate the stabilisation term in (9.8), we add and subtract the continuous solution v

$$\alpha h^s(\nabla P_h v,\partial_t\nabla\xi_h^v)_{Q_t} = \alpha h^s\left((\nabla v,\partial_t\nabla\xi_h^v)_{Q_t} - (\nabla\eta_h^v,\partial_t\nabla\xi_h^v)_{Q_t}\right). \tag{9.9}$$

We use integration by parts for the first term, first in time, then in space

$$\begin{aligned}
\alpha h^s(\nabla v,\partial_t\nabla\xi_h^v)_{Q_t} = \alpha h^s\Big(&(\partial_t\Delta v,\xi_h^v)_{Q_t} - (\partial_t\partial_n v,\xi_h^v)_{\partial\Omega\times I_t} \\
&- (\Delta v(t),\xi_h^v(t))_\Omega + (\partial_n v(t),\xi_h^v(t))_{\partial\Omega}\Big).
\end{aligned} \tag{9.10}$$

For the discrete function ξ_h^v, we have the inverse inequality $\|\xi_h^v\|_{\partial\Omega} \le ch^{-1/2}\|\xi_h^v\|_\Omega$. Thus, application of the Cauchy-Schwarz and the trace inequality lead to

$$\alpha h^s(\nabla v,\partial_t\nabla\xi_h^v)_{Q_t} \le ch^{s-1/2}\left(\|\xi_h^v\|_{Q_t} + \|\xi_h^v(t)\|_\Omega\right)\left(\|\partial_t v\|_{L^2(I_t,H^2(\Omega))} + \|v(t)\|_{H^2(\Omega)}\right).$$

For the second term in (9.9), we use integration by parts in time, the projection error (9.6) and an inverse estimate in space

$$\alpha h^s(\nabla\eta_h^v,\partial_t\nabla\xi_h^v)_{Q_t} \le ch^s\left(\|\xi_h^v\|_{Q_t} + \|\xi_h^v(t)\|_\Omega\right)\left(\|\partial_t v\|_{L^2(I_t,H^2(\Omega))} + \|v(t)\|_{H^2(\Omega)}\right).$$

Altogether, we have shown that

$$\begin{aligned}
\frac{1}{2}\Big(\lambda\|\nabla\xi_h^u(t)\|_\Omega^2 + \|\xi_h^v(t)\|_\Omega^2 + \alpha h^s\|\nabla\xi_h^v(t)\|_\Omega^2\Big)& \\
\le Ch^{\min(s-1/2),1)}&\left(\|\partial_t^2 u\|_{L^2(I_t,H^2(\Omega))} + \|\partial_t u(t)\|_{H^2(\Omega)}\right)\left(\|\xi_h^v\|_{Q_t} + \|\xi_h^v(t)\|_\Omega\right).
\end{aligned}$$

Finally, we apply Young's inequality to the terms on the right-hand side. Integration in time over $t \in [0,T]$ in combination with the projection errors (9.6) yields the estimate for the norms on the space-time domain Q. For the estimates of $u - u_h$ in the L^2-norms, we use the Poincaré inequality applied to ξ_h^u. The estimates at time t follow with Gronwall's lemma (see e.g. Wloka[147]). □

	$\|\|u-u_h\|\|_{L^2}$				$\|\|\nabla(u-u_h)\|\|_{L^2}$			
#nodes	$s=1$	$s=1.5$	$s=2$	$s=\infty$	$s=1$	$s=1.5$	$s=2$	$s=\infty$
81	0.434	0.232	$9.32\cdot10^{-2}$	$3.12\cdot10^{-2}$	4.63	2.62	1.26	0.605
289	0.354	0.122	$2.99\cdot10^{-2}$	$8.13\cdot10^{-3}$	3.93	1.50	0.50	0.298
1089	0.227	0.050	$8.09\cdot10^{-3}$	$2.09\cdot10^{-3}$	2.45	0.66	0.20	0.148
Conv.	0.43	1.01	1.67	1.94	0.41	0.91	1.35	1.02
Lem. 9.2	0.50	1.00	1.50	2.00	0.50	1.00	1.00	1.00

	$\|\|v-v_h\|\|_{L^2}$				$\|\|v-v_h\|\|_{L^\infty}$			
#nodes	$s=1$	$s=1.5$	$s=2$	$s=\infty$	$s=1$	$s=1.5$	$s=2$	$s=\infty$
81	2.49	1.55	$9.37\cdot10^{-1}$	$2.88\cdot10^{-1}$	5.23	2.94	1.94	0.680
289	1.95	0.91	$3.81\cdot10^{-1}$	$7.52\cdot10^{-2}$	4.19	2.08	1.19	0.201
1089	1.35	0.48	$1.93\cdot10^{-2}$	$1.93\cdot10^{-2}$	2.94	1.59	0.62	0.053
Conv.	0.42	0.81	1.34	1.94	0.40	0.45	0.78	1.78
Lem. 9.2	0.50	1.00	1.50	2.00	-	-	-	-

Table 9.1. Computed error in different norms and on different mesh levels for the wave equation on a fixed domain. Furthermore, we estimated the convergence order by a least squares fit of the function $e(h)=ch^\alpha$ and show the convergence predicted by Lemma 9.2 for comparison.

Remark 9.3. *The upper bound $s-1/2$ for the convergence order stems from the stabilisation term, more precisely from the trace terms appearing in (9.10) after integration by parts. The bound could be improved to s if we would add the additional term $(\partial_n v_h, \psi_h)_{\partial\Omega\times I}$ to the discrete system of equations (9.3). With this, however, the stability estimate in Lemma 9.1 would not be valid anymore and the stabilisation would lack the desired effect.*

Remark 9.4. *The error estimates hold true in the case $s=\infty$ which corresponds to the non-stabilised system of equations.*

Lemma 9.2 suggests the choice of $s=3/2$ for optimal convergence in the H^1-norm and $s=5/2$ for optimal convergence in the L^2-norms. Nevertheless, in view of Lemma 9.1, a smaller choice of s might be necessary to guarantee the stabilising effect of the approach. To investigate the effect of different choices, we will provide some numerical results next.

9.1.3 Numerical results

Example 1: Numerical example on a fixed domain with an analytical solution

As a first simple example, we study a problem on a fixed domain $\Omega=(0,1)^2$ with $\lambda=0.5$. We choose the data in such a way that the analytical solution is given by

$$u(x,y,t)=\sin(2\pi x)\sin(2\pi y)\sin(2\pi t),$$
$$v(x,y,t)=2\pi\sin(2\pi x)\sin(2\pi y)\cos(2\pi t).$$

To study the spatial discretisation error, we choose the very small time step size $k=10^{-4}$. We show the discretisation errors at the end time $T=0.1$ in Table 9.1 for $s=1$, $s=1.5$ and $s=2$ as well as without stabilisation ($s=\infty$). The stabilisation parameter has been chosen $\alpha=0.5$.

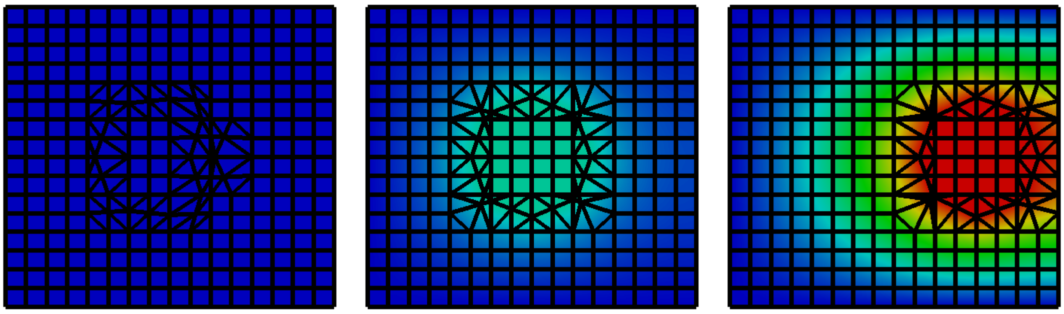

Figure 9.1. Moving circle at start time $t = 0$, at $t = 0.8$ and at the end time $t = 1.6$. The colour illustrates the horizontal velocity of the solution and its harmonic extension to the exterior domain.

The numerically computed convergence orders are in reasonable agreement with the convergence estimates shown in Lemma 9.2. Here, stabilisation does not yield any improvement. The non-stabilised discretisation yields the best convergence orders. Even the L^∞-norm error for the velocity, which is not covered by Lemma 9.2, converges faster without stabilisation and shows nearly second-order convergence. In the following section, we will provide a second example where stabilisation will be necessary.

Example 2: Numerical example on a moving domain

We consider an example on a moving domain where no analytical solution is available. As initial domain, we use a circle of radius 0.4: $\Omega(t=0) = B_{0.4}(0)$. We apply a spatially constant force $g = \min\{0.1t, 0.1\}$ as Neumann condition $\partial_n u = g$ on its boundary and set $\lambda = 10$.

As for fluid-structure interactions, we prescribe the movement of the domain by the solid deformation itself. To be precise, the domain $\Omega(t)$ at time $t > 0$ is defined by the map

$$\Omega(t) = T(\Omega(0), t), \quad T(x,t) = \begin{pmatrix} x_1 + u(x,t) \\ x_2 \end{pmatrix}.$$

Due to the applied force, the circle moves towards the right-hand side.

For spatial discretisation, we use the *locally modified finite element scheme*, see Section 6. We discretise a domain $\Omega_b = [-1, 1.2] \times [-1, 1]$ that contains the moving domain $\Omega(t)$ for all times $t \in [0, 1.6]$. For convenience, we extend deformation and velocity by a harmonic extension to the domain $\Omega_b \setminus \Omega(t)$. An illustration of the movement of the circle as well as the spatial discretisation is given in Figure 9.1. In order to capture the interface, we use the *Initial Point Set function* (see (3.1)).

For the temporal discretisation, we considered both a standard backward Euler scheme as well as a locally modified $dG(0)$ time discretisation as defined in Section 8 with a small time step size $k = 10^{-2}$. The results we obtained differed only marginally for the two approaches. Thus, we will only present results based on the standard implicit Euler scheme here.

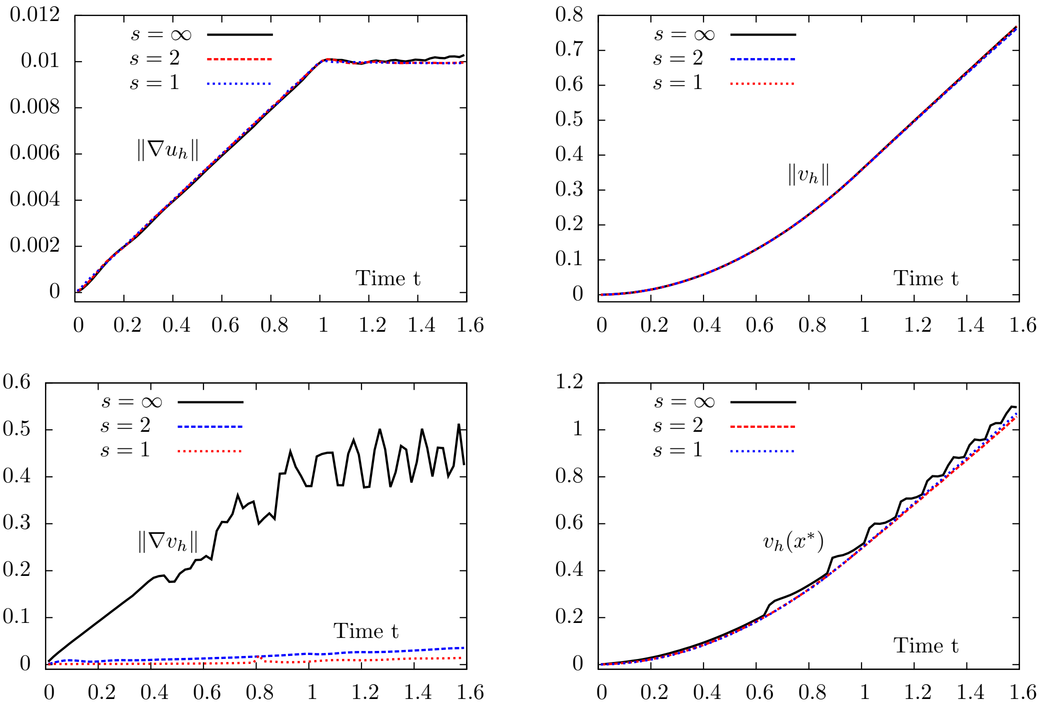

Figure 9.2. Functionals over time for the wave equation on a moving domain. We observe strong oscillations for the solution of the non-stabilised system of equations.

In Figure 9.2, we plot the values of the three norms estimated in Lemma 9.2 as well as the point value $v_h(x^*)$ at the (moving) point x^* on the very right of the circle over time. We observe very strong oscillations for the solution of the non-stabilised system of equations in the H^1-norm of the velocity, and also considerable oscillations for the point functional $v_h(x^*)$. The instabilities for the point functional occur every time the point (and thus the interface) jumps over a patch edge. On the other hand, it was sufficient to use the stabilisation with $s = 2$ to dampen (almost) all visible oscillations. The solutions of the stabilised system for $s = 1$ and $s = 2$ show very good agreement in all functionals. For the L^2-norm of the velocity (and also of the deformation), the values for the solutions with and without stabilisation are almost identical.

In Table 9.2, we show functional values of the L^2-norm of v_h as well as the point value $v_h(x^*)$ at time $t = 1$. The L^2-norm of v_h (as well as the L^2- and H^1-norm of u that are not shown here) converge well with and without stabilisation terms. The convergence orders for the stabilised version are slightly reduced in comparison to the non-stabilised version.

On the other hand, we observe a big difference when looking at the point value $v_h(x^*)$. Here, the non-stabilised approach converges very slowly due to the oscillations observed in Figure 9.2. With stabilisation, the values converge with approximately second order. These results indicate that in the context of fluid-structure interaction problems, where the fluid dynamics might be significantly driven by the velocity at the interface, we may expect severe stability issues if the solid equations are not stabilised.

	$\|\|v_h\|\|_{L^2}$			$\|v_h(x^*)\|$		
#nodes	$s=1$	$s=2$	$s=\infty$	$s=1$	$s=2$	$s=\infty$
289	$3.66\cdot 10^{-1}$	$3.65\cdot 10^{-1}$	$3.65\cdot 10^{-1}$	$5.25\cdot 10^{-1}$	$5.23\cdot 10^{-1}$	$5.22\cdot 10^{-1}$
1089	$3.60\cdot 10^{-1}$	$3.59\cdot 10^{-1}$	$3.59\cdot 10^{-1}$	$5.02\cdot 10^{-1}$	$4.99\cdot 10^{-1}$	$5.15\cdot 10^{-1}$
4225	$3.58\cdot 10^{-1}$	$3.57\cdot 10^{-1}$	$3.58\cdot 10^{-1}$	$4.96\cdot 10^{-1}$	$4.94\cdot 10^{-1}$	$5.10\cdot 10^{-1}$
Extr.	$3.57\cdot 10^{-1}$	$3.57\cdot 10^{-1}$	$3.58\cdot 10^{-1}$	$4.93\cdot 10^{-1}$	$4.93\cdot 10^{-1}$	$4.98\cdot 10^{-1}$
Conv.	1.96	1.69	2.29	2.43	1.79	0.48

Table 9.2. Functional values of the L^2-norm of v_h and the point value $|v_h(x^*)|$ at time $t=1$. Furthermore, we give an extrapolated value and estimated convergence rates. For the non-stabilised discretisation ($s=\infty$), the point functional converges very slowly.

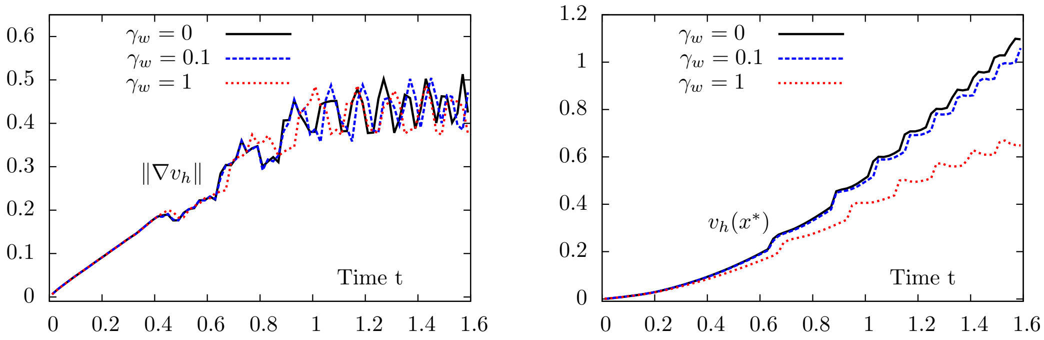

Figure 9.3. Functionals over time for the wave equation on a moving domain with weak damping for $\gamma_w = 0.1$ and $\gamma_w = 1$. In this test, weak damping does not help to reduce the non-physical oscillations.

9.2 Damping of the solid equation

As mentioned in Section 4.1, a second possibility to ensure the well-posedness of the trace of the solid velocity is to add damping terms. For the case of the linear wave equation, weak and strong damping are defined in the following way

$$\begin{aligned}(\partial_t v,\phi)+\lambda(\nabla u,\nabla\phi)+\gamma_s(\nabla v,\nabla\phi)+\gamma_w(v,\phi)=0 \quad \forall \phi\in\mathcal{W},\\ (\partial_t u,\psi)-(v,\psi)=0 \quad \forall\psi\in\mathcal{V}.\end{aligned} \tag{9.11}$$

with damping parameters $\gamma_s,\gamma_w\geq 0$. To study the effect of damping, we consider again the numerical example on a moving domain studied in the previous section. In Figure 9.3, we analyse the effect of weak damping. Therefore, we plot the H^1-norm of the velocity as well as the point value $v(x^*)$ for $\gamma_w = 1$ and $\gamma_w = 0.1$ over time and compare them to the solution of the non-damped (and non-stabilised) system of equations. We observe that the oscillations could not be reduced in both functionals. Furthermore, for $\gamma_w = 1$, the solution differs already significantly from the solution without damping.

Next, we analyse the effect of strong damping in Figure 9.4. For $\gamma_s = 0.1$, the oscillations in the point functional $v_h(x^*)$ are significantly reduced. In the H^1-seminorm of the velocity, however,

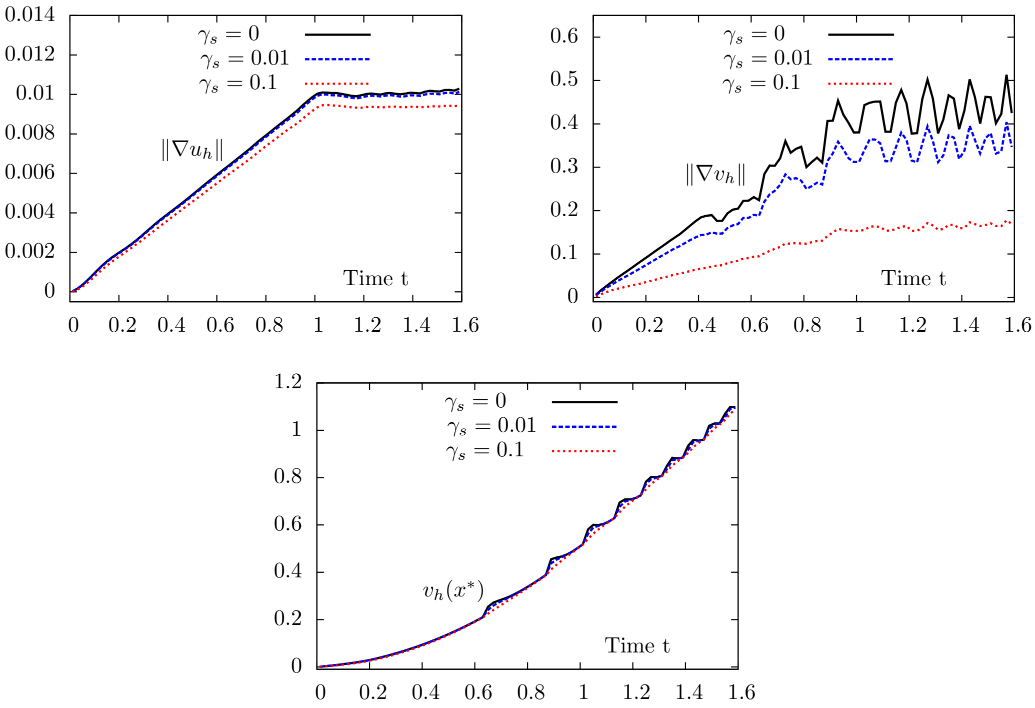

Figure 9.4. H^1-norm of the deformation and velocity and point value of the velocity over time for the wave equation on a moving domain with strong damping for $\gamma_s = 0.01$ and $\gamma_s = 0.1$. Strong damping is capable to reduce the oscillations, but has a considerable influence on ∇u_h.

they are still clearly visible. On the other hand, the H^1-seminorm of the deformation differs already significantly from the one of the non-damped solution. We know from the previous section that these values are a good approximation to the one of the continuous solution (see Figure 9.2). Thus, we conclude, that the additional error due to damping is much larger than the one due to the stabilisation technique analysed in the previous section.

To conclude, we found that only strong damping was able to reduce the oscillations in the test example. To obtain a smooth behaviour of the point functional $v(x^*)$, however, a relatively strong damping was necessary that had considerable influence on the solution. The solutions of the stabilised system shown in the previous section deviated much less from each other and converged faster towards the continuous solution. We remark, however, that damping has physical relevance in some applications where an idealised material model as the wave equation or the Saint Venant-Kirchhoff equations are only a very rough approximation of the reality.

9.3 Streamline upwind Petrov-Galerkin stabilisation

When solid equations are formulated in Eulerian coordinates, a convective term is usually present. The second equation

$$\partial_t u - v \cdot \nabla u - v = 0,$$

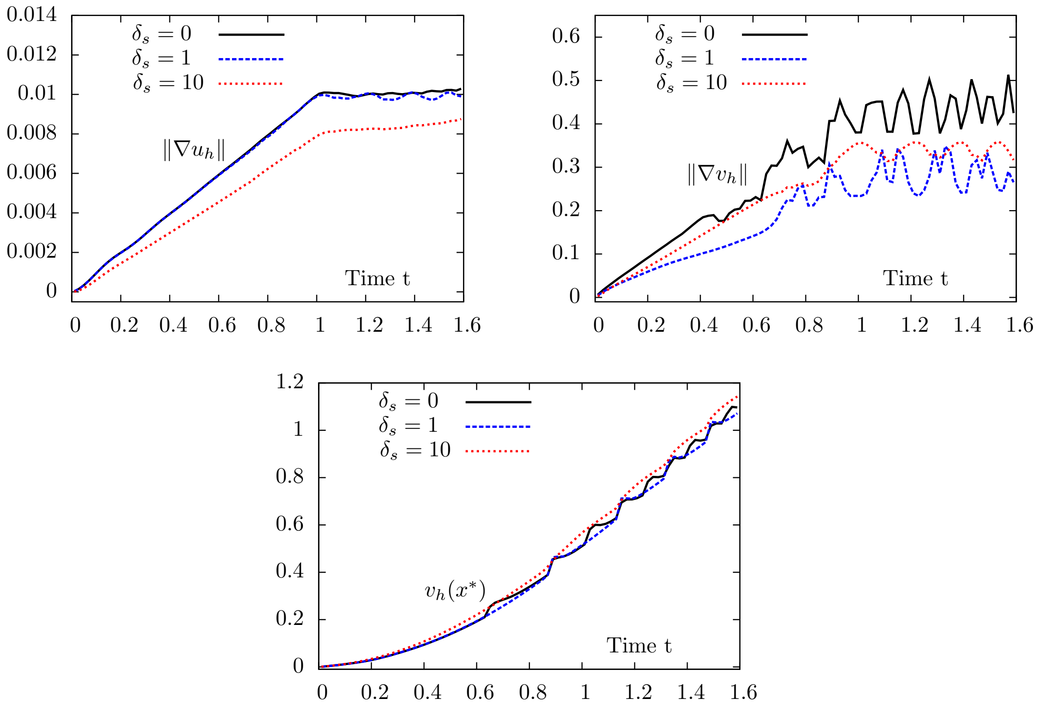

Figure 9.5. H^1-norm of the deformation and velocity and point value of the velocity $v_h(x^*)$ over time for the wave equation on a moving domain with SUPG stabilisation for $\delta_s = 1$ and $\delta_s = 10$. Choosing the large parameter $\delta_s = 10$, the oscillations are reduced, but we observe a strong influence on the H^1-norm of the deformation.

is convection-dominated, as no diffusive appears. It is well-known that standard finite element discretisation schemes have to be stabilised to solve convection-dominated equations. One popular choice is the *Streamline upwind Petrov Galerkin* stabilisation (SUPG, Brooks & Hughes[31]). Here, stabilisation in streamline direction is added to the variational equation

$$S_h^{\text{SUPG}}(u,\phi) := \gamma_{\text{SUPG}}(h)(v\cdot\nabla u, v\cdot\nabla\phi).$$

In this section, we want to analyse if this stabilisation is able to reduce the instabilities we observed in the previous sections. As their is no convection present in the system of equations (9.1), we even add the larger stabilisation term

$$S_h^{\text{SUPG}}(u,\phi) := \gamma_{\text{SUPG}}(h)(\nabla u, \nabla\phi)$$

that stabilises in all directions. The h-dependence of the stabilisation is typically chosen as

$$\gamma_{\text{SUPG}}(h) = \delta_s h^2.$$

The discrete system of equations reads: *Find $v_h \in \mathcal{V}_h$, $u_h \in \mathcal{W}_h$ such that*

$$\begin{aligned} (\partial_t v_h, \phi_h) + \lambda(\nabla u_h, \nabla\phi_h) + S_h^{\text{SUPG}}(v_h,\phi_h) &= 0 \quad \forall \phi_h \in \mathcal{W}_h, \\ (\partial_t u_h, \psi_h) - (v_h, \psi_h) + S_h^{\text{SUPG}}(u_h,\psi_h) &= 0 \quad \forall \psi_h \in \mathcal{V}_h. \end{aligned} \tag{9.12}$$

To compare with the stabilisation introduced in Section 9.1, we write the discrete system of equations again in matrix-vector form

$$\begin{pmatrix} \lambda A_h & \frac{1}{k}M_h + \delta_s h_P^2 A_h \\ -\frac{1}{k}M_h - \delta_s h_P^2 A_h & M_h \end{pmatrix} \begin{pmatrix} u_h^{m+1} \\ v_h^{m+1} \end{pmatrix} = \begin{pmatrix} \frac{1}{k} v_h^m \\ -\frac{1}{k} u_h^m \end{pmatrix}.$$

We observe that, in contrast to the stabilisation technique introduced in Section 9.1, the SUPG method does not increase the diagonal part of the matrix.

Numerical result

We study again Example 2 from Section 9.1 on a moving domain. The course of the three output functionals studied in the previous section are shown in Figure 9.5 for $\delta_s = 1$ and $\delta_s = 10$. For $\delta_s = 1$, we observe almost no reduction of the non-physical oscillations in both the H^1-norm of the velocity and the point value $v_h(x^*)$. For the larger parameter $\delta_s = 10$, the oscillations are reduced, but still clearly visible. On the other hand, we observe already a very strong influence on the H^1-norm of the deformation which is significantly damped and far away from the real solution (compare Figure 9.2).

We conclude that neither the damping strategies analysed in the previous section nor the SUPG stabilisation were able to reduce the non-physical oscillations without a significant loss of accuracy. Hence, we will use the stabilisation introduced in Section 9.1 in the applications presented in the next chapter. In the case of convection-dominated structure problems, we propose a combination of this stabilisation technique with the SUPG stabilisation.

10 Discretisation of fluid-structure interaction problems

In this section, we describe how to combine the discretisation schemes derived in the previous sections for fluid-structure interaction problems in Eulerian coordinates. To combine spatial and temporal discretisation, we use the Rothe method, i.e. first, we apply a time discretisation scheme to the continuous system of equations and then we discretise the time-discrete system in space by using the *locally modified finite element scheme*. Before we describe these two steps in Section 10.2 and Section 10.3 in detail, we make some practical considerations regarding the *Initial Point Set function* which is used to determine the domain affiliation of a point $x \in \Omega(t)$.

10.1 Initial point set function: Practical aspects

The initial point set function is defined by (cf. Section 3.1)

$$\Phi_{\mathrm{IPS}}(x,t) := \begin{cases} x - u_s(x,t) & x \in \Omega_s(t), \\ x - \mathrm{ext}(u_s)(x,t) & x \in \Omega_f(t). \end{cases}$$

It remains to define a suitable extension of the solid deformation u_s to the fluid domain $\Omega_f(t)$. The only condition that this extension has to fulfil is that the points in the fluid domain are not mapped to the initial solid domain. In contrast to the ALE method, there is no regularity requirement as the extension does not enter the fluid equations. It is not even necessary that $\Phi_{\mathrm{IPS}}(x,t)$ maps to $\Omega(0)$.

As mentioned in Section 3.1, Richter[121] proposed to use an extension by only one layer of cells around the previous solid domain $\Omega_s(t_{n-1})$ at $t = t_n$. The underlying assumption is that the interface does not jump over more than one cell within one time step (which is a reasonable assumption as typically small time steps are needed anyway for stability reasons).

For ease of implementation, however, we take a different approach here and define an extension $u_f = \mathrm{ext}(u_s)$ in all of $\Omega_f(t)$. We use a harmonic extension

$$\begin{aligned} -\alpha \Delta u_f &= 0 \quad \text{in } \Omega_f(t), \\ u_f &= u_s \quad \text{on } \Gamma_i(t), \\ \alpha \partial_n u_f &= 0 \quad \text{on } \partial\Omega_f(t). \end{aligned}$$

In order to avoid steep gradients in the interface region, we choose α sufficiently large there, e.g.

$$\alpha(x) = \frac{\alpha_0}{\mathrm{dist}_{\Gamma_i}(x) + \varepsilon},$$

where dist_{Γ_i} measures the shortest distance to the interface and $\varepsilon > 0$ is a small constant. If α is sufficiently large, this avoids that points in $\Omega_f(t)$ are mapped to $\Omega_s(0)$.

As $u_f = u_s$ on Γ_i, we can define a global deformation u and use a global trial space

$$\mathcal{W} = H_0^1(\Omega(t); \Gamma_s(t)).$$

It is, however, not recommendable to use a continuous global test space for the equations

$$(\partial_t u + v \cdot \nabla u - v, \psi)_{\Omega_s(t)} + (\alpha \nabla u, \nabla \psi)_{\Omega_f(t)} = 0 \quad \forall \psi \in \mathcal{W}, \tag{10.1}$$

as this formulation would include the interface condition

$$\alpha \partial_n u_f = 0 \quad \text{on } \Gamma_i \tag{10.2}$$

which can be seen after integration by parts. In combination with the continuity of traces $u_f = u_s$ (hidden in the global trial space $\mathcal{W}$), this leads to a non-physical feedback from the fluid extension to the solid deformation. Therefore, we define separate test functions $\psi_f \in \mathcal{W}_f = H_0^1(\Omega_f(t); \Gamma_i(t))$ and $\psi_s \in \mathcal{W}_s = H_0^1(\Omega_s(t); \Gamma_s^d)$ and solve

$$(\partial_t u + v \cdot \nabla u - v, \psi_s)_{\Omega_s(t)} + (\alpha \nabla u, \nabla \psi_f)_{\Omega_f(t)} = 0 \quad \forall \psi_s \in \mathcal{W}_s, \psi_f \in \mathcal{W}_f. \tag{10.3}$$

With this definition the trace of a function $\psi_f \in \mathcal{W}_f$ vanishes at the interface. Now the equation for the fluid deformation u_f is the solution of the Poisson problem with the Dirichlet boundary condition $u_f = u_s$ at the interface. Therefore, (10.2) does not hold anymore and a feedback from the fluid extension to the solid deformation is avoided.

With these definitions, we can now define a global space $\tilde{\mathcal{W}}$ by extending the functions by zero in the respective other subdomain and combining both spaces $\tilde{\mathcal{W}} := \mathcal{W}_f \oplus \mathcal{W}_s$. Note that the elements of $\tilde{\mathcal{W}}$ can be discontinuous across the interface. We will use such a space in the discrete setting in Section 10.3.

Finally, we remark that in the applications we will present in Chapter III, we use the deformation u^{m-1} at the previous time step to determine the interface location as well as the domain affiliation in an explicit way. This is reasonable as typical small time steps are required anyway. In principle, one could use the new deformation u^m as well. This, however, would mean that the interface position and the domain affiliation change in each Newton step.

10.2 Time discretisation

For time discretisation, we use the modified time-stepping scheme presented in Section 8. In this section, we will give practical details of how to compute a suitable mapping $T_m : \Omega_m \times I_m \to Q^m$ for a time interval $m = 1, \ldots, M$.

As mentioned above, here, we use the old deformation u^{m-1} to define the subdomains Ω_f^m and Ω_s^m and the interface Γ_i^m explicitly. Then, we use the new domain Ω^m as reference domain for the time interval $I_m = [t_{m-1}, t_m]$ and define a map $T_m : \Omega_m \times I_m \to Q^m$ which is linear in time. Due to $T_m(x, t_m) = x$, we set

$$T_m(x,t) = \frac{t_m - t}{t_m - t_{m-1}} T_m(x, t_{m-1}) + \frac{t - t_{m-1}}{t_m - t_{m-1}} x.$$

It remains to specify the mapping T_m at time t_{m-1} in such a way that points x lying on the interface $\Gamma_i(t_m)$ at time t_m are mapped to points on the interface $\Gamma_i(t_{m-1})$ at time t_{m-1}. We have already seen in Section 8.6.2 that this requirement is fulfilled by the function

$$\tilde{T}_m(t_{m-1}) = (\Phi_{\mathrm{IPS}}(t_{m-1}))^{-1} \circ \Phi_{\mathrm{IPS}}(t_m)$$

where $\phi_{\mathrm{IPS}}(t_i)$ denotes the *Initial point set* function at time t_i. In practice, we calculate $x^{m-1} := \tilde{T}_m(x^m, t_{m-1})$ in a point $x^m \in \Omega^m$ by applying Newton's method to

$$\Phi_{\mathrm{IPS}}(t_{m-1})(x^{m-1}) = \Phi_{\mathrm{IPS}}(t_m)(x^m),$$

i.e.

$$x^{m-1} - u^{m-2}(x^{m-1}) = x^m - u^{m-1}(x^m). \tag{10.4}$$

It is sufficient to use this mapping $\tilde{T}_m$ in the interface region. Far away from the interface, we define the mapping T_m as the identity. In between, we use a smooth transition by using a function g depending on the distance to the interface with $g = 1$ in a point $x \in \Omega^{m-1}$ with $\mathrm{dist}_{\Gamma_i(t_{m-1})}(x) < \varepsilon$ and $g = 0$ if $\mathrm{dist}_{\Gamma_i(t_{m-1})}(x) > \delta$ for $\delta > \varepsilon > 0$. We set

$$T_m(t,x) = g(x)\tilde{T}_m(t,x) + (1 - g(x))\,\mathrm{id}.$$

The modified $cG(1)$ time-stepping scheme introduced in Section 8 and the analogously defined $dG(0)$ variant can be generalised to the following θ-scheme:

$$\begin{aligned}
(\bar{J}_\theta \rho(v^m - v^{m-1}, \phi)_{\Omega^m} + k\theta(\rho\nabla v^m \overline{JF}_\theta^{-1}(v^m - \overline{\partial_t T}_\theta), \phi)_{\Omega^m}& \\
+k(1-\theta)(\rho\nabla v^{m-1}\overline{JF}_\theta^{-1}(v^{m-1} - \overline{\partial_t T}_\theta), \phi)_{\Omega^m}& \\
+k(\theta\sigma_\theta^m + (1-\theta)\sigma_\theta^{m-1}, \nabla\phi\overline{JF}_\theta^{-1})_{\Omega^m}& \\
-k(\rho_f\nu_f\overline{JF}_\theta^{-T}(\theta\nabla^T v_f^m + (1-\theta)\nabla^T v_f^{m-1})\overline{F}_\theta^{-T} n, \phi)_{\Gamma_f\setminus\Gamma_f^d}& \\
= k(\bar{J}_\theta(\theta f^m + (1-\theta)f^{m-1}), \phi)_{\Omega^m}& \quad \forall \phi \in \mathcal{V}^m, \\
(\bar{J}_\theta(u^m - u^{m-1}) - kv^m, \psi_s)_{\Omega_s^m} + k\theta(\nabla u^m \overline{JF}_\theta^{-1}(v^m - \overline{\partial_t T}_\theta), \psi_s)_{\Omega_s^m}& \\
+k(1-\theta)(\nabla u^{m-1}\overline{JF}_\theta^{-1}(v^{m-1} - \overline{\partial_t T}_\theta), \psi_s)_{\Omega_s^m} = 0& \quad \forall \psi_s \in \mathcal{W}_s^m, \\
(\alpha\nabla u^m, \nabla\psi_f)_{\Omega_f^m} = 0& \quad \forall \psi_f \in \mathcal{W}_f^m, \\
(\mathrm{div}(\overline{JF}_\theta^{-1} v^m), \xi_f)_{\Omega_f(t)} + S(p^m, \xi_f) = 0& \quad \forall \xi_f \in \mathcal{L}_f^m.
\end{aligned}$$

Here, we have used the abbreviations

$$\bar{J}_\theta = \theta J(t_m) + (1-\theta)J(t_{m-1})$$

and analogously for $\overline{F}_\theta$,$\overline{JF}_\theta$ and $\overline{\partial_t T}_\theta$. The fluid stresses are defined by

$$\begin{aligned}
\sigma_\theta^m|_{\Omega_f^m} &:= \sigma_{f,\theta}^m = \rho_f\nu_f(\nabla v^m \overline{F}_\theta^{-1} + \overline{F}_\theta^{-T}\nabla^T v^m) - \frac{1}{\theta}p^m \\
\sigma_\theta^{m-1}|_{\Omega_f^{m-1}} &:= \sigma_{f,\theta}^{m-1} = \rho_f\nu_f(\nabla v^{m-1}\overline{F}_\theta^{-1} + \overline{F}_\theta^{-T}\nabla^T v^{m-1}).
\end{aligned}$$

For the solid stresses, we have

$$\sigma_\theta^m|_{\Omega_s^m} := \sigma_{s,\theta}^m = J_m F_m^{-1} \Sigma_s^m F_m^{-T} = J_m F_m^{-1} \left(2\mu_s E_s^m + \lambda_s \mathrm{tr}(E_s^m)\right) F_m^{-T},$$

where

$$E_s^m = \frac{1}{2}\left(F_m^{-T} F_m^{-1} - I\right), \quad F_m = I - \nabla^m u^m \overline{JF}_\theta^{-1}, \quad J_m = \det F_m.$$

$\sigma_\theta^{m-1}|_{\Omega_s^{m-1}}$ is defined analogously by replacing m with $m-1$. For $\theta = 1$, we obtain a modified $dG(0)$ or backward Euler scheme, for $\theta = 0.5$ a modified $cG(1)$ or Crank-Nicolson-type scheme.

Note that in the $dG(0)$ scheme ($\theta = 1$), the system of equations simplifies considerably as we have $\overline{J}_1 = J(t_m) = 1$ and $\overline{F}_1 = F(t_m) = I$. The only remaining term that includes the mapping T_m is the domain velocity $\overline{\partial_t T}_1$. To calculate $\overline{\partial_t T}_1$, we compute the point $x^{m-1} = T_m(x^m, t_{m-1})$ by (10.4) and use the relation

$$\partial_t T(x^m, t_m) = \partial_t T(x^{m-1}, t_{m-1}) = \frac{x^m - x^{m-1}}{t_m - t_{m-1}}.$$

For the $cG(1)$ scheme, we further need to calculate $F(t_{m-1})$ and $J(t_{m-1})$. Therefore, we can use that by the implicit function theorem applied to (10.4), we have

$$F(x^{m-1}, t_{m-1}) = \left(I - \nabla^{m-1} u^{m-2}(x^{m-1})\right)^{-1} (I - \nabla^m u^{m-1}(x^m)).$$

Finally, we note that with this time discretisation real contact is not possible as this would destroy the local regularity of the mappings T_m. However, choosing the time step sufficiently small, structures can get arbitrarily close.

10.2.1 Pressure stabilisation

For non-stationary problems, we will sometimes add a further stabilisation term to the divergence equation that penalises oscillations of the pressure at the interface, namely

$$S_p^m(p, \psi) = \gamma_p h_P (p^m - p^{m-1}, \psi^m)_{\Gamma_i}.$$

This term might increase the stability in the interface region. Note that due to $h_P(p^m - p^{m-1}) \approx h_P k \partial_t p$ this term should get small for a small mesh and time step sizes $h_P, k \to 0$. This kind of stabilisation is not new but has been used e.g. by Burman & Fernández[34] within an Euler-Lagrangian approach using a Nitsche-type coupling (see Section 3.2.3).

10.3 Spatial discretisation

For spatial discretisation, we use the *locally modified finite element scheme* introduced in Section 6. This means that we use a combination of linear and bilinear elements for the deformation u, the velocity v and the pressure p. As described in Section 7, we add certain pressure stability terms $S(p, \xi_f)$ to the divergence equation to guarantee the well-posedness of the system of equations. Furthermore, we add the stabilisation of the structure equation analysed in Section 9.1 to the velocity-displacement relation.

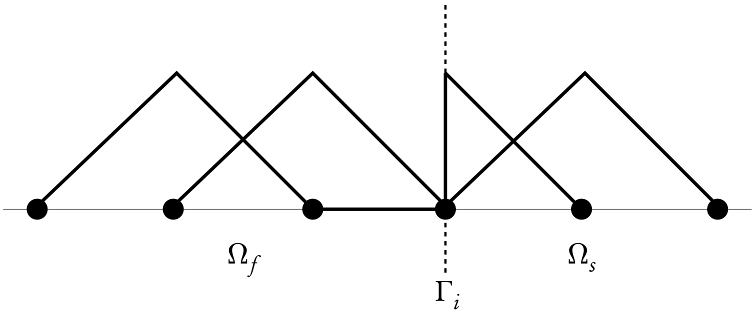

Figure 10.1. 1d illustration of the cutting of interface degrees of freedom in the test space $\tilde{\mathcal{W}}_h$ to avoid an non-physical feedback from the fluid extension u_f to the solid deformation u_s. We cut the basis functions on the fluid side and extend them by zero in Ω_f.

The complete system of equations reads in each time step: *Find velocity* $v_h^m \in v^d + \mathcal{V}_h^m$, *displacement* $u_h^m \in u_s^d + \mathcal{W}_h^m$ *and fluid pressure* $p_h^m \in \mathcal{L}_{f,h}^m$ *such that*

$$\begin{aligned}
(\bar{J}_\theta \rho(v_h^m - v_h^{m-1}), \phi_h)_{\Omega^m} + k\theta(\rho \nabla v_h^m \overline{JF}_\theta^{-1}(v_h^m - \overline{\partial_t T}_\theta), \phi_h)_{\Omega^m} \\
+k(1-\theta)(\rho\nabla v_h^{m-1}\overline{JF}_\theta^{-1}(v_h^{m-1} - \overline{\partial_t T}_\theta), \phi_h)_{\Omega^m} \\
+k(\theta\sigma_{\theta,h}^m + (1-\theta)\sigma_{\theta,h}^{m-1}, \nabla\phi_h \overline{JF}_\theta^{-1})_{\Omega^m} \\
-k(\rho_f \nu_f \overline{JF}_\theta^{-T}(\theta\nabla^T v_{f,h}^m + (1-\theta)\nabla^T v_{f,h}^{m-1})\overline{F}_\theta^{-T} n, \phi_h)_{\Gamma_f \setminus \Gamma_f^d} \\
= k(\bar{J}_\theta(\theta f^m + (1-\theta) f^{m-1}), \phi_h)_{\Omega^m} \quad \forall \phi_h \in \mathcal{V}_h^m, \\
(\bar{J}_\theta(u_h^m - u_h^{m-1}) - k v_h^m, \psi_{s,h})_{\Omega_s^m} + k\theta(\nabla u_h^m \overline{JF}_\theta^{-1}(v_h^m - \overline{\partial_t T}_\theta), \psi_{s,h})_{\Omega_s^m} \\
+k(1-\theta)(\nabla u_h^{m-1}\overline{JF}_\theta^{-1}(v_h^{m-1} - \overline{\partial_t T}_\theta), \psi_{s,h})_{\Omega_s^m} \\
+\alpha k h_P^s(\nabla v_h^m, \nabla \psi_{s,h}^m)_{\Omega_s^m} = 0 \quad \forall \psi_{s,h} \in \mathcal{W}_{s,h}^m, \\
(\alpha \nabla u_h^m, \nabla \psi_{f,h})_{\Omega_f^m} = 0 \quad \forall \psi_{f,h} \in \mathcal{W}_{f,h}^m, \\
\left(\operatorname{div}(\overline{JF}_\theta^{-1} v_h^m), \xi_{f,h}\right)_{\Omega_f(t)} + S(p_h^m, \xi_{f,h}) = 0 \quad \forall \xi_{f,h} \in \mathcal{L}_{f,h}^m.
\end{aligned} \tag{10.5}$$

The fluid and solid stress tensors are defined as in the previous section.

For a domain Ω and a Dirichlet part of the boundary Γ, we define the locally modified finite element space

$$V_h(\Omega;\Gamma) = \left\{\phi \in C(\bar{\Omega}) \cap H_0^1(\Omega;\Gamma),\ \phi \circ T_P^{-1}\Big|_P \in \hat{Q}_P \text{ for all patches } P \in \Omega_h\right\}$$

where $\hat{Q}_P$ is again the space of piecewise linear or piecewise bilinear functions on a patch P, depending whether the patch is cut by the interface or not. We define the trial and test functions in (10.5) as

$$\begin{aligned}
&\mathcal{V}_h = V_h(\Omega;\Gamma_f^d), && \mathcal{L}_{f,h} = V_h(\Omega_h^f;\emptyset), && \\
&\mathcal{W}_h = V_h(\Omega;\Gamma_s^d), && \mathcal{W}_{f,h} = V_h(\Omega_h^f;\Gamma_h^i) && \mathcal{W}_{s,h} = V_h(\Omega_h^s;\Gamma_s^d).
\end{aligned}$$

In our practical implementation, we use a global test space $\tilde{\mathcal{W}}_h$ instead of $\mathcal{W}_{s,h}$ and $\mathcal{W}_{f,h}$. To avoid an non-physical feedback from the fluid extension to the solid displacement (cf. Section 10.2), we modify the standard space $\mathcal{W}_h$ by cutting the fluid part of the basis functions that are non-zero at the interface and extend them to zero in Ω_f (see Figure 10.1 for a 1d illustration of the cut). This corresponds to the implementation of the Dirichlet condition $u_f = u_s$ on the fluid side. As in the continuous case (Section 10.2), the test space $\tilde{\mathcal{W}}_h$ contains functions that are discontinuous at the interface.

Part III

Applications

11 Numerical validation via benchmark problems

In this section, we apply the Eulerian approach and the discretisation techniques derived in the previous sections to two FSI benchmark problems proposed by Hron & Turek [88]. These benchmark problems are widely used to test approaches and software for fluid-structure interaction. To name only a few they have been studied by Hron et al. [90], Dunne et al. [57], Degroote et al. [48] and Kollmannsberger et al. [97]. A comparison of different results has been published by Turek et al. [139]. These results include monolithic ALE approaches as well as implicitly and explicitly coupled partitioned schemes, where the latter ones might use entirely different solvers for fluid and structure (e.g. Finite Volume solver or a Lattice-Boltzmann method for the fluid and finite elements for the solid). Most of the approaches use an ALE technique to include the domain movement. Finally, Dunne & Rannacher contributed some first results obtained with the *Fully Eulerian* approach.

11.1 Setting of the benchmark problems

In these benchmark problems, a two-dimensional elastic beam is attached to a fixed and rigid cylinder, see Figure 11.1. Due to a non-symmetry in the position of the beam and the cylinder, a flow field causes a movement of the beam as well as elastic deformations. If the Reynolds number of the flow configuration is large enough, we observe self-induced oscillations of the beam.

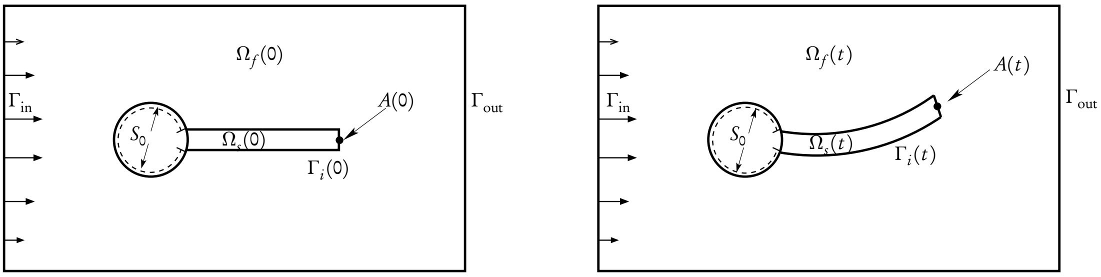

Figure 11.1. FSI benchmark configuration (Hron and Turek [88]): The vertical position of the tip of the beam is initially $A(0) = 0.2$, while the total height of the channel is $H = 0.41$. Due to this non-symmetric setting the beam starts to move when a parabolic inflow is applied at Γ_{in}. We measure the deformation at the tip $A(t)$ and drag and lift mean values at the FSI boundary $\Gamma_i(t)$ and the (fixed) boundary of the cylinder S_0. *Right:* initial configuration, *left:* current system at time $t > 0$.

As in Section 2.1, the equations are given by the incompressible Navier-Stokes equations in the fluid domain and a non-linear St.Venant-Kirchhoff material in the solid domain, together

Parameter	Unit	FSI1	FSI3
ρ_s^0	$[10^3 \frac{\mathrm{kg}}{\mathrm{m}^3}]$	1	1
μ_s	$[10^6 \frac{\mathrm{kg}}{\mathrm{ms}^2}]$	0.5	2
λ_s	$[10^6 \frac{\mathrm{kg}}{\mathrm{ms}^2}]$	2	8
ρ_f	$[\ 10^3 \frac{\mathrm{kg}}{\mathrm{m}^3}\ ]$	1	1
ν_f	$[\ 10^{-3} \frac{\mathrm{m}^2}{\mathrm{s}}\ ]$	1	1
$\overline{v}^{\mathrm{in}}$	$[\ \frac{\mathrm{m}}{\mathrm{s}}]$	0.2	2

Table 11.1. Set of parameters for the FSI benchmarks[88]

.

with the coupling conditions described in Section 2.2.3:

$$\left.\begin{aligned} \rho_f \partial_t v_f + \rho_f (v_f \cdot \nabla) v_f - \operatorname{div} \sigma_f &= 0 \\ \operatorname{div} v_f &= 0 \end{aligned}\right\} \quad \text{in } \Omega_f(t),$$

$$\left.\begin{aligned} J \rho_s^0 (\partial_t v_s + v_s \cdot \nabla v_s) - \operatorname{div} \sigma_s &= 0 \\ \partial_t u_s + v_s \cdot \nabla u_s - v_s &= 0 \end{aligned}\right\} \quad \text{in } \Omega_s(t),$$

$$\left.\begin{aligned} v_f &= v_s \\ \sigma_f n &= \sigma_s n \end{aligned}\right\} \quad \text{on } \Gamma_i(t).$$

The boundary conditions for the fluid are given by a parabolic inflow profile on Γ_{in} on the left side with average velocity $\overline{v}^{\mathrm{in}}$

$$v(0,y) = 1.5 \overline{v}^{\mathrm{in}} \frac{y(H-y)}{(H/2)^2} \tag{11.1}$$

where $H = 0.41$ denotes the height of the channel. Furthermore, we use a *no-slip* condition on the upper and lower boundary and the *do-nothing* outflow condition $\rho_f \nu_f \partial_n v_f - p_f n = 0$ on the right boundary Γ_{out}. As suggested by Hron & Turek[88], we start the simulation with zero initial velocity and increase the Dirichlet values gradually by multiplying (11.1) by $g(t) = 0.5(1 - \cos(\pi t/2))$ for $t \leq 2$.

Hron & Turek specified three different sets of material parameters. Here, we will study their first and third set of parameters, see Table 11.1. While the first set (FSI1) leads to a movement of the beam in the vertical direction that converges to a stationary state, the third set (FSI3) results in oscillatory movements. Hron & Turek proposed four different functionals to compare the results: horizontal and vertical deflection of the beam at the tip (point A(t) in Figure 11.1) $u_x(A(t))$ and $u_y(A(t))$ and the drag and lift mean values at the boundary of the cylinder and the beam

$$F_{\mathrm{drag}} = \int\limits_{S_0 \cup \Gamma_i(t)} \sigma_f n_f e_1 \, ds, \qquad F_{\mathrm{lift}} = \int\limits_{S_0 \cup \Gamma_i(t)} \sigma_f n_f e_2 \, ds.$$

Here, e_1 and e_2 denote the unit vectors in horizontal and vertical direction, respectively.

Most of the methods applied to study the benchmark problem are based on the *Arbitrary Lagrangian Eulerian* method. As the displacements are rather moderate, it is possible to use the same reference domain for all time steps without any remeshing. Hence, for these problems, we cannot expect that the *Fully Eulerian* approach is able to fully compete with an ALE approach. As mentioned previously, the *Fully Eulerian* approach is designed for problems where the ALE method has problems due to large movement of the structure. We will give such examples in the following two sections. Here, however, we want to show that the results obtained with the *Fully Eulerian* approach converge to known reference values both with respect to time and space discretisation.

11.2 Practical implementation

Software

All results shown in this and the following sections have been obtained with the finite element library *Gascoigne 3D*[18]. To solve the non-linear system of equations, *Gascoigne 3D* uses Newton's method. The resulting linear systems have been solved with a direct solver. Therefore, we use the *Trilinos*[127] interface of the *SuperLU_DIST* solver[104].

Discretisation

We use the discretisation techniques that have been summarised in Section 10. Here, we use the $dG(0)$ variant of the modified time-stepping scheme which is more robust than both the $cG(1)$ variant of the modified scheme and the standard backward Euler time-stepping scheme.

For spatial discretisation, we use the *locally modified finite element scheme* introduced in Section 6, with one particular modification. In the present application, the fluid-structure interface Γ_i is not smooth at the corners near the tip of the beam. Hence, using the standard linear approximation of the interface described in Section 6 may lead to an unsatisfactory approximation in these regions. On the other hand, we have one additional freedom that we have not exploited yet, i.e. the position of the patch midpoint. Here, we set the midpoint of the patch that contains the corner to the corner itself (see Figure 11.2). In some specific situations, we have to move some further nodes in order to ensure a maximum angle condition.

For pressure stabilisation, we use a *Continuous Interior Penalty* stabilisation as described in Section 7. Here, however, we use the mean value of the pressure gradient on each edge and the local cell sizes h_n and h_τ (see Section 7.4)

$$S_4(p_h, \psi_h) := \gamma \sum_{e \in \mathcal{E}_h} \int_e \{h_n(h_n^2 \partial_n p_h \partial_n \psi_h + h_\tau^2 \partial_\tau p_h \cdot \partial_\tau \psi_h)\}_e \, do. \tag{11.2}$$

In comparison to using jumps of the gradient, this yields a slightly bigger stabilisation term and hence, more stable results. Furthermore, in our numerical results this stabilisation performed better in terms of accuracy compared to the corresponding one that uses the patch size h_P in the weights.

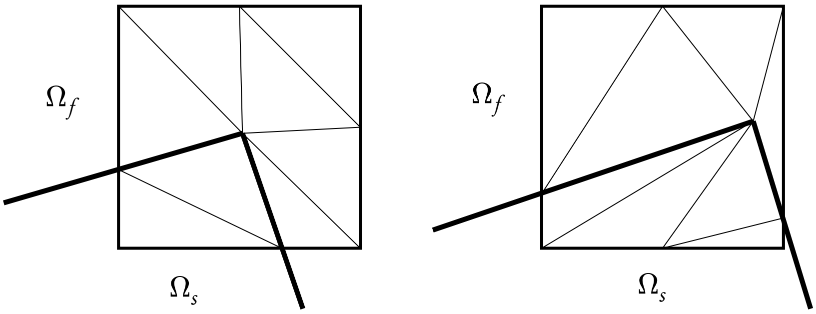

Figure 11.2. Modification of the original *locally modified finite element method* to resolve the corners of the beam by moving the patch midpoint.

Moreover, we add the additional stabilisation term

$$S_p^m(p,\psi) = \gamma_p h_P (p^m - p^{m-1}, \psi^m)_{\Gamma_i} \tag{11.3}$$

at the fluid-structure interface Γ_i (see Section 10.2). This term penalises non-physical pressure oscillations in the interface region.

Evaluation of surface integrals

We evaluate the drag and lift functionals using the *Babuška-Miller trick*[7]. Here, we show the derivation exemplarily for the drag functional. We define a function $\phi \in [H^1(\Omega(t))]^2$ whose second component ϕ_2 vanishes in Ω. We require for the traces of its first component that

$$\phi_1 = 1 \quad \text{on } S_0 \cup \Gamma_i(t), \qquad \phi_1 = 0 \text{ on } \partial\Omega \setminus S_0.$$

We apply the divergence theorem on Ω_f

$$F_{\text{drag}} = \int_{S_0 \cup \Gamma_i(t)} \sigma_f n_f e_1 \, ds = \int_{S_0 \cup \Gamma_i(t)} \sigma_f n_f \phi \, ds = \int_{\Omega_f} \sigma_f \nabla\phi + \operatorname{div}(\sigma_f)\phi \, dx.$$

Finally, we use the strong form of the momentum equation in the fluid domain and obtain

$$F_{\text{drag}} = (\sigma_f, \nabla\phi)_{\Omega_f} + (\rho_f(\partial_t v_f + v_f \cdot \nabla v_f) - f, \phi)_{\Omega_f} := a(v_f, p_f, \phi).$$

Now, $a(v_f, p_f, \phi)$ is exactly the bilinear form that we have to evaluate when we set up the right-hand side and the system matrix. Furthermore, this way of evaluating the surface forces is much more accurate than the direct evaluation of the boundary integrals, as has been shown by Braack & Richter[26]. In the present case of linear/bilinear finite elements, we expect an accuracy of $\mathcal{O}(h^2)$ compared to $\mathcal{O}(h^{1/2})$ for a direct evaluation of the surface force. In practice, we use the discrete function with $\phi(x_i) = 1$ in a grid point $x_i \in S_0 \cup \Gamma_i(t)$ and $\phi(x_i) = 0$ in all other grid points.

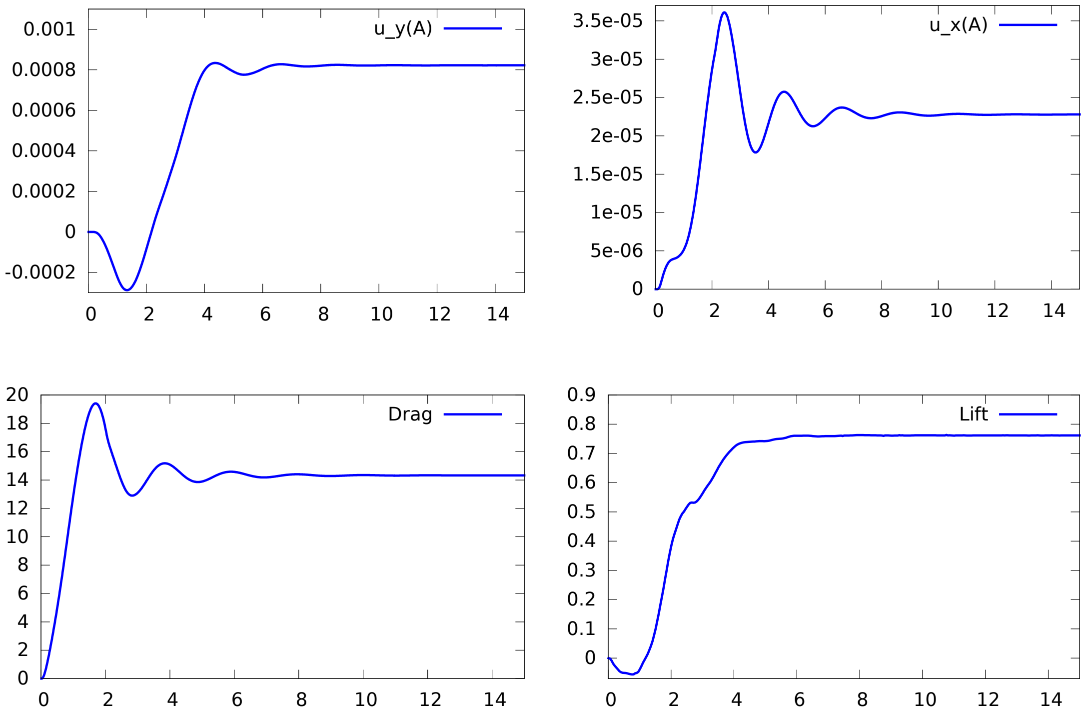

Figure 11.3. Functional values for the FSI1 benchmark over time.

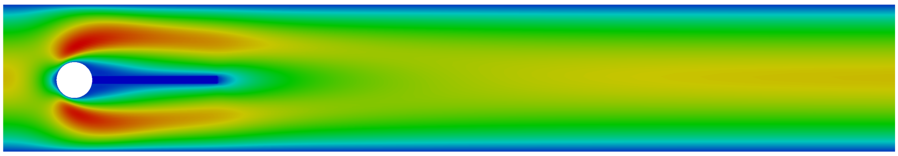

Figure 11.4. Snapshot of the stationary state of the FSI1 benchmark. The tip of the beam is slightly deflected towards the top. The colour illustrates the Euclidean norm of the velocity field.

#nodes	$u_x(A)$	$u_y(A)$	F_{drag}	F_{lift}
4128	$2.278 \cdot 10^{-5}$	$8.455 \cdot 10^{-4}$	14.328	0.7721
16192	$2.274 \cdot 10^{-5}$	$8.263 \cdot 10^{-4}$	14.305	0.7656
64128	$2.272 \cdot 10^{-5}$	$8.211 \cdot 10^{-4}$	14.298	0.7637
Ref[139]	$2.270 \cdot 10^{-5}$	$8.209 \cdot 10^{-4}$	14.294	0.7637

Table 11.2. Results for the FSI1 benchmark for four different functionals. We observe a very good convergence behaviour. Furthermore, the results on the finest grid are in excellent agreement with the reference values.

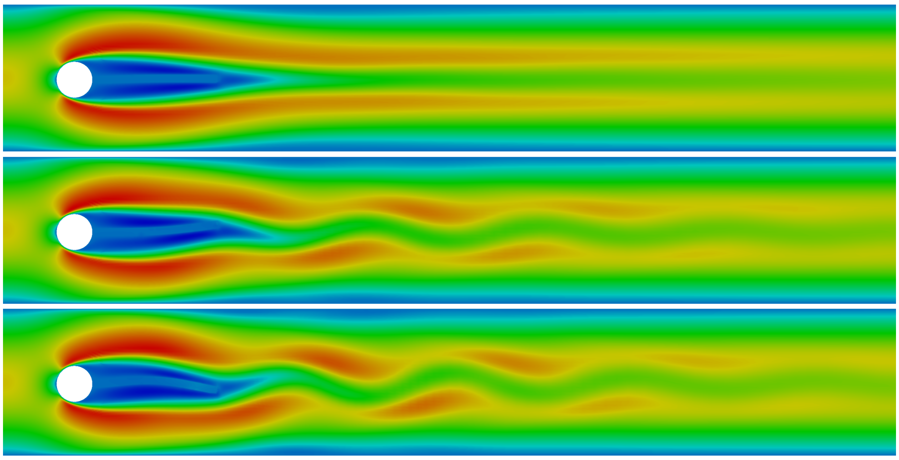

Figure 11.5. Snapshots of the FSI3 benchmark at three different instants of time. First, we see a slight movement of the beam towards the top (top). Then, the beam starts to oscillate (middle) and a periodic movement can be observed (bottom). The colour illustrates the Euclidean norm of the velocity field.

11.3 FSI1 benchmark

Due to a low Reynolds number $Re = 20$, the FSI1 configuration converges to a stationary state which is reached after a slight vertical movement of the tip of the beam towards the top. In Figure 11.3, we show the horizontal and vertical deflection as well as the drag and lift functional over time. After a short settling time, a stationary state is attained after approximately $8s$. In Figure 11.4, we illustrate the velocity of the solution at the stationary state.

For pressure stabilisation, we use the parameters $\gamma = 5 \cdot 10^{-4}$ and $\gamma_p = 2 \cdot 10^{-3}$ in (11.2) and (11.3). For the FSI1 configuration it is not necessary to add stabilisation terms to the solid equation as the solid velocity is relatively small and vanishes in the stationary state. We use a time step size of $k = 10^{-2}$.

In Table 11.2, we show values for the four functionals on three different grids with 4'128, 16'192 and 64'128 nodes, respectively. The functional values show a very good convergence behaviour in all the functionals. While we observe approximately linear convergence in the horizontal deflection $u_x(A)$ and the drag functional, the vertical deflection $u_y(A)$ and the lift functional converge much faster. The values on the finest grid are in excellent agreement with the reference values obtained by Turek et al. on a grid with more than 19 million degrees of freedom with an ALE approach[139]. We observe the biggest deviation from the reference values in the horizontal deflection $u_x(A)$ showing a relative error below 0.1 %.

When we compare these values with the results of other approaches presented in[139], we observe that many of them are far less accurate even on much finer meshes. This is especially true for most of the approaches that use a partitioned coupling of different fluid and solid solvers.

Furthermore, the *Fully Eulerian* approach contributed by Dunne & Rannacher in its early version without the discretisation techniques derived in this thesis yielded relatively poor results with relative errors of up to 8%.

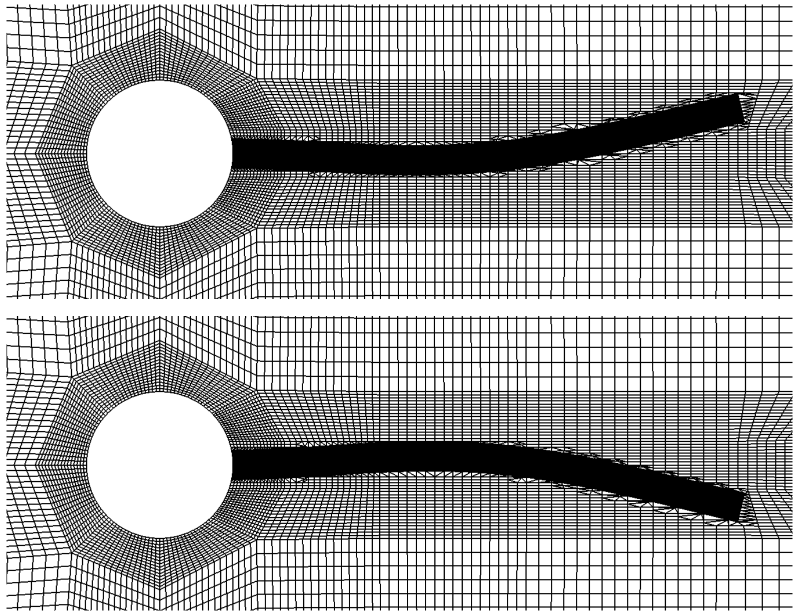

Figure 11.6. Illustration of the grid obtained with the locally modified finite element discretisation with 13'104 mesh points at the time of minimum and maximum displacement. For better visualisation of the subdomains, the grid in the solid part is not shown here, but filled with black colour.

11.4 FSI3 benchmark

The FSI3 benchmark has a Reynolds number of $Re = 200$ which, at first, causes a slightly larger displacement of the beam towards the top compared to the FSI1 benchmark. Then, after some time, the beam starts to oscillate periodically. This leads to the formation of vortices in the fluid domain behind the beam. Some snapshots of the solution are given in Figure 11.5. In Figure 11.6, we show a visualisation of a grid obtained with the *locally modified finite element* method. For better illustration, we show only the mesh for the fluid part and plot the solid domain in black.

For pressure stabilisation, we choose exactly the same parameters ($\gamma = 5 \cdot 10^{-4}$ and $\gamma_p = 2 \cdot 10^{-3}$) as for the FSI1 benchmark. In addition, here, it is necessary to stabilise the solid equation. We use the parameter $\alpha = 10$ and $s = 1$, i.e.

$$S_v(v,\phi) = 10 h_P (\nabla v, \nabla \phi)_{\Omega_s(t)}.$$

In Figure 11.7, we show the course of the four functionals over time. A uniform oscillatory movement is observed after approximately $t = 8s$. Before, we observe small overshoots in both the vertical and horizontal displacement. This is in agreement with results obtained with ALE calculations, but in contrast to the findings of Dunne with the Fully Eulerian approach in its early version who observed a uniform increase of the oscillations[55].

For $t > 8s$, the horizontal and vertical displacements show nearly perfectly uniform oscillations. For the horizontal displacements, we have to remark that two maxima and minima are attained within one period as the horizontal displacement gets minimal both when the beam

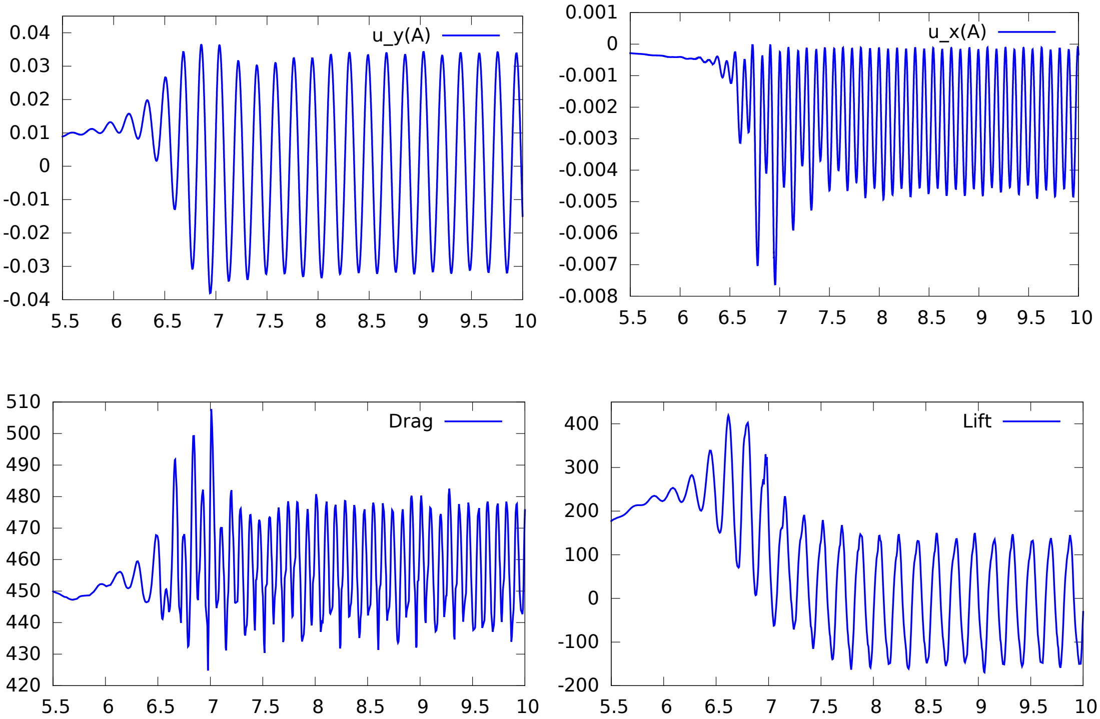

Figure 11.7. Functional values for the FSI3 benchmark over time. A state of uniform oscillations is reached after approximately $8s$.

reaches its uppermost and its lowermost position. The same holds true for the drag functional. The oscillations in the drag and lift functional are not exactly uniform. Having a closer look at the times of minimum and maximum deviation, we observe small instabilities in the pressure around the corners of the beam. These instabilities can be reduced by further increasing the pressure stabilisation. In this case, however, all four functionals show considerably smaller values as the pressure stabilisation dampens too much. Nevertheless, the functional values obtained here serve to get a good estimate for the surface forces.

While the results obtained for the FSI1 benchmarks are relatively close for the different approaches compared in [139] where on fine grids most of the approaches showed relative errors of at most 2 %, the results for the FSI3 benchmark differ much more significantly. For the horizontal deflection and both of the surface functionals some approaches show relative errors of around 50 % in the amplitude of the oscillations.

In Table 11.3, we give our results of the mean value and the amplitude of the four functionals on two different meshes and for three different time step sizes after the system reached a state of uniform oscillations. To get precise values, we calculated the mean value of 10 minima and maxima for all of the functionals. In all functionals, we observe that we get considerably closer to the reference values after mesh refinement which indicates good convergence properties in space. In time, we observe a strong improvement of the values when decreasing the time step size from $k = 10^{-3}$ to $k = 5 \cdot 10^{-4}$. Decreasing the time step once more by a factor of two has

Vertical deflection $u_y(A)$ in $10^{-2}m$

#nodes $\backslash$ k	10^{-3}	$5 \cdot 10^{-4}$	$2.5 \cdot 10^{-4}$
13104	0.135 ± 2.847	0.130 ± 3.039	0.190 ± 3.086
51808	0.039 ± 3.167	0.114 ± 3.288	0.055 ± 3.214
Ref[139]			0.147 ± 3.499

Horizontal deflection $u_x(A)$ in $10^{-3}m$

#nodes $\backslash$ k	10^{-3}	$5 \cdot 10^{-4}$	$2.5 \cdot 10^{-4}$
13104	-1.87 ± 1.81	-2.15 ± 2.07	-2.23 ± 2.16
51808	-2.29 ± 2.16	-2.49 ± 2.38	-2.29 ± 2.19
Ref[139]			-2.88 ± 2.72

Drag surface force

#nodes $\backslash$ k	10^{-3}	$5 \cdot 10^{-4}$	$2.5 \cdot 10^{-4}$
13104	466.9 ± 13.8	469.4 ± 16.0	468.9 ± 22.8
51808	452.6 ± 13.4	456.3 ± 22.5	453.1 ± 24.7
Ref[139]			460.5 ± 27.7

Lift surface force

#nodes $\backslash$ k	10^{-3}	$5 \cdot 10^{-4}$	$2.5 \cdot 10^{-4}$
13104	-4.6 ± 164.8	-1.4 ± 176.9	-9.4 ± 193.6
51808	-5.0 ± 130.6	-10.2 ± 148.4	-27.9 ± 162.6
Ref[139]			2.5 ± 153.9

Table 11.3. Functional values $u_y(A)$, $u_x(A)$, F_{drag} and F_{lift} for the FSI3 benchmark with different time step sizes and on different grids.

only positive impact on the drag force and on horizontal and vertical deflections on the coarser grid. Here, the spatial discretisation error seems to dominate the temporal error. We suppose that this is mainly caused by the rather large pressure stabilisation term which was used to ensure stability.

Comparing these values to the results that have been presented in [139], we observe -as expected- that we cannot fully compete with monolithic ALE discretisations. To reach the same level of accuracy, we would need a much finer grid. The relative errors in the amplitude, that we get for the best values, range between 3.6% for the lift functional and 13.3% for the drag functional. The monolithic ALE approach submitted by Rannacher & Dunne in contrast shows relative errors of 0.8% to 5.6%. Similar results have been contributed by Schäfer who used an implicitly coupled partitioned approach using an ALE finite volume technique for the fluid and a Lagrangian finite element solver for the structure. All the other contributed results show either accuracies that are comparable to our results or are significantly worse. As mentioned previously, two of the contributions yielded relative errors of around 50% in the horizontal deformation $u_x(A)$ and the drag or lift functional, respectively.

To summarise, we have shown in this section that the *Fully Eulerian* method with the discretisation techniques developed in this thesis yields results that converge against known reference values in both space and time. Our results are slightly less accurate than results obtained with a monolithic ALE approach. This was expected, as the advantage of the *Fully Eulerian* approach lies in the ability to deal with large solid movements and contact. We will present such applications in the following two sections. On the other hand, our results are better than most of the other contributed results summarised in [139], including established partitioned algorithms.

12 The bounce of an elastic ball in a viscous fluid: a contact problem

In this section, we study contact problems of an elastic ball that falls down to the ground in a viscous fluid. At the time of contact the ball is compressed and bounces off. We study the vertical fall of a ball towards a horizontal wall and its vertical rebound in Section 12.1. In Section 12.3, we consider a more complex situation where a ball drops onto an inclined plane and bounces three stairs down afterwards.

As mentioned previously, problems of this kind cannot be simulated with standard ALE approaches as we have to deal with large structural displacements, and, in the case of "real contact" (meaning that no fluid layer remains between ball and ground), with topology changes in the fluid domain. In this case a monolithic Eulerian approach is a promising alternative.

The objective of this section is to analyse the ability of the Eulerian approach to model contact. Furthermore, we want to address the question of whether a small fluid film remains between ball and ground at the time of contact. Therefore, we give detailed convergence and parameter studies in Sections 12.1.2 and 12.1.3, respectively.

From a modelling point of view, it is questionable if the Navier-Stokes equations are a valid model in the case of real contact, see Hillairet[85], Feireisl[62] or Gérart-Varet et al.[74] for analytical results regarding this question. For this case, we introduce a simple contact model in Section 12.2 that prevents the solid from touching the ground. As the model is based on an artificial contact force, we investigate its influence on the contact dynamics in detail.

As in the previous section the equations under consideration are given by the non-stationary FSI equations summarised in (2.16). In contrast to the situation there, we apply a non-trivial volume force $f_s = (0, -1)$ that represents gravity.

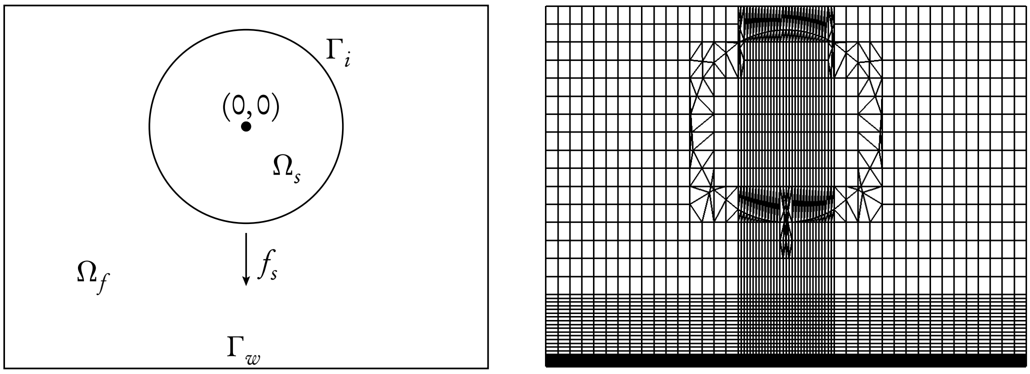

Figure 12.1. Sketch of the configuration of the first test case and the initial mesh. To simulate the contact dynamics accurately, fine mesh cells are used in the contact region.

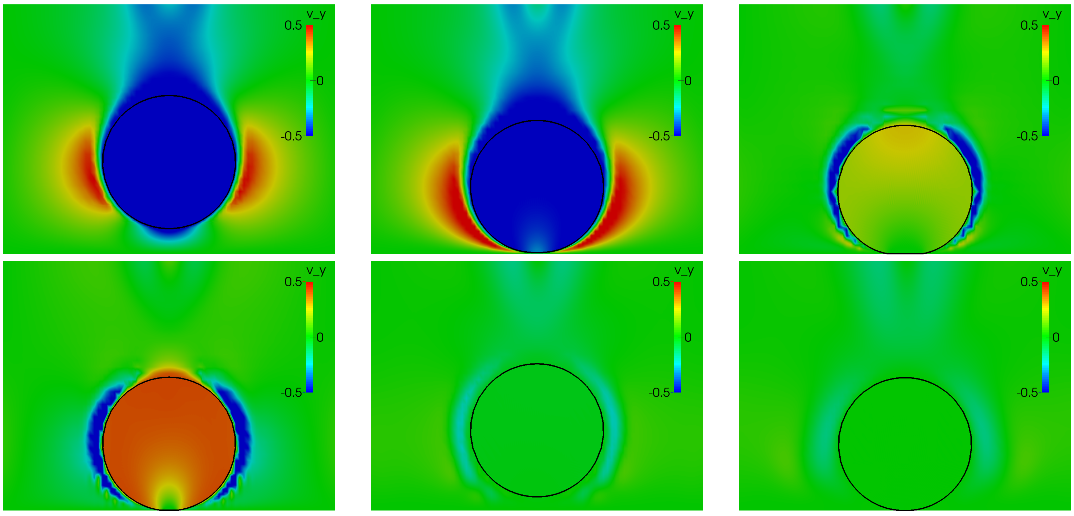

Figure 12.2. Illustration of the free fall of an elastic ball, its contact with the ground and the subsequent rebound at six different times. The ball falls down by gravity (*top left*, $t \approx 1.3$), is almost in contact with the ground (*top middle:* before contact, $t \approx 1.6$, *top right:* smallest distance, $t \approx 1.8$, *bottom left:* after contact, $t \approx 1.81$) and bounces off. It reaches its highest elevation again at $t \approx 2.4$ (*bottom middle*). After a second bounce, it comes to rest at $t \approx 4.4$ (*bottom right*) being in real contact with the ground. The colour illustrates the vertical velocity v_y and the black contour line is the discrete interface.

12.1 Example 1: Vertical fall

A sketch of our first test problem is given in Figure 12.1. We consider a ball of radius $r = 0.4$ whose midpoint is initially located at the origin. Due to gravity it falls down towards a horizontal wall $\Gamma_w = \{(x,y) \in \mathbb{R}^2 \,|\, y = -1\}$. As boundary condition, we impose a homogeneous velocity on Γ_w. In combination with the *kinematic condition* and the velocity-displacement relation $d_t u_s = v_s$ this ensures that the solid cannot pass “through the wall”. Note that in this section, we do not use any contact algorithm.

On the remaining boundaries, we use the *do-nothing* outflow condition. The same example but with different material parameters has been studied by Richter[121]. To simulate the interval of contact accurately, we use an anisotropic mesh with fine cells around the lower boundary (see Figure 12.1, right).

For the first test, we choose the Lamé parameters $\mu_s = 2 \cdot 10^5$ and $\lambda_s = 8 \cdot 10^5$ and the fluid viscosity $\mu_f = 10^{-3}$. Fluid and solid density are set as $\rho_s = \rho_f = 10^3$. Before we discuss the numerical parameters, we describe the temporal dynamics by means of some simulation results.

In Figure 12.2, we show the falling ball at six different times. The colouring illustrates the vertical velocity. First, the ball is accelerated by gravity and falls down. At time $t \approx 1.6$, the bottom is almost reached and the ball slows down due to a high fluid pressure. It comes closest to the ground at time $t \approx 1.8$, where the minimal distance is $d \approx 1.2 \cdot 10^{-3}$. At this time the ball is significantly compressed at its bottom.

The discretisation at this point is illustrated in Figure 12.3 (top) for the coarsest mesh we used. The interface shows a domed shape due to a high fluid pressure in the middle and the minimal

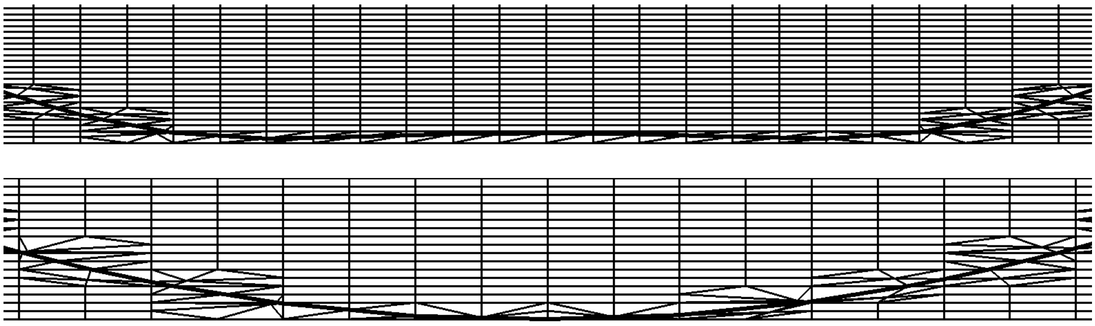

Figure 12.3. Illustration of a coarse mesh during the first rebound (top sketch) and at the end time when the ball is at rest (lower sketch). During the first rebound, a small layer of fluid remains between ball and ground.

distance is not attained in the centre but left and right of it at position $x \approx \pm 7.5 \cdot 10^{-2}$. In this configuration, there is no real contact but a small layer of fluid remains between ball and ground. Nevertheless, here and in the following we will call this period the “contact time” or “contact interval“ for simplicity.

Then, due to the compression at the bottom the ball is accelerated upwards. The ball reaches its highest elevation at a maximum distance $d \approx 8.3 \cdot 10^{-2}$ from the ground at time $t \approx 2.4$ and falls down again. After a smaller second bounce with distance $d \approx 4.6 \cdot 10^{-3}$, it comes to rest, being in real contact with the ground at time $t \approx 4.4$ (see Figure 12.3 (bottom) for an illustration of the mesh at the time of real contact).

In Figure 12.4, we plot the minimal distance between the ball and the ground including a zoom-in of the contact and rebound interval in the upper row. Furthermore, we show the distance between the top and the bottom of the ball and an averaged vertical velocity of the solid in the lower row.

In the lower left plot, we observe that the distance between the top and the bottom of the ball attains minima at the two contact times due to the compression. After the first rebound, we observe oscillations that get smaller over time. These oscillations are also visible in the deformation (see top right sketch) and in the vertical velocity plot (lower right sketch). They can be explained in the following way: First, the ball is maximally compressed at the bottom at the time of contact. Once the ball bounces off again, the deformation is relaxed. The ball is even overstretched at some point and starts to oscillate between an expanded and a compressed state periodically.

The averaged vertical velocity is negative before the first contact time and reaches a minimum of $\overline{v}_y \approx -0.586$ at time $t = 1.438$ right before the contact. Then, the velocity increases again and reaches a maximum short after the contact time at $t = 1.768$ with approximately two thirds of the absolute value of $\overline{v}_y$ during the fall. After the point of inflection, we observe the same oscillations as in the displacement functionals. They are smaller here as we are plotting an average over the whole solid domain and the oscillations in the lower and the upper part of the ball are opposed. The behaviour at the second contact point is similar although with much smaller velocities.

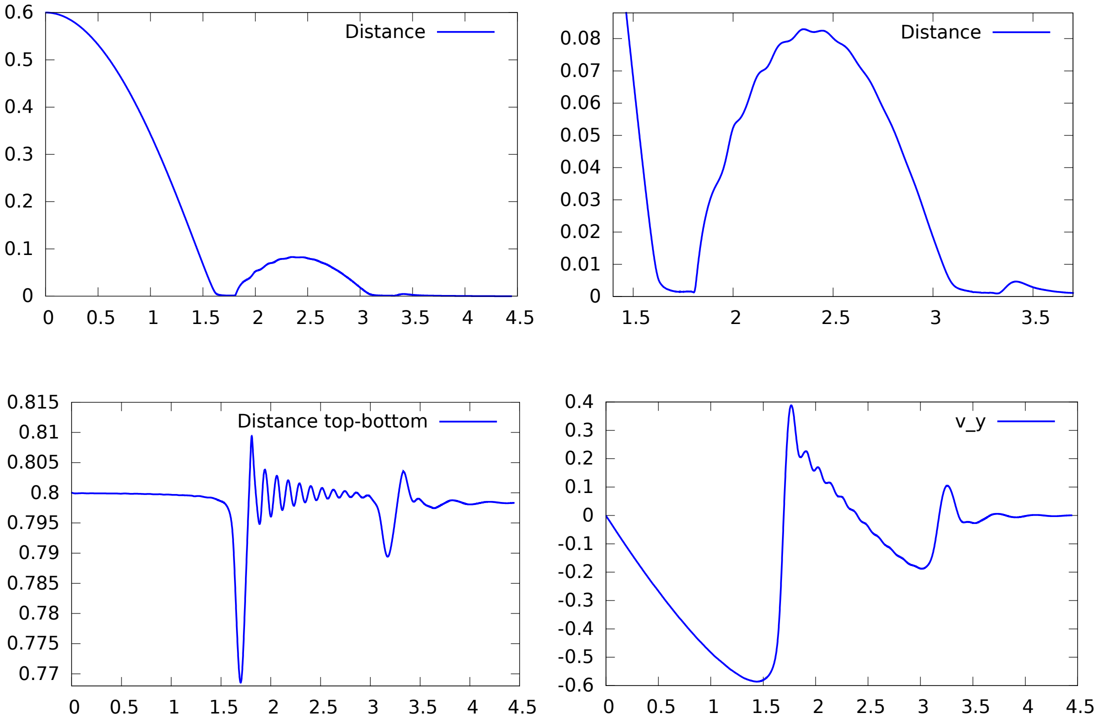

Figure 12.4. *Top:* Minimal distance between ball and ground over time and a zoom-in at the interval of contact and rebound. *Bottom:* Distance between top and bottom of the ball and average vertical velocity over time.

12.1.1 Numerical parameters

We are using the discretisation described in Section 10 with a few modifications. In this example, we do not use any structural stabilisation. Using the stabilisation proposed in Section 9.1 might be dangerous here as it alters the velocity-displacement relation $d_t u_s = v_s$. If the ball is close to the ground, this relation is crucial as it ensures that the ball cannot "pass" through the ground.

At the time of contact the fluid pressure shows a high peak in the contact region, see Figure 12.5. Resolving this peak accurately is important as it prevents the ball from touching the ground. Therefore, the mesh has to be sufficiently fine in the contact region and the pressure stabilisation has to be sufficiently small. In contrast to the previous section, we use the following (smaller) pressure stabilisation scheme (see Section 7.4)

$$S_3(p_h,\psi_h) = \gamma\Big(\sum_{e\in\mathcal{E}_h^{f,i}} \int_e \{h_n(h_n^2\partial_n p_h \partial_n \psi_h + h_\tau^2 \partial_\tau p_h \cdot \partial_\tau \psi_h)\}_e \, do \\ + \sum_{e\in\mathcal{E}_h^{f,0}} \int_e h_n^3 [\nabla p_h]_e \cdot [\nabla \psi_h]_e \, do\Big).$$

We choose two different stabilisation parameters $\gamma_i = 2\cdot 10^{-5}$ and $\gamma_c = 10^{-3}$. The first parameter γ_i has been chosen small so that it alters the pressure profile in the interface region as little as

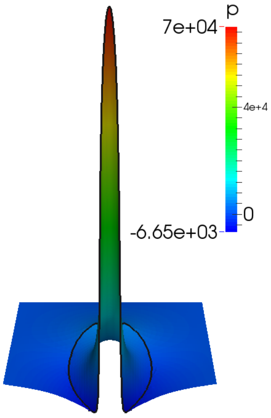

Figure 12.5. Illustration of the pressure peak during the contact between ball and ground.

possible at the time of contact. Furthermore, we do not use the additional temporal pressure stabilisation defined in (11.3) at the interface.

For time discretisation we use the modified dG(0) scheme. This scheme is able to handle the case that two structures come arbitrarily close, but requires a modification when it comes to real contact. In this case, we set $T = \mathrm{id}$ in the contact region which results in the standard backward Euler scheme there.

Both the time step size k in and around the contact interval and the spatial discretisation in the contact region have to be sufficiently fine in order to capture the contact dynamics accurately. We will see in the next section that a coarse resolution might change the results considerably.

12.1.2 Convergence studies

In this section, we study the test configuration on different grids and for different time step sizes. The coarsest mesh we use is shown in Figure 12.1, right sketch. It consists of patches of size 0.1×0.15 in the upper right and upper left part and of size $3.1 \cdot 10^{-3} \times 2.5 \cdot 10^{-2}$ in the contact region. Furthermore, we show the results on two finer meshes that are constructed from this coarse mesh by global refinement.

In Table 12.1, we analyse the minimal distance during the first contact, the maximum elevation after the first rebound and the error in mass conservation on these meshes for three different time step sizes. First, we observe that the calculation with the largest time step size $k = 2 \cdot 10^{-3}$ on the finest mesh broke down before the contact point. Here the restriction that the interface may not pass more than one patch per time step was violated.

Next, we observe that both the minimal distance during the contact and the maximal distance after the rebound are significantly smaller on the coarsest mesh. On the other hand, the results on the finer meshes show good agreement. Thus, we conclude that the resolution of the contact region in the coarse mesh was not fine enough to resolve the contact dynamics accurately. On the finer meshes, we observe also a very good convergence behaviour in time both with respect to the distances and the times $t_{\min}$ and $t_{\max}$ where minimal and maximal distance are attained. We conclude that in this configuration a fluid layer of size $\mathrm{d}_{\min} \approx 1.3 \cdot 10^{-3}$ seems to remain

	First contact: Minimum distance			$t_{\min}$		
#nodes \ k	$2 \cdot 10^{-3}$	10^{-3}	$5 \cdot 10^{-4}$	$2 \cdot 10^{-3}$	10^{-3}	$5 \cdot 10^{-4}$
4225	$6.383 \cdot 10^{-4}$	$6.487 \cdot 10^{-4}$	$6.256 \cdot 10^{-4}$	1.830	1.827	1.829
16641	$1.218 \cdot 10^{-3}$	$1.244 \cdot 10^{-3}$	$1.237 \cdot 10^{-3}$	1.806	1.803	1.804
66049	-	$1.270 \cdot 10^{-3}$	$1.267 \cdot 10^{-3}$	-	1.795	1.795

	First bounce: Maximum distance			$t_{\max}$		
#nodes \ k	$2 \cdot 10^{-3}$	10^{-3}	$5 \cdot 10^{-4}$	$2 \cdot 10^{-3}$	10^{-3}	$5 \cdot 10^{-4}$
4225	$4.712 \cdot 10^{-2}$	$5.188 \cdot 10^{-2}$	$5.203 \cdot 10^{-2}$	2.270	2.270	2.271
16641	$7.408 \cdot 10^{-2}$	$8.294 \cdot 10^{-2}$	$8.485 \cdot 10^{-2}$	2.356	2.353	2.351
66049	-	$8.712 \cdot 10^{-2}$	$8.957 \cdot 10^{-2}$	-	2.343	2.341

	Relative mass conservation error		
#nodes \ k	$2 \cdot 10^{-3}$	10^{-3}	$5 \cdot 10^{-4}$
4225	$8.960 \cdot 10^{-3}$	$8.941 \cdot 10^{-3}$	$8.937 \cdot 10^{-3}$
16641	$2.543 \cdot 10^{-3}$	$2.361 \cdot 10^{-3}$	$2.312 \cdot 10^{-3}$
66049	-	$5.073 \cdot 10^{-4}$	$5.053 \cdot 10^{-4}$

Table 12.1. *Top:* Minimal distance between ball and ground during the first contact interval and time $t_{\min}$ of minimal distance. *Middle:* Maximal distance after the first rebound and time $t_{\max}$ of maximal distance. *Bottom:* Relative error in mass conservation at time $t = 3$. The three functionals are calculated for three different time step sizes and on three different meshes.

between the ball and the ground.

The relative error in mass conservation is given by

$$j_{\text{mass}} = \frac{\left| \int_{\Omega_s} J \rho_s^0 \, \mathrm{dx} - \pi r^2 \rho_s^0 \right|}{\pi r^2 \rho_s^0}.$$

Here, we observe a good convergence behaviour in both space and time, even on the coarsest mesh. The spatial discretisation error is dominating and decreases with order $\mathcal{O}(h_P^2)$. This convergence behaviour was expected, as it is the approximation error of the interface, see Section 6.

12.1.3 Influence of material parameters

In this subsection, we study the effect of different solid and fluid parameters. In particular, we will address the question of whether a small layer of fluid is maintained between ball and ground or if it comes to real contact.

Solid parameters

We start by varying the solid parameters. Keeping the ratio between the Lamé parameters μ_s and λ_s constant, $\lambda_s = 4\mu_s$ (which corresponds to a Poisson ration of $\nu_s = 0.4$), we vary the magnitude of λ_s and μ_s simultaneously.

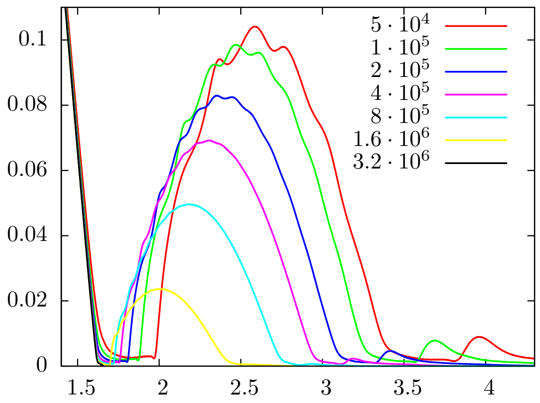

Figure 12.6. Distance between ball and ground over time for different solid parameters μ_s during the contact and rebound interval. The first Lamé parameter is chosen as $\lambda_s = 4\mu_s$. The rebound height is higher the softer the solid is.

	Solid parameter μ_s					
	$5 \cdot 10^4$	10^5	$2 \cdot 10^5$	$4 \cdot 10^5$	$8 \cdot 10^5$	$1.6 \cdot 10^6$	$3.2 \cdot 10^6$
$\mathrm{d}_{\mathrm{min},1}$	$2.34 \cdot 10^{-2}$	$1.72 \cdot 10^{-3}$	$1.24 \cdot 10^{-3}$	$1.06 \cdot 10^{-3}$	$6.31 \cdot 10^{-4}$	$2.56 \cdot 10^{-5}$	0
$\mathrm{d}_{\mathrm{max},1}$	$1.04 \cdot 10^{-1}$	$9.85 \cdot 10^{-2}$	$8.29 \cdot 10^{-2}$	$6.92 \cdot 10^{-2}$	$4.96 \cdot 10^{-2}$	$2.36 \cdot 10^{-2}$	-
$\mathrm{d}_{\mathrm{max},2}$	$8.95 \cdot 10^{-3}$	$7.82 \cdot 10^{-3}$	$4.63 \cdot 10^{-3}$	$2.29 \cdot 10^{-3}$	$6.80 \cdot 10^{-4}$	-	-

Table 12.2. Minimal distance $\mathrm{d}_{\mathrm{min},1}$ during the first contact period and first and second rebound heights $\mathrm{d}_{\mathrm{max},1}$ and $\mathrm{d}_{\mathrm{max},2}$ for different solid parameters. The ratio between the Lamé parameters is kept constant ($\lambda_s = 4\mu_s$). For $\mu_2 = 3.2 \cdot 10^6$ no fluid layer remained between ball and ground and the calculation broke down at the first contact point. For $\mu_s = 1.6 \cdot 10^6$ this happened during the second contact.

For a set of parameters ranging from $\mu_s = 5 \cdot 10^4$ to $3.2 \cdot 10^6$, we plot the distances between ball and ground over time in Figure 12.6. For the stiffest material ($\mu_s = 3.2 \cdot 10^6$) no fluid layer remains during the first contact interval. Ball and ground are in real contact and the ball does not bounce off at all. It is, however, questionable whether this corresponds to the physical situation. Instead the contact might be caused by numerical errors due to a too large time step or an insufficient resolution in the contact region. On the other hand, a sufficiently fine resolution might cause considerable computational costs. Once the ball is in contact with the ground the homogeneous Dirichlet condition on Γ_w prevents it from bouncing. We give details below on contact algorithms that enable us to handle such situations without increasing the computational cost.

Next, we analyse the minimum distance during the first contact as well as the maximum elevation after the first and second rebound for the different material parameters, see Table 12.2. The ball comes closer to the ground for larger solid parameters. For the second-largest parameter $\mu_s = 1.6 \cdot 10^6$, only a minimum distance of $d \approx 2.56 \cdot 10^{-5}$ remains. While the smaller parameters $\mu_s \leq 8 \cdot 10^5$ result in a second rebound after the second contact, the ball remains at rest at the ground for $\mu_s = 1.6 \cdot 10^6$. Again this might be due to an insufficient resolution in the contact interval.

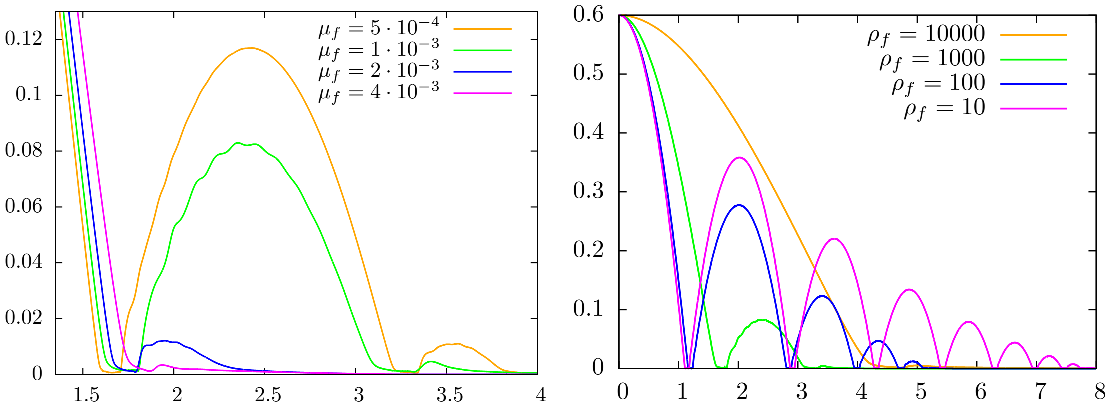

Figure 12.7. Distance between ball and ground over time for different values of the fluid viscosity μ_f and the fluid density ρ_f. The rebound height is higher for smaller viscosities and smaller densities. For smaller densities we observe several bounces.

Due to a higher compression during the contact and a bigger bounce-off force, the first and the second rebound heights are bigger, the softer the solid is. Finally, we see in Figure 12.6 that the oscillations of the solid deformation after the first rebound are bigger for softer solids. For $\mu_s \geq 8 \cdot 10^5$ they are almost not visible.

Fluid parameters

Next, we study the influence of the fluid viscosity and the fluid density, see Figure 12.7 (left). For the fluid viscosity, we use a range from $\mu_f = 5 \cdot 10^{-4}$ to $4 \cdot 10^{-3}$ and fix the density to $\rho_f = 1000$. For a bigger viscosity, the minimal distance at the contact is smaller, e.g. $\mathrm{d}_{\mathrm{min},1} \approx 6.13 \cdot 10^{-4}$ for $\mu_f = 4 \cdot 10^{-3}$ and the rebound height is significantly reduced. The reason for this is that before the contact the ball slows down considerably by the fluid forces such that the bounce-off force is relatively small. For the two larger viscosities no second rebound takes place at all while for the smaller viscosities we observe a small second bounce with heights $\mathrm{d}_{\mathrm{max},2} \approx 4.63 \cdot 10^{-3}$ and $1.1 \cdot 10^{-2}$, respectively.

The effect of the fluid density is similar, see Figure 12.7 (right). Here we fix the viscosity to $\mu_f = 10^{-3}$ and alter the density in a range of $\rho_f = 10$ to $\rho_f = 10^4$. The smaller the density is, the larger is the rebound height. Again this can be explained by the fact that the velocity is slowed down less before and after the contact. While for fluid density $\rho_f = 10^4$ we observe only one bounce and for $\rho_f = 10^3$ two bounces, for the smaller densities $\rho_f = 100$ and $\rho_f = 10$, we get five and eight bounces, respectively. For $\rho_f = 10$ the rebound height reduces only by a factor of approximately two in each bounce.

12.2 A simple contact algorithm

In the case where no fluid layer is maintained between the ball and the ground, it is difficult to decide from the numerical simulations if the corresponding physical situation is that the ball remains at the ground or if it rebounds. In many cases, numerical errors caused by too large

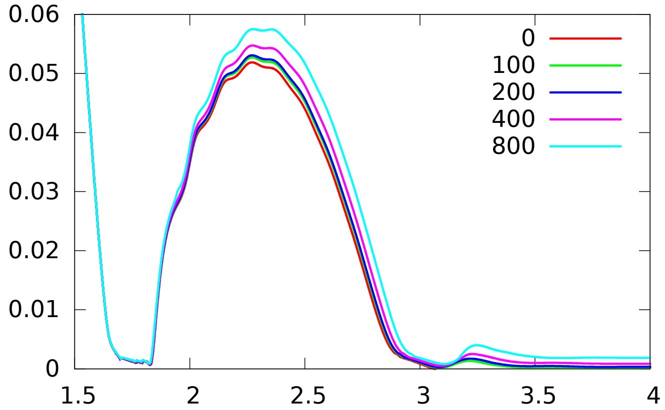

Figure 12.8. Influence of different contact parameters γ_c for contact distance $\text{dist}_0 = 10^{-2}$ and Lamé parameters $\mu_s = 2 \cdot 10^5$, $\lambda_s = 8 \cdot 10^5$.

time steps or too much pressure stabilisation have the effect that the ball either "passes" through the ground at some time or it remains in contact with it for all times. Furthermore, once the ball is in real contact, the homogeneous Dirichlet condition for the velocity forces the ball to stick to the ground for all times.

Several possibilities have been proposed in literature for the cases that a rebound is expected. A simple contact algorithm has been used by Sathe & Tezduyar[128]. Their strategy is to add an artificial contact force g_c on the interface to the balance of momentum if the ball comes very close to the ground. The force depends on the distance to the ground and goes to infinity as the distance tends to zero. In this way, contact becomes impossible if the time step size is sufficiently small.

The interface condition becomes

$$(\sigma_f - g_c I)n_f = \sigma_s n_f,$$

where the contact force is defined by

$$g_c(x) = \begin{cases} 0 & \text{dist}(x, \Gamma_w) \geq \text{dist}_0, \\ \gamma_c \frac{\text{dist}(x,\Gamma_w) - \text{dist}_0}{\text{dist}(x,\Gamma_w)} & \text{dist}(x, \Gamma_w) < \text{dist}_0, \end{cases}$$

on Γ_i with a contact parameter γ_c. The additional force g_c acts like an additional fluid pressure onto the solid.

One additional advantage of such a contact force is that the usage of the structure stabilisation techniques and a larger pressure stabilisation are possible again. This is important for many applications in order to dampen inherent instabilities. However, the size of the parameters dist_0 and γ_c has to be chosen carefully. If we choose the force too big, the results will not be physical anymore. If they are too small, the contact might not be prevented.

More involved contact strategies are based on variational inequalities (see e.g. Diniz dos Santos

	Contact force parameter γ_c ($\mathrm{dist}_0 = 10^{-2}$)				
	0	100	200	400	800
$d_{\mathrm{min},1}$	$6.49 \cdot 10^{-4}$	$6.86 \cdot 10^{-4}$	$7.19 \cdot 10^{-4}$	$7.82 \cdot 10^{-4}$	$9.09 \cdot 10^{-4}$
$d_{\mathrm{max},1}$	$5.19 \cdot 10^{-2}$	$5.27 \cdot 10^{-2}$	$5.31 \cdot 10^{-2}$	$5.47 \cdot 10^{-2}$	$5.75 \cdot 10^{-2}$
$d_{\mathrm{max},2}$	-	$1.36 \cdot 10^{-3}$	$1.72 \cdot 10^{-3}$	$2.52 \cdot 10^{-3}$	$4.01 \cdot 10^{-3}$
d_{rest}	-	$1.47 \cdot 10^{-4}$	$3.84 \cdot 10^{-4}$	$9.42 \cdot 10^{-4}$	$1.97 \cdot 10^{-3}$

	Contact force parameter γ_c ($\mathrm{dist}_0 = 10^{-3}$)				
	0	100	200	400	800
$d_{\mathrm{min},1}$	$6.49 \cdot 10^{-4}$	$6.49 \cdot 10^{-4}$	$6.49 \cdot 10^{-4}$	$6.50 \cdot 10^{-4}$	$6.52 \cdot 10^{-4}$
$d_{\mathrm{max},1}$	$5.19 \cdot 10^{-2}$	$5.19 \cdot 10^{-2}$	$5.19 \cdot 10^{-2}$	$5.19 \cdot 10^{-2}$	$5.19 \cdot 10^{-2}$
$d_{\mathrm{max},2}$	-	-	-	$9.54 \cdot 10^{-2}$	$9.92 \cdot 10^{-2}$
d_{rest}	-	-	-	$3.37 \cdot 10^{-5}$	$7.91 \cdot 10^{-5}$

Table 12.3. Minimal distance $d_{\mathrm{min},1}$ during the first contact period, first and second rebound heights $d_{\mathrm{max},1}$ and $d_{\mathrm{max},2}$ and distance at rest d_{rest} depending on the applied contact force for $\mu_s = 2 \cdot 10^5$ and $\lambda_s = 8 \cdot 10^5$. *Top:* $\mathrm{dist}_0 = 10^{-2}$, *bottom:* $\mathrm{dist}_0 = 10^{-3}$.

et al.[52], Mayer et al.[108]) that impose the constraint

$$\mathrm{dist}(x, \Gamma_w) \geq 0 \quad \text{on } \Gamma_i.$$

To ensure the well-posedness of the system of equations, a Lagrange multiplier is added to the balance of momentum that acts similar to the contact force g_c when the constraint is active. Due to the additional computational complexity of numerical algorithms for variational inequalities, we prefer here the prior simple contact algorithm.

12.2.1 Influence of the contact force

As this simple contact algorithm is not physically motivated but is based on an artificial force, we have to analyse its effect on the contact dynamics. We study here two configurations we have already analysed in Section 12.1. First, we use the Lamé parameters $\mu_s = 2 \cdot 10^5$ and $\lambda_s = 8 \cdot 10^5$, the fluid viscosity $\mu_f = 10^{-3}$ and the densities $\rho_s = \rho_f = 1000$. For these parameters, a fluid layer remains between ball and ground during the first contact interval and thus using a contact algorithm is not a necessity.

In contrast to Section 12.1, we use a coarser mesh with 4225 nodes. On this coarser mesh, the ball bounces only once if we do not use a contact algorithm (due to an insufficient resolution of the contact region). From the second contact time on, it remains in contact with the ground. Second, we apply the contact algorithm to the configuration with the stiffest material parameters $\mu_s = 3.2 \cdot 10^6$ and $\lambda_s = 1.28 \cdot 10^7$ where the simulation broke down at the first contact time (see Section 12.1.3).

For the first case, we choose two different contact distances $\mathrm{dist}_0 = 10^{-2}$ and $\mathrm{dist}_0 = 10^{-3}$ and a set of parameters γ_c ranging from 100 to 800. We plot the distances between ball and ground over time for $\mathrm{dist}_0 = 10^{-2}$ in Figure 12.8. For the whole set of parameters γ_c, we observe a

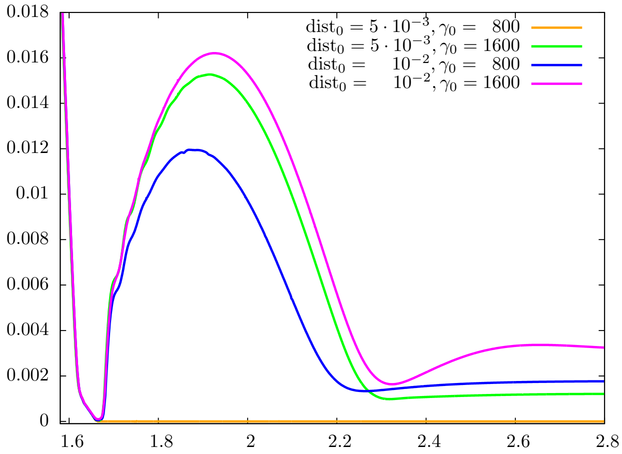

Figure 12.9. Influence of different contact parameters γ_c and dist_0 for the Lamé parameters $\mu_s = 3.2 \cdot 10^6$, $\lambda_s = 1.28 \cdot 10^7$. The contact force with parameters $\gamma_c = 800$ and $\mathrm{dist}_0 = 5 \cdot 10^{-3}$ as well as for $\gamma_c \leq 400$ or $\mathrm{dist}_0 \leq 10^{-3}$ was not large enough to prevent the contact.

second rebound with a small elevation. Afterwards, the ball comes to rest at a position with a positive distance to the ground. The rebound height is higher the bigger the contact force (i.e. the parameter γ_c) is.

For $\mathrm{dist}_0 = 10^{-2}$ and $\gamma_c = 800$ the influence of the contact force on the minimal and maximal distances to the ground is quite significant, see Table 12.3. The minimal contact distance is about 40 percent and the first rebound height about 11 percent higher compared to the simulation without a contact force. The second rebound height varies between $\mathrm{d}_{\mathrm{max},2} \approx 1.36 \cdot 10^{-3}$ and $\mathrm{d}_{\mathrm{max},2} \approx 4.01 \cdot 10^{-3}$ for the smallest and largest parameters $\gamma_c = 100$ and $\gamma_c = 800$. Finally, we note that for $\gamma_c = 800$ a notable difference of $\mathrm{d}_{\mathrm{rest}} \approx 1.97 \cdot 10^{-3}$ is kept between ball and ground at rest. This distance is more than 10 times larger as for $\gamma_c = 100$.

For $\mathrm{dist}_0 = 10^{-3}$, the influence of the contact force is much smaller. The difference of the minimal distance $\mathrm{d}_{\mathrm{min},1}$ and the first maximal elevation $\mathrm{d}_{\mathrm{max},1}$ to the simulation without a contact force are below 0.5 percent, even for the largest parameter $\gamma_c = 800$. On the other hand for $\gamma_c \leq 200$, the contact force was not large enough to prevent contact at the second contact time. We conclude that in this example the choice of $\mathrm{dist}_0 = 10^{-3}$ and $\gamma_c \geq 400$ seems to yield the most reliable results.

Secondly, we consider the situation with the stiff material parameters $\mu_s = 3.2 \cdot 10^6$ and $\lambda_s = 1.28 \cdot 10^7$ where a contact algorithm is necessary. We use $\mathrm{dist}_0 = 10^{-3}$, $5 \cdot 10^{-3}$ and 10^{-2} and choose contact parameters ranging from $\gamma_c = 400$ to 1600. Even for the biggest contact parameter $\gamma_c = 1600$, the contact force was not large enough to prevent the contact for $\mathrm{dist}_0 = 10^{-3}$. For $\mathrm{dist}_0 = 5 \cdot 10^{-3}$, the contact was only prevented for $\gamma_c = 1600$. For $\mathrm{dist}_0 = 10^{-2}$ the parameter $\gamma_c = 800$ was sufficient.

In Figure 12.9, we plot the distances to the ground over time for $\mathrm{dist}_0 = 5 \cdot 10^{-3}$ and 10^{-2}, and $\gamma_c = 800$ and 1600. The plot shows significant differences. For $\mathrm{dist}_0 = 10^{-2}$ and $\gamma_c = 1600$ the rebound height is 35 percent bigger than for $\gamma_c = 800$. Furthermore, for $\gamma_c = 1600$ and $\mathrm{dist}_0 = 10^{-2}$ the ball stays at rest at a distance of $3.18 \cdot 10^{-3}$ from the ground which is rather

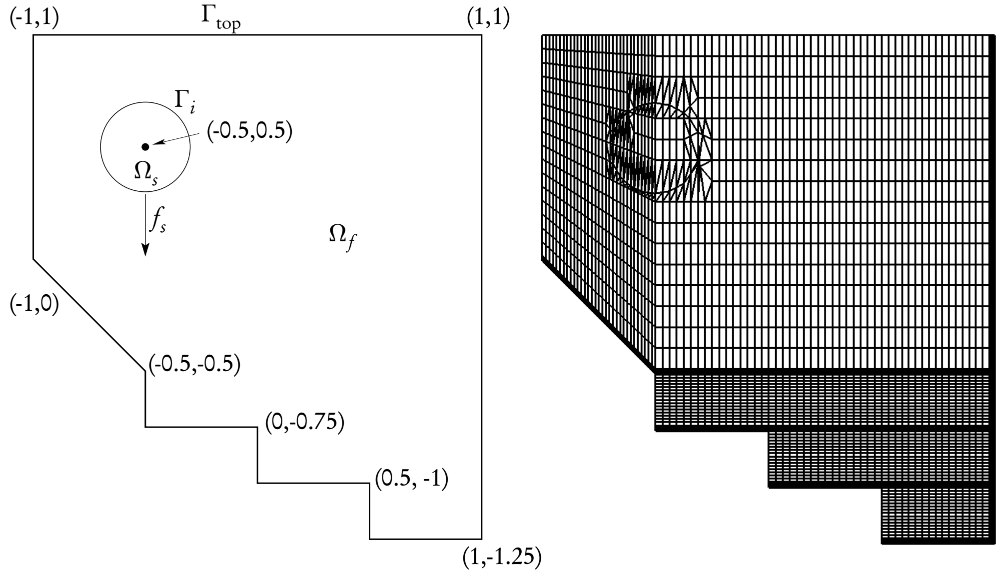

Figure 12.10. Sketch of the configuration of the second example and the initial mesh. To simulate the contact dynamics accurately, fine mesh cells are used in the contact regions.

large compared to $\mathrm{d}_{\text{rest}} \approx 1.77 \cdot 10^{-3}$ for $\gamma_c = 800$ and $\mathrm{d}_{\text{rest}} \approx 1.21 \cdot 10^{-3}$ for $\text{dist}_0 = 5 \cdot 10^{-3}$. Here it is obvious that this distance depends more on the artificial contact force (especially on the reference distance dist_0) than on physical effects.

We conclude that the contact parameters have to be chosen individually for each configuration. Furthermore, their influence must be taken into account when interpreting the results and should be checked carefully by means of parameter studies.

12.3 Example 2: Bouncing down the stairs

After these preparations, we will study a more complex numerical example, i.e. an elastic ball bouncing down some stairs. We give a sketch of the geometry under consideration in Figure 12.10, left sketch. The ball has a radius of 0.2 and its initial position is $(-0.5, 0.5)$. In order to get the desired direction, we let the ball bounce on an inclined plane first. Afterwards, it bounces down three stairs. Depending on the material parameters it can bounce once or several times on a stair or just roll over it. We consider the lower, left and right walls as rigid and impose a homogeneous Dirichlet condition for the velocity there. On the top Γ_{top}, we use again a *do-nothing* boundary condition. We use the same material parameters as in Section 12.1 and vary only the fluid density to $\rho_f = 100$, 150, 300 and 1000.

In the right sketch of Figure 12.10, we show the mesh we use. In order to capture the contact dynamics accurately, we use very fine mesh cells around all walls the ball can possibly touch. While the coarsest patches in the upper right part have a size of approximately 0.06×0.18, the size of the finest patches at the lower right corner is approximately $3 \cdot 10^{-3} \times 3 \cdot 10^{-3}$.

12.3.1 Numerical parameters and contact parameters

In this example, structural stabilisation is necessary. Furthermore, compared to the previous example we need a considerably larger pressure stabilisation in order to get stable results without increasing the computational costs too much. As in Section 11 we use the pressure stabilisation based on penalising mean values of gradients over edges

$$S_4(p_h,\psi_h) := \gamma \sum_{e\in\mathcal{E}_h} \int_e \{h_n(h_n^2 \partial_n p_h \partial_n \psi_h + h_\tau^2 \partial_\tau p_h \cdot \partial_\tau \psi_h)\}_e \, do$$

with $\gamma = 5 \cdot 10^{-3}$. Furthermore, we add the temporal pressure stabilisation

$$S_p^m(p,\psi) = \gamma_p h_P (p^m - p^{m-1}, \psi^m)_{\Gamma_i} \tag{12.1}$$

with $\gamma_p = 10^{-3}$. For structural stabilisation, we use

$$S_v(v,\phi) = 10 h_P (\nabla v, \nabla \phi)_{\Omega_s(t)}.$$

The usage of these stabilisation terms leads to problems at the contact time. The relation between solid velocity and deformation is altered, and thus the homogeneous Dirichlet condition does not necessarily prevent the solid from “passing through the bottom” anymore. Additionally, the fluid pressure is significantly smaller per se compared to Section 12.1, as the ball, and thus the contact region are smaller. Finally, on coarse grids the pressure stabilisation might dampen the fluid pressure too much.

Altogether, these issues imply that without a contact algorithm the contact between ball and ground is not prevented. In fact, we need relatively large contact parameters to avoid real contact. Therefore, we use $\text{dist}_0 = 10^{-2}$ and the contact parameters $\gamma_c = 2.5 \cdot 10^3$, $5 \cdot 10^3$, 10^4 and $2 \cdot 10^4$ studying there influence on the contact dynamics carefully.

For time discretisation, we use again the modified $dG(0)$ scheme with time step size $k = 5{\cdot}10^{-4}$. The mesh we use is illustrated in the right sketch of Figure 12.10 consisting of 7′905 nodes.

12.3.2 Results

For $\rho_f = 300$, we show snapshots of the horizontal velocity at twelve different times in Figure 12.11. The ball drops onto the inclined plane and bounces to the right. The next contact is on the right part of the first stair at position $x \approx -0.11$. Then, it falls down towards the second stair. On the second stair the ball bounces three times: at position $x \approx 0.31$, $x \approx 0.44$ and at the very end of the stair $x \approx 0.5$. After two small bounces on the lowest stair at $x \approx 0.76$ and $x \approx 0.77$, the ball comes to rest. The horizontal velocity of the solid attains a maximum after the first bounce and becomes continuously smaller from then on.

Next, we compare the simulation results for different densities. In Figure 12.12, we show contours of the ball for calculations with $\rho_f = 100$, 150, 300 and 1000. For the two larger density values, we use a contact force with parameter $\gamma_c = 5 \cdot 10^3$. For $\rho_f \leq 150$ this force was not large enough to prevent the contact (see the contact parameter studies below). Here, we use $\gamma_c = 10^4$.

As in Section 12.1.3, the rebounds are higher the smaller the fluid density is. For $\rho_f = 100$ the rebound at the first stair is so high that the ball jumps over the second stair and has its next

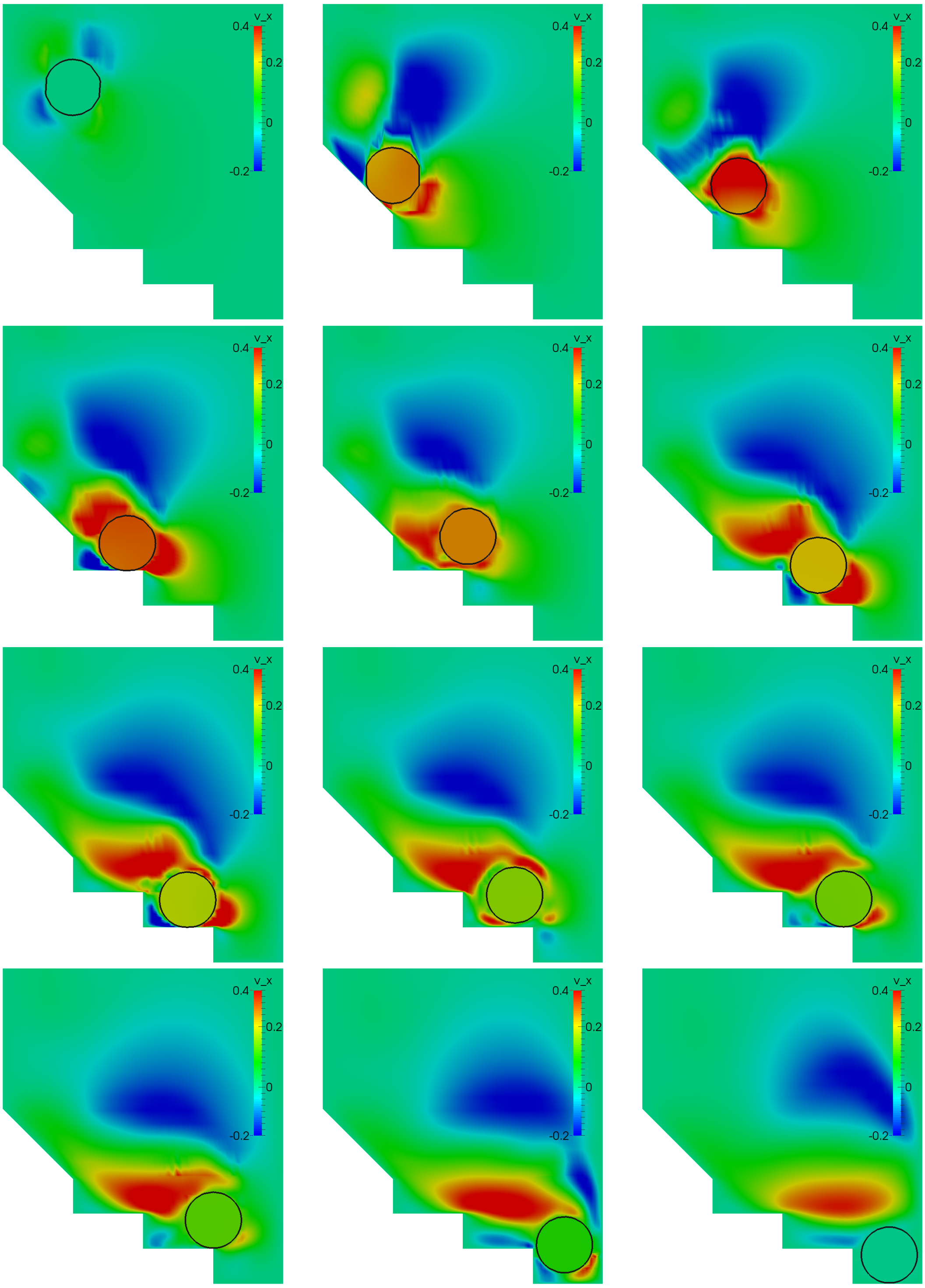

Figure 12.11. Ball bouncing down three stairs for $\rho_f = 300$ at twelve different times. The colour illustrates the horizontal velocity v_x, the black contour line is the discrete interface. *First column:* Free fall, contact with the inclined plane and rebound. *Second column:* Contact with the first stair and rebound. *Third column:* First contact with the second stair, small bounce and second contact. *Last column:* Third contact with the second stair, fall and position at rest.

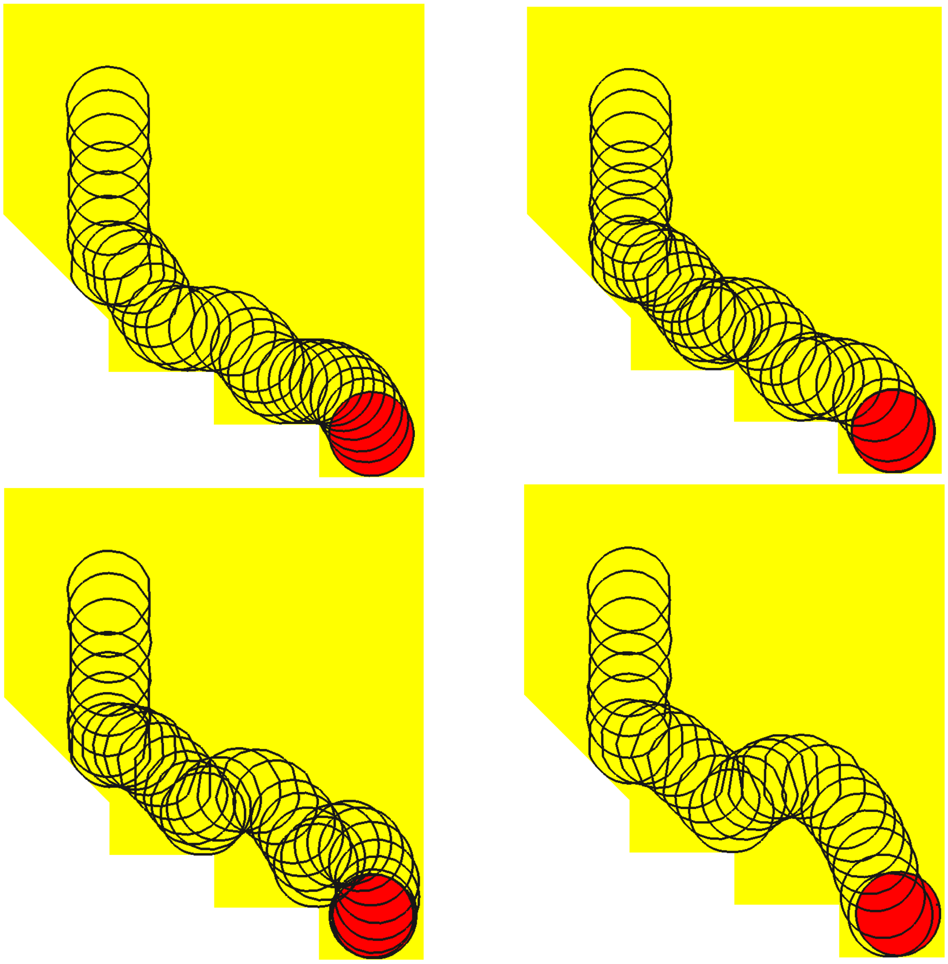

Figure 12.12. Contour plots of the interface at several times. *Top left:* $\rho_f = 1000$, *top right:* $\rho_f = 300$, *bottom left:* $\rho_f = 150$, *bottom right:* $\rho_f = 100$. While for $\rho_f = 1000$ the ball rolls over the stairs, the ball bounces exactly once on each stair for $\rho_f = 150$. For $\rho_f = 100$, the ball jumps over the second stair.

contact on the third one. On the third stair we obtain six small bounces before the ball comes to rest. On this stair the ball comes to rest for all densities as there is a rigid wall on the right. However, the ball is never in contact with the right wall and the distance to the wall is never below the reference distance $\text{dist}_0 = 10^{-2}$ where the contact force would become active. This is due to the fluid forces between the ball and the wall that slow down the horizontal movement.

For $\rho_f = 150$, the ball bounces exactly once on the first and second stair. Before dropping onto the last stair, the ball gets quite close to the right wall with a minimal distance of approximately $2 \cdot 10^{-2}$. At this point the ball is pushed to the left by fluid forces before the contact force corresponding to the right wall would get active. For $\rho_f = 300$, the rebounds are already significantly smaller and for $\rho_f = 1000$, the ball bounces once on each stair and continues rolling to the right. Afterwards, it falls down almost immediately after the stair towards the next one.

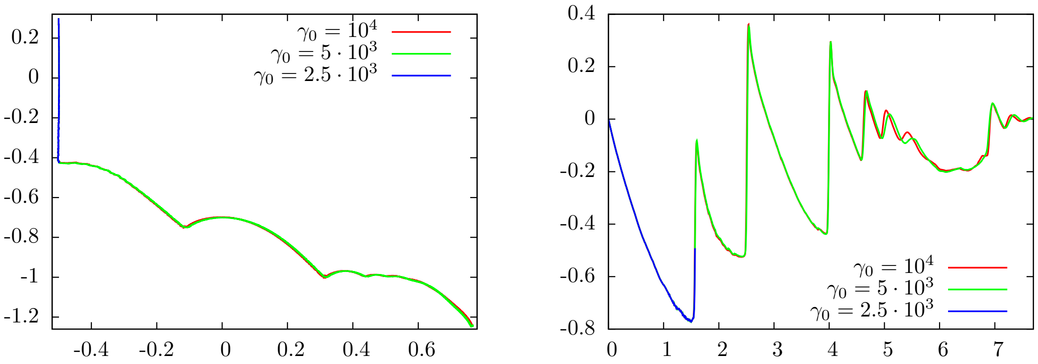

Figure 12.13. *Left:* Position of the bottom of the ball. *Right:* Averaged velocity over time for $\rho_f = 300$ and different values of the contact force. For $\gamma_c = 2.5 \cdot 10^3$ the contact could not be prevented at the first contact time. The results for $\gamma_c = 5 \cdot 10^3$ and $\gamma_c = 10^4$ are very similar.

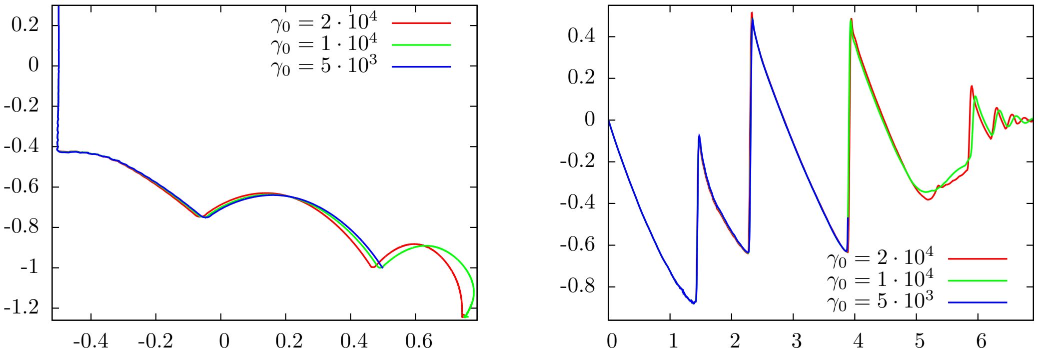

Figure 12.14. *Left:* Position of the bottom of the ball. *Right:* Averaged velocity over time for $\rho_f = 150$ and different values of the contact force. For $\gamma_c = 5 \cdot 10^3$ the contact could not be prevented at the contact time with the second stair.

12.3.3 Influence of the contact force

Finally, we study the influence of the contact force. In Figures 12.13 and 12.14 (left sketch), we plot the trajectories of the lower bottom of the ball for $\rho_f = 300$ and $\rho_f = 150$, respectively. On the right, we plot an averaged vertical velocity $\overline{v}_y$ over time. We study three different contact force parameters γ_c for both densities. For $\rho_f = 300$, we use the parameters $\gamma_c = 2.5 \cdot 10^3$, $5 \cdot 10^3$ and 10^4. For the smallest parameter, the contact force was not large enough to prevent the contact with the inclined plane and the simulation broke down. For the larger parameters, we observe very good agreement. Here, the size of the contact force seems to have less influence on the contact dynamics than in the examples studied in Section 12.2.

For $\rho_f = 150$, the contact parameter $\gamma_c = 5 \cdot 10^3$ prevents the contact on the inclined plane and on the first stair, but the contact algorithm failed on the second one. Furthermore, we observe that for larger contact parameters the velocity of the ball is slightly higher, and the ball bounces earlier on each stair. On the second stair, the ball bounces at position $x \approx 0.47$ for $\gamma_c = 2 \cdot 10^4$ compared to $x \approx 0.492$ short before the stair ends for $\gamma_c = 10^4$. As a consequence, the ball almost

	$\rho_f = 300$			$\rho_f = 150$		
γ_c	$2.5 \cdot 10^3$	$5 \cdot 10^3$	10^4	$5 \cdot 10^3$	10^4	$2 \cdot 10^4$
$d_{\text{min},1}$	0	$1.25 \cdot 10^{-3}$	$2.78 \cdot 10^{-3}$	$4.17 \cdot 10^{-4}$	$2.33 \cdot 10^{-3}$	$3.39 \cdot 10^{-3}$
$d_{\text{max},1}$	-	$4.96 \cdot 10^{-2}$	$5.17 \cdot 10^{-2}$	$1.10 \cdot 10^{-1}$	$1.13 \cdot 10^{-1}$	$1.20 \cdot 10^{-1}$
d_{rest}	-	$8.02 \cdot 10^{-3}$	$8.63 \cdot 10^{-3}$	-	$8.75 \cdot 10^{-3}$	$9.13 \cdot 10^{-3}$

Table 12.4. Minimal distance $d_{\text{min},1}$ on the first stair, subsequent rebound height $d_{\text{max},1}$ and distance at rest d_{rest} depending on the contact parameters γ_0 and dist_0 for $\rho_f = 150$ and 300. The reference distance is chosen $\text{dist}_0 = 10^{-2}$.

touches the right wall for $\gamma_c = 10^4$ when it falls down towards the third stair, while it remains at a significantly larger distance of around $6 \cdot 10^{-2}$ for $\gamma_c = 2 \cdot 10^4$. The averaged velocities show good agreement until the bounce on the second stair and differ slightly afterwards due to the different trajectories. On the third stair, we observe again higher velocities for the simulation with a higher contact force.

In Table 12.4, we show some numbers for the minimal distance during contact on the first stair as well as the subsequent rebound height and the distance at rest for both densities. The contact distance on the first stairs shows significant differences for different contact parameters. For $\rho_f = 300$, the distance for $\gamma_c = 10^4$ is more than twice as big as for $\gamma_c = 5 \cdot 10^3$. For $\rho_f = 150$, the distances for the same contact parameters differ by more than a factor of 4. These distances are significantly altered by the contact algorithm.

On the other hand, the rebound heights are in reasonable agreement and differ by at most 10 percent. The distance at rest lies between $8 \cdot 10^{-3}$ and $9.2 \cdot 10^{-3}$ for both densities and both contact parameters. Clearly, these distances are determined by the reference distance $\text{dist}_0 = 10^{-2}$ rather than by the FSI model.

We conclude that in this final example the influence of the size of the contact force was relatively small. Thus, we suppose that the simulation results might be relatively close to the ones we would get with a very fine discretisation or even to the real physical situation. However, some features of the real problem, e.g. the contact distance or the distance at rest, cannot be determined with this contact algorithm.

Finally, a full verification of the results can only be achieved by a comparison to physical experiments.

13 Simulation of plaque growth in blood vessels: A mechano-chemical fluid-structure interaction model

In this final section, we consider a mechano-chemical fluid-structure interaction problem, namely the formation and growth of plaque in blood vessels. The challenges here are threefold: first, a large coupled system of reaction, fluid- and solid-dynamics. Second, very large deformation up to a clogging of blood vessels. Third, the necessity to incorporate a wide range of time-scales, which includes the mechanical dynamics of the pulsating heart flow (<1s) and ranges up to several months, the typical scale for plaque growth. Although we focus on plaque formation here, the numerical framework presented in this section covers a wider and more general scope. Another application (with small deformation however) is e.g. the investigation of chemical flows in pipelines, where long-time effects of weathering, accelerated by the transported substances, cause material alteration.

To face the different challenges, a monolithic Eulerian approach seems promising. First, we need a method that is able to handle large deformations and secondly, it has to be able to incorporate the range of temporal scales. Numerically, this second request demands for robust implicit discretisation schemes, which allow to use large time steps. In terms of fluid-structure interactions, only monolithic formulations allow for strictly implicit schemes. In biomedical applications, monolithic schemes are preferable anyway, as the stiff coupling coming from similar densities of blood and tissue, known as the added-mass effect (see Section 3.2.1), calls for strongly coupled methods.

For validation and comparison, we also derive the complete system of equations including solid growth in ALE coordinates and present simulation results for both an ALE and a *Fully Eulerian* approach. The results of this section will be published in [69].

The organisation of this section is as follows: In Section 13.1, we introduce the coupled model for mechano-chemical fluid-structure interactions based on a simplified model for plaque growth. We formulate a long-scale problem for the coupled FSI-growth dynamics as well as a short-scale problem that will serve to estimate effective parameters. In Section 13.2, we derive the monolithic variational formulations in both ALE and fully Eulerian coordinates. Finally, we present numerical results that allow us to compare the different numerical schemes in Section 13.3.

13.1 Equations

We introduce a simplified model that describes the formation and growth of plaques in large blood vessels. For simplicity, we denote by $\Omega(t) \subset \mathbb{R}^2$ a two-dimensional domain, split into

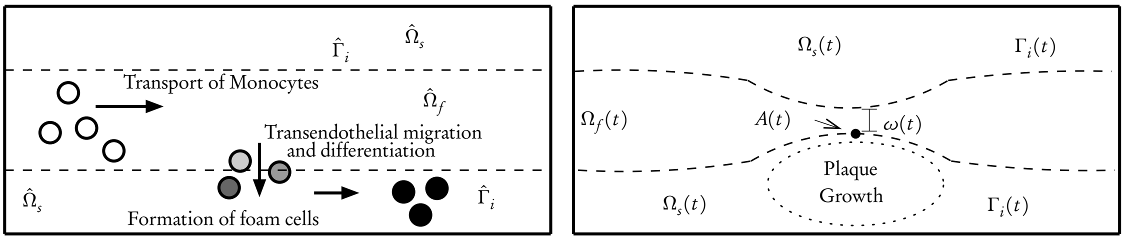

Figure 13.1. Configuration of the domain and mechanism of plaque formation. *Left:* Domain in reference configuration split into the fluid part $\hat{\Omega}_f$ and the solid $\hat{\Omega}_s$ divided by the interface $\hat{\Gamma}_i$. *Right:* Domain in the current (Eulerian) description with plaque formation and narrowing of the vessel.

the vessel wall $\Omega_s(t) \subset \mathbb{R}^2$ and the fluid domain $\Omega_f(t) \subset \mathbb{R}^2$, occupied by blood. The interface between fluid and solid is denoted by $\Gamma_i(t)$, see Figure 13.1. We model blood as an incompressible Newtonian and homogeneous fluid. The vessel wall is described by the Saint Venant-Kirchhoff material law. These models must be considered as simplification suitable for the study at hand. For advanced modelling of hemodynamical configurations, we refer to the literature (Holzapfel[87], Janela et al.[95]). Growth of the solid is modelled by a multiplicative decomposition of the deformation gradient, see Rodriguez et al.[126] and Section 13.1.3.

13.1.1 Modelling of plaque growth

For a derivation of the full model describing the bio-medical background and the mechano-chemical dynamics of plaque formation and plaque growth, we refer to Van Epps & Vorp[59], Xu et al.[149], Yang[150], Yang et al.[151] and the references cited therein. In short, the biological mechanism is evolving as follows (compare Figure 13.1): First, monocytes are transported by an advection-diffusion process within the blood flow. Secondly, they penetrate damaged parts of the vessel wall where they are transformed to macrophages. The migration rate depends on the wall stress and the damage condition of the wall. Thirdly, within the vessel wall, the macrophages are transformed into foam cells (called c_s). Finally, accumulation of foam cells leads to plaque growth. This mechano-chemical process involves a large variety of different coupled effects such as geometrical deformations, mechanical remodelling and alteration of blood and tissue behaviour. Most of these effects are not completely understood. We refer to the works of Ambrosi, Humphrey et al.[1,92] and the literature cited therein for detailed modelling of growth and remodelling in vascular mechanics. Here, however, we will strongly simplify this model.

The process of plaque formation is coupled to the dynamics of the fluid-structure interaction problem. Due to hemodynamical forces driven by the pulsating flow, the geometry deforms substantially. Furthermore, the formation of plaques significantly changes the domains. Finally, the hemodynamical forces influence the penetration of monocytes into the vessel wall and therefore a two-way coupled problem must be considered. The complete set of equations is given by

$$
\left.\begin{aligned}
\rho_f(\partial_t v_f + v_f \cdot \nabla v_f) - \operatorname{div} \sigma_f &= 0 \\
\operatorname{div} v_f &= 0
\end{aligned}\right\} \text{ in } \Omega_f(t),
$$

$$
\left.\begin{aligned}
\rho_s(\partial_t v_s + v_s \cdot \nabla v_s) - \operatorname{div} \sigma_s(c_s) &= 0 \\
\partial_t u_s + v_s \cdot \nabla u_s - v_s &= 0 \\
\partial_t c_s &= \gamma(\sigma_{WS})
\end{aligned}\right\} \text{ in } \Omega_s(t), \tag{13.1}
$$

$$
\left.\begin{aligned}
\sigma_f n_f + \sigma_s n_s &= 0 \\
v_f &= v_s
\end{aligned}\right\} \text{ on } \Gamma_i(t).
$$

The solid growth in (13.1) depends on the concentration of foam cells c_s and enters the equation via the solid stress tensor σ_s. The concentration of foam cells c_s, on the other hand, depends on the fluid wall stress σ_{WS} as described below. Models for the material laws for the stress tensors σ_f and σ_s including solid growth will be given in Section 13.1.3.

Rather than developing a quantitative model, we concentrate in this section on a robust numerical framework for the coupled long-term dynamics of fluid-structure interaction with active growth processes and large deformation. Therefore, the approximation of the chemical dynamics plays a minor role. For modelling the accumulation of foam cells c_s in (13.1), we use the simplified ODE model

$$
\gamma(\sigma_{WS}) = \gamma_0 \left(1 + \frac{\sigma_{WS}}{\overline{\sigma}}\right)^{-1}, \quad \overline{\sigma} = \frac{50\,g}{cm \cdot s^2}, \quad \gamma_0 = 5 \cdot 10^{-7}. \tag{13.2}
$$

where by σ_{WS} we denote the mean wall stress in main flow direction, averaged over the entire fluid-structure interface (see Figure 13.1)

$$
\sigma_{WS} = \int_{\Gamma_i} |\sigma_f n_f \cdot e_1| \, do.
$$

The exact role and influence of the wall stress on the migration rate is not yet completely understood. For further discussion, we refer to Bulelzai & Dubbeldam[33] and Cilla er al.[112]. Growth - depending on c_s - will take part in the middle part of the vessel walls, see Figure 13.1 and Section 13.3 for details.

Simulations of plaque growth must extend over large periods of time. The migration rate of monocytes, however, is strongly influenced by the hemodynamical forces on the vessel walls. These depend significantly on the pulsation of the blood flow. A direct simulation that resolves this short time scale and that covers a period of months is out of bounds. This very fundamental problem occurs in various applications, such as the mechanical weathering of constructions induced by the periodic cycles of day and night (due to temperature effects). In the following section, we will propose a simple strategy to include both long-term and short-scale effects.

13.1.2 Separation of the temporal scales

The big difference of temporal scales is one of the major challenges in plaque modelling: while the heart beats once in about every $1s$, plaque growth takes place in a time span of months, i.e. $t > 10^6 s$. Although all scales have a significant influence on the coupled dynamics, a numerical simulation will not be able to resolve each detail while following the long-term process. Instead, we - as most approaches - consider an averaged flow problem and focus on the long-scale dynamics of (13.2). To incorporate the effects of the short-scale dynamics, we compute effective wall stresses with the help of isolated small-scale simulations.

Accurate handling of the different time-scales is an open problem. Most approaches use an averaging in time and focus on the long-scale dynamics only (Chen et al.[39], Yang et al.[151]). Here, we will introduce two different models: first a long-scale problem, that basically corresponds to the averaging approaches found in literature. The long-scale time variable is denoted by τ, measured in units of days. Secondly, we introduce local short-scale problems resolving the pulsating flow in a short time scale denoted by t, measured in seconds, that will be used to compute an effective wall stress guiding the long-scale computations.

Remark 13.1 (Partitioning of the temporal scales). *To separate the long-scale problem from the short-scale influence, we make the following assumptions: Considering the long scale τ (days), dynamic effects of the mechanical fluid-structure interaction system do not play a role. Instead, fluid and solid are assumed to be in a stationary limit. As the long-scale problem cannot resolve the pulsating flow, a time-averaged inflow velocity $\bar{v}^{in}$ is taken as boundary condition. The only remaining temporal effect in the long-scale problem is that of the evolving chemical dynamics causing material growth.*

The short-scale effect is given by the nonlinear dynamics of the pulsating blood flow on the effective wall stress. We assume, that during the short time-period $[\tau, \tau + \delta t]$ (some heart beats), no significant change in chemistry (growth) takes place. Furthermore, we assume that the influence of the short-scale dynamics on the initial condition is small. This is important, as exact initial data is not available for isolated short-scale problems. This assumption is justified by the damping of the viscous fluid.

By the assumptions outlined in Remark 13.1, we can formulate the long-scale problem including growth:

Problem 1 (Long-scale growth). *In $I = [0, T]$, find fluid velocity v_f, pressure p_f, solid deformation u_s and foam cell concentration c_s, given by*

$$\begin{aligned} \rho_f v_f \cdot \nabla v_f - \operatorname{div} \sigma_f = 0, \quad \operatorname{div} v_f &= 0 \quad \text{in } \Omega_f(\tau) \\ -\operatorname{div} \sigma_s(c_s) &= 0 \quad \text{in } \Omega_s(\tau) \\ v_f = 0, \quad \sigma_f n_f + \sigma_s(c_s) n_s &= 0 \quad \text{on } \Gamma_i(\tau) \\ \partial_\tau c_s = \gamma(\sigma_{WS}), \quad c_s(0) &= 0 \quad \text{in } \Omega_s(\tau). \end{aligned} \tag{13.3}$$

The boundary data is given by

$$v_f = \bar{v}^{in} \text{ on } \Gamma_f^{in}, \quad \rho_f v_f n \cdot \nabla v_f - p_f n = 0 \text{ on } \Gamma_f^{out}, \quad u_s = 0 \text{ on } \Gamma_s^d, \tag{13.4}$$

where n is the outward facing normal vector and $\bar{v}^{in}$ is an averaged inflow profile that depends on the width of the blood vessel and that will be specified in Section 13.3. The average inflow rate reflects the average blood flow during one cardiac cycle.

As second problem, we consider the short-scale problem of a pulsating flow. Here, we assume, that the time scale is so short (some few cycles of the pulsation, e.g. $\delta t \approx 3s$), that further growth can be neglected. Hence, at time τ we freeze the growth and consider the problem:

Problem 2 (Short-scale pulsation). *For $\tau \geq 0$ let $c_s(\tau)$ be given. In $I^* = [\tau, \tau + \delta t]$ find fluid-velocity v_f, pressure p_f, solid deformation u_s and velocity v_s, given by*

$$\begin{aligned} \rho_f(\partial_t v_f + v_f \cdot \nabla v_f) + \operatorname{div} \sigma_f = 0, \quad \operatorname{div} v_f = 0 \quad & in\, \Omega_f(t), \\ \rho_s(\partial_t v_s + v_s \cdot \nabla v_s) + \operatorname{div} \sigma_s(c_s(\tau)) = 0, \quad \partial_t u_s + v_s \cdot \nabla u_s - v_s = 0 \quad & in\, \Omega_s(t), \\ v_f = v_s, \quad \sigma_f n_f + \sigma_s(c_s(\tau)) n_s = 0 \quad & on\, \Gamma_i(t). \end{aligned} \tag{13.5}$$

The boundary data is given by:

$$v_f = v^{in} \text{ on } \Gamma_f^{in}, \quad \rho_f \nu_f n \cdot \nabla v_f - p_f n = 0 \text{ on } \Gamma_f^{out}, \quad u_s = 0 \text{ on } \Gamma_s^d, \tag{13.6}$$

where v^{in} is a pulsating velocity profile, that depends on the width of the blood vessel and will be specified in Section 13.3.

The idea behind this two-level approach is to use the short-scale problem for the determination of an effective wall stress entering the long-scale problem. New coefficients must be computed, whenever the growth led to a significant modification of the geometry. An automatic feedback approach is possible by means of model error estimation, see Braack & Ern[25]. This, however, is subject to current research.

13.1.3 Material laws and incorporation of growth

We model blood as an incompressible Newtonian fluid and consider the Saint Venant-Kirchhoff model for the vessel wall. We will first derive the growth model in Lagrangian coordinates and carry it over to the Eulerian coordinate framework afterwards. In Lagrangian coordinates, the 2nd Piola-Kirchhoff stress tensor reads

$$\hat{\Sigma}_e := 2\mu_s \hat{E}_e + \lambda_s \operatorname{tr}(\hat{E}_e) I, \qquad \hat{E}_e := \frac{1}{2}(\hat{F}_e^T \hat{F}_e - I).$$

As in Section 2 the hats indicate, that all these quantities are given in the Lagrangian reference system. By $\hat{F}_e$, we denote the elastic deformation gradient that will be specified below, by μ_s and λ_s the Lamé material parameters.

For incorporating growth, we follow the ideas of Rodriguez and co-workers[126]. We shortly recapitulate this concept and refer the reader to Figure 13.2. By $\hat{V}$ we denote the Lagrangian, stress-free and growth-free reference system. By $\hat{V}_g$ we denote an intermediate system, that results from active growth. $\hat{V}_g$ can be considered as stress-free, but as non-physical, as growth results in an overlapping of control volumes. Finally, V is the current configuration which is stress-loaded and which is physically adjusted to the grown intermediate configuration. The deformation $\hat{u}_s$ describes the full transition from $\hat{V}$ to V:

$$\hat{T}_s := \mathrm{id} + \hat{u}_s : \hat{V} \to V, \qquad \hat{F}_s := \hat{\nabla} \hat{T}_s = I + \hat{\nabla} \hat{u}_s.$$

By $\hat{T}_g$ we denote the transition due to active growth

$$\hat{T}_g : \hat{V} \to \hat{V}_g, \quad \hat{F}_g := \hat{\nabla} \hat{T}_g.$$

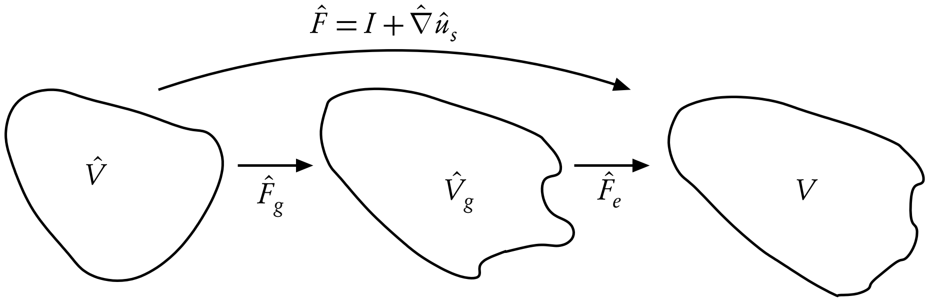

Figure 13.2. Volume elements $\hat V, \hat V_g, V$ and deformation gradients linking them. $\hat V$ denotes the stress-free Lagrangian configuration, $\hat V_g$ an intermediate (non-physical) configuration after growth and V the current volume element.

As $\hat V_g$ is considered to be stress-free, the elastic response is only based on the mapping T_e between $\hat V_g$ and V

$$\hat T_e : \hat V_g \to V, \quad \hat F_e := \hat\nabla \hat T_e,$$

see also Figure 13.2. Given a growth model $\hat T_g$, the elastic deformation gradient $\hat F_e$ can be computed from the total deformation gradient $\hat F_s = I + \hat\nabla \hat u_s$ by

$$\hat F_s = \hat F_e \hat F_g \quad \Leftrightarrow \quad \hat F_e = \hat F_s \hat F_g^{-1} = [I + \hat\nabla \hat u_s]\hat F_g^{-1}. \tag{13.7}$$

In this article, we use an isotropic growth tensor $\hat T_g(\tau) : \hat V \to \hat V_g$ such that with (13.7) it follows that

$$\hat F_g = \hat g I \quad \Rightarrow \quad \hat F_e := \hat g^{-1} \hat F_s.$$

Here, $\hat g = \hat g(\hat x, \tau)$ is a scalar function depending on the concentration of foam cells c_s that will be specified in Section 13.3.
Altogether, the elastic Green Lagrange strain is given by

$$\hat{\boldsymbol{E}}_e = \frac{1}{2}(\hat F_e^T \hat F_e - I) = \frac{1}{2}(\hat g^{-2} \hat F_s^T \hat F_s - I),$$

resulting in the Piola-Kirchhoff stresses

$$\hat F_e \hat\Sigma_e = 2\mu_s \hat F_e \hat{\boldsymbol{E}}_e + \lambda_s \operatorname{tr}(\hat{\boldsymbol{E}}_e) \hat F_e, = 2\mu_s \hat g^{-1} \hat F_s \hat{\boldsymbol{E}}_e + \lambda_s \hat g^{-1} \operatorname{tr}(\hat{\boldsymbol{E}}_e) \hat F_s.$$

13.2 Monolithic schemes for the coupled problem

In this section, we derive monolithic variational formulations for Problems 1 and 2. For both these problems we will derive two formulations: First, in Section 13.2.1 based on arbitrary Lagrangian-Eulerian coordinates (ALE). Second, in Section 13.2.2 we derive the variational formulation in fully Eulerian coordinates. While the ALE method has been applied to growth problems previously (Yang et al.[152]), the incorporation of solid growth in a fully Eulerian description is novel.

13.2.1 Coupled model in Arbitrary Lagrangian Eulerian coordinates

As in Section 3.2.2, we denote the fluid reference domain by $\hat{\Omega}_f$, and set $\hat{\Omega}_f = \Omega_f(0)$, the initial fluid domain. We define the ALE-map onto the (moving) Eulerian domain by

$$\hat{T}_f(t) : \hat{\Omega}_f \to \Omega_f(t), \quad \hat{F}_f := \hat{\nabla}\hat{T}_f, \quad \hat{J}_f := \det(\hat{F}_f).$$

To specify the map, we introduce an artificial fluid-domain deformation $\hat{u}_f$ and define

$$\hat{T}_f(\hat{x}, t) := \hat{x} + \hat{u}_f(\hat{x}, t),$$

where $\hat{u}_f$ is an extension of $\hat{u}_s$ from the interface $\hat{\Gamma}_i$ to the fluid domain. Here, we choose two different realisations. First, the harmonic extension

$$-\hat{\Delta}\hat{u}_f = 0 \text{ in } \hat{\Omega}_f, \quad \hat{u}_f = \hat{u}_s \text{ on } \hat{\Gamma}_i,$$

and second, the biharmonic extension

$$\hat{\Delta}^2\hat{u}_f = 0 \text{ in } \hat{\Omega}_f, \quad \hat{u}_f = \hat{u}_s \text{ and } \hat{n}\cdot\hat{\nabla}\hat{u}_f = \hat{n}\cdot\hat{\nabla}\hat{u}_s \text{ on } \hat{\Gamma}_i.$$

As argued in Section 3.2.2, the harmonic extension might lack regularity, in particular for problems with reentrant corners. The biharmonic extension, on the other hand, is numerically very costly, but usually gives very good mappings.

The variational systems for Problems 1 and 2 in ALE coordinates read:

Variational Formulation 1 (Long-scale, ALE). *Find the fluid velocity $\hat{v}_f \in \bar{v}^{in}(t) + \mathcal{V}_f$, deformation $\hat{u} \in \mathcal{W}$ and the pressure $\hat{p}_f \in \mathcal{L}_f$, such that*

$$(\hat{\rho}_f\hat{J}_f\hat{v}_f \cdot \hat{F}_f^{-1}\hat{\nabla}\hat{v}_f, \hat{\phi})_{\hat{\Omega}_f} + (\hat{J}_f\hat{\sigma}_f\hat{F}_f^{-T}, \hat{\nabla}\hat{\phi})_{\hat{\Omega}_f} + (\hat{F}_e\hat{\Sigma}_e, \hat{\nabla}\hat{\phi})_{\hat{\Omega}_s} = 0 \quad \forall\hat{\phi} \in \mathcal{W},$$

$$(\widehat{\operatorname{div}}(\hat{J}_f\hat{F}_f^{-1}\hat{v}_f), \hat{\xi}_f)_{\hat{\Omega}_f} = 0 \quad \forall\hat{\xi}_f \in \mathcal{L}_f,$$

where the fluid Cauchy stress is given by

$$\hat{\sigma}_f := \rho_f\nu_f(\hat{F}_f^{-1}\hat{\nabla}\hat{v}_f + \hat{\nabla}\hat{v}_f^T\hat{F}_f^{-T}) - \hat{p}_f I.$$

and the extension $\hat{u}_f$ is defined as

$$(\hat{\nabla}\hat{u}_f, \hat{\nabla}\hat{\psi}_f)_{\hat{\Omega}_f} = 0 \quad \forall\hat{\psi}_f \in \mathcal{W}_f,$$

in the case of the harmonic extension. For the biharmonic extension, we use

$$(\hat{w}_f, \hat{\chi}_f)_{\hat{\Omega}_f} - (\hat{\nabla}u_f, \hat{\nabla}\hat{\chi}_f)_{\hat{\Omega}_f} + (\hat{\nabla}\hat{w}_f, \hat{\nabla}\hat{\psi}_f)_{\hat{\Omega}_f} = 0 \quad \forall\{\hat{\psi}_f, \hat{\chi}_f\} \in \tilde{\mathcal{W}}_f \times \mathcal{W}_f.$$

The elastic deformation gradient is defined as in (13.7) depending on the concentration of foam cells. The latter one is defined by the ODE

$$\partial_\tau c_s = \gamma(\sigma_{WS}), \quad c_s(0) = 0.$$

The function spaces are given by

$$\mathcal{V}_f = [H_0^1(\hat{\Omega}_f; \hat{\Gamma}_i \cup \hat{\Gamma}_f^{in})]^2, \qquad \mathcal{L}_f = L^2(\hat{\Omega}_f),$$

$$\mathcal{W} = [H_0^1(\hat{\Omega}; \hat{\Gamma}_f^{in} \cup \hat{\Gamma}_s^d)]^2, \quad \mathcal{W}_f = [H_0^1(\hat{\Omega}_f)]^2, \quad \tilde{\mathcal{W}}_f = [H^1(\hat{\Omega}_f)]^2.$$

Remark 13.2 (Biharmonic mesh model). *We have chosen a mixed formulation for the biharmonic extension, such that an efficient discretisation with simple C^0-conforming finite elements is possible.*

Next, and in a similar fashion, we can define the ALE formulation of the short-scale problem 2:

Variational Formulation 2 (Short-scale, ALE). *For $\tau \geq 0$ let $c_s := c_s(\tau)$ be given. Find the velocity $\hat{v} \in v^{in} + \mathcal{V}$, deformation $\hat{u} \in \mathcal{W}$ and the pressure $\hat{p}_f \in \mathcal{L}_f$, such that*

$$\begin{aligned}(\rho_f \hat{J}_f \hat{\partial}_t \hat{v}_f, \hat{\phi}_f)_{\hat{\Omega}_f} + (\rho_f \hat{J}_f \hat{\nabla} \hat{v}_f \hat{F}_f^{-1}(\hat{v}_f - \partial_t \hat{u}_f), \hat{\phi})_{\hat{\Omega}_f} + (\hat{J}_f \hat{\sigma}_f \hat{F}_f^{-T}, \hat{\nabla}\hat{\phi})_{\hat{\Omega}_f} \\ + (\hat{\rho}_s^0 \hat{\partial}_t \hat{v}_s, \hat{\phi})_{\hat{\Omega}_s} + (\hat{F}_e(c_s)\hat{\Sigma}_e(c_s), \hat{\nabla}\hat{\phi})_{\hat{\Omega}_s} &= 0 \; \forall \hat{\phi} \in \mathcal{W} \\ (\widehat{\mathrm{div}}(\hat{J}_f \hat{F}_f^{-1} \hat{v}_f), \hat{\xi}_f)_{\hat{\Omega}_f} &= 0 \; \forall \hat{\xi}_f \in \mathcal{L}_f. \\ (d_t \hat{u} - \hat{v}_s, \hat{\psi}_s)_{\hat{\Omega}_s} &= 0 \; \forall \hat{\psi}_s \in \mathcal{L}_s.\end{aligned}$$

The extension $\hat{u}_f$ as well as the function spaces are defined as in Formulation 1. For the velocity, we use the global space

$$\mathcal{V} = [H_0^1(\hat{\Omega}; \hat{\Gamma}_f^{in} \cup \hat{\Gamma}_s^d)]^2,$$

the test space $\mathcal{L}_s$ is defined by

$$\mathcal{L}_s := L^2(\hat{\Omega}_s).$$

13.2.2 Coupled model in the fully Eulerian formulation

In this section, we transform the growth model introduced in the previous section from Lagrangian to Eulerian coordinates and formulate the complete system of equations in Eulerian coordinates.

As in Section 2.1, we use the mapping

$$T_s : \Omega_s(t) \to \hat{\Omega}_s, \quad T_s(x,t) := x - u_s(x,t).$$

from the current to the reference system. We denote the deformation gradient by $F_s := I - \nabla u_s$ and its determinant by $J_s := \det F_s$. From (2.6), we have the relations

$$F_s = \hat{F}_s^{-1}, \quad J_s = \hat{J}_s^{-1}. \tag{13.8}$$

As in the Lagrangian coordinate system, the Eulerian deformation gradient is split into a growth part and an elastic part. We denote the inverse mappings of $\hat{T}_g$ and $\hat{T}_e$ by T_g and T_e and their gradients by F_g and F_e respectively. Using relation (13.8), we have that

$$F_s = \hat{F}_s^{-1} = \hat{F}_g^{-1} \hat{F}_e^{-1} =: F_g F_e. \tag{13.9}$$

We will derive the correct form of the momentum equations by an integral transformation from the Lagrangian variational formulation to the Eulerian coordinate framework. The only non-standard transformation is the one including the solid stresses:

$$(\hat{F}_e \hat{\Sigma}_e, \hat{\nabla}\hat{\phi})_{\hat{\Omega}_s} = (J_s F_e^{-1} \Sigma_e, \nabla \phi F_s^{-1})_{\Omega_s(t)}.$$

Here, the determinant J_s as well as the deformation gradient F_s^{-T} stem from transformation from the Lagrangian to the Eulerian coordinate system. Furthermore, we have used the relation $\hat{F}_e = F_e^{-1}$. By the relations $J_s = J_g J_e$ and $F_s^{-1} = F_g^{-1} F_e^{-1}$, we can define the symmetric Eulerian Cauchy stress tensor of the Saint Venant-Kirchhoff solid

$$J_s F_e^{-1} \Sigma_e F_s^{-T} = J_g \underbrace{J_e F_e^{-1} \Sigma_e F_e^{-T}}_{=:\sigma_e} F_g^{-T} = J_g \sigma_e F_g^{-T}.$$

The term $J_s F_e^{-1} \Sigma_e F_s^{-T} = J_g \sigma_e F_g^{-T}$ is called the Piola transformation of $\hat{F}_e \hat{\Sigma}_e$. In strong form, the solid equations including solid growth read

$$\left.\begin{aligned} J_s \rho_s^0 (\partial_t v_s + v_s \cdot \nabla v_s) - \operatorname{div}\left(J_g \sigma_e F_g^{-T}\right) &= 0 \\ \partial_t u_s + v_s \cdot \nabla u_s - v_s &= 0 \end{aligned}\right. \quad \text{in } \Omega_s(t).$$

Solid growth in Eulerian coordinates

Next, we carry over the growth model to the Eulerian representation. We will use again the simple isotropic growth model

$$\hat{F}_g = \hat{g} I$$

and define the Eulerian growth function g by setting $g(x, \tau) = \hat{g}(\hat{x}, \tau)$. By the relation $\hat{F}_g = F_g^{-1}$, it holds that

$$F_g = g^{-1} I.$$

By the decomposition (13.9), it follows that

$$F_e = F_g^{-1} F_s = g F_s, \quad J_e = g^2 J_s. \tag{13.10}$$

The complete Eulerian stresses are given by

$$J_g \sigma_e F_g^{-T} = J_s F_e^{-1} \Sigma_e F_s^{-T} = g^{-1} J_s F_s^{-1} (2\mu_s \boldsymbol{E}_e + \lambda_s \operatorname{tr}(\boldsymbol{E}_e) I) F_s^{-T},$$

with the Eulerian elastic strain tensor

$$\boldsymbol{E}_e = \frac{1}{2}(g^{-2} F_s^{-T} F_s^{-1} - I).$$

Finally, we derive the equation of mass conservation in Eulerian coordinates. We assume, that homogeneous material with the same parameters is added, such that the density is constant $\hat{\rho}_g = \hat{\rho}_s^0$. Hence, if $m(\hat{V})$ is the mass of the reference state, $m(\hat{V}_g)$ is the mass of the grown material, which is conserved in the current configuration V

$$m(\hat{V}) = \int_{\hat{V}} \hat{\rho}_s^0 \, \mathrm{d}\hat{x}, \quad m(\hat{V}_g) = \int_{\hat{V}_g} \hat{\rho}_g \, \mathrm{d}\hat{x}^g = \int_{\hat{V}} \hat{\rho}_s^0 \hat{J}_g \, \mathrm{d}\hat{x} = \int_V \rho_s^0 \hat{J}_g J_s \, \mathrm{d}x.$$

Here, $\hat{J}_g := \det(\hat{F}_g) = \hat{g}^2$ is the determinant of the growth part. Due to mass conservation. it holds for the density ρ of the current configuration that

$$\rho = g^2 \rho_s^0 J_s.$$

Note that Eulerian quantities as e.g. ρ are again linked to Lagrangian quantities $\hat{\rho}$ by the relation $\rho(x) = \hat{\rho}(\hat{x})$.

Complete formulation in Eulerian coordinates

Variational Formulation 3 (Long-scale, Fully Eulerian). *Find velocity* $v_f(t) \in \bar{v}^{in} + \mathcal{V}_f$*, deformation* $u \in \mathcal{W}_s$ *and pressure* $p_f \in \mathcal{L}_f$*, such that*

$$\begin{aligned}(\rho_f v_f \cdot \nabla v_f, \phi_f)_{\Omega_f(\tau)} + (\sigma_f, \nabla\phi)_{\Omega_f(\tau)} + (J_g \sigma_e F_g^{-T}, \nabla\phi)_{\Omega_s(\tau)} &= 0 \quad \forall \phi \in \mathcal{W} \\ (\operatorname{div} v_f, \xi_f)_{\Omega_f(\tau)} &= 0 \quad \forall \xi_f \in \mathcal{L}_f.\end{aligned}$$

The elastic deformation gradient is defined in (13.10). Accumulation of foam cells is described by the ODE

$$\partial_\tau c_s = \gamma(\sigma_{WS}, \tau).$$

The function spaces are defined as

$$\begin{aligned}\mathcal{V}_f &= [H_0^1(\Omega_f(\tau); \Gamma_i(\tau) \cup \Gamma_f^{in})]^2, \quad & \mathcal{L}_f &= L^2(\Omega_f(\tau)), \\ \mathcal{W} &= [H_0^1(\Omega(\tau); \Gamma_f^{in} \cup \Gamma_s^d)]^2, & \mathcal{W}_s &= [H_0^1(\Omega_s(\tau); \Gamma_s^d)]^2.\end{aligned}$$

The short-scale problem is given by

Variational Formulation 4 (Short-scale, Fully Eulerian). *Find velocity* $v \in v^{in} + \mathcal{V}$*, deformation* $u \in \mathcal{W}_s$ *and pressure* $p_f \in \mathcal{L}_f$*, such that*

$$\begin{aligned}(\rho_f(\partial_t v + v \cdot \nabla v), \phi)_{\Omega_f(t)} &+ (J_s g^2 \rho_s^0 (\partial_t v + v \cdot \nabla v), \phi)_{\Omega_s(t)} \\ &+ (\sigma_f, \nabla\phi)_{\Omega_f(t)} + (J_g \sigma_e F_g^{-T}, \nabla\phi)_{\Omega_s(t)} = 0 \quad \forall \phi \in \mathcal{W}, \\ &(\operatorname{div} v_f, \xi_f)_{\Omega_f(t)} = 0 \quad \forall \xi_f \in \mathcal{L}_f, \\ &(\partial_t u + v \cdot \nabla u - v, \psi_s)_{\Omega_s(t)} = 0 \quad \forall \psi_s \in \mathcal{W}_s.\end{aligned}$$

The elastic deformation gradient is defined in (13.10). The growth function $g(\tau)$ *is set constant within the short time scale. The function spaces are given as in the previous problem except the global velocity space*

$$\mathcal{V} = [H_0^1(\Omega(t); \Gamma_f^{in} \cup \Gamma_s^d)]^2.$$

In order to capture the interface, we use again the Initial Point Set method (see Section 3.1.1).

13.3 Numerical tests

In this section, we compare results obtained with the ALE approach and the Fully Eulerian method as well as a temporal two-scale approach with a pure long-scale calculation. The objectives of these studies are threefold:

- Comparison of the two variational approaches (ALE and Fully Eulerian) with respect to accuracy, convergence and capability to simulate large deformation
- Showing the capability of the Fully Eulerian approach to model closure

- Investigation of a temporal two-scale algorithm and comparison with a simple long-scale calculation.

In Section 13.3.1 we start by discussing the long-scale case, Problem 1, only. Here, we will in particular analyse the coupled growth-FSI model and the convergence behaviour of the different numerical schemes in certain functionals, such as wall deformation, vorticity and wall stress.

The long-scale problem uses an averaged inflow velocity profile and underestimates the wall stress in main stream direction. As this output directly enters the growth model, it has a significant impact on the coupled model. Hence, in Section 13.3.2, we propose a long-scale/short-scale algorithm, where subsequent runs of the short-scale problem, Problem 2, are included to achieve better estimates for the wall stress, entering the long-scale problem.

Problem setting

As geometry we use a channel of length 10 cm and an initial width $\omega(0)$ of 2 cm as illustrated in Figure 13.1. The solid parts on the top and bottom have an initial thickness of 1 cm each. Fluid density and viscosity are given by $\rho_f = 1\,\mathrm{g/cm^3}$ and $\nu_f = 0.3\,\mathrm{cm^2/s}$. The solid parameters are given by $\rho_s = 1\,\mathrm{g/cm^3}$ and the Lamé parameters $\mu_s = 10^4$ and $\lambda_s = 4 \cdot 10^4\,\mathrm{dyn/cm^2}$. We prescribe a pulsating velocity inflow profile on Γ_f^{in} given by

$$v^{\text{in}}(t,x,y) = \frac{3}{2}\begin{pmatrix} v^{\text{in}}(t)(1-y^2) \\ 0 \end{pmatrix}, \quad v^{\text{in}}(t) = \big(\varepsilon_\omega + 5\omega(t)\big)(1+\sin(2\pi t))\,\mathrm{cm/s}, \qquad (13.11)$$

depending on the width of the channel $\omega(t)$ (see Figure 13.1). The parameter ε_ω is used to control the minimum flow rate and will be specified below. These parameters are chosen such that the temporal dynamics of the coupled problem are close to a real plaque growth situation. The remaining boundary conditions are specified in (13.4) and (13.6). For the growth, we specify a function that depends on the concentration of foam cells c_s which is defined by the ODE (13.2). We assume that growth is centered around the middle part of the vessel

$$\hat{g}(\hat{x},\hat{y},\tau) = 1 + c_s(\tau)\exp\left(-\hat{x}^2\right)(2-|\hat{y}|), \quad \hat{F}_g(\hat{x},\hat{y},\tau) := \hat{g}(\hat{x},\hat{y},\tau)I.$$

Note that both the growth $\hat{g}$ and the inflow rate v^{in} depend implicitly on the solution. As the configuration is symmetric in vertical direction, we can restrict the simulation domain to the lower half of the geometry.

Discretisation

Temporal discretisation is again based on the Rothe method. Therefore, we split the time interval I into equidistant time intervals $I_n = [\tau_n, \tau_{n+1}]$. For the Eulerian approach, we use the discretisation techniques summarised in Section 10 with the modified dG(0) time-stepping scheme ($\theta = 1$) and the *Continuous Interior Penalty* pressure stabilisation defined in (11.2). For the ALE method, we use the standard implicit Euler scheme and a Galerkin finite element scheme on a mesh consisting of quadrilaterals. We use two different codes in order to test our developments. In Gascoigne 3d[18], we use Q_2 *equal-order* finite elements with LPS-stabilisation (Becker & Braack[16]), in deal.II[10] (based on the FSI template[144]), we use the Q_2/P_1^{dc} element for the fluid part, which is *inf-sup stable* and locally mass conserving. Consequently, no pressure stabilisation is needed. The solid is again discretised with Q_2 elements.

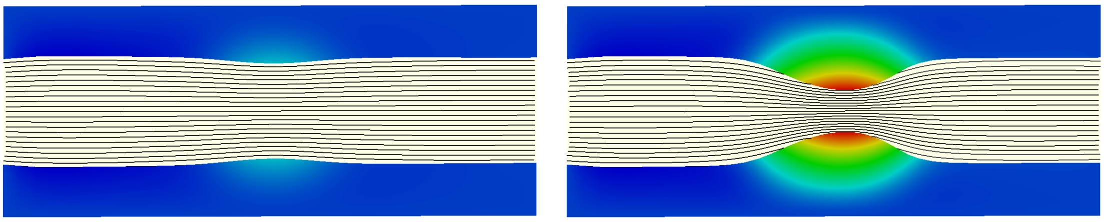

Figure 13.3. Long-scale problem: Solution of the long-scale problem after 10 days (left) and 50 days (right). Streamlines of the fluid and the deformation of the vessel wall are shown.

13.3.1 Long-scale problem

The long-scale problem is driven by a parabolic inflow profile with an average inflow rate $\bar{v}^{\text{in}}(\tau)$. We use the averaged inflow profile (13.11)

$$\bar{v}^{\text{in}}(\tau) = \big(\varepsilon_\omega + 5\omega(\tau)\big)\text{cm/s}.$$

We discretise the coupled system by a splitting in time and approximate the long-scale problem by the following iteration:

Long-scale iteration
Initialise $v^0 = 0$, $u^0 = 0$, $g^0 = 0$ and the vessel-width $\omega^0 = 2$. Set the time step $k_l = 0.1\,\text{days} = 8\,640\,s$. Iterate for $n = 1, 2, \dots$:

1. Solve the quasi-stationary long-scale problem 1:

$$\{c_s^{n-1}, \omega^{n-1}\} \mapsto \{v^n, u^n, p^n\}$$

2. Compute the width of the vessel in point $A(\tau_n)$

$$\omega^n = 2 - 2u_2^n(A(\tau_n), \tau_n)$$

3. Compute the wall stress in main stream direction

$$\sigma_{WS}^n = \int_{\Gamma_i} |\sigma_f(v^n, p^n)n \cdot e_1| \,\text{d}o \qquad (13.12)$$

4. Update the foam cell concentration

$$c_s^n = c_s^{n-1} + k_l \gamma_0 \big(1 + \sigma_{WS}^n / \overline{\sigma}\big)^{-1}$$

Long-scale problem with $\varepsilon_\omega = 0.1\,\text{cm/s}$

For our first study we choose a minimum inflow velocity of $\varepsilon_\omega = 0.1\,\text{cm/s}$. In Figure 13.3, we show the streamlines of the fluid and the deformed vessel walls at times $\tau = 10$ days and $\tau = 50$ days.

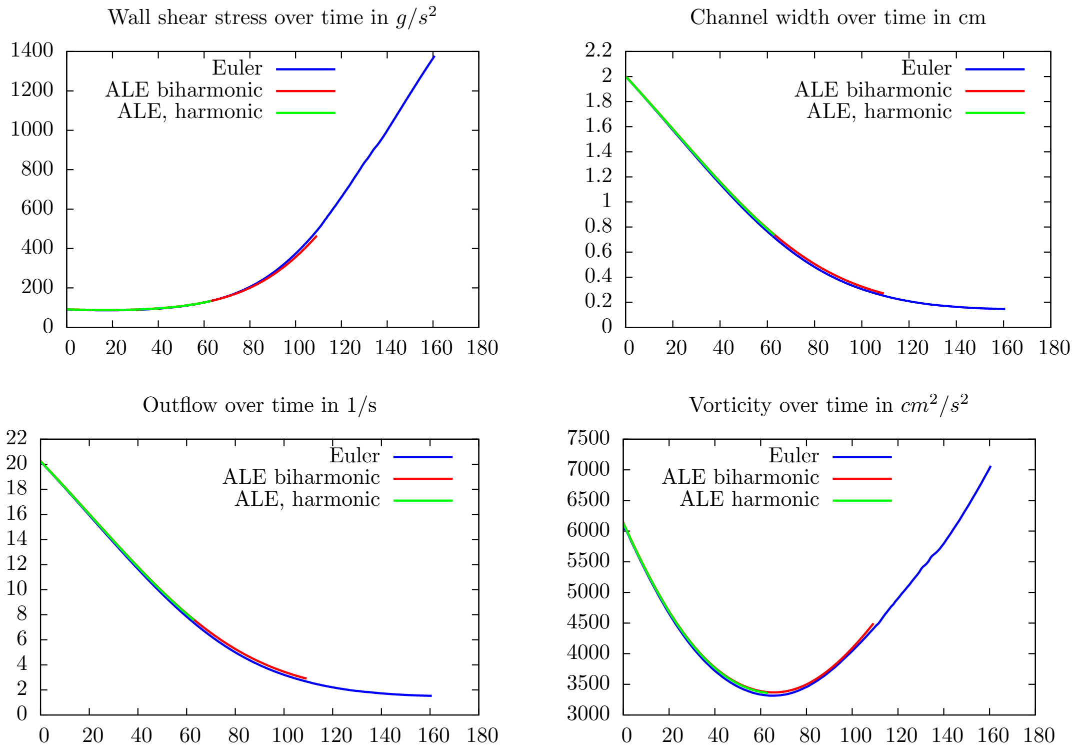

Figure 13.4. Long-scale problem: Course of different functionals over time.

In Figure 13.4 we show the course of different output functionals over time: the wall stress in main stream direction on the vessel wall Γ_i (13.12), the channel width $\omega(\tau) = 2 - 2u_2(A(\tau))$ in the centre of growth $A(\tau)$ (see Figure 13.1), the vorticity of the solution in the L^2-norm and the outflow at the right boundary defined by

$$J_{\text{vort}} = \int_{\Omega_f(\tau)} \left(\partial_y v_1 - \partial_x v_2\right)^2 dx, \qquad J_{\text{out}} = \int_{\Gamma_f^{\text{out}}} v \cdot n \, ds.$$

The functional values for the ALE method (harmonic and biharmonic extension) and the Fully Eulerian approach show very good agreement. Using the harmonic extension, the ALE method broke down at $\tau = 63.2$ days due to degeneration of mesh cells. With the biharmonic extension, we were able to get results up to $\tau = 109.3$ days.

The Fully Eulerian method, on the other hand, was able to yield reliable results until the channel was almost closed. As the inflow velocity is bounded from below by $\varepsilon_\omega = 0.1\,\text{cm/s}$ and the fluid is incompressible, a passage must always remain. As higher wall stresses slow down plaque growth, see (13.2), the vertical displacement approaches a limit. However, increasing fluid-dynamical forces cause strong horizontal deflections that finally result in a break-down of the simulation at time $t = 160.1$ days.

As the results for the ALE method with harmonic and biharmonic extension are nearly identical until time $\tau = 63.1$ days, we will not consider the harmonic variant anymore in the following tests.

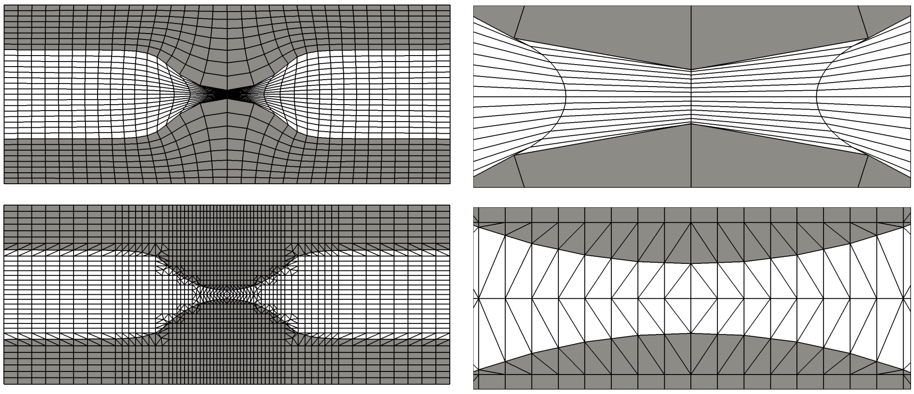

Figure 13.5. Biharmonic deformation (on top) close to break-down at $\tau = 109.3$ days and zoom-in at right. On the bottom the corresponding meshes at the same time instance $\tau = 109.3$ days for the Fully Eulerian approach are shown.

#patches	Wall Stress	Width	Vorticity	Outflow
Euler 256	$1.033 \cdot 10^2$	1.092	$3.408 \cdot 10^3$	9.251
1024	$1.050 \cdot 10^2$	1.064	$3.457 \cdot 10^3$	9.547
4096	$1.060 \cdot 10^2$	1.052	$3.472 \cdot 10^3$	9.648
Extrapol.	$1.074 \cdot 10^2$	1.047	$3.479 \cdot 10^3$	9.700
Conv.	0.77	1.81	1.71	1.55
ALE 160	$1.087 \cdot 10^2$	1.033	$3.527 \cdot 10^3$	9.892
640	$1.076 \cdot 10^2$	1.037	$3.515 \cdot 10^3$	9.849
2560	$1.073 \cdot 10^2$	1.038	$3.510 \cdot 10^3$	9.834
Extrapol.	$1.072 \cdot 10^2$	1.039	$3.506 \cdot 10^3$	9.826
Conv.	1.87	1.49	1.26	1.52

Table 13.1. Convergence of functional values at $\tau = 50$ days on three different grids for the Fully Eulerian and the ALE approach. We indicate estimated convergence rates and extrapolated values.

In Figure 13.5, we show the deformed meshes at time $\tau = 109.3$ days for the ALE approach with biharmonic mesh deformation and the Fully Eulerian approach. In the case of the biharmonic ALE approach, this was the last mesh before the calculation broke down.

Next, we study convergence with respect to the spatial grid size h for both the Fully Eulerian and the ALE approach in Table 13.1. For the Fully Eulerian approach, we use Q_1 equal-order elements and meshes with 256, 1024 and 4096 patch elements. For the ALE approach we use Q_2^c/P_1^{dc} elements and choose slightly coarser meshes for a fair comparison.

We evaluate the functionals at $\tau = 50$ days. The functional values for the ALE and the Fully Eulerian approach converge roughly against the same values. Small differences are due to time discretisation (the time step has been chosen 0.1 days) and the fact that in the ALE method, the deformation enters implicitly which means that the deformation u^n at time τ_n defines the domains Ω_f^n, Ω_s^n, while in the Fully Eulerian method, we apply the deformation explicitly, which means that the deformation u^{n-1} at time τ_{n-1} determines the domains Ω_f^n, Ω_s^n in the next time step.

Furthermore, we estimate the convergence order for all of the functionals, see Table 13.1. Besides the wall stress, all estimated convergence orders lie between linear and quadratic convergence and the ALE and the Fully Eulerian approach converge similarly. The ALE approach, however, seems to yield better values already on very coarse grids. Furthermore, the ALE approach shows faster convergence in the wall stress functional. The reason for this better performance is the use of inf-sup stable Q_2 elements in the case of ALE, which is not yet possible with the parametric interface approximation scheme described in Section 6, where stabilised $Q_1 - Q_1$ elements are used.

Long-scale problem with $\varepsilon_\omega = 0\,\mathrm{cm/s}$

An interesting aspect from a modelling point of view is the question if the channel closes completely or if there will remain a small layer of fluid between the vessel walls. As discussed before, a complete closure of the channel is not possible as long as the inflow rate ε_ω is positive. To study closure, we decrease the minimal inflow velocity ε_ω from 0.1 to 0 and reduce the velocity inflow by a factor 10 to

$$v_1^{\text{in}}(\tau) = 0.15 \cdot (5\omega(\tau))(1 - y^2)\,\mathrm{cm/s}.$$

In this configuration, the flow through the narrow part of the channel will be considerably smaller when the channel is almost closed. This has two important effects: First, the fluid forces acting against the growth of the solid are much smaller. Secondly, the wall stress becomes smaller which has a strengthening impact on the solid growth in our model. Altogether, this has the effect that the growth is much faster. Furthermore, in our simulation the channel closes completely at time $\tau = 55.8$ days.

In Figure 13.6, we show plots of the channel width and the vorticity over time. In contrast to the larger inflow velocity studied above, the fluid forces (e.g. the vorticity) decrease after $\tau \approx 40$ days which makes the closure of the channel possible. In Figure 13.7, we show the last mesh obtained with the Fully Eulerian approach ($\tau = 55.8$ days) where the channel is completely closed. The ALE calculation (with biharmonic extension) broke down at time $\tau = 40.6$ days.

13.3.2 Long-scale/short-scale problem

In the previous section, we have advanced the growth function (13.2) by

$$c_s^{n+1} = c_s^n + k\gamma_0 (1 + \sigma_{WS}^n / \overline{\sigma})^{-1},$$

where σ_{WS}^n is the wall stress in main stream direction estimated from the quasi-stationary solution at time τ_n that was obtained using the averaged inflow profile (13.11). We will see, that this value is only a very coarse prediction compared to the averaged wall stress of the short-scale problem. Hence, to enhance the quality of the coupled solution, we propose and study the following algorithm:

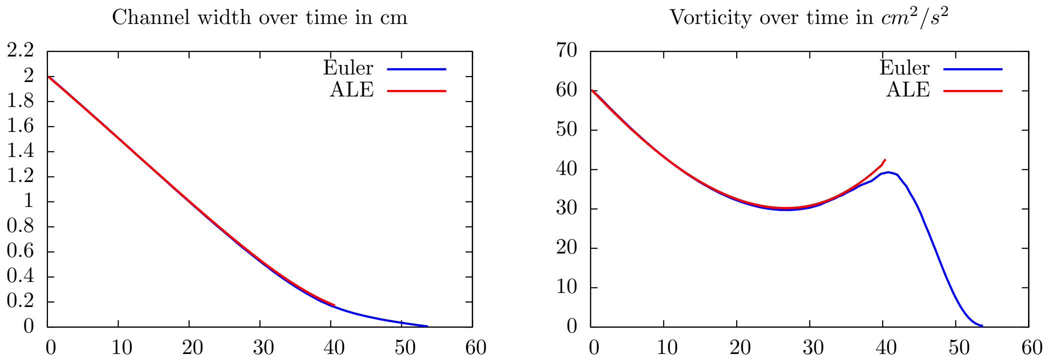
Channel width over time in cm

Vorticity over time in cm^2/s^2

Figure 13.6. Channel width and vorticity for a long-scale simulation with reduced inflow velocity. The inflow velocity goes to zero when the channel closes. This makes the complete closure of the channel possible.

Long-scale/short-scale iteration
Initialise $v^0 = 0$, $u^0 = 0$, $g^0 = 0$ and the vessel-width $\omega^0 = 2$. Set the time step $k_l = 1\,\text{day} = 86\,400\,s$. Iterate for $n = 1, 2, \dots$:

1.a) Solve the quasi-stationary long-scale problem, Problem 1:

$$\{c_s^{n-1}, \omega^{n-1}\} \mapsto \{v^n, u^n, p^n\}$$

1.b) Compute the width of the vessel in the point $A(\tau_n)$

$$\omega^n = 2 - 2u_2^n(A(\tau_n), \tau_n)$$

2.a) Set $v^{s,0} = v^n$, $u^{s,0} = u^n$ and solve the short-scale problem 2 in $I_n = (\tau_{n-1}, \tau_{n-1} + 1s)$

$$\{v^{s,0}, u^{s,0}, c_s^{n-1}, \omega^n\} \mapsto \{v^{s,m}, u^{s,m}, p^{s,m}\},\ m = 1, \dots, N_s$$

2.b) Compute the average wall stress in main stream direction

$$\sigma_{WS}^n = \frac{1}{N_s} \sum_{m=1}^{N_s} \int_{\Gamma_{\text{dam}}} |\sigma_f(v^{s,m}, p^{s,m})n \cdot \boldsymbol{e}_1| \,\mathrm{d}o$$

2.c) Update the foam cell concentration

$$c_s^n = c_s^{n-1} + k_l \gamma_0 \big(1 + \sigma_{WS}^n / \overline{\sigma}\big)^{-1}$$

Remark 13.3 (Long-scale vs. Long-scale/short-scale)**.** *The only difference between the two algorithms is the computation of the wall stress. In the long-scale algorithm, σ_{WS}^n is computed based on the long-scale solution using an averaged inflow velocity $\overline{v}_{\text{in}}$, whereas in the present section, the wall stress is computed as average of the short-scale solution in $I_{n-1} = (\tau_{n-1}, \tau_{n-1} + 1s)$ using a pulsating*

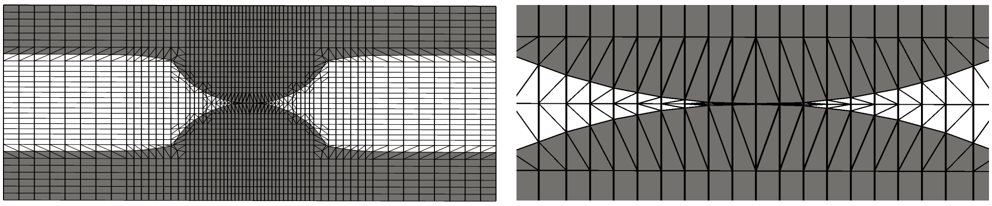

Figure 13.7. Example 13.3.1: Fully Eulerian deformation when the channel is completely closed at $\tau = 55.8$ days.

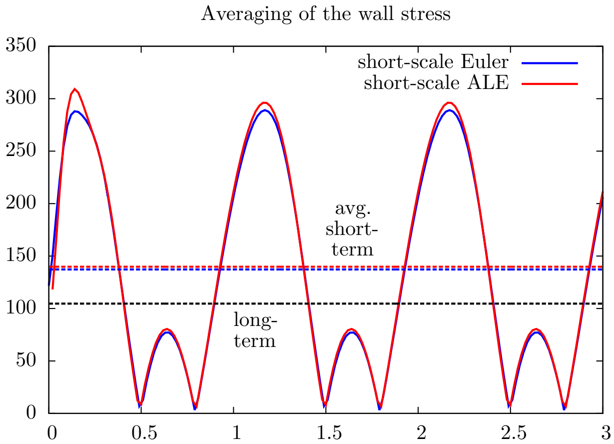

Figure 13.8. Dynamic wall stresses of the short-term problem and average values (dashed red and blue lines). Comparison with the wall stress of the long-term problem (dashed black line).

flow $v_{\text{in}}(t)$. We expect (and see) differences, as the dependency of the wall stress on the inflow profile is strongly nonlinear, such that the order of averaging has an impact.

Due to the high computational cost of the non-stationary small-scale problem we enlarge the step-size of the long-scale problem to $k = 1$ day. Using $k_s = 0.02$ s for the short-scale problem, 50 time steps of the short-scale problem are required to evaluate a prediction of the wall stress in every long-scale time step.

Analysis of the short-scale problem

We start the analysis by comparing the effect of the short-scale stress prediction. In Figure 13.8 we show the dynamic wall stress over three cycles of the heart beat $\delta t = 3$ s. The channel width as well as initial values for v_s, u_s, ω and c_s were taken from the long-term simulation at time $\tau = 50$ days. The minimum inflow velocity is again set to $\varepsilon_\omega = 0.1\,\text{cm/s}$ as in Section 13.3.1. In Figure 13.8, we compare the average of the wall stress as estimated from the dynamic short-term simulation with the wall stress coming from the long-term simulation. It turns out that, using the long-term value, we have an underestimation of about 30%. The short-term results differ only marginally between the ALE and the Eulerian formulation.

In Table 13.2, we show results of the short-scale problem for different time step sizes k_s.

k_s	Euler, 1 cycle	Euler, 3 cycles	ALE, 1 cycle	ALE, 3 cycles
0.04	$1.353 \cdot 10^2$	$1.379 \cdot 10^2$	$1.379 \cdot 10^2$	$1.409 \cdot 10^2$
0.02	$1.348 \cdot 10^2$	$1.372 \cdot 10^2$	$1.358 \cdot 10^2$	$1.398 \cdot 10^2$
0.01	$1.342 \cdot 10^2$	$1.367 \cdot 10^2$	$1.354 \cdot 10^2$	$1.389 \cdot 10^2$

Table 13.2. Local wall stress, computed from short-scale computations with the ALE and Fully Eulerian approach and for one cycle $I_n = [\tau_n, \tau_n + 1s]$ and 3 cycles $I_n = [\tau_n, \tau_n + 3s]$.

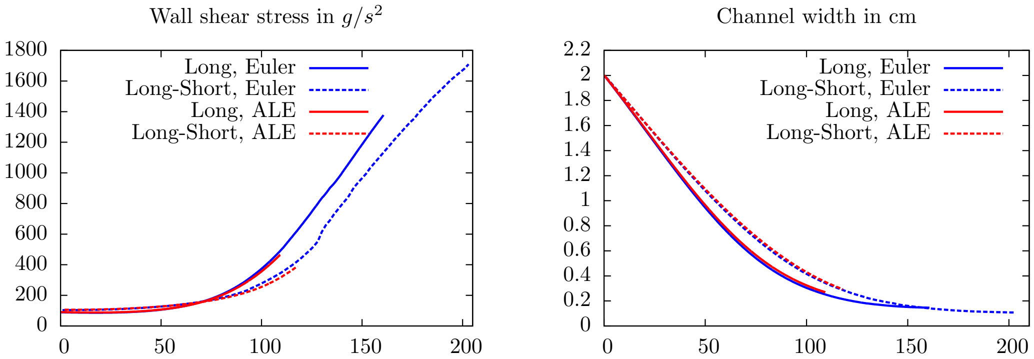

Figure 13.9. Comparison of pure long-scale computations with the long-scale/short-scale iteration. We compare wall stress and the channel width over time. The pure long-scale approach underestimates the wall stress in the beginning such that the channel closes faster.

Furthermore, we compare the locally computed mean wall stress calculated by one cycle of the periodic inflow $I_n = [\tau_n, \tau_n + 1s]$ to the mean calculated from 3 cycles $I_n = [\tau_n, \tau_n + 3s]$ and for both the ALE and the Fully Eulerian method. The values for 1 and 3 cycles differ by 1.8% and 2.8%. Considering the computational cost of these short-scale computations it seems justifiable to use only one cycle for a full long-scale/short-scale calculation. The values obtained for ALE calculations and the Fully Eulerian approach are also within reasonable agreement and seem to converge (slowly) against similar values for $k_s \to 0$. We suppose that the deviations are mainly caused by the spatial discretisation errors.

Analysis of the coupled long-scale/short-scale problem

Finally, we compare the pure long-scale strategy with the two-scale approach in a long-term simulation. In Figure 13.9, we plot the channel width and the wall stress over time. As mentioned above, the pure long-scale approach underestimates the wall stress in the beginning. Thus, the solid grows significantly faster (which on the other hand has a positive effect on the wall stress such that the plots cross at $\tau \approx 70$ days). A bisection of the channel width is reached at $\tau \approx 56$ days when using the coupled model compared to $\tau \approx 48$ days when using the pure long-scale approach in Section 13.3.1. This is a discrepancy of 17%.

As seen before, the channel width reaches a limit $\omega(\tau) \approx 0.15$ cm at $t \approx 160$ days. With the two-scale approach, the channel closes slower and a limit is reached at $\tau \approx 190$ days with a channel width $\omega(\tau) \approx 0.11$ cm. Again, the ALE and the Fully Eulerian method show reasonable agreement up to the time where the ALE mesh degenerates.

14 Conclusion and Outlook

In this thesis, we have developed accurate discretisation schemes in space and time for interface problems in Eulerian coordinates involving moving interfaces. We found that for both accuracy and stability resolving the interface within the discretisation is desirable. While our main focus was on fluid-structure interactions, the discretisation techniques are applicable for a much larger class of interface problems.

In particular, we have developed a *locally modified finite element scheme* for discretisation in space and a modified continuous Galerkin (cG) time-stepping scheme of degree 1. We provided a detailed convergence analysis for both schemes, showing second-order convergence in space and time, respectively.

The *locally modified finite element scheme* is easy to implement and shows a number of advantages in comparison to other fitted or enriched finite element methods. The background patch mesh, the number of degrees of freedom and the structure of the system matrix remain identical independent of the position of the interface. Furthermore, the conditioning of the system matrix is of optimal order if a hierarchical finite element basis is used. In combination with a *Continuous Interior Penalty* pressure stabilisation scheme, we applied the *locally modified finite element scheme* to the Stokes equation on curved domains and showed optimal-order error estimates. When we used the method to solve the wave equation on a moving domain, we found that only a non-standard stabilisation scheme that alters the velocity-displacement relation was able to reduce the inherent instabilities.

Concerning time discretisation, a space-time error analysis for standard Galerkin discretisations in time revealed that their convergence order is limited if the moving interface is not taken into account. Therefore, we modified the Galerkin trial and test spaces by using functions that are polynomial on trajectories that do not cross the interface instead of polynomials in the direction of time. We gave a detailed convergence analysis for the modified cG(1) scheme. Higher-order schemes or discontinuous Galerkin approaches can be modified analogously. We observed not only a gain in accuracy, but also in the robustness of the approach. All the analytical findings have been substantiated with numerical examples.

In the final part, we used the discretisation techniques to solve fluid-structure interaction problems within a monolithic Eulerian framework based on the *Fully Eulerian* approach (Dunne & Rannacher [56]). This monolithic approach is particularly interesting for strongly-coupled problems with large structural displacements. The novel discretisation techniques led to a significant improvement of the approach with respect to both accuracy and stability.

We studied three different applications to test the approach and to demonstrate its abilities. First, we validated the approach by means of well-studied FSI benchmark problems introduced by Hron & Turek [88]. Detailed convergence studies revealed good convergence properties in both space and time. Compared to the results of other numerical approaches that have been published, the Eulerian approach performs considerably well and the obtained functional values are in good agreement with reference values given by Turek et al.[139].

Next, we presented two applications that demonstrated the ability of the Eulerian approach to handle large structural displacements up to contact of different structures. First, we applied the framework to simulate the free fall of an elastic ball, including its contact with the ground and the subsequent rebound. When the structure was relatively soft, we found that a thin fluid layer was maintained between the ball and the ground. In the opposite case, we applied a simple contact algorithm by Sathe & Tezduyar[128]. With this approach, we were able to simulate a ball bouncing down some stairs.

Finally, we used the framework to simulate plaque growth in blood vessels using a mechano-chemical fluid-structure interaction model. In addition to a strong coupling and large displacements, this application brings a further difficulty, i.e. a significant difference in time-scales between plaque growth and flow dynamics. We proposed a simple two-scale approach to include the short-scale dynamics in a long-term simulation. Compared to a monolithic ALE approach, we found very good agreement and similar convergence behaviour in space and time, although with slightly larger constants. We found that, depending on the fluid inflow, growth led either to a complete clogging of the vessel or the system converged to a stationary state leaving a small gap between the vessels. While the ALE calculations broke down before the channel was closed, the Eulerian approach yielded reliable results up to the complete closure.

Outlook

While the Eulerian framework already performs well in the numerical examples and application problems studied above, further advances are necessary before complex real-world applications can be approached.

Further improvement of the numerical framework could focus on the following points:

- *Development of inf-sup-stable finite elements for the locally modified finite element method*
  In the applications presented in Chapter III, pressure stabilisation was one of the main issues limiting the accuracy. Stabilisation parameters had to be chosen rather small in order to allow for features such as contact and to avoid a damping of relevant dynamics. If they are too small, however, severe instabilities might arise. Within the *locally modified finite element* method, the implementation of a combined Taylor-Hood element of $Q_2 - Q_1$ type in regular patches and $P_2 - P_1$-type in interface patches seems promising. To ensure mass conservation, a discontinuous pressure space could be used, e.g. using the $Q_2 - P_1^{\mathrm{dc}}$ element. The question of whether these elements are suitable for use on anisotropic grids requires further investigation, however (see e.g. Braack et al.[27] for some available results).

- *Investigation of further time-stepping schemes for moving interface problems*
  In Section 8, we analysed a modified cG(1) time-stepping scheme. As mentioned before, the underlying techniques can be easily generalised to higher-order schemes and discontinuous Galerkin (dG) schemes. In this thesis, we used both a cG(1) and a dG(0) variant. It would be interesting to develop a general analysis for continuous and discontinuous Galerkin schemes of arbitrary order. Furthermore, the framework can be applied to the *Fractional Step Theta scheme*[30], which can be seen as a three-step Galerkin approach (Meidner & Richter[109]). The *Fractional Step Theta scheme* combines various desirable properties such

as second-order accuracy, strong A-stability and low numerical dissipation and might be of great interest in future applications.

- *Extension of the locally modified finite element scheme to three-dimensional problems*
  In most real-word applications a three-dimensional simulation is necessary. While the extension of the proposed time discretisation technique to three dimensions is straightforward, the extension of the *locally modified finite element scheme* requires some fairly technical work. In three dimensions, many more possible cut configurations have to be considered. Instead of using hexagonal patches, we propose to use tetrahedral patches here, as the number of possible cut configurations is considerably smaller. The technical difficulties thus raised are very similar to the difficulties that have to be considered for numerical quadrature in enriched or unfitted finite element schemes in three dimensions. In this context, solutions are already available in literature and in different finite element libraries (see e.g. Sudakhar & Wall[133], Bastian & Engwer[13]).

- *Efficient solvers for monolithic Eulerian approaches*
  One inherent challenge of three-dimensional simulations is the high computational cost. Therefore, the construction of efficient iterative solvers is necessary. While a lot of progress has been made recently in monolithic ALE approaches (see Section 3.2.1), no iterative solvers are available for monolithic Eulerian schemes yet. As in the case of the ALE approach, promising candidates are Krylov space solvers with a partitioned solver as a preconditioner, and monolithic multigrid approaches with a partitioning in subproblems within the smoother.

- *Adaptive grid refinement*
  A further significant reduction of the computational cost can be expected from adaptive grid refinement. This is especially promising as in many applications most of the dynamics arise in the interface region, including e.g. boundary layers that have to be resolved carefully. Thus, a first step could be a relatively simple refinement strategy that focuses on refinement in the interface region. Moreover, due to the monolithic nature of the Eulerian approach, the application of more complex refinement strategies based on gradient-based error estimation techniques (e.g. the *dual-weighted-residual method* (DWR), Becker & Rannacher[17]) is relatively straightforward (see Dunne[55]).

In addition, a variety of interesting applications can be tackled with the Eulerian framework developed in this thesis:

- *Further applications of fluid-structure interactions with large displacements or contact*
  There is a wide range of possible applications with large structural displacements for which the Eulerian framework is a promising numerical approach. One interesting example is the simulation of blood flow around the mitral valve leaflets. This application includes both a strong coupling and contact or near-contact of the leaflets. The application has been studied since the early 1970s, but still poses severe difficulties for most numerical approaches. In engineering applications, a similar contact problem can be found by the flow control by check valves.

- *Multiphase flow problems and multicomponent structures*
  Further applications for the discretisation schemes include multiphase flow problems and multicomponent structures. In the context of multiphase problems we have to distinguish between *diffuse* interfaces and *sharp* interfaces. In the case of sharp interfaces, similar challenges have to be faced as in fluid-structure interaction problems, and many of the developed techniques are directly applicable. The pressure is typically discontinuous across the interface and thus the development of an *inf-sup-stable locally modified finite element scheme* with a discontinuous pressure space is desirable.

  In the case of multicomponent structures, moving interfaces are not as common, but in the context of shape or topology optimisation problems the state equations have to be solved several times for different interface positions (see e.g. Gangl et al.[71]). To avoid the need for remeshing in every step of the optimisation algorithm, the *locally modified finite element scheme* is a promising alternative.

- *Contact algorithms*
  In the application studied in Section 12, we applied a simple contact algorithm based on an artificial surface force. We observed a significant influence of the artificial force on the contact dynamics in Section 12.2. The question of whether the observed behaviour is physical requires further investigation. More complex contact algorithms are based on variational inequalities and Lagrange multipliers (see e.g. Diniz dos Santos et al.[52], Mayer et al.[108]).

- *Fluid-structure interaction with solid growth*
  For the numerical simulation of plaque growth in Section 13, we used a greatly simplified growth model. It would be interesting to include a more realistic growth model including several chemical species and the governing equations that determine their distribution. As there are different models available in the literature there is a need to compare the numerical results with experimental observations. Furthermore, it would be interesting to try to predict where plaque growth will initiate.

- *Gradient-based optimisation*
  The monolithic Eulerian formulation allows for the application of gradient-based optimisation techniques in a rather straightforward way. Besides the computational complexity, one of the main challenges is the implicit dependency of the subdomains on the displacement variable, which has to be considered when calculating derivatives with respect to primal variables. This leads to the computation of so-called *shape derivatives* (see e.g. Sokolowski & Zolésio[131]). In the context of *a posteriori* error estimation with the *dual-weighted residual method* these derivatives have already been calculated by Dunne[55].

Acknowledgements

First of all, I would like to thank my adviser *Thomas Richter* for the opportunity to work on this very interesting and challenging topic, the funding and the excellent advising. I am grateful that he almost always had time for me, even at short notice, and that he had solutions almost immediately to nearly every problem arising in mathematical, computational or organisational matters.

I would like to thank *Rolf Rannacher* for the helpful advice, the funding in the last year and the excellent environment in the Numerical Analysis Group where I basically learned everything about Numerical Analysis that I know today.

In this context, I also want to mention *Thomas Carraro, Winnifried Wollner, Stefan Knauf, Elfriede Friedmann, Thomas Wick, Matthias Maier, Matthias Klinger, Michael Geiger, Jevgeni Vihharev, Adrian Hirn, Christian Goll, Daniel Gerecht, Sara Lee, Felix Brinkmann, Sven Wetterauer, Victoria Ponce, Florian Sonner, Ina Schüssler, Carolin Mehlmann, Simon Dörsam* and many more for fruitful discussions and the pleasant time I had within the working group. Thanks to *Thomas Richter* and *Rolf Rannacher* also for the liberty and the trust they gave me in both research and teaching.

A special thanks goes to my office mates, *Felix* and *Matthias Maier*. I shared an office with Matthias for almost four years and profited a lot from his knowledge and many discussions about Scientific Computing, Mathematics, Science or life.

I am grateful to *Thomas Wick* for the collaboration, many scientific discussions, the invitation to RICAM in Linz and the interesting conference on FSI we organised together with Thomas Richter, Huidong and Bärbel. Furthermore, I would like to thank him, *Sara, Sven* and *Felix* for the proof reading of this thesis.

I also want to mention the support and the great opportunities offered by the Heidelberg Graduate School of Mathematical and Computational Methods for the Sciences (hgs mathcomp) from which I could benefit during my doctoral research at the Faculty of Mathematics and Computer Sciences. This enabled me to participate in several conferences, to invite guest scientists and to organise the aforementioned conference.

Finally, I would like to thank my wife *Lisseth* for all her patience and the work she had, especially with our son *Fernando*, while I worked late at university. I want to thank both of them for all the joy and energy they have given me over the last years.

Schließlich danke ich meinen Eltern, die mir den Weg bis hierhin geebnet haben und ohne deren langjährige Unterstützung und Fürsorge so ziemlich nichts in meinem Leben möglich gewesen wäre.

Bibliography

[1] D Ambrosi, GA Ateshian, EM Arruda, SC Cowin, J Dumais, A Goriely, GA Holzapfel, JD Humphrey, R Kemkemer, E Kuhl, JE Olberding, LA Taber, and K Garikipati. Perspectives on biological growth and remodeling. *Journal of the Mechanics and Physics of Solids*, 59(4):863–883, 2011.

[2] Thomas Apel. *Anisotropic finite elements: Local estimates and applications*. Advances in Numerical Mathematics. Teubner, Stuttgart, 1999.

[3] Matteo Astorino and Céline Grandmont. Convergence analysis of a projection semi-implicit coupling scheme for fluid–structure interaction problems. *Numerische Mathematik*, 116(4):721–767, 2010.

[4] A Kadir Aziz and Peter Monk. Continuous finite elements in space and time for the heat equation. *Mathematics of Computation*, 52:255–274, 1989.

[5] Frank PT Baaijens. A fictitious domain/mortar element method for fluid-structure interaction. *International Journal for Numerical Methods in Fluids*, 35(7):743–761, 2001.

[6] Ivo Babuška. The finite element method for elliptic equations with discontinuous coefficients. *Computing*, 5:207–213, 1970.

[7] Ivo Babuška and Anthony Miller. The post-processing approach in the finite element method. Part 1. Calculation of displacements, stresses, and other higher derivatives of the displacements. Technical report, DTIC Document, 1982.

[8] Ivo Babuška, Uday Banarjee, and John E Osborn. Generalized finite element methods: Main ideas, results, and perspective. *International Journal of Computational Methods*, 1: 67–103, 2004.

[9] Joan Baiges and Ramon Codina. The fixed-mesh ALE approach applied to solid mechanics and fluid–structure interaction problems. *International Journal for Numerical Methods in Engineering*, 81(12):1529–1557, 2010.

[10] Wolfgang Bangerth, Timo Heister, Luca Heltai, Guido Kanschat, Martin Kronbichler, Matthias Maier, Bruno Turcksin, and Toby D Young. The `deal.II` library, version 8.2. *Archive of Numerical Software*, 3, 2015.

[11] Randolph E Bank and L Ridgeway Scott. On the conditioning of finite element equations with highly refined meshes. *SIAM Journal on Numerical Analysis*, 26(6):1383–1394, 1989.

[12] Eberhard Bänsch and Stephan Weller. Fully implicit time discretization for a free surface flow problem. *PAMM*, 11(1):619–620, 2011.

[13] Peter Bastian and Christian Engwer. An unfitted finite element method using discontinuous Galerkin. *International Journal for Numerical Methods in Engineering*, 79(12): 1557–1576, 2009.

[14] Steffen Basting and Rodolphe Prignitz. An interface-fitted subspace projection method for finite element simulations of particulate flows. *Computer Methods in Applied Mechanics and Engineering*, 267:133–149, 2013.

[15] Yuri Bazilevs, Kenji Takizawa, and Tayfun E. Tezduyar. *Computational fluid-structure interaction: methods and applications*. John Wiley & Sons, 2013.

[16] Roland Becker and Malte Braack. A finite element pressure gradient stabilization for the Stokes equations based on local projections. *Calcolo*, 38(4):173–199, 2001.

[17] Roland Becker and Rolf Rannacher. An optimal control approach to a posteriori error estimation in finite element methods. In A. Iserles, editor, *Acta Numerica 2001*, volume 37, pages 1–225. Cambridge University Press, 2001.

[18] Roland Becker, Malte Braack, Dominik Meidner, Thomas Richter, and Boris Vexler. The finite element toolkit Gascoigne3d. http://www.gascoigne.uni-hd.de.

[19] Ted Belytschko, James M Kennedy, and Daniel F Schoeberle. Quasi-Eulerian finite element formulation for fluid-structure interaction. *Journal of Pressure Vessel Technology*, 102(1):62–69, 1980.

[20] Christine Bernardi, Yvon Maday, and Anthony T Patera. Domain decomposition by the mortar element method. In *Asymptotic and numerical methods for partial differential equations with critical parameters*, pages 269–286. Springer, 1993.

[21] Daniele Boffi and Lucia Gastaldi. A finite element approach for the immersed boundary method. *Computers & Structures*, 81(8):491–501, 2003.

[22] Daniele Boffi, Lucia Gastaldi, and Luca Heltai. A finite element approach to the immersed boundary method. In *Progress in Engineering Computational Technology, B.H.V. Topping and C.A. Mota Soares Eds.*, pages 271–298. Saxe-Coburg Publications, Stirling, Scotland, 2004.

[23] Christoph Börgers. A triangulation algorithm for fast elliptic solvers based on domain imbedding. *SIAM Journal on Numerical Analysis*, 27:1187–1196, 1990.

[24] M. Braack and T. Richter. Local projection stabilization for the Stokes system on anisotropic quadrilateral meshes. In Bermudez de Castro et al., editor, *Enumath*, pages 770–778. Springer, 2005.

[25] Malte Braack and Alexandre Ern. Coupling multimodeling with local mesh refinement for the numerical solution of laminar flames. *Combustion Theory and Modelling*, 8(4): 771–788, 2004.

[26] Malte Braack and Thomas Richter. Solutions of 3D Navier-Stokes benchmark problems with adaptive finite elements. *Computers and Fluids*, 35(4):372–392, 2006.

[27] Malte Braack, Gert Lube, and Lars Röhe. Divergence preserving interpolation on anisotropic quadrilateral meshes. *Computer Methods in Applied Mathematics*, 12(2):123–138, 2012.

[28] James H Bramble and J Thomas King. A robust finite element method for nonhomogeneous Dirichlet problems in domains with curved boundaries. *Mathematics of Computation*, 63:1–17, 1994.

[29] James H Bramble and J Thomas King. A finite element method for interface problems in domains with smooth boundaries and interfaces. *Advances in Computational Mathematics*, 6:109–138, 1996.

[30] Marie Odile Bristeau, Roland Glowinski, and Jacques Periaux. Numerical methods for the Navier-Stokes equations. Applications to the simulation of compressible and incompressible viscous flows. *Computer Physics Reports*, 6(1):73–187, 1987.

[31] Alexander N Brooks and Thomas JR Hughes. Streamline upwind Petrov-Galerkin formulation for convection dominated flows with particular emphasis on the incompressible Navier-Stokes equations. *Computer Methods in Applied Mechanics and Engineering*, 32: 199–259, 1982.

[32] E Harald van Brummelen, Kristoffer G van der Zee, and René de Borst. Space/time multigrid for a fluid-structure-interaction problem. *Applied Numerical Mathematics*, 58 (12):1951–1971, 2008.

[33] Muhammad AK Bulelzai and Johan LA Dubbeldam. Long time evolution of atherosclerotic plaques. *Journal of Theoretical Biology*, 297:1–10, 2012.

[34] Erik Burman and Miguel A Fernández. An unfitted Nitsche method for incompressible fluid–structure interaction using overlapping meshes. *Computer Methods in Applied Mechanics and Engineering*, 279:497–514, 2014.

[35] Erik Burman and Peter Hansbo. Edge stabilization for Galerkin approximations of convection–diffusion–reaction problems. *Computer Methods in Applied Mechanics and Engineering*, 193(15):1437–1453, 2004.

[36] Erik Burman and Peter Hansbo. Edge stabilization for the generalized Stokes problem: a continuous interior penalty method. *Computer Methods in Applied Mechanics and Engineering*, 195(19):2393–2410, 2006.

[37] Erik Burman, Miguel A Fernández, and Peter Hansbo. Edge stabilization for the incompressible Navier-Stokes equations: a continuous interior penalty method. Technical report, 2004.

[38] Paola Causin, Jean-Frédéric Gerbeau, and Fabio Nobile. Added-mass effect in the design of partitioned algorithms for fluid-structure problems. *Computer Methods in Applied Mechanics and Engineering*, 194:4506–4527, 2005.

[39] Colin X Chen, Yan Ding, and John A Gear. Numerical simulation of atherosclerotic plaque growth using two-way fluid-structural interaction. *ANZIAM Journal*, 53:278–291, 2012.

[40] Philippe G Ciarlet. Basic error estimates for elliptic problems. In P.G. Ciarlet and J.L. Lions, editors, *Handbook of Numerical Analysis*, volume 2, pages 17–351. Elsevier, 1991.

[41] Philippe Clément. Approximation by finite element functions using local regularization. *RAIRO: Analyse numérique*, 9:77–84, 1975.

[42] Ramon Codina, Guillaume Houzeaux, Herbert Coppola-Owen, and Joan Baiges. The fixed-mesh ALE approach for the numerical approximation of flows in moving domains. *Journal of Computational Physics*, 228(5):1591–1611, 2009.

[43] Georges-Henri Cottet, Emmanuel Maitre, and Thomas Milcent. An Eulerian method for fluid-structure coupling with biophysical applications. In *ECCOMAS CFD 2006: Proceedings of the European Conference on Computational Fluid Dynamics, Egmond aan Zee, The Netherlands, September 5-8, 2006*. Delft University of Technology; European Community on Computational Methods in Applied Sciences (ECCOMAS), 2006.

[44] Georges-Henri Cottet, Emmanuel Maitre, and Thomas Milcent. Eulerian formulation and level set models for incompressible fluid-structure interaction. *ESAIM: Mathematical Modelling and Numerical Analysis*, 42(3):471–492, 2008.

[45] Daniel Coutand and Steve Shkoller. Motion of an elastic solid inside an incompressible viscous fluid. *Archive for rational mechanics and analysis*, pages 25–102, 2005.

[46] Daniel Coutand and Steve Shkoller. The interaction between quasilinear elastodynamics and the Navier-Stokes equations. *Archive for rational mechanics and analysis*, 179(3): 303–352, 2006.

[47] Paolo Crosetto, Simone Deparis, Gilles Fourestey, and Alfio Quarteroni. Parallel algorithms for fluid-structure interaction problems in haemodynamics. *SIAM Journal on Scientific Computing*, 33(4):1598–1622, 2011.

[48] Joris Degroote, Robby Haelterman, Sebastiaan Annerel, Peter Bruggeman, and Jan Vierendeels. Performance of partitioned procedures in fluid–structure interaction. *Computers & Structures*, 88(7):446–457, 2010.

[49] Simone Deparis, Marco Discacciati, Gilles Fourestey, and Alfio Quarteroni. Fluid–structure algorithms based on Steklov–Poincaré operators. *Computer Methods in Applied Mechanics and Engineering*, 195(41):5797–5812, 2006.

[50] Jean Donea, P Fasoli-Stella, and S Giuliani. Lagrangian and Eulerian finite element techniques for transient fluid-structure interaction problems. In *Structural mechanics in reactor technology*. 1977.

[51] Jean Donea, Antonio Huerta, Jean-Philippe Ponthot, and Antonio Rodríguez-Ferran. *Arbitrary Lagrangian–Eulerian Methods*. John Wiley & Sons, Ltd, 2004.

[52] N Diniz dos Santos, Jean-Frédéric Gerbeau, and Jean-François Bourgat. A partitioned fluid–structure algorithm for elastic thin valves with contact. *Computer Methods in Applied Mechanics and Engineering*, 197(19):1750–1761, 2008.

[53] Qiang Du, Max D Gunzburger, L Steven Hou, and Jeehyun Lee. Semidiscrete finite element approximations of a linear fluid-structure interaction problem. *SIAM Journal on Numerical Analysis*, 42(1):1–29, 2004.

[54] Thomas Dunne. An Eulerian approach to fluid-structure interaction and goal-oriented mesh refinement. *International Journal for Numerical Methods in Fluids*, 51:1017–1039, 2006.

[55] Thomas Dunne. *Adaptive finite element approximation of fluid-structure interaction based on Eulerian and Arbitrary Lagrangian-Eulerian variational formulations*. PhD thesis, University of Heidelberg, 2007.

[56] Thomas Dunne and Rolf Rannacher. Adaptive finite element approximation of fluid-structure interaction based on an Eulerian variational formulation. In H.-J. Bungartz and M. Schäfer, editors, *Fluid-Structure Interaction: Modeling, Simulation, Optimization*, Lecture Notes in Computational Science and Engineering, pages 110–145. Springer, 2006.

[57] Thomas Dunne, Rolf Rannacher, and Thomas Richter. Numerical simulation of fluid-structure interaction based on monolithic variational formulations. In G.P. Galdi and R. Rannacher, editors, *Comtemporary Challenges in Mathematical Fluid Mechanics*. World Scientific, Singapore, 2010.

[58] Raja Dziri and Jean-Paul Zolésio. Eulerian derivative for non-cylindrical functionals. In *Shape optimization and optimal design*, volume 216, pages 87–108. J. Cagnol, M.P. Polis, J.-P. Zolésio, 2001.

[59] J Scott Van Epps and David A Vorp. Mechanopathobiology of atherogenesis: A review. *Journal of Surgical Research*, 142:202–217, 2007.

[60] Kenneth Eriksson, Don Estep, Peter Hansbo, and Claes Johnson. *Computational differential equations*. Cambridge Univ. Press, 1996.

[61] Xufa Fang. An isoparametric finite element method for elliptic interface problems with nonhomogeneous jump conditions. *WSEAS Transactions on Mathematics*, 12, 2013.

[62] Eduard Feireisl. On the motion of rigid bodies in a viscous incompressible fluid. In *Nonlinear Evolution Equations and Related Topics*, pages 419–441. Springer, 2003.

[63] Miroslav Feistauer and Veronika Sobotíková. Finite element approximation of nonlinear problems with discontinuous coefficients. *ESAIM: Mathematical Modelling and Numerical Analysis*, 24:457–500, 1990.

[64] Peter W Fick, E Harald van Brummelen, and Kristoffer G van der Zee. On the adjoint-consistent formulation of interface conditions in goal-oriented error estimation and adaptivity for fluid-structure interaction. *Computer Methods in Applied Mechanics and Engineering*, 199:3369–3385, 2010.

[65] Robert M Franck and Roger B Lazarus. Mixed Eulerian-Lagrangian method. In *Methods in Computational Physics, vol.3: Fundamental methods in Hydrodynamics*. Academic Press: New York, 1964.

[66] Stefan Frei and Thomas Richter. A locally modified parametric finite element method for interface problems. *SIAM Journal on Numerical Analysis*, 52(5), 2014.

[67] Stefan Frei, Thomas Richter, and Thomas Wick. Eulerian techniques for fluid-structure interactions: Part I–Modeling and simulation. In *Numerical Mathematics and Advanced Applications-ENUMATH 2013*, pages 745–753. Springer, 2015.

[68] Stefan Frei, Thomas Richter, and Thomas Wick. Eulerian techniques for fluid-structure interactions: Part II–Applications. In *Numerical Mathematics and Advanced Applications-ENUMATH 2013*, pages 755–762. Springer, 2015.

[69] Stefan Frei, Thomas Richter, and Thomas Wick. Long-term simulation of large deformation, mechano-chemical fluid-structure interactions in ALE and fully Eulerian coordinates. *Journal of Computational Physics*, to appear, 2016.

[70] Thomas-Peter Fries and Andreas Zilian. On time integration in the XFEM. *International Journal for Numerical Methods in Engineering*, 79(1):69–93, 2009.

[71] Peter Gangl, Ulrich Langer, Antoine Laurain, Houcine Meftahi, and Kevin Sturm. Shape optimization of an electric motor subject to nonlinear magnetostatics. *SIAM Journal on Scientific Computing*, 37(6):B1002–B1025, 2015.

[72] Evan S Gawlik and Adrian J Lew. High-order finite element methods for moving boundary problems with prescribed boundary evolution. *Computer Methods in Applied Mechanics and Engineering*, 278:314–346, 2014.

[73] Michael W Gee, Ulrich Küttler, and Wolfgang A Wall. Truly monolithic algebraic multigrid for fluid–structure interaction. *International Journal for Numerical Methods in Engineering*, 85(8):987–1016, 2011.

[74] David Gérard-Varet, Matthieu Hillairet, and Chao Wang. The influence of boundary conditions on the contact problem in a 3d Navier–Stokes flow. *Journal de Mathématiques Pures et Appliquées*, 103(1):1–38, 2015.

[75] Axel Gerstenberger and Wolfgang A Wall. An extended finite element method/Lagrange multiplier based approach for fluid–structure interaction. *Computer Methods in Applied Mechanics and Engineering*, 197(19):1699–1714, 2008.

[76] Antonio J Gil, Aurelio Arranz Carreño, Javier Bonet, and Oubay Hassan. An enhanced immersed structural potential method for fluid–structure interaction. *Journal of Computational Physics*, 250:178–205, 2013.

[77] Roland Glowinski, Tsorng-Whay Pan, and Jacques Periaux. A fictitious domain method for Dirichlet problem and applications. *Computer Methods in Applied Mechanics and Engineering*, 111(3):283–303, 1994.

[78] Céline Grandmont. Existence for a three-dimensional steady state fluid-structure interaction problem. *Journal of Mathematical Fluid Mechanics*, 4:1–94, 2002.

[79] Christian Großmann, Hans-Görg Roos, and Martin Stynes. *Numerical treatment of partial differential equations*. Springer, 2007.

[80] Anita Hansbo and Peter Hansbo. An unfitted finite element method, based on Nitsche's method, for elliptic interface problems. *Computer Methods in Applied Mechanics and Engineering*, 191(47-48):5537–5552, 2002.

[81] Anita Hansbo and Peter Hansbo. A finite element method for the simulation of strong and weak discontinuities in solid mechanics. *Computer Methods in Applied Mechanics and Engineering*, 193:3523–3540, 2004.

[82] Peter Hansbo and Joakim Hermansson. Nitsche's method for coupling non-matching meshes in fluid-structure vibration problems. *Computational Mechanics*, 32(1-2):134–139, 2003.

[83] Matthias Heil, Andrew L Hazel, and Jonathan Boyle. Solvers for large-displacement fluid-structure interaction problems: Segregated vs. monolithic approaches. *Computational Mechanics*, 43, 2008.

[84] John G Heywood and Rolf Rannacher. Finite-element approximation of the nonstationary Navier–Stokes problem. Part IV: Error analysis for second-order time discretization. *SIAM Journal on Numerical Analysis*, 27(2):353–384, 1990.

[85] M. Hillairet. Lack of collision between solid bodies in a 2d incompressible viscous flow. *Communications in Partial Differential Equations*, 32:1345–1371, 2007.

[86] Cyril W Hirt and Billy D Nichols. Volume of fluid (vof) method for the dynamics of free boundaries. *Journal of computational physics*, 39(1):201–225, 1981.

[87] Gerhard A Holzapfel. *Nonlinear Solid Mechanics: A Continuum Approach for Engineering*. Wiley-Blackwell, 2000.

[88] Jaroslav Hron and Stefan Turek. Proposal for numerical benchmarking of fluid-structure interaction between an elastic object and laminar incompressible flow. In H.-J. Bungartz and M. Schäfer, editors, *Fluid-Structure Interaction: Modeling, Simulation, Optimization*, Lecture Notes in Computational Science and Engineering, pages 371–385. Springer, 2006.

[89] Jaroslav Hron and Stefan Turek. A monolithic FEM/multigrid solver for an ALE formulation of fluid-structure interaction with applications in biomechanics. In H.-J. Bungartz and M. Schäfer, editors, *Fluid-Structure Interaction: Modeling, Simulation, Optimization*, Lecture Notes in Computational Science and Engineering, pages 146–170. Springer, 2006.

[90] Jaroslav Hron, Stefan Turek, Martin Madlik, Mudassar Razzaq, Hilmar Wobker, and Jens F. Acker. Numerical simulation and benchmarking of a monolithic multigrid solver for fluid-structure interaction problems with application to hemodynamics. In H.-J.

Bungartz and M. Schäfer, editors, *Fluid-Structure Interaction II: Modeling, Simulation, Optimization*, Lecture Notes in Computational Science and Engineering, pages 197–220. Springer, 2010.

[91] Thomas JR Hughes, Wing Kam Liu, and Thomas K Zimmermann. Lagrangian-Eulerian finite element formulation for incompressible viscous flows. *Computer Methods in Applied Mechanics and Engineering*, 29(3):329–349, 1981.

[92] Jay D Humphrey. Vascular mechanics, mechanobiology and remodeling. *Journal of Mechanics in Medicine and Biology*, 9(2):243–257, 2009.

[93] Mihaela Ignatova, Igor Kukavica, Irena Lasiecka, and Amjad Tuffaha. On well-posedness and small data global existence for an interface damped free boundary fluid–structure model. *Nonlinearity*, 27(3):467, 2014.

[94] Satoshi Ii, Kazuyasu Sugiyama, Shu Takagi, and Yoichiro Matsumoto. A computational blood flow analysis in a capillary vessel including multiple red blood cells and platelets. *Journal of Biomechanical Science and Engineering*, 7(1):72–83, 2012.

[95] João Janela, Alexandra Moura, and Adélia Sequeira. Absorbing boundary conditions for a 3d non-Newtonian fluid-structure interaction model for blood flow in arteries. *International Journal of Engineering Science*, 2010.

[96] Shintaro Takeuchi Shu Takagi Kazuyasu Sugiyama, Satoshi Ii and Yoichiro Matsumoto. Full Eulerian simulations of biconcave neo-Hookean particles in a Poiseuille flow. *Computational Mechanics*, 46:147–157, 2010.

[97] Stefan Kollmannsberger, Sebastian Geller, Alexander Düster, Jonas Tölke, Christian Sorger, Manfred Krafczyk, and Ernst Rank. Fixed-grid fluid–structure interaction in two dimensions based on a partitioned Lattice Boltzmann and p-FEM approach. *International Journal for Numerical Methods in Engineering*, 79(7):817–845, 2009.

[98] Ulrich Küttler and Wolfgang A Wall. Fixed-point fluid–structure interaction solvers with dynamic relaxation. *Computational Mechanics*, 43(1):61–72, 2008.

[99] Aymen Laadhari, Ricardo Ruiz-Baier, and Alfio Quarteroni. Fully Eulerian finite element approximation of a fluid-structure interaction problem in cardiac cells. *International Journal for Numerical Methods in Engineering*, 96(11):712–738, 2013.

[100] Stig Larsson, Vidar Thomée, and Lars B Wahlbin. Finite-element methods for a strongly damped wave equation. *IMA Journal of Numerical Analysis*, 11(1):115–142, 1991.

[101] Patrick Le Tallec and Saloua Mani. Numerical analysis of a linearised fluid-structure interaction problem. *Numerische Mathematik*, 87(2):317–354, 2000.

[102] Antoine Legay, Jack Chessa, and Ted Belytschko. An Eulerian-Lagrangian method for fluid-structure interaction based on level sets. *Computer Methods in Applied Mechanics and Engineering*, 195:2070–2087, 2006.

[103] Christoph Lehrenfeld and Arnold Reusken. Analysis of a Nitsche XFEM-DG discretization for a class of two-phase mass transport problems. *SIAM Journal on Numerical Analysis*, 51(2):958–983, 2013.

[104] Xiaoye S Li and James W Demmel. SuperLU_DIST: A scalable distributed-memory sparse direct solver for unsymmetric linear systems. *ACM Transactions on Mathematical Software*, 29(2):110–140, 2003.

[105] Mitchell Luskin and Rolf Rannacher. On the smoothing property of the Crank-Nicolson scheme. *Applicable Analysis*, 14:117–135, 1982.

[106] Robert J MacKinnon and Graham F Carey. Treatment of material discontinuities in finite element computations. *International Journal for Numerical Methods in Engineering*, 24:393–417, 1987.

[107] André Massing, Mats G Larson, Anders Logg, and Marie E Rognes. A Nitsche-based cut finite element method for a fluid–structure interaction problem. *ArXiv e-prints*, 2015.

[108] Ursula M Mayer, Alexander Popp, Axel Gerstenberger, and Wolfgang A Wall. 3d fluid–structure-contact interaction based on a combined XFEM FSI and dual mortar contact approach. *Computational Mechanics*, 46(1):53–67, 2010.

[109] Dominik Meidner and Thomas Richter. Goal-oriented error estimation for the fractional step theta scheme. *Computational Methods in Applied Mathematics*, 14(2):203–230, 2014.

[110] Dominik Meidner and Boris Vexler. A priori error analysis of the Petrov-Galerkin Crank-Nicolson scheme for parabolic optimal control problems. *SIAM Journal on Control and Optimization*, 49:2183–2211, 2011.

[111] Nicolas Moës, John Dolbow, and Ted Belytschko. A finite element method for crack growth without remeshing. *International Journal for Numerical Methods in Engineering*, 46:131–150, 1999.

[112] Estefanía Peña Myriam Cilla and Miguel A Martínez. Mathematical modelling of atheroma plaque formation and development in coronary arteries. *Journal of The Royal Society Interface*, 11(90), 2013.

[113] Joachim A Nitsche. Über ein Variationsprinzip zur Lösung von Dirichlet-Problemen bei Verwendung von Teilräumen, die keinen Randbedingungen unterworfen sind. *Abhandlungen aus dem Mathematischen Seminar der Universität Hamburg*, 36:9–15, 1970.

[114] Fabio Nobile and Christian Vergara. Partitioned algorithms for fluid-structure interaction problems in haemodynamics. *Milan Journal of Mathematics*, 80(2):443–467, 2012.

[115] William F Noh. CEL: A time-dependent, two-space-dimensional, coupled Eulerian-lagrange code. Technical report, Lawrence Radiation Lab., Univ. of California, Livermore, 1963.

[116] Kwang-Chun Park, Carlos A Felippa, and Roger Ohayon. Partitioned formulation of internal fluid–structure interaction problems by localized Lagrange multipliers. *Computer Methods in Applied Mechanics and Engineering*, 190(24):2989–3007, 2001.

[117] Charles S Peskin. Flow patterns around heart valves: a numerical method. *Journal of Computational Physics*, 10(2):252–271, 1972.

[118] Serge Piperno, Charbel Farhat, and Bernard Larrouturou. Partitioned procedures for the transient solution of coupled aroelastic problems. Part i: Model problem, theory and two-dimensional application. *Computer Methods in Applied Mechanics and Engineering*, 124(1):79–112, 1995.

[119] Rolf Rannacher and Thomas Richter. An adaptive finite element method for fluid-structure interaction problems based on a fully Eulerian formulation. In H.J. Bungartz, M. Mehl, and M. Schäfer, editors, *Fluid-Structure Interaction II, Modelling, Simulation, Optimization*, number 73 in Lecture notes in computational science and engineering, pages 159–192. Springer, 2010.

[120] Thomas Richter. Goal oriented error estimation for fluid-structure interaction problems. *Computer Methods in Applied Mechanics and Engineering*, 223-224:28–42, 2012.

[121] Thomas Richter. A fully Eulerian formulation for fluid-structure interactions. *Journal of Computational Physics*, 233:227–240, 2013.

[122] Thomas Richter. *Finite Elements for Fluid-Structure Interactions*. Springer, 2015. in preparation.

[123] Thomas Richter. A monolithic geometric multigrid solver for fluid-structure interactions in ALE formulation. *International Journal for Numerical Methods in Engineering*, 104(5): 372–390, 2015.

[124] Thomas Richter and Thomas Wick. Finite elements fo fluid-structure interaction in ALE and fully Eulerian coordinates. *Computer Methods in Applied Mechanics and Engineering*, 2010.

[125] Thomas Richter and Thomas Wick. Optimal control and parameter estimation for stationary fluid-structure interaction problems. *SIAM Journal on Scientific Computing*, 35 (5):B1085–B1104, 2013.

[126] Edward K Rodriguez, Anne Hoger, and Andrew D McCulloch. Stress-dependent finite growth in soft elastic tissues. *J. Biomechanics*, 4:455–467, 1994.

[127] Marzio Sala, Kendall S Stanley, and Michael A Heroux. On the design of interfaces to sparse direct solvers. *ACM Transactions on Mathematical Software (TOMS)*, 34(2):9, 2008.

[128] Sunil Sathe and Tayfun E Tezduyar. Modeling of fluid–structure interactions with the space–time finite elements: contact problems. *Computational Mechanics*, 43(1):51–60, 2008.

[129] L Ridgeway Scott and Shangyou Zhang. Finite element interpolation of nonsmooth functions satisfying boundary conditions. *Mathematics of Computation*, 54(190):483–493, 1990.

[130] Gregory R Shubin and John B Bell. An analysis of grid orientation effect in numerical simulation of miscible displacement. *Computer Methods in Applied Mechanics and Engineering*, 47:47–71, 1984.

[131] Jan Sokolowski and Jean-Paul Zolesio. *Introduction to shape optimization*. Springer, 1992.

[132] Keith Stein, Tayfun E Tezduyar, and Richard Benney. Mesh moving techniques for fluid-structure interactions with large displacements. *Journal of Applied Mechanics*, 70(1): 58–63, 2003.

[133] Yogaraj Sudhakar and Wolfgang A Wall. Quadrature schemes for arbitrary convex/concave volumes and integration of weak form in enriched partition of unity methods. *Computer Methods in Applied Mechanics and Engineering*, 258:39–54, 2013.

[134] Kazuyasu Sugiyama, Satoshi Ii, Shintaro Takeuchi, Shu Takagi, and Yoichiro Matsumoto. A full Eulerian finite difference approach for solving fluid-structure coupling problems. *Journal of Computational Physics*, 230:596–627, 2011.

[135] Roger Temam. *Navier-Stokes Equations: Theory and Numerical Analysis*. American Mathematical Society, 2000.

[136] Tayfun E Tezduyar, Marek Behr, and James Liou. A new strategy for finite element computations involving moving boundaries and interfaces - the deforming-spatial-domain/space-time procedure: I the concept and the preliminary numerical tests. *Computer Methods in Applied Mechanics and Engineering*, 94:339–351, 1992.

[137] Andrej N Tikhonov and Aleksandr A Samarskii. Homogeneous difference schemes. *USSR Computational Mathematics and Mathematical Physics*, 1:5–67, 1962.

[138] Clifford A Truesdell. A first course in rational continuum mechanics. *Pure and applied mathematics*, 71:3–375, 1991.

[139] Stefan Turek, Jaroslav Hron, Mudassar Razzaq, Hilmar Wobker, and Michael Schäfer. *Numerical benchmarking of Fluid-Structure Interaction: A comparison of different discretization and solution approaches*. Springer, 2010.

[140] Alexander Ženíšek. The finite element method for nonlinear elliptic equations with discontinuous coefficients. *Numerische Mathematik*, 58:51–77, 1990.

[141] Xiaodong Wang and Wing Kam Liu. Extended immersed boundary method using FEM and RKPM. *Computer Methods in Applied Mechanics and Engineering*, 193(12):1305–1321, 2004.

[142] Thomas Wick. Fluid-structure interactions using different mesh motion techniques. *Computers and Structures*, 89:1456–1467, 2011.

[143] Thomas Wick. *Adaptive Finite Element Simulation of Fluid-Structure Interaction with Application to Heart-Valve Dynamics*. PhD thesis, University of Heidelberg, 2011.

[144] Thomas Wick. Solving monolithic fluid-structure interaction problems in arbitrary Lagrangian Eulerian coordinates with the deal.ii library. *Archive of Numerical Software*, 1:1–19, 2013.

[145] Thomas Wick. Fully Eulerian fluid–structure interaction for time-dependent problems. *Computer Methods in Applied Mechanics and Engineering*, 255:14 – 26, 2013.

[146] Thomas Wick. Flapping and contact FSI computations with the fluid–solid interface-tracking/interface-capturing technique and mesh adaptivity. *Computational Mechanics*, 53(1):29–43, 2014.

[147] Joseph T Wloka. *Partielle Differentialgleichungen*. Teubner, Stuttgart, 1982.

[148] Hui Xie, Kazufumi Ito, Zhilin Li, and Jari Toivanen. A finite element method for interface problems with locally modified triangulation. *Contemporary Mathematics*, 466: 179–190, 2008.

[149] Zhiliang Xu, Nan Chen, Shawn C Shadden, Jerrold E Marsden, Malgorzata M. Kamocka, Elliot D. Rosen, and Mark Alber. Study of blood flow impact on growth of thrombi using a multiscale model. *Soft Matter*, 5:769–779, 2009.

[150] Yifan Yang. Mathematical modeling and simulation of the evolution of plaques in blood vessels. PhD thesis, Heidelberg University, 2014.

[151] Yifan Yang, Willi Jäger, Maria Neuss-Radu, and Thomas Richter. Mathematical modeling and simulation of the evolution of plaques in blood vessels. *Journal of Mathematical Biology*, pages 1–24, 2014.

[152] Yifan Yang, Thomas Richter, Willi Jäger, and Maria Neuss-Radu. An ALE approach to mechano-chemical processes in fluid-structure interactions. *International Journal for Numerical Methods in Fluids*, submitted, 2015.

[153] Zhaosheng Yu. A DLM/FD method for fluid/flexible-body interactions. *Journal of Computational Physics*, 207(1):1–27, 2005.

[154] Kristoffer G van der Zee, E Harald van Brummelen, Ido Akkerman, and René de Borst. Goal-oriented error estimation and adaptivity for fluid-structure interaction using exact linearized adjoints. *Computer Methods in Applied Mechanics and Engineering*, 200:2738–2757, 2011.

[155] Lucy Zhang, Axel Gerstenberger, Xiaodong Wang, and Wing Kam Liu. Immersed finite element method. *Computer Methods in Applied Mechanics and Engineering*, 193(21): 2051–2067, 2004.

[156] Paolo Zunino. Analysis of backward Euler/extended finite element discretization of parabolic problems with moving interfaces. *Computer Methods in Applied Mechanics and Engineering*, 258:152–165, 2013.

Colophon

This document is typeset in URW Garamond
with LaTeX 2$_\varepsilon$ using the TeX *Live* distribution.